Multiscale modeling of fracture mechanism in cementitious composites using the peridynamic method and enhancement in its implementation

by

Amin Yaghoobi

(Under the Direction of Mi G. Chorzepa)

Abstract

In the present dissertation, a multiscale meshless framework based on peridynamic theory is developed to study fracture behavior of cementitious composite materials. The most general form, non-ordinary state-based peridynamics (NOSBPD) is implemented as a promising computational tool in fracture analysis while using classical constitutive equations. The NOSBPD is successfully implemented for finite strain material. The dynamic relaxation method is also adopted to obtain quasi-static solution of the system of peridynamic equations. Furthermore, a higher-order approximation method is introduced to control the spurious deformation mode conventionally found in the NOSBPD formulation. This dissertation considers two major efforts in fracture modeling of heterogeneous cementitious composite materials. First, a framework is proposed to predict the response of fiber reinforced concrete (FRC) structures. This approach includes a semi-discrete method in modeling the fiber reinforcement. Second, a mesoscale modeling of concrete members is proposed in which heterogeneous concrete material is represented by four phases (cementitious matrix, coarse aggregates, interfacial transition zone and air voids) in the NOSBPD framework. A statistical study is provided to comprise the effect of random distributions of constituent materials. Finally, two approaches are considered to decrease the computational cost in NOSBPD simulations. The first approach accounts for symmetry boundary conditions in a peridynamic

body. The present formulation introduces constraints which allow modeling of local symmetry conditions. Furthermore, in the second approach, the NOSBPD is coupled with the finite element method (FEM). The coupling method enables using peridynamics at discontinuities such as cracks, while using more efficient finite elements for the surrounding body. These two methods effectively reduce the solution time while maintaining accuracy. The validity of the proposed approaches is studied through various examples, and they are found successful and worthwhile for fracture analysis of brittle materials.

INDEX WORDS: State-based peridynamics, Non-ordinary formulation,
Multiscale modeling, Fracture analysis, Cementitious composites,
Stability, Fiber reinforcement

Multiscale modeling of fracture mechanism in cementitious composites using the peridynamic method and enhancement in its implementation

by

Amin Yaghoobi

B.S., University of Tabriz, Iran, 2006

M.S., University of Tabriz, Iran, 2009

A Dissertation Submitted to the Graduate Faculty

of The University of Georgia in Partial Fulfillment

of the

Requirements for the Degree

Doctor of Philosophy

Athens, Georgia

2017

© 2017

Amin Yaghoobi

All Rights Reserved

Multiscale modeling of fracture mechanism in cementitious composites using the peridynamic method and enhancement in its implementation

by

Amin Yaghoobi

Approved:

Major Professor: Mi G. Chorzepa

Committee: Stephan A. Durham
Xianqiao Wang
Sung-Hee Sonny Kim

Electronic Version Approved:

Suzanne Barbour
Dean of the Graduate School
The University of Georgia
May 2017

Dedication

To my parents, Nasrin and Yadollah, who supported me in every part of my life.

To my amazing wife, Ida, whose sacrificial love and care always makes me strong.

Acknowledgments

I would like to convey my gratitude and respect for my advisor, Professor Mi G. Chorzepa. She has inspired me to become an independent researcher and helped me realize the power of critical reasoning. My sincere thanks must also go to the members of my dissertation advisory and exam committee: Professors Stephan A. Durham, Xianqiao Wang, and Sung-Hee Sonny Kim. They generously gave their time to offer me valuable comments toward improving my work.

I would like to express my gratitude to my parents for all their support and endless kindness. Their heart-warming kindness has been a great gift and inspiration to reach my academic milestones.

Finally, and most importantly, I would like to thank my lovely wife Ida. Her support, encouragement, quiet patience and unwavering love was in the end what made this dissertation possible. I am blessed to have her by my side throughout my PhD.

Table of Contents

Page

Acknowledgments v

List of Figures ix

List of Tables xvi

Chapter

1 Introduction and Literature Review 1

1.1 Background 1

1.2 Problem statement 11

1.3 Objectives 11

1.4 Methodology 12

1.5 Dissertation outline 13

2 Higher-order approximation to suppress the zero-energy mode in non-ordinary state-based peridynamics 17

2.1 Introduction 18

2.2 State of the research on suppressing spurious zero-energy modes in peridynamics 21

2.3 Framework for proposed higher-order approximation to the deformation gradient tensor 26

2.4 Implementation of the proposed treatment to zero-energy modes 27

2.5 Discussion 51

2.6 Conclusion 56

3 Meshless Modeling Framework for Fiber Reinforced Concrete Structures 57

3.1 Introduction 58

3.2 Formulation: Meshless Modeling Methodology for FRC Structures 62

3.3 Verification of the proposed meshless method 71

3.4 Comparison of Predictions and Experimental Results . . 79

3.5 Discussion and future work 83

3.6 Conclusion 85

4 Fracture analysis of fiber reinforced concrete structures in the micropolar peridynamic analysis framework 86

4.1 Introduction 87

4.2 Background 90

4.3 Proposed analysis method 93

4.4 Implementation of the proposed method in fracture analysis 98

4.5 Discussion of results 107

4.6 Conclusion 108

5 Mesoscale Fracture Analysis of Multiphase Cementitious Composites Using Peridynamics 109

5.1 Introduction 110

5.2 Proposed Mesoscale Concrete Model 115

5.3 Analysis of a Concrete Specimen in Tension 123

5.4 Analysis Results and Discussion of the Results 125

5.5 Sensitivity Study 132

5.6 Discussion 137
5.7 Conclusions 139
6 Formulation of symmetry boundary modeling in non-ordinary state-based peridynamics and coupling with FEA 141
6.1 Introduction 142
6.2 Formulation 146
6.3 Symmetry boundary modelling 152
6.4 Coupling of FE and NOSBPD methods 155
6.5 Results 159
6.6 Conclusion 174
7 Conclusion 177
8 Future Work 180
Bibliography 182
Appendix
A Discretization of the force state 198
B Dynamic relaxation 201

List of Figures

1.1 Schematic of force components between two material particles in the (a) bond-based, (b) micropolar, (c) ordinary state-based and (d) non-ordinary state-based peridynamics. 4

2.1 A schematic peridynamic body. 22

2.2 Discretization of a one-dimensional problem. 27

2.3 Weight functions to yield a higher-order approximation to the deformation gradient tensor, and the order of the corresponding error. 30

2.4 1D model with varying axial stiffness. 32

2.5 Displacement solutions for various weight functions, including the proposed higher-order terms. 33

2.6 Strain distributions for varying weight functions, including the proposed higher-order terms. 34

2.7 The impact of constant C_I on the (a) relative displacement error and (b) relative strain energy error for various discretization patterns. 36

2.8 The impact of constant C_{II} on the (a) relative displacement error and (b) relative strain energy error for various discretization patterns. 36

2.9 The impact of zero-energy mode control methods on relative displacement error. 37

2.10 The impact of zero-energy mode control methods on relative strain energy error. 37

2.11 Two discretization patterns used in 2D problems. 38

2.12 All possible horizon shapes with $\delta/h < 4$ for quadrilateral pattern. 39

2.13 Particles in the hexagonal pattern ($\delta/h < 4$). 40

2.14 2D plate with an opening subjected to tension. 41

2.15 Comparison of the horizontal displacement, u_x, distribution of quadrilateral models for no zero-energy mode control and for higher-order approximation method. 43
2.16 Comparison of the horizontal displacement, u_x, distribution of hexagonal models for no zero-energy mode control and for higher-order approximation method. 44
2.17 Peridynamic prediction of horizontal displacements and stresses along Axis-1 for quadrilateral models comparing to FEA results. 44
2.18 Peridynamic prediction of horizontal displacements and stresses along Axis-1 for hexagonal models comparing to FEA results. 45
2.19 Peridynamic prediction of horizontal displacements and stresses along Axis-2 for quadrilateral models comparing to FEA results. 46
2.20 Peridynamic prediction of horizontal displacements and stresses along Axis-2 for hexagonal models comparing to FEA results. 47
2.21 Displacement errors along a) Axis-1 and b) Axis-2 for various quadrilateral models. 48
2.22 Strain energy errors along a) Axis-1 and b) Axis-2 for various quadrilateral models. 48
2.23 The compact tension specimen (Lengths given in millimeters, and the thickness of the specimen is 25 mm). 49
2.24 Load-CMOD responses of the CT specimen. 51
2.25 A schematic 1D irregular particle distribution. 52
2.26 Proposed higher-order weight function vs. discrete higher-order weight function for $\delta/h_m = 3$. 53
2.27 (a) Displacement error; (b) strain energy error for five zero-energy control cases with random particle distributions. 53
2.28 Illustration of horizon in a 3D discretization for $\delta/h_m = 2$. 56

3.1 Modeling of fiber reinforcement. (a) Fully-discrete method: an explicitly modeled fiber as a truss or beam element; (b) Semi-discrete method: fiber force is distributed over selected elements around fiber end points. 63
3.2 Horizon of a material point, H, within a peridynamic body B. 64
3.3 Distribution of fiber forces with respect to fiber end point (red point): (a) Constant Weight Function (CWF) and (b) Linear Weight Function (LWF). . 65
3.4 Peridynamic states: Position state X, deformation state Y, and force state T. 66
3.5 Schematic for interaction of fiber and matrix points. 71
3.6 The rectangular plate used in convergence study 72
3.7 Graphical representation showing discretization of particles. (a) Reference state, (b) (δh)-convergence, and (c) δ-convergence. 73
3.8 The relative error, (a) $(\delta h)-$convergence, and (b) $\delta-$convergence 73
3.9 The relative processing time, (a) $(\delta h)-$convergence, and (b) $\delta-$convergence. 74
3.10 A plate with single fiber in tension. 74
3.11 Force-displacement plot of the composite material. 75
3.12 2D FRC plate with two semi-circle symmetric notches. 76
3.13 Randomly distributed fibers in the notched plate:(a) $V_f = 0.6\%$, (b) $V_f = 1.2\%$, and (c) $V_f = 2.4\%$. 76
3.14 Force-displacement plot of the notched plate. 77
3.15 Damage patterns for varying fiber volume fractions at selected displacements. 78
3.16 Strain energy contours for varying fiber volume fractions at selected displacements. 79
3.17 Beam geometry and four-point bending test setup. 80
3.18 Comparison of numerically obtained force-deflection results and experimental results [89] for 4 point bending beam with $V_f = 1.12\%$. 81
3.19 2D three point bending beam model. 82

3.20 Comparison of analytical and experimental results [90] for 3 point bending beam. 82
4.1 Schematics of force components between two material particles in the (a) bond-based and (b) micropolar peridynamics. 91
4.2 Proposed bond force-stretch relationship for modeling concrete material. . . 94
4.3 Semi-discrete fiber modeling in FEA showing the fiber force simply distributed to element nodes (a) around the fiber ends; and (b) along the fiber embedment length. 95
4.4 Semi-discrete fiber modeling approach employed in the proposed peridynamics framework in which the fiber force is distributed to cementitious material points over the fiber length. 96
4.5 A schematic showing fiber activation and engagement, noting that the fiber force is uniformly distributed along the fiber length. 97
4.6 Test setup and configuration of a FRC beam with a notch under three point bending. 99
4.7 FRC beam with a notch located at $a/l = 0$ and a fiber volume fraction of 0%. 101
4.8 FRC beam with a notch located at $a/l = 0$ and a fiber volume fraction of 0.25%. 101
4.9 FRC beam with a notch located at $a/l = 0$ and a fiber volume fraction of 0.50%. 102
4.10 FRC beam with a notch located at $a/l = 1/6$ and a fiber volume fraction of 0%. 102
4.11 FRC beam with a notch located at $a/l = 1/6$ and a fiber volume fraction of 0.25%. 103
4.12 FRC beam with a notch located at $a/l = 1/6$ and a fiber volume fraction of 0.50%. 103
4.13 FRC beam with a notch located at $a/l = 1/4$ and a fiber volume fraction of 0%. 104
4.14 FRC beam with a notch located at $a/l = 1/4$ and a fiber volume fraction of 0.25%. 104

4.15 FRC beam with a notch located at $a/l = 1/4$ and a fiber volume fraction of 0.50%. 105
4.16 The ultimate force, P_u, for varying fiber volume fraction v_f. 105
4.17 The residual force, P_r, where the deflection equals to $2\,mm$ for varying fiber volume fraction v_f. 106
4.18 A progression of the crack growth for increasing fiber reinforcement fraction. 107
5.1 Schematic of mesoscale multiphase model subjected to tension. 117
5.2 Numerical specimens with varying aggregate volume fraction and porosity. . 117
5.3 Aggregate gradations achieved by simulation versus the Fuller curve. (**a**) $P_{agg} = 20\%$; (**b**) $P_{agg} = 30\%$; (**c**) $P_{agg} = 40\%$; (**d**) $P_{agg} = 50\%$. 118
5.4 Kinematics of state-based peridynamics. 121
5.5 Numerical specimens with varying particle spacing, h. (**a**) $h = 1/2$ mm; (**b**) $h = 1/3$ mm; (**c**) $h = 1/4$ mm. 126
5.6 Tensile stress versus applied displacement for varying particle spacing. (**a**) $h = 1/2$ mm; (**b**) $h = 1/3$ mm; (**c**) $h = 1/4$ mm. 127
5.7 Effect of discretization on: (**a**) mean stress-displacement curves; and (**b**) sample number with reference to mean peak stress. 128
5.8 Effect of particle spacing size on crack pattern. (**a**) $h = 1/2$ mm; (**b**) $h = 1/3$ mm; (**c**) $h = 1/4$ mm. 128
5.9 Effect of discretization on simulation time. 129
5.10 Effect of (**a**) the displacement loading increment and (**b**) the dynamic relaxation threshold on the mean stress curve. 130
5.11 The effect of (**a**) the displacement loading increment and (**b**) the dynamic relaxation threshold on the simulation time. 131
5.12 Comparison with experimental and available FEM results. 132
5.13 Effect of (**a**) aggregate volume fraction, P_{agg}, and (**b**) porosity, P_{pore}, on the mean stress curve. 133

5.14 Mean peak stress for varying (**a**) aggregate volume fraction, P_{agg}, and (**b**) porosity, P_{pore}. 134
5.15 Crack pattern for selected specimens with $P_{pore} = 2\%$ and $P_{agg} = 20\%$. . . . 134
5.16 Crack pattern for selected specimens with $P_{pore} = 2\%$ and $P_{agg} = 30\%$. . . . 135
5.17 Crack pattern for selected specimens with $P_{pore} = 2\%$ and $P_{agg} = 40\%$. . . . 135
5.18 Crack pattern for selected specimens with $P_{pore} = 2\%$ and $P_{agg} = 50\%$. . . . 136
5.19 Crack pattern for selected specimens with $P_{pore} = 0\%$ and $P_{agg} = 40\%$. . . . 136
5.20 Crack pattern for selected specimens with $P_{pore} = 4\%$ and $P_{agg} = 40\%$. . . . 137
5.21 Crack pattern for selected specimens with $P_{pore} = 6\%$ and $P_{agg} = 40\%$. . . . 137
6.1 Configuration of a continuum body in the Peridynamics framework. 147
6.2 A schematic for introducing symmetry particles. 153
6.3 Symmetry modeling in 1D. 154
6.4 Three types of symmetry alongside Cartesian coordinates. 155
6.5 Schematic of the body, **B**, showing sub-regions with the proposed NOSBPD-FE coupling method. 156
6.6 (a) Schematic provided to describe NOSBPD-FE coupling concept using interface elements, and (b) an interface element and distribution of coupling force to FE nodes. 157
6.7 1D bar under tension with varying stiffness, and peridynamic models to study symmetry modeling. 160
6.8 Comparison of numerical results with analytical results (a) displacement field, (b) strain field. 161
6.9 The effect of particle spacing, h, and horizon size, δ, on (a) relative displacement error, and (b) relative strain energy error, for the 1D problem. 162
6.10 a) 2D model with circular opening, b) quarter model. 163

6.11 Comparison of a) horizontal displacement, u_x, b) horizontal strain, ϵ_x, and c) horizontal stress, σ_x, along Axis 1 obtained from a complete model, 1/4 model with fixed and with symmetry boundary condition 163
6.12 Comparison of a) vertical displacement, u_y, b) vertical strain, ϵ_y, and c) vertical stress, σ_y, along Axis 2 obtained from a complete model, 1/4 model with fixed and with symmetry boundary condition 164
6.13 The effect of particle spacing, h, on (a) relative displacement error, and (b) relative strain energy error, along Axis 1 and Axis 2 for 2D specimen. 165
6.14 Schematics of 2D plane stress model under tension showing the PD and FE sub-regions. 165
6.15 The effect of coupling factor α, on displacement error in PD-subregion. . . . 166
6.16 The longitudinal displacement u_x, for various coupling factor α, with $h_{PD} = 0.50\ mm$ and $h_{FE} = 5.0\ mm$. 167
6.17 The longitudinal displacement u_x, for various coupling factor α, with $h_{PD} = 0.25\ mm$ and $h_{FE} = 2.5\ mm$. 167
6.18 Displacement error for different discretization schemes. 167
6.19 The FE-subregion and PD-subregion in the notched 2D model (see Fig. 6.10a).168
6.20 The longitudinal displacement and stress along Axis 1. 169
6.21 The vertical displacement and stress along Axis 2. 169
6.22 The longitudinal displacement and stress contour results for NOSBPD-FE coupling model. 170
6.23 The compact tension specimen models (Lengths given in millimeters, and the thickness of the specimen is 25 mm). 171
6.24 Comparison of the load-CMOD response for 4 CT models. 173
6.25 The vertical displacement, u_y, contours for presented CT specimen models subjected to displacement loading (1.2 mm) at the center of hole(s). 173
6.26 Comparison of simulation time for four models. 174

List of Tables

2.1 1D approximations to the deformation gradient tensor for varying horizon size. 28

2.2 Order of error corresponding to each approximation. 29

2.3 Weight functions to obtain highest-order approximate deformation gradient tensor for quadrilateral pattern. 40

2.4 Weight functions to obtain a higher-order approximate deformation gradient tensor using the hexagonal pattern. 41

5.1 Gradation of the coarse aggregate [111]. 123

5.2 Material properties [111]. 124

6.1 Deformation, strain and stress fields of symmetry particles in 2D. 155

Chapter 1

Introduction and Literature Review

1.1 Background

Concrete is one of the most important building materials with billions of tons produced worldwide each year. It is a composite material widely used in great variety of applications from commercial and residential buildings to military facilities. Therefore, it is of great interest for researchers to characterize and understand the fracture behavior and brittle damage such as crack initiation and propagation in concrete. To improve our understanding of the performance of different concrete mixtures, it is necessary to apply cutting-edge numerical techniques and study concrete mixtures in terms of the composition, in conjunction with advanced empirical approaches such as microscopy, x-ray diffraction, and nuclear magnetic resonance (NMR) spectroscopy.

Many numerical studies consider concrete as a homogeneous material at the macroscopic scale. This assumption often results in inaccurate predictions of crack paths and load carrying capacity because concrete is a complex heterogeneous material. At the mesoscale, concrete is composed of four phases: coarse aggregate, air void, paste and the interfacial transition zone (ITZ), which exists between the coarse aggregate and paste. Aggregates, such as gravels or macroscale fibers are added into a cement-like binder to achieve improved performance such as increased ductility, strength, and durability.

Due to its highly heterogeneous microstructure, concrete shows exceedingly complex and nonlinear mechanical behavior. Some behaviors such as strain softening, microcrack propagation, failure mechanism, and size effect have been not fully understood thus far. Experimental studies provide important evidence of the fracture behavior of cementitious com-

posites; however, full-scale tests involving such fracture analysis are not always available due to limited resources. Therefore, theoretical studies are required to enable the successful design of cementitious composites, determine the sensitivity of constituents, provide important evidence about interactions among various components of concrete, and to deduce the macroscopic constitutive relationship of concrete materials.

Several models are available in the literature for fracture analysis of concrete members. Most popular models are based on the finite element method (FEM) [1–6], the discrete element method (DEM) [7, 8] and lattice modeling methods [9–14]. The majority of fracture analysis models have utilized the FEM, where for instance, failure is represented by inserting a zero-thickness cohesive interface element between homogeneous concrete elements. In this cohesive zone method (CZM), cohesive elements are zero-thickness elements that are placed between finite elements. Therefore, the finite element modeling of crack growth is mesh-dependent because it occurs only between finite elements where cohesive elements are present. Furthermore, crack paths are highly sensitive to mesh alignment and/or refinement, particularly when they are unknown or unspecified a priori [1, 3, 4].

When strong discontinuities exist, advanced finite element methods, such as the extended finite element method (XFEM) [2, 5] are used. XFEM introduces local enrichment functions in the standard finite element approximation methods. Therefore, XFEM is able to model crack initiation and growth without mesh refinement. Although XFEM has been successfully used to predict fracture in heterogeneous materials, its disadvantage includes the fact that an external criterion is needed to predict crack growth [2] in cement-based composites. Other major disadvantages of this method include increased computational expense and complex enrichment functions, which make the implementation of XFEM complex and thus difficult.

A discrete element method (DEM) is a numerical technique for calculating the motion of small particles. In the discrete element method (DEM) approach used in cementitious composites, discrete elements (or particles) interact by means of contact forces. In a lattice modeling approach, a continuum (such as a cement binder) is represented by a network

of discrete elements. Schlangen and Van Mier [10] used the DEM approach for mesoscale modeling in order to numerically characterize the fracture behavior in heterogeneous brittle materials. Schlangen and Garboczi [12] studied the effect of lattice element types, mesh orientations, and damage criteria on the accuracy of fracture prediction.

1.1.1 Peridynamic theory

Peridynamics introduced by Silling [15] is one of the nonlocal methods which reformulate the classical continuum mechanics by substituting the governing partial differential equations with integral equations. Therefore, the peridynamic equation of motion holds true anywhere in a rigid body, despite the presence of cracks and other discontinuities. Furthermore, material damage is an inherent feature and thus a key component of the peridynamic constitutive laws. These attributes permit modeling of fracture initiation and propagation, with arbitrary paths, i.e., without the need for a crack growth treatment.

1.1.2 Bond-based peridynamics

Peridynamics assumes that any material point, $\mathbf{x}$, which belongs to the spatial region, R, interacts with any arbitrary material point, $\mathbf{x}'$, within a finite distance of δ. The interaction between the material points is defined by a "bond" relationship between material points. In the first introduced peridynamics method, so called the "bond-based peridynamics", the interaction between material points is limited to a pair-wise force function, $\mathbf{f}$, defined by Eq. (1.1), as illustrated in Fig. 1.1a:

$$\mathbf{f} = \mathbf{f}(\mathbf{x}, \mathbf{x}', \mathbf{u}(\mathbf{x}, t), \mathbf{u}(\mathbf{x}', t)) \qquad |\mathbf{x}' - \mathbf{x}| \leq \delta \tag{1.1}$$

where $\mathbf{u}$ denotes the displacement field, and t is time. Therefore, the acceleration of material point, $\mathbf{x}$, is obtained from a summation of all bond forces as shown in Eq. (1.2)

$$\rho\ddot{\mathbf{u}}\left(\mathbf{u}, t\right) = \int_{\mathcal{H}_{\mathbf{x}}} \mathbf{f}(\mathbf{x}, \mathbf{x}', \mathbf{u}(\mathbf{x}, t), \mathbf{u}(\mathbf{x}', t))\mathrm{d}V_{\mathbf{x}'} + \mathbf{b}\left(\mathbf{x}, t\right) \tag{1.2}$$

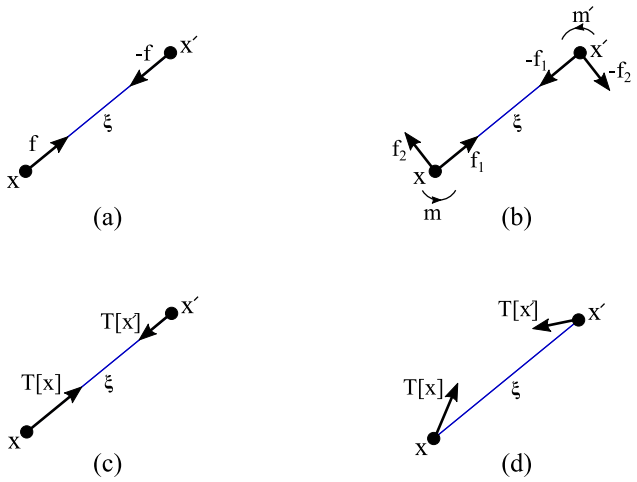


Figure 1.1: Schematic of force components between two material particles in the (a) bond-based, (b) micropolar, (c) ordinary state-based and (d) non-ordinary state-based peridynamics.

where ρ is mass density in the reference configuration, $\mathrm{d}V_{\mathbf{x}'}$ is an infinitesimal volume associated with material point $\mathbf{x}'$, $\mathbf{b}$ is the external body force density field, and $\mathcal{H}_{\mathbf{x}}$ is the domain of neighboring material points and is referred to as "horizon".

In peridynamic literature, the relative position of two points $\mathbf{x}$ and $\mathbf{x}'$ in the reference configuration is denoted by $\boldsymbol{\xi}$

$$\boldsymbol{\xi} = \mathbf{x}' - \mathbf{x} \tag{1.3}$$

and the relative displacement is denoted by $\boldsymbol{\eta}$

$$\boldsymbol{\eta} = \mathbf{u}\left(\mathbf{x}', t\right) - \mathbf{u}\left(\mathbf{x}, t\right) \tag{1.4}$$

In Eq. (1.4), $\boldsymbol{\xi} + \boldsymbol{\eta}$ represents the relative position in the deformed configuration, $|\boldsymbol{\xi}|$ is the undeformed bond length, and $|\boldsymbol{\xi} + \boldsymbol{\eta}|$ is the deformed bond length.

Constitutive modeling: For a homogeneous material which does not result in time-dependent deformations, the magnitude of pair-wise force, f, is obtained as a function of stretch, s, in the form of $f = f(s)$, where the stretch, s, is defined by

$$s = \frac{|\boldsymbol{\xi} + \boldsymbol{\eta}| - |\boldsymbol{\xi}|}{|\boldsymbol{\xi}|} \tag{1.5}$$

Therefore, the pair-wise force function takes the form of

$$\mathbf{f} = \omega\left(|\boldsymbol{\xi}|\right) f(s) \frac{\boldsymbol{\xi} + \boldsymbol{\eta}}{|\boldsymbol{\xi} + \boldsymbol{\eta}|} \tag{1.6}$$

where $\omega\left(|\boldsymbol{\xi}|\right)$ is a radially symmetric weight function and $\frac{\boldsymbol{\xi}+\boldsymbol{\eta}}{|\boldsymbol{\xi}+\boldsymbol{\eta}|}$ denotes the unit vector of current relative position of two points.

It is noteworthy that the pair-wise force function, $f(s)$, contains the material constitutive information. For example, for elastic materials, f, is a linear function of s (i.e., $f = cs$), where the stiffness c depends on both material and the geometrical property of the material. c, so called "material micromodulus", is generally obtained directly by an empirical study. Silling and Askari [16] obtained the material micromodulus by comparing the peridynamic micro-potential with the strain energy density in the classical theory of elasticity for the same material, noting that, the pair-wise force is defined by a nonlinear function of the stretch, s, for materials with nonlinearity and damage parameters.

Damage in the peridynamic theory is associated with bond breakage between material points. A bond can break if its stretch, s, exceeds a critical stretch, s_0. The critical stretch can be obtained experimentally. Furthermore, Silling and Askari [16] represented a formulation to calculate the critical stretch by comparing the fracture energy of the material, G_0, with the total energy required to generate a fracture surface within the horizon of a material point. The simplest way to introduce failure into peridynamic formulation is to modify the weight function, $\omega\left(|\boldsymbol{\xi}|\right)$, introducing additional term to capture the bond breakage as follows:

$$\bar{\omega}\left(|\boldsymbol{\xi}|\right) = \begin{cases} \omega\left(|\boldsymbol{\xi}|\right) & : s < s_0 \\ 0 & : otherwise \end{cases} \tag{1.7}$$

Horizon size: A constitutive parameter, called 'the horizon', in the peridynamic theory represents the extent (e.g., the radius of influence) of nonlocal interactions in a continuum model. The peridynamic horizon is the region around a material point and usually takes as a circular domain centered at the point $\mathbf{x}$, with a radius of δ, in a two-dimensional problem. In a similar manner, the horizon becomes a sphere in three-dimensional problems. Nonlocality is a key component of peridynamic formulations because the spatial derivative term is replaced with an integral term to overcome shortcomings of the classical mechanics in modeling discontinuities.

In certain problems where the physical interactions between points are visible, the horizon size can be correlated to an intrinsic material length-scale [17–19]. However, the actual length scale is undetectable at the macroscale [18, 19]. In such cases, the horizon size is mostly expressed as a function of discretization (or grid) size using a comprehensive convergence study to predict the results of experimental data. For macroscopic modeling, it is reported in several studies where the selection of the peridynamic horizon size is approximately three times the grid size, the results is obtained with reasonable stability [16, 17, 20–23]. Smaller horizon size is known to result in undesirable grid effects [22]. For larger horizons, it is reported that excessive wave dispersion could occur for dynamic solutions [22]. Furthermore, a larger horizon size lowers efficiency as the total number of interactions between material points increases. It will also lead to increased computation time and a higher degree of difficulty for implementation.

It is important to note that a relatively large horizon at the macroscale (e.g., 1 mm) does not indicate that there is a physical connection between material points spaced at such distance. It simply indicates that the material response such as linear/nonlinear deformation or damage evolution is well captured by the peridynamic model with such horizon size [22].

It is also important to recognize that the horizon size does not have to be constant over the domain. In certain problems involving adaptive mesh refinement around a stress concentration zone [17, 19] or multiscale modeling [24], spatial distribution of points with variable horizon size is necessary for computational efficiency. However, when the horizon size varies between points, the bond forces are no longer pairwise which could result in spurious wave reflections in solutions. Refined peridynamics [17,19] and dual horizon concept [25] are been studied by researchers in an effort to deal with spurious wave reflection issues and ghost force problems between points.

Fixed Poisson's ratio in bond-based peridynamics: As describes in Section 1.1.2, in the bond-based peridynamics, two points interact utilizing the central pair-wise bond force concept. The assumption results in a fixed Poisson's ratio for all bond-based peridynamic materials. Poisson's ratio can be obtained by comparing the stress tensor under small homogeneous deformation for linear microelastic bond-based peridynamic body with the classic stress tensor under the same deformation field [26]. For a linear microelastic bond-based peridynamic material undergoing small homogeneous deformation in three-dimensional, the Poisson's ratio is obtained as 1/4 [26]. In two-dimensional bond-based peridynamic problems, the Poisson's ratio is 1/3 and 1/4 for plane stress and plane strain problems, respectively [16].

1.1.3 Micropolar peridynamics

A generalized peridynamic formulation is developed by Grestle et al. [27] to address the deficiency of the bond-based peridynamics in modeling material behavior with varying Poisson's ratio. The so called "micropolar peridynamics" allows pair-wise moments to act between the material points in addition to pairwise force, as illustrated in Fig. 1.1b. Therefore in addition to Eq. (1.2), the equation of motion is expressed in terms of moments as presented in Eq. (1.9), where $\boldsymbol{\theta}$ denotes the material particle rotation; I is the mass moment of inertia, $\mathbf{m}$

is the pair-wise peridynamic moments; and $\mathbf{m}_b$ is the externally applied moment vector per unit volume.

$$\rho\ddot{\mathbf{u}}\left(\mathbf{x},t\right)=\int_{\mathcal{H}_{\mathbf{x}}}\mathbf{f}(\mathbf{x},\mathbf{x}',\mathbf{u}(\mathbf{x},t),\mathbf{u}(\mathbf{x}',t),\boldsymbol{\theta}(\mathbf{x},t),\boldsymbol{\theta}(\mathbf{x}',t))\mathrm{d}V_{\mathbf{x}'}+\mathbf{b}\left(\mathbf{x},t\right) \tag{1.8}$$

$$I\ddot{\boldsymbol{\theta}}\left(\mathbf{x},t\right)=\int_{\mathcal{H}_{\mathbf{x}}}\mathbf{m}(\mathbf{x},\mathbf{x}',\mathbf{u}(\mathbf{x},t),\mathbf{u}(\mathbf{x}',t),\boldsymbol{\theta}(\mathbf{x},t),\boldsymbol{\theta}(\mathbf{x}',t))\mathrm{d}V_{\mathbf{x}'}+\mathbf{m}_b\left(\mathbf{x},t\right) \tag{1.9}$$

Generally, the micropolar peridynamics [27] assumes that the bond relationship between two material points interact as a beam element, rather than a truss element used in the bond-based peridynamics [16]. In the case of quasi-static motion, the accelerations are zero, so that for each point,

$$\int_{\mathcal{H}_{\mathbf{x}}}\mathbf{f}(\mathbf{x},\mathbf{x}',\mathbf{u}(\mathbf{x},t),\mathbf{u}(\mathbf{x}',t),\boldsymbol{\theta}(\mathbf{x},t),\boldsymbol{\theta}(\mathbf{x}',t))\mathrm{d}V_{\mathbf{x}'}+\mathbf{b}\left(\mathbf{x},t\right)=\mathbf{0} \tag{1.10}$$

$$\int_{\mathcal{H}_{\mathbf{x}}}\mathbf{m}(\mathbf{x},\mathbf{x}',\mathbf{u}(\mathbf{x},t),\mathbf{u}(\mathbf{x}',t),\boldsymbol{\theta}(\mathbf{x},t),\boldsymbol{\theta}(\mathbf{x}',t))\mathrm{d}V_{\mathbf{x}'}+\mathbf{m}_b\left(\mathbf{x},t\right)=\mathbf{0} \tag{1.11}$$

1.1.4 State-based peridynamics

Introducing rotational degrees of freedom into a bond-based peridynamic model, the micropolar peridynamics offers an important improvement over the original theory in modeling material behavior with varying Poisson's ratio. However, it remains difficult to represent all aspects of material response, particularly when a collective response among material point bonds was involved (e.g., a volume change). To avoid this type of restriction, a generalized peridynamic formulation, so-called state-based peridynamics was introduced. The state-based peridynamics method allows interaction between bonds [28]. Therefore, the collective deformation of the bonds around a material point defines the response of the point [28].

In the state-based peridynamic formulation, the equation of motion in Eq. (1.2) is replaced by:

$$\rho\ddot{\mathbf{u}}\left(\mathbf{x},t\right)=\int_{\mathcal{H}_{\mathbf{x}}}\left(\mathbf{T}[\mathbf{x},t]\langle\mathbf{x}'-\mathbf{x}\rangle-\mathbf{T}[\mathbf{x}',t]\langle\mathbf{x}-\mathbf{x}'\rangle\right)\mathrm{d}V_{\mathbf{x}'}+\mathbf{b}\left(\mathbf{x},t\right) \tag{1.12}$$

where $\mathbf{T}[\mathbf{x},t]$ is the force vector state field applied on material point $\mathbf{x}$ at time t. The angle bracket, $\langle\ \rangle$, is used to indicate that the state operates on the vector in $\langle\ \rangle$. To determine the force vector state, $\mathbf{T}$, two formulations were developed: ordinary method and non-ordinary method.

Ordinary formulation: In the ordinary state-based peridynamics, the force density vectors having unequal magnitudes while being parallel as shown in Fig. 1.1c. Thus, they can be defined in the form

$$\mathbf{T}[\mathbf{x},t]\langle\mathbf{x}'-\mathbf{x}\rangle=\frac{1}{2}As\frac{\boldsymbol{\xi}+\boldsymbol{\eta}}{|\boldsymbol{\xi}+\boldsymbol{\eta}|} \tag{1.13}$$

$$\mathbf{T}[\mathbf{x},t]\langle\mathbf{x}'-\mathbf{x}\rangle=-\frac{1}{2}Bs\frac{\boldsymbol{\xi}+\boldsymbol{\eta}}{|\boldsymbol{\xi}+\boldsymbol{\eta}|} \tag{1.14}$$

where A and B are the auxiliary parameters that are dependent on engineering material constants, deformation field, and the horizon. The selection force density vectors in this form referred by Silling et al. [28] as "ordinary state-based" peridynamics.

Non-ordinary formulation: The main goal of NOSBPD was to allow interactions among the bonds [29]. Therefore, the collective deformation of the bonds around a material point defines the response of the point [29,30]. In NOSBPD, each bond between two material points is capable of carrying loads in all directions (See Fig. 1.1d), which allows characterizing materials with any thermodynamically-admissible Poissons ratio [28–30]. Furthermore, the NOSBPD is capable of representing genuine material behaviors, such as a volume or shear angle change. Furthermore, the force state is represented by the classical stress and strain tensors, which enable the use of constitutive and damage models from the classical mechanics theory.

In the state-based peridynamics, the relative position of two material points is defined as the position state, $\mathbf{X}\langle \mathbf{x}' - \mathbf{x} \rangle = \boldsymbol{\xi} = \mathbf{x}' - \mathbf{x}$. The deformation state, $\mathbf{Y}$, is the position state in the deformed configuration and expressed as:

$$\mathbf{Y}\langle \mathbf{x}' - \mathbf{x} \rangle = \boldsymbol{\xi} + \boldsymbol{\eta} = \mathbf{y}' - \mathbf{y} \tag{1.15}$$

The deformation state, $\mathbf{Y}$, represents the basic kinematic quantity used for a constitutive model in the state-based peridynamic method. Therefore, for an elastic material, the strain energy density, W, is given by a function of the deformation state, instead of deformation gradient tensor, $\mathbf{F} = \partial \mathbf{y}/\partial \mathbf{x}$, used in the classical continuum mechanics. In order to employ a constitutive model from the classical solid mechanics in the NOSBPD, a deformation gradient tensor must be described in forms of peridynamic states. An approximation of the nonlocal deformation gradient tensor was proposed by Silling et al. [28] as:

$$\mathbf{F}(\mathbf{x}) = [\int_{\mathcal{H}_\mathbf{x}} \omega(\xi) [(\mathbf{y}' - \mathbf{y}) \otimes (\mathbf{x}' - \mathbf{x})] \mathrm{d}V_{\mathbf{x}'}] \cdot \mathbf{K}^{-1} \tag{1.16}$$

where $\otimes$ denotes dyadic product and $\mathbf{K}$ is a shape tensor, expressed as follows at point $\mathbf{x}$.

$$\mathbf{K}(\mathbf{x}) = \int_{\mathcal{H}_\mathbf{x}} \omega(\xi) [(\mathbf{x}' - \mathbf{x}) \otimes (\mathbf{x}' - \mathbf{x})] \mathrm{d}V_{\mathbf{x}'} \tag{1.17}$$

The force state $\mathbf{T}$ is defined in terms of changes in strain energy density, $W(\mathbf{Y})$, for any infinitesimal change in the deformation state, $d\mathbf{Y}$, and formulated as follows [29]:

$$\mathbf{T}[\mathbf{x}]\langle \mathbf{x}' - \mathbf{x} \rangle = \omega(\xi) \boldsymbol{\sigma} \cdot \mathbf{K}^{-1} \cdot (\mathbf{x}' - \mathbf{x}) \tag{1.18}$$

$\sigma = \partial W/\partial \mathbf{F}$ is the first Piola-Kirchhoff stress. For an isotropic elastic material with small strain tensor of $\epsilon = (\mathbf{F} + \mathbf{F}^T)/2 - \mathbf{I}$, the stress is obtained through $\sigma = \mathbf{C} : \epsilon$, where $\mathbf{C}$ is the isotropic elastic moduli matrix and $\mathbf{I}$ is the identity matrix.

1.2 Problem statement

Cementitious composites are highly heterogeneous materials and exhibit highly complex fracture behavior. Therefore, modeling complex fracture behavior of cementitious composites is challenging, particularly within the realm of classical continuum mechanics. In contrast, the peridynamics theory, a nonlocal model, is well suited to investigate such complex fracture behavior observed in brittle cementitious composite materials and thus provides the potential of improving prediction accuracy by increasing the local damage modes such as crack initiation and propagation. However, the non-ordinary state-based peridynamics theory and implementation is in its infancy. The non-ordinary state-based peridynamic formulations in their original form are highly complex and thus have not been endeavored for implementation. Furthermore, implementing solution techniques for dynamic and quasi-static problems remains complex. The non-ordinary state-based peridynamic theory is a promising computational tool in fracture analysis of brittle cementitious composites because it enables the implementation of the classical material constitutive equations and formulations. However, at present, a major challenge for optimizing the computational cost remains unresolved.

1.3 Objectives

The two main objectives of this study are: (1) to improve the peridynamics analysis method; and (2) to propose an efficient peridynamic analysis framework and implement the proposed method for fracture analysis of cementitious composites.

In light of the first goal, specific objectives are to:

1. Implement of the non-ordinary state-based peridynamics (NOSBPD) for small strain material.

2. Formulize a dynamic relaxation method to obtain the quasi-static solution of the NOSBPD equations.

3. Modify the NOSBPD formulation to overcome its associated instability problem.

4. Develop the peridynamic analysis framework using FORTRAN codes.

5. Verify and validate the analysis codes and results by studying benchmark problems.

6. Evaluate methodologies to reduce the computational cost by presenting a nonlocal symmetry modeling technique and coupling method (i.e., peridynamics coupled with the finite element method).

For the implementation of peridynamics methods, the specific objectives are to:

1. Include a nonlinear constitutive material model for concrete in the FORTRAN code.

2. Propose a meshless framework to incorporate composite material (e.g., fiber-reinforced concrete) modeling to predict the fracture response of fiber reinforced concrete structures.

3. Perform mesoscale modeling framework to take into account the heterogeneity of cementitious composites.

4. Compare the analysis results with available experimental test results.

Overall, current study aims to develop a powerful and computationally effective framework to study the fracture behavior of cementitious composites using peridynamic theory.

1.4 Methodology

The nonlocal peridynamic theory is employed to study the complex fracture behavior in cementitious composites. The most general form of the peridynamic method (non-ordinary state-based peridynamics) is implemented as a promising computational tool in fracture analysis while using classical constitutive equations. The dynamic relaxation method is adopted to obtain quasi-static solution of the system of peridynamic equations. The non-ordinary state-based peridynamic formulation suffers from an instability issue, so called "zero-energy mode". There are available methods in the literature to control the zero-energy mode. In

this work, an alternative method is proposed to suppress the zero energy mode. The proposed method employs higher order terms in definition of the nonlocal deformation gradient tensor, and therefore provide an effective solution in controlling zero-energy method. Furthermore, to reduce the computational cost of the peridynamic solution, a finite element and peridynamic coupling strategy is proposed to take the advantages of peridynamics in damaged area, while the computational efficiency in ensured in surrounding areas using the finite element method.

The stabilized peridynamic theory is used to obtain the steady-state fracture in cementitious composites. A nonlinear constitutive relation is implemented within the non-ordinary state-based peridynamic for modeling concrete. A meshless framework is proposed to incorporate fiber modeling to predict the fracture response of fiber reinforced concrete structures. Finally, a mesoscale modeling is performed to take into account the heterogeneity of cementitious composites.

1.5 Dissertation outline

Chapter 1 provides the fundamentals of the peridynamics theory and reviews basic formulations of four available peridynamics methods, namely, bond-based, micropolar, ordinary state-based and non-ordinary state-based peridynamics.

Chapter 2 is dedicated to an instability problem related to non-ordinary state-based peridynamics known as "zero-energy mode". The spurious zero energy mode oscillations in non-ordinary state-based peridynamic solutions are attributed to a weak form integration in providing nonlocal approximations to the deformation gradient tensor. Available methods in literature to reduce or control the undesired oscillation are described. A new treatment is proposed in this chapter to effectively suppress the zero-energy mode. The proposed approach extends the first-order Taylor approximation to a higher-order method, in order to obtain approximate solutions to the deformation gradient tensor and to solve the nonlocal peridynamic equations. The proposed scheme has been implemented in 1-D and 2-D problems using

varying horizon sizes and discretization patterns which are integral features of peridynamics. The proposed higher-order formulation is inherently included in the weight function necessary to define a deformation gradient tensor in the peridynamic analysis framework. Three example problems are studied in Chapter 2 to demonstrate the capability of the proposed method for relieving the oscillations conventionally found in the displacement and stress solutions. A comparative study is performed for varying particle spacing, horizon size, and weight functions. Through the examples demonstrated in this study, it is demonstrated that the proposed method is far more effective in suppressing the zero-energy mode oscillations than other existing methods. A nonlinear elastic-plastic simulation is performed to illustrate the capability of the proposed method.

A meshless analysis framework based on the non-ordinary state-based peridynamic method is proposed in Chapter 3 to formulate the analysis framework of fiber reinforced concrete (FRC) structures and predict the response. The approach includes a semi-discrete method in order to characterize the fiber reinforcement. With this approach, additional degrees of freedom from fibers are not present, and thus the computational efficiency is enhanced. Furthermore, there is no need to monitor fiber bond-slip behavior, concrete crack paths as the crack initiation, growth, and coalescence are an inherent outcome of the proposed framework. The capability of the proposed FRC modeling methodology is demonstrated through several examples. The accuracy is maintained for a failure analysis of FRC beams under bending.

Chapter 4 contains fracture analysis of cracks in fiber reinforced concrete structures using the micropolar peridynamic approach, whereas Chapter 3 considered the non-ordinary state-based peridynamic method. A semi-discrete approach is incorporated in the micropolar peridynamic analysis framework to study the effect of fiber reinforcement on the fracture analysis of cracks in cementitious materials. Therefore in the proposed fiber reinforced concrete modeling approach, the macroscale fibers are randomly distributed in the cementitious material, and the forces developed in the fibers are indirectly applied to the cementitious

material points. This fracture analysis method used for fiber-cementitious material composites improves the computational efficiency. Furthermore in contrast to the finite element method, there is no need for monitoring crack initiations/propagations in the proposed peridynamic framework. The crack development is an inherent feature of the proposed analysis framework. Finally, the accuracy of the proposed fracture analysis model is demonstrated through a comparison of available experimental results and simulation outcomes of fiber reinforced concrete beams with a notch at varying locations along the span.

In Chapter 5, a mesoscale model is developed for cementitious composites using a non-ordinary state-based peridynamics. This chapter predicts fracture behavior of a concrete cube specimen subjected to pure tension. The presence of heterogeneous materials consisting of coarse aggregates, interfacial transition zones, air voids, and cementitious matrix is characterized as material points in a two-dimensional mesoscale model. Coarse aggregates and voids are generated using uniform probability distributions, while a statistical study is provided to comprise the effect of random distributions of constituent materials. In obtaining the steady-state response, an incremental and iterative solver is adopted for the dynamic relaxation method. Load-displacement curves and damage patterns are compared with available experimental and the FEM results. Although the proposed model uses much simpler material damage models and discretization schemes, the load-displacement results are comparable to the FEA results. Furthermore, no mesh refinement is necessary in the proposed mesoscale models, as fracture is inherently characterized by bond breakages. Finally, a sensitivity study is conducted to understand the effect of aggregate volume fraction and porosity on the load capacity of the proposed mesoscale model.

Chapter 6 presents two effective approaches in an effort to reduce the computational expense of the non-ordinary state-based peridynamic analysis. The first method is the symmetry boundary modeling approach in which the solution time of a symmetric body is reduced by a factor of 2. The method introduces symmetry points where their kinetics are obtained through symmetry rules. The accuracy of the approach is studied through 1-D

and 2-D symmetric models in Sections 6.5.1 and 6.5.2, respectively. The results agree well with both exact solutions and peridynamic analysis solutions, whereas the 'fixed' boundary models fail to provide the accuracy near the symmetry axis. In the second approach, the interface element coupling method is adopted to couple the non-ordinary state-based peridynamics and finite element methods. The proposed coupling model enhances the accuracy by using peridynamics near discontinuities, while the FE method is utilized to model the remaining body (i.e., continuum without local damage) for efficiency. The calibration of the coupled model is performed using a 2-D plate specimen under tension in Section 6.5.3, and the method is validated through a 2-D notched plate analysis presented in Section 6.5.4. A Compact Tension (CT) specimen model is used for a crack growth study in Section 6.5.5 and illustrates the successful implementation of both the symmetry boundary and coupling models. The combination of these two approaches significantly reduces the computational time, while the accuracy is significantly maintained.

Chapter 2

Higher-order approximation to suppress the zero-energy mode in non-ordinary state-based peridynamics[1]

[1] A. Yaghoobi and M. G. Chorzepa. "Higher-order approximation to suppress the zero-energy mode in non-ordinary state-based peridynamics." Accepted by Computers & Structures. Reprinted here with permission of publisher, 2017.

ABSTRACT

This paper presents a numerical method to control the spurious deformation mode conventionally found in a non-ordinary state-based peridynamic formulation. The proposed approach introduces a higher-order approximation for a deformation gradient tensor in order to suppress oscillations from the zero-energy mode. The results are compared to those determined by other available methods. The findings of this study well demonstrate that the proposed method provides highly effective solutions for controlling zero-energy modes in peridynamic models. Contrasting other available zero-energy control methods, the proposed method remains robust for relatively large horizon sizes. The method is incorporated by implicit weight functions in peridynamics.

2.1 Introduction

Nonlocal methods in computational solid mechanics have recently gained popularity as an alternative method to the classical continuum mechanics methods, such as the finite element method (FEM). Peridynamics introduced by Silling [15] is one of the nonlocal mesh-free methods which reformulate the classical continuum mechanics by substituting the governing partial differential equations with integral equations. Therefore, it is considered that the peridynamic equation of motion is valid everywhere despite the presence of cracks and other discontinuities [16, 24, 27, 28, 30–33].

Peridynamics has undergone significant changes since first proposed. When first introduced, so called bond-based peridynamics (BBPD) only considered independent central interaction forces between any pair of material particles. As a consequence of this assumption, the bond-based method was restricted to a fixed value of Poisson's ratio ($\nu = 1/4$ for the 3D and 2D plane strain cases and $\nu = 1/3$ for 2D plane stress cases) [27–30, 34]. Due to this limitation, BBPD had lost its generality and credence for modeling material response such as plasticity. The non-ordinary state-based peridynamics (NOSBPD) is a generalized form

of peridynamics which allows material particle bonds to carry forces in all directions. Therefore, the NOSBPD can represent material behavior with any Poisson's ratio [28–30, 35–37]. Furthermore, the bond forces in the NOSBPD are defined by stress tensors; therefore, the classical constitutive equations and failure criteria can be implemented in the NOSBPD analysis framework [23, 38–41].

However, computational problems related to the NOSBPD include an instability problem, known as a 'zero-energy mode' mechanism [39, 42]. It is mainly observed in regions with high strain gradients. The term 'zero-energy mode' associated with reference to the Finite Element Analysis (FEA) refers to a nodal displacement vector that is not a rigid-body motion, yet produces zero strain energy. Instabilities arise because of weak-form element formulation processes such as a the use of a low-order Gauss quadrature rule. Certain higher-order polynomial terms vanish at Gauss points, thus eliminating these terms from contribution to the system stiffness [43, 44].

In the context of peridynamics, the zero-energy mode is associated to a weak coupling of material particles with their surrounding particles and thus results in oscillations in the deformation and stress fields. Various control methods have been proposed. For example, introducing a viscosity term in the peridynamic equation of motion or decreasing particle spacing size have relieved the zero-energy mode oscillations [45]; however, another level of effort is required to significantly reduce the undesired oscillations. Several other methods have been developed by Littlewood [46], Breitenfeld et al. [39], and Wu and Ren [47] to suppress the zero-energy mode.

The zero-energy mode is also present in the other available meshfree methods such as smoothed particle hydrodynamics (SPH) and element-free Galerkin method (EFG). The meshfree methods suffer from another stability problem known as "tensile stability". Although the tensile stability is beyond the scope of this study, it is worth understanding the background. The zero-energy method in meshfree methods comes from 'rank-deficiency' in evaluating the integrals of weak forms due to a relatively small number of integration

points. Additional integration points were first introduced to increase the instability of the SPH by Dyka and Ingel [48], and this method was extended for higher dimensions by Randles and Libersky [49]. In the so called "stress point integration method", additional slave points are embedded into particles created in an existing particle arrangement. The slave or stress points are only needed in evaluation of governing equations used in the weak form, and all their field values are obtained through an interpolation from the original particles. Belytschko et al. [50] illustrated that the stress point integration method does not affect the tensile instability but removes the instability due to rank-deficiency. Rabczuk et al. [51] employed a modified stress integration method to eliminate the rank-deficiency. They included the quadrature of the Galerkin weak form over both original particles and stress points. While the stress point integration method provides improved stability over nodal integration methods, it is likely to impair computational efficiency of the meshfree method, particularly in a large structural analysis problem.

Introducing a supplementary term to the force vector-state, which resembles the process of providing an artificial stiffness for stability in the classical FEM, represents an extra coupling of each particle with neighboring particles. Various forms for the supplementary term have been provided by Littlewood [46] and Breitenfeld et al. [39], However, these solutions do not provide resolutions to the fundamental problem; that is, they are mesh (or particle spacing size) sensitive. Wu and Ren [47] introduced a stabilized displacement field to control the zero-energy mode. The stabilized displacement of each particle is determined by providing a weighted average displacement of all other particles and yields reduced oscillations in the deformation field. This approach eliminated the need for the spring coefficient required for the supplementary force. However unfortunately, the oscillation problem appears to remain in the strain and stress fields with the Wu and Ren model [47].

In this paper, it is proposed to extend the first-order Taylor approximation to higher-order in order to obtain approximate deformation gradient tensor and to solve the nonlocal peridynamic equations. The proposed scheme has been implemented in 1D and 2D problems

with varying horizon sizes and discretization patterns which are integral features of peridynamics. The proposed higher-order formulation is naturally included in the weight function necessary to define a deformation gradient tensor in the peridynamics framework. Three example problems are studied herein to demonstrate the capability of the proposed method for relieving the oscillations conventionally found in the displacement and stress solutions. A comparative study is performed for varying particle spacing, horizon size, and weight functions. Through the examples demonstrated in this study, it is demonstrated that the proposed method is far more effective in suppressing the zero-energy mode oscillations than existing methods described above. A nonlinear elastic-plastic simulation is performed to illustrate the capability of the proposed method as well as the considerably reduced oscillations when the method is implemented in the peridynamics analysis framework.

2.2 State of the research on suppressing spurious zero-energy modes in peridynamics

2.2.1 Non-ordinary state-based peridynamics

The kinematics of peridynamics for a 2D body is illustrated in Fig. 2.1. In peridynamics, a particle located at position $\mathbf{x}$, interacts with its surrounding particles within an area of influence, so called 'horizon' $\mathcal{H}_{\mathbf{x}}$, where δ is the horizon size. The position vector-state, $\mathbf{X}\langle\mathbf{x}'-\mathbf{x}\rangle = \boldsymbol{\xi} = \mathbf{x}'-\mathbf{x}$, also referred to as the 'bond' between two particles $\mathbf{x}$ and $\mathbf{x}'$, represents the relative position in the undeformed body, $\mathbf{B}_0$. The deformation vector-state, $\mathbf{Y}\langle\mathbf{x}'-\mathbf{x}\rangle = \boldsymbol{\xi}+\boldsymbol{\eta} = \mathbf{y}'-\mathbf{y}$, maps the bond, $\mathbf{X}\langle\boldsymbol{\xi}\rangle$, in the deformed body, $\mathbf{B}$, where $\boldsymbol{\eta} = \mathbf{u}'-\mathbf{u}$ is the relative displacement of particles $\mathbf{x}$ and $\mathbf{x}'$.

In the NOSBPD, the steady-state equilibrium equations for particle $\mathbf{x}$ is given in Eq. (2.1) where $\mathbf{b}$ is the body force applied on the particle $\mathbf{x}$, and $dV_{\mathbf{x}'}$ is the volume of particle $\mathbf{x}'$. The force vector-state, $\mathbf{T}$, can be obtained by Eq. (2.2), where $\omega(\xi)$ denotes an weight function and $\xi = |\boldsymbol{\xi}| = |\mathbf{x}'-\mathbf{x}|$. The stress tensor, $\boldsymbol{\sigma}$, is the first Piola-Kirchhoff stress, and the shape factor, $\mathbf{K}$, at particle $\mathbf{x}$ is defined by Eq. (2.3). $\otimes$ denotes the tensor product.

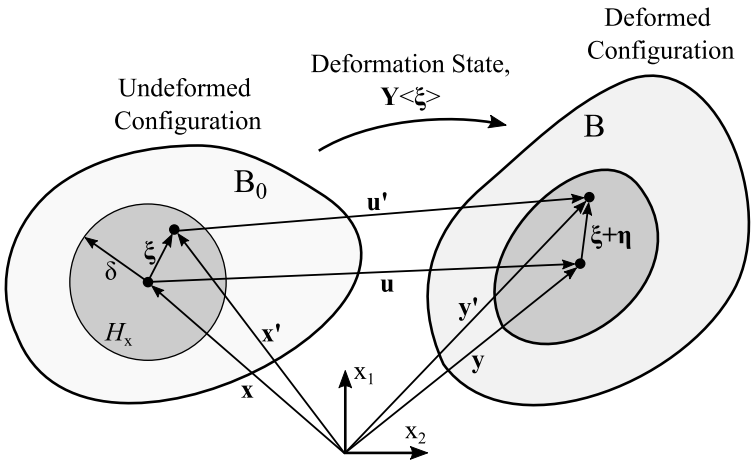


Figure 2.1: A schematic peridynamic body.

$$\int_{\mathcal{H}_{\mathbf{x}}} \left(\mathbf{T}[\mathbf{x}]\langle \mathbf{x}' - \mathbf{x}\rangle - \mathbf{T}[\mathbf{x}']\langle \mathbf{x} - \mathbf{x}'\rangle\right) \mathrm{d}V_{\mathbf{x}'} + \mathbf{b}\left(\mathbf{x}\right) = \mathbf{0} \tag{2.1}$$

$$\mathbf{T}[\mathbf{x}]\langle \mathbf{x}' - \mathbf{x}\rangle = \omega\left(\xi\right) \boldsymbol{\sigma} \cdot \mathbf{K}^{-1} \cdot \left(\mathbf{x}' - \mathbf{x}\right) \tag{2.2}$$

$$\mathbf{K}\left(\mathbf{x}\right) = \int_{\mathcal{H}_{\mathbf{x}}} \omega\left(\xi\right) \left[\left(\mathbf{x}' - \mathbf{x}\right) \otimes \left(\mathbf{x}' - \mathbf{x}\right)\right] \mathrm{d}V_{\mathbf{x}'} \tag{2.3}$$

A nonlocal approximation of deformation gradient tensor, $\mathbf{F}$, is defined by Silling et al. [28] to formulate the classical continuum mechanics' constitutive equations in peridynamics.

$$\mathbf{F}\left(\mathbf{x}\right) = \left[\int_{\mathcal{H}_{\mathbf{x}}} \omega\left(\xi\right) \left[\left(\mathbf{y}' - \mathbf{y}\right) \otimes \left(\mathbf{x}' - \mathbf{x}\right)\right] \mathrm{d}V_{\mathbf{x}'}\right] \cdot \mathbf{K}^{-1} \tag{2.4}$$

The small strain tensor for isotropic elastic materials is determined by $\boldsymbol{\epsilon} = 1/2(\mathbf{F}+\mathbf{F}^T)-\mathbf{I}$, where the stress is obtained by $\boldsymbol{\sigma} = \mathbf{C} : \boldsymbol{\epsilon}$, where $\mathbf{C}$ is the isotropic elastic moduli matrix; and $\mathbf{I}$ is the identity matrix. To obtain the implicit solutions for a quasi-static peridynamic equilibrium equation (Eq. (2.1)), an incremental and iterative method is developed. For a virtual displacement state of $\delta\mathbf{u}$, the dynamic relaxation method is adapted to iteratively

update the displacement field, $\mathbf{u}$, until $||\delta\mathbf{u}|| < \varepsilon$, where ε is a small numerical cut-off. Dynamic relaxation is an explicit iterative method for obtaining steady-state solutions [40,52, 53]. This type of dynamic relaxation method determines steady-state solutions for a dynamic system by introducing fictitious mass and damping matrices and is particularly effective for solving highly nonlinear problems including geometric and material nonlinearities.

2.2.2 Available treatments for zero-energy modes

The spurious zero-energy mode oscillations in the NOSBPD solutions are attributed to weak form integration in nonlocal approximations to the deformation gradient tensor. The definition of the zero-energy mode has been given by Breitenfeld et al. [39] and described herein. Consider a rigid-body with a deformation vector-state, $\mathbf{Y}$, and its approximate deformation gradient tensor of $\mathbf{F}$. For an interior particle, $\mathbf{x}$, away from the boundaries, a symmetric horizon provides $\int_{\mathcal{H}_\mathbf{x}} \omega\left(\xi\right) \boldsymbol{\xi} \mathrm{d}V_{\mathbf{x}'} = 0$. While holding all other particles fixed, an arbitrary displacement, $\hat{\mathbf{u}}$, in the particle $\mathbf{x}$, yields a new deformation state of $\hat{\mathbf{Y}}\left(\boldsymbol{\xi}\right) = \mathbf{Y}\left(\boldsymbol{\xi}\right) - \hat{\mathbf{u}}$. The corresponding approximate deformation gradient tensor, $\hat{\mathbf{F}}$, is obtained by Eq. (2.5).

$$\hat{\mathbf{F}} = \mathbf{F} - \hat{\mathbf{u}} \otimes \left(\int_{\mathcal{H}_\mathbf{x}} \omega\left(\xi\right) \boldsymbol{\xi} \mathrm{d}V_{\mathbf{x}'} \right) \cdot \mathbf{K}^{-1} = \mathbf{F} \tag{2.5}$$

This indicates that the arbitrary displacement, $\hat{\mathbf{u}}$, results in no strain energy as calculated by the approximate deformation gradient tensor presented in Eq. (2.5). The presence of the zero-energy modes result in fictitious solutions (e.g., oscillations in the stress and strain fields) that are not physically explained. Therefore, the zero-energy mode may affect the failure and damage pattern.

There are a few methods to alleviate this problem. Decreasing the particle spacing is one of available treatments which may reduce the zero-energy mode oscillations. For dynamic problems, providing artificial viscosity in the NOSBPD equation of motion is also mentioned to alleviate the zero-energy mode oscillations [45]. However, another level of effort is required to significantly reduce the undesired oscillations. Several other methods have been developed

by Littlewood [46], Breitenfeld et al. [39], and Wu and Ren [47] to suppress the zero-energy mode.

The methods developed by Littlewood [46] and Breitenfeld et al. [39] share the fundamental notion that a supplementary force introduced into the force vector-state in peridynamics ($\mathbf{T}_{ZE}$ in Eq. (2.6)) can relieve the zero-energy mode, although the definition of the supplementary forces vary in their models. Littlewood [46] defined a penalty term based on differences between the actual position of each particle and its numerical position predicted by the nonlocal deformation gradient tensor. Therefore, the supplementary force is defined proportional to the penalty term. Breitenfeld et al. [39] introduced two approaches for the supplementary term. In the first approach, the extra force is proportional to the relative displacement of the bond, whereas in the second approach, it is proportional to the averaged displacement of all other particles in the horizon.

$$\mathbf{T}[\mathbf{x}]\langle\mathbf{x}'-\mathbf{x}\rangle = \omega\left(\xi\right)\boldsymbol{\sigma}\mathbf{K}^{-1}\cdot\left(\mathbf{x}'-\mathbf{x}\right) + \mathbf{T}_{ZE}[\mathbf{x}]\langle\mathbf{x}'-\mathbf{x}\rangle \tag{2.6}$$

Breitenfeld et al. [39] listed three possible forms for the $\mathbf{T}_{ZE}[\mathbf{x}]\langle\mathbf{x}'-\mathbf{x}\rangle$ as below, where C_I, C_{II} and C_{III} are constants and required to be obtained. K is the bulk modulus and $h = (\mathbf{F}-\mathbf{I})(\mathbf{x}'-\mathbf{x}) - (\mathbf{u}'-\mathbf{u})$ is the hourglass vector.

$$\mathbf{T}_{ZE}[\mathbf{x}]\langle\mathbf{x}'-\mathbf{x}\rangle = C_I\omega\left(|\mathbf{x}'-\mathbf{x}|\right)\left(\mathbf{u}'-\mathbf{u}\right) \tag{2.7}$$

$$\mathbf{T}_{ZE}[\mathbf{x}]\langle\mathbf{x}'-\mathbf{x}\rangle = C_{II}\int_{\mathcal{H}_{\mathbf{x}}}\omega\left(|\mathbf{x}''-\mathbf{x}|\right)\left(\mathbf{u}''-\mathbf{u}\right)\mathrm{d}V_{\mathbf{x}''} \tag{2.8}$$

$$\mathbf{T}_{ZE}[\mathbf{x}]\langle\mathbf{x}'-\mathbf{x}\rangle = -C_{III}\left(\frac{18K}{\pi\delta^4}\right)\mathbf{h}\cdot\left(\mathbf{y}'-\mathbf{y}\right)\frac{\mathbf{y}'-\mathbf{y}}{||\mathbf{y}'-\mathbf{y}||^2}\mathrm{d}V_{\mathbf{x}}\mathrm{d}V_{\mathbf{x}'} \tag{2.9}$$

These expressions introduce a spring-like bond forces to give an additional coupling of a particle with its neighboring particles. In the first method (Eq. (2.7)), the spring-like bond force is calculated simply as a function of relative displacement of the bond. In the second

method (Eq. (2.8)), the average of relative displacement over all bonds around the particle is used in calculation of the force. For simplicity, these two methods by Breitenfeld et al. [39] are referred to as ZEI and ZEII. In the third form (Eq. (2.9)) originally developed by Littlewood [46], the additional force vector-state term is based on the penalty term. It is noteworthy that the penalty approach resembles the ZEI as both apply the zero- energy force along the bond; and therefore, this model will not be compared to other methods.

Moreover, the performance of each method is highly dependent on the spring coefficients, C_I, C_{II} and C_{III}. Evidently, it becomes ineffective to use a very small spring coefficient in controlling zero-energy mode. On the other hand, for too large spring coefficients, the spring force dominates the solution [39], and it can lead to a numerical divergence. Therefore, an optimum value of the spring coefficient needs to be adjusted based on material model and the discretization scheme such as particle spacing and horizon size, and the shape of a weight function. As a result, multiple attempts are required to determine a suitable spring coefficient for each problem.

Wu and Ren [47] introduced a control method for suppressing zero-energy mode by replacing the deformation field, $\mathbf{u}(\mathbf{x})$, by the stabilized displacement field, $\bar{\mathbf{u}}(\mathbf{x})$, defined by Eq. (2.10), where $\bar{\omega}(\xi)$ is the modified weight function and takes the form of normalized weight function as shown in Eq. (2.11).

$$\bar{\mathbf{u}}(\mathbf{x}) = \int_{\mathcal{H}_{\mathbf{x}}} \bar{\omega}\left(|\mathbf{x}' - \mathbf{x}|\right) \mathbf{u}(\mathbf{x}) \, \mathrm{d}V_{\mathbf{x}'} \tag{2.10}$$

$$\bar{\omega}\left(|\mathbf{x}' - \mathbf{x}|\right) = \frac{\omega\left(|\mathbf{x}' - \mathbf{x}|\right)}{\int_{\mathcal{H}_{\mathbf{x}}} \omega\left(|\mathbf{x}'' - \mathbf{x}|\right) \mathrm{d}V_{\mathbf{x}''}} \tag{2.11}$$

The stabilized displacement of each particle is determined by providing weighted average displacement of all other particles and yields reduced oscillations in the deformation field. The approach eliminated the need to obtain the spring coefficient. However unfortunately, the oscillation problem remains in the strain and stress fields with the Wu and Ren model. This method will be referred as ZEIII in the following sections.

2.3 Framework for proposed higher-order approximation to the deformation gradient tensor

It is hypothesized in this study that the use higher-order terms provided in a nonlocal deformation gradient tensor significantly reduces the zero-energy mode oscillations. In this section, the expression for the nonlocal deformation gradient tensor is extended using the Taylor series expansion. For the particle $\mathbf{x}'$, within the horizon of particle $\mathbf{x}$, the deformed state, $\mathbf{y}'$, can be obtained through the Taylor series expansion as:

$$\mathbf{y}' = \mathbf{y} + (\mathbf{x}' - \mathbf{x}) \frac{\partial \mathbf{y}}{\partial \mathbf{x}} + \frac{1}{2!} (\mathbf{x}' - \mathbf{x})^2 \frac{\partial^2 \mathbf{y}}{\partial \mathbf{x}^2} + \frac{1}{3!} (\mathbf{x}' - \mathbf{x})^3 \frac{\partial^3 \mathbf{y}}{\partial \mathbf{x}^3} + ... \tag{2.12}$$

Considering the first-order derivative only, and multiplying Eq. (2.12) by $(\mathbf{x}' - \mathbf{x})$ provides:

$$(\mathbf{y}' - \mathbf{y}) \otimes (\mathbf{x}' - \mathbf{x}) = \frac{\partial \mathbf{y}}{\partial \mathbf{x}} (\mathbf{x}' - \mathbf{x}) \otimes (\mathbf{x}' - \mathbf{x}) + O\left(h^3\right) \tag{2.13}$$

The weighted integration of Eq. (2.13) over the horizon of the particle $\mathbf{x}$, using a radially symmetric weight function of $\omega(\xi)$, yields:

$$\int_{\mathcal{H}_\mathbf{x}} \omega(\xi) [(\mathbf{y}' - \mathbf{y}) \otimes (\mathbf{x}' - \mathbf{x})] \mathrm{d}V_{\mathbf{x}'} = \frac{\partial \mathbf{y}}{\partial \mathbf{x}} \int_{\mathcal{H}_\mathbf{x}} \omega(\xi) [(\mathbf{x}' - \mathbf{x}) \otimes (\mathbf{x}' - \mathbf{x})] \mathrm{d}V_{\mathbf{x}'} + O\left(h^3\right) \tag{2.14}$$

From the classical definition of deformation gradient tensor, $\mathbf{F} = \partial \mathbf{y} / \partial \mathbf{x}$, and the definition of shape tensor, $\mathbf{K}$, the approximate deformation gradient tensor is given by Eq. (2.15):

$$\mathbf{F}(\mathbf{x}) = \frac{\partial \mathbf{y}}{\partial \mathbf{x}} = [\int_{\mathcal{H}_\mathbf{x}} \omega(\xi) [(\mathbf{y}' - \mathbf{y}) \otimes (\mathbf{x}' - \mathbf{x})] \mathrm{d}V_{\boldsymbol{\xi}}] \cdot \mathbf{K}^{-1} + O(h) \tag{2.15}$$

The terms of error are presented by using the big O notation herein. The error in calculation of the nonlocal deformation gradient tensor is $O(h)$. For a symmetric horizon away from the particle boundaries, the second order derivative term is eliminated, and the error will

be second order, $O(h^2)$. With the presented expression of the nonlocal approximate deformation gradient tensor using Taylor series, it is possible to select explicit weight functions in Eq. (2.15) to obtain higher-order error terms. The order of error depends on the horizon size-to-particle spacing ratio, δ/h, which describes the number of particles within a horizon. Increased precision in the deformation gradient tensor can result in decreased oscillations in displacement solutions, as well as reduced noise in strain and stress solutions.

2.4 Implementation of the proposed treatment to zero-energy modes

Based on the framework developed in Section 2.3, the implementation in one-dimensional (1D) and two-dimensional (2D) problems are presented in this section, and the capability of the proposed higher-order approximation scheme in suppressing the zero-energy modes is demonstrated through three numerical examples in Sections 2.4.2, 2.4.4, and 2.4.5: (1) a 1D bar; (2) a 2D object, (3) crack growth in 2D Compact Tension (CT) specimen. Sections 2.4.1 and 2.4.3 presents the 1D and 2D discretization method, respectively, used for this study before presenting the numerical examples.

2.4.1 Formulation: One-dimensional discretization

Consider a 1D peridynamic problem with a constant particle spacing, $h = \mathbf{x}_{i+1} - \mathbf{x}_i$. As shown in Fig. 2.2, four different horizon sizes, δ, are considered: $\delta/h = 1, 2, 3$ and 4. Therefore, for $\delta/h = j$, the particles $\mathbf{x}_{i\pm j}$ are also included in the horizon of $\mathbf{x}_i$.

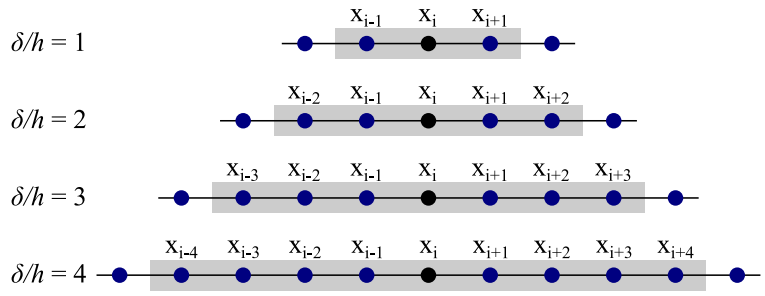


Figure 2.2: Discretization of a one-dimensional problem.

Table 2.1: 1D approximations to the deformation gradient tensor for varying horizon size.

δ/h	Deformation gradient tensor, $\mathbf{F}(\mathbf{x}_i)$
1	$\frac{(\mathbf{y}_{i+1}-\mathbf{y}_{i-1})}{2h}$
2	$\frac{2\omega_2(\mathbf{y}_{i+2}-\mathbf{y}_{i-2})+\omega_1(\mathbf{y}_{i+1}-\mathbf{y}_{i-1})}{2h(4\omega_2+\omega_1)}$
3	$\frac{3\omega_3(\mathbf{y}_{i+3}-\mathbf{y}_{i-3})+2\omega_2(\mathbf{y}_{i+2}-\mathbf{y}_{i-2})+\omega_1(\mathbf{y}_{i+1}-\mathbf{y}_{i-1})}{2h(9\omega_3+4\omega_2+\omega_1)}$
4	$\frac{4\omega_4(\mathbf{y}_{i+4}-\mathbf{y}_{i-4})+3\omega_3(\mathbf{y}_{i+3}-\mathbf{y}_{i-3})+2\omega_2(\mathbf{y}_{i+2}-\mathbf{y}_{i-2})+\omega_1(\mathbf{y}_{i+1}-\mathbf{y}_{i-1})}{2h(16\omega_4+9\omega_3+4\omega_2+\omega_1)}$

The weight function is assumed to be symmetric and expressed as $\omega_j = \omega(|\mathbf{x}_{i+j} - \mathbf{x}_i|) = \omega(|\mathbf{x}_{i-j} - \mathbf{x}_i|)$ for $j = 1, 2, ..., \delta/h$ and $\omega_j = 0$ for $j > \delta/h$. The Taylor series expansion for the neighboring particle, $\mathbf{y}_{i\pm j}$, is shown in Eq. (2.16), where $\mathbf{F} = \partial\mathbf{y}/\partial\mathbf{x}$, $\mathbf{F}' = \partial^2\mathbf{y}/\partial\mathbf{x}^2$, and $\mathbf{F}'' = \partial^3\mathbf{y}/\partial\mathbf{x}^3$ to list the first three terms of the sequence.

$$\mathbf{y}_{i\pm j} - \mathbf{y}_i = (\pm jh)\,\mathbf{F}(\mathbf{x}_i) + \frac{(\pm jh)^2}{2!}\mathbf{F}'(\mathbf{x}_i) + \frac{(\pm jh)^3}{3!}\mathbf{F}''(\mathbf{x}_i) + ... \tag{2.16}$$

As described in the previous section, for a discretized body, the nonlocal approximate deformation gradient tensor, $\mathbf{F}(\mathbf{x}_i)$, can be obtained through a weighted summation of terms in the Taylor series. For the 1D problem shown in Fig. 2.2, for a general form of the weight function, the approximate deformation gradient tensors and error terms are presented in Tables 2.1 and 2.2, respectively. Table 2.1 indicates that a larger horizon involves more neighboring particles; however, the error in numerical derivative is the second order, $O(h^2)$, as shown in Table 2.2.

Furthermore, for positive weight functions, $\omega_j > 0$, the coefficients for the calculated errors increase as the horizon size increases. This explains why increased oscillations are reported in peridynamic solutions for increased horizon size. In fact, increasing horizon size increases the number of integration points, however, yields larger errors. Therefore in this study, a higher-order formulation is developed to approximate the deformation gradient

Table 2.2: Order of error corresponding to each approximation.

δ/h	Error term $\left(\times \frac{h^2}{3!}\mathbf{F}''(\mathbf{x}_i)\right)$
1	1
2	$\frac{16\omega_2+\omega_1}{4\omega_2+\omega_1}$
3	$\frac{81\omega_3+16\omega_2+\omega_1}{9\omega_3+4\omega_2+\omega_1}$
4	$\frac{256\omega_4+81\omega_3+16\omega_2+\omega_1}{16\omega_4+9\omega_3+4\omega_2+\omega_1}$

tensor. The weight functions are key components of the proposed approximation scheme and include higher-order approximation terms for the deformation gradient tensor.

For $\delta/h = 1$ where two symmetric particles exist within the horizon of particle $\mathbf{x}_i$, the deformation gradient tensor and the corresponding error are independent of the weight function and the error is in order of two, $O(h^2)$. Therefore, the present formulation focuses on larger horizon sizes, $\delta/h \geq 2$. For $\delta/h = 2$, the particle $\mathbf{x}_i$, interacts with four neighboring particles, $\mathbf{y}_{i-2}$, $\mathbf{y}_{i-1}$, $\mathbf{y}_{i+1}$ and $\mathbf{y}_{i+2}$. The deformation gradient tensor will be obtained by a Taylor series expansion for these particles. The Taylor series are multiplied by $(\mathbf{x}_{i+j} - \mathbf{x}_i)\cdot\omega_j$. The summation can be used to derive the nonlocal deformation gradient tensor as described in Section 2.3:

$$
\begin{aligned}
2h\omega_2\{\mathbf{y}_{i+2} - \mathbf{y}_i &= 2h\mathbf{F}(\mathbf{x}_i) + \frac{(2h)^2}{2!}\mathbf{F}'(\mathbf{x}_i) + \frac{(2h)^3}{3!}\mathbf{F}''(\mathbf{x}_i) + \frac{(2h)^4}{4!}\mathbf{F}'''(\mathbf{x}_i) + O\left(h^5\right)\}\\
h\omega_1\{\mathbf{y}_{i+1} - \mathbf{y}_i &= h\mathbf{F}(\mathbf{x}_i) + \frac{h^2}{2!}\mathbf{F}'(\mathbf{x}_i) + \frac{h^3}{3!}\mathbf{F}''(\mathbf{x}_i) + \frac{h^4}{4!}\mathbf{F}'''(\mathbf{x}_i) + O\left(h^5\right)\}\\
-h\omega_1\{\mathbf{y}_{i-1} - \mathbf{y}_i &= -h\mathbf{F}(\mathbf{x}_i) + \frac{(-h)^2}{2!}\mathbf{F}'(\mathbf{x}_i) + \frac{(-h)^3}{3!}\mathbf{F}''(\mathbf{x}_i) + \frac{(-h)^4}{4!}\mathbf{F}'''(\mathbf{x}_i) + O\left(h^5\right)\}\\
-2h\omega_2\{\mathbf{y}_{i-2} - \mathbf{y}_i &= -2h\mathbf{F}(\mathbf{x}_i) + \frac{(-2h)^2}{2!}\mathbf{F}'(\mathbf{x}_i) + \frac{(-2h)^3}{3!}\mathbf{F}''(\mathbf{x}_i) + \frac{(-2h)^4}{4!}\mathbf{F}'''(\mathbf{x}_i) + O\left(h^5\right)\}
\end{aligned}
$$

$$
2h\omega_2(\mathbf{y}_{i+2} - \mathbf{y}_{i-2}) + h\omega_1(\mathbf{y}_{i+1} - \mathbf{y}_{i-1}) = 2h^2(4\omega_2 + \omega_1)\mathbf{F}(\mathbf{x}_i) + \frac{2h^4}{3!}(16\omega_2 + \omega_1)\mathbf{F}''(\mathbf{x}_i) + O(h^6)
$$

Given $16\omega_2 + \omega_1 = 0$, the deformation gradient tensor, $\mathbf{F}(\mathbf{x}_i)$, is obtained as:

$$\mathbf{F}(x_i) = \frac{2h\omega_2(\mathbf{y}_{i+2} - \mathbf{y}_{i-2}) + h\omega_1(\mathbf{y}_{i+1} - \mathbf{y}_{i-1})}{2h^2(4\omega_2 + \omega_1)} + O(h^4) \tag{2.17}$$

In other words, for $\omega_1 = 1$ and $\omega_2 = -1/16$, the approximate deformation gradient tensor produces an error that is $O(h^4)$ for $\delta/h = 2$. The same procedure can be applied for larger horizon sizes to obtain higher-order error in driving an approximation scheme for the deformation gradient tensor. Fig. 2.3 presents the weight functions and order of error for various horizon sizes. It is evident that the larger the horizon size there is, the more terms can be eliminated in the Taylor series expansion. Therefore, the order of error can be increased.

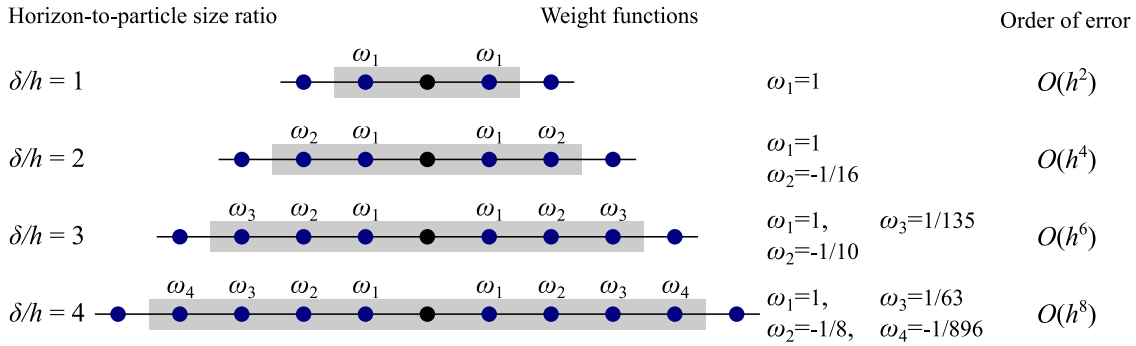


Figure 2.3: Weight functions to yield a higher-order approximation to the deformation gradient tensor, and the order of the corresponding error.

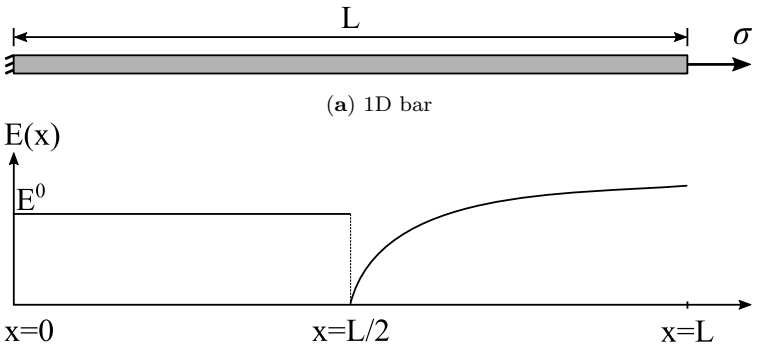
With the weight functions provided in Fig. 2.3, Eq. (2.15) increases accuracy in the deformation gradient tensor. The proposed higher-order formulation has a couple of advantages over previously used zero-energy control methods described in Section 2.2. First, it can effectively suppress the zero-energy mode oscillations. Computational efficiency increases as the horizon size increases. The order of error increases particularly for higher horizon size-to-particle spacing ratios (δ/h), and the accuracy of analysis results improves as well. The proposed approach can be easily implemented within the peridynamic framework, by defining higher-order weight functions. Therefore, no additional computational effort is necessary to implement this method. The effectiveness of the proposed higher-order approximation scheme is studied through three numerical examples in the following sub-sections.

As in Eq. (2.17), the higher-order approximation for nonlocal deformation gradient tensor is obtained for internal particles with a fully symmetric horizon. The internal particles refer to particles with a symmetric horizon and in this case represent particles not located at the boundary. At the boundary, some particles are missing within a horizon of (boundary) particles, and thus the particle arrangement is not perfectly symmetric close to the boundary. Therefore, the weight function used for Fig. 2.3 cannot provide a higher-order approximation to the deformation gradient tensor for boundary particles. One solution is to decrease the horizon size of boundary particles in order to provide a symmetric horizon. In this manner, only one layer of boundary particles is influenced by zero-energy instability. In another approach, the deformation gradient tensor of boundary particles is considered identical to the deformation gradient tensor of the nearest particle with a fully symmetric horizon. In this study, it is assumed that the weight functions used for internal particles are identical to those used for the boundary particles such that a consistent formulation for all particles is used to study the zero-energy mode. This assumption may be reasonable as the boundary particles are generally protected from the zero-energy mode instability. As described earlier in Section 2.2.2, the presence of the zero-energy mode is strongly associated to a symmetrical horizon.

2.4.2 Example No. 1: A 1D bar in tension

A 1D problem is used in this section to illustrate how the proposed method effectively suppresses the zero-energy mode. For a comparison, the same example used by Breitenfeld et al. [39] is used herein. A 1D bar with the length of L and varying stiffness (see Eq. (2.18)) is fixed at $x = 0$ and is subjected to a tensile stress of σ at $x = L$ (Fig. 2.4). The axial stiffness E (Young's modulus), varies along the length of the bar as follows:

$$E(x) = \begin{cases} E^0 = \sigma/\alpha & : x \leq L/2 \\ \sigma \left(\alpha + \frac{\beta}{2\sqrt{L}\sqrt{x/L - 1/2}} \right)^{-1} & : x > L/2 \end{cases} \tag{2.18}$$



(**a**) 1D bar

(**b**) Axial stiffness

Figure 2.4: 1D model with varying axial stiffness.

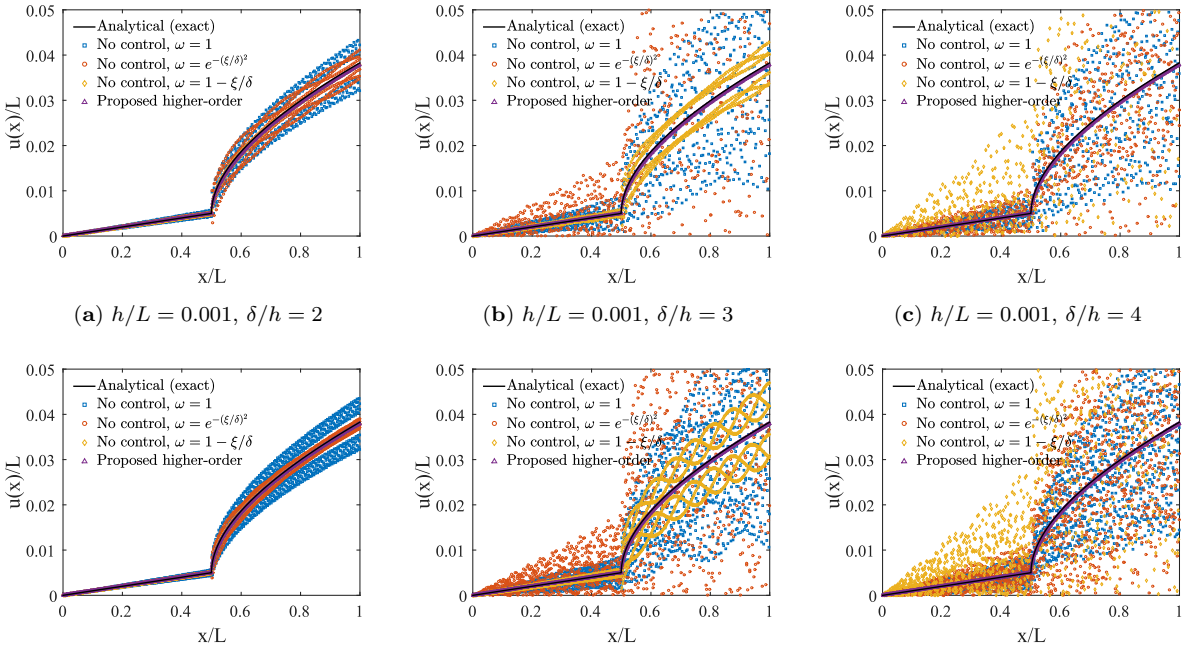
The analytical (local) solutions for the axial displacement, $u(x)$, and strain, $\epsilon(x)$, are provided by Breitenfeld et al. [39] as shown in Eqs. (2.19) and (2.20).

$$\frac{u(x)}{L} = \begin{cases} \alpha x/L & : x \leq L/2 \\ \alpha x/L + \frac{\beta}{\sqrt{L}}\sqrt{x/L - 1/2} & : x > L/2 \end{cases} \tag{2.19}$$

$$\epsilon(x) = \begin{cases} \alpha & : x \leq L/2 \\ \alpha + \frac{\beta}{2\sqrt{L}\sqrt{x/L - 1/2}} & : x > L/2 \end{cases} \tag{2.20}$$

Two particle spacing-to-length ratios ($h/L = 0.001$ and 0.0005) are used to study the effect of particle spacing on the extent of reduced oscillations or the zero-energy mode. $\alpha = 0.01$ and $\beta = 0.01$ are used in the simulations.

The axial displacement obtained from the peridynamic simulation including the proposed higher-order control method is compared to the results from a peridynamic simulation with no zero-energy mode control in Fig. 2.5. It is noted that the results for 'no control' on the zero-energy mode have been determined with three different weight functions, constant $\omega(\xi) = 1$, linear $\omega(\xi) = 1 - \xi/\delta$ and exponential $\omega(\xi) = exp\left(-(\xi/\delta)^2\right)$. Because an extensive study including the effect of weight function on the zero-energy mode is completed by Breitenfeld et al. [39], a few selected weight functions are studied herein. The higher-order approximation



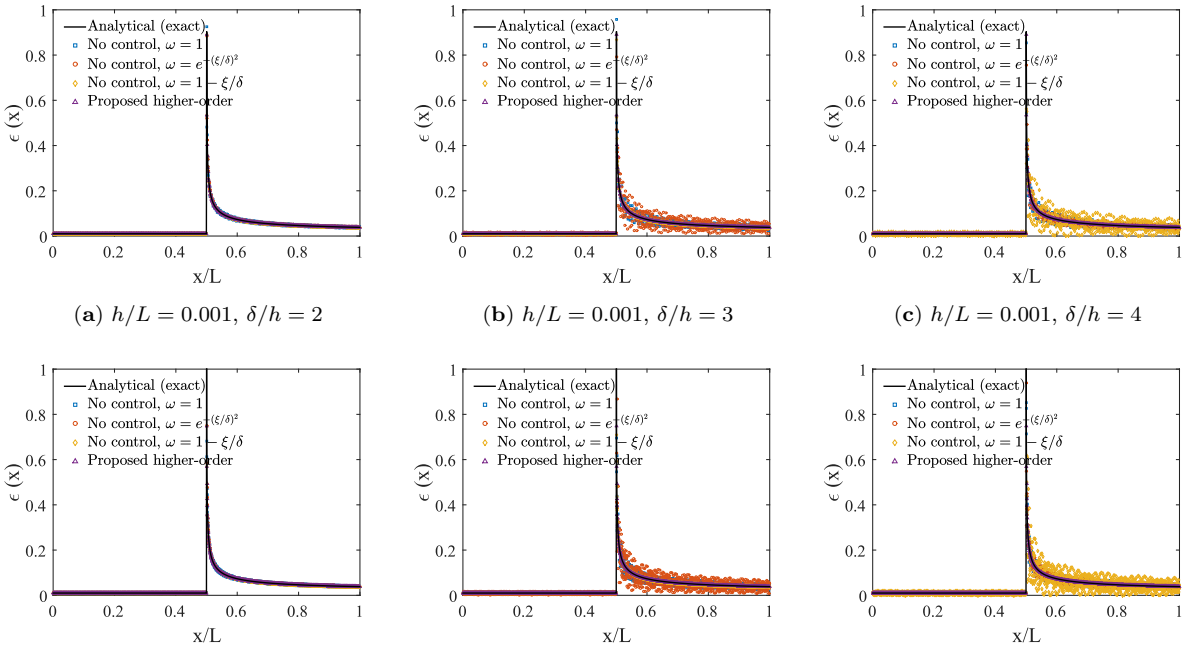
(**a**) $h/L = 0.001$, $\delta/h = 2$ (**b**) $h/L = 0.001$, $\delta/h = 3$ (**c**) $h/L = 0.001$, $\delta/h = 4$

(**d**) $h/L = 0.0005$, $\delta/h = 2$ (**e**) $h/L = 0.0005$, $\delta/h = 3$ (**f**) $h/L = 0.0005$, $\delta/h = 4$

Figure 2.5: Displacement solutions for various weight functions, including the proposed higher-order terms.

method is applied to a weight function as described in Fig. 2.3 for explicitly selected horizon size. It is indicated from the figure that for a given particle spacing, larger horizon size results in increased oscillations in the solutions, where none of the above presented weight functions has an significant effect on oscillations. Generally, smaller particle spacing (more particles) has a small effect in reducing the zero-energy mode oscillations. On the other hand, the simulation results indicate that the higher-order approximation method can effectively suppress the spurious zero-energy mode oscillations, regardless of horizon size and particle spacing, and yields a good agreement with the exact solutions, indicated as 'Analytical' in Figs. 2.5 and 2.6.

The axial strain results obtained from peridynamic simulations are compared to the exact analytical solution in Fig. 2.6. Discrepancy exist in the axial strain field when no control method is applied to alleviate zero-energy mode. Furthermore, regardless of the particle



(**a**) $h/L = 0.001$, $\delta/h = 2$ (**b**) $h/L = 0.001$, $\delta/h = 3$ (**c**) $h/L = 0.001$, $\delta/h = 4$

(**d**) $h/L = 0.0005$, $\delta/h = 2$ (**e**) $h/L = 0.0005$, $\delta/h = 3$ (**f**) $h/L = 0.0005$, $\delta/h = 4$

Figure 2.6: Strain distributions for varying weight functions, including the proposed higher-order terms.

spacing size and form of the weight function, more oscillations in the axial strain solutions is provided for larger horizon sizes. However, the higher-order approximate method alleviates the oscillation and produces the results which agree well with the analytical results.

The performance of the higher-order approximate deformation gradient tensor is compared with other available zero-energy mode control methods described in Section 2.2. The first step in applying the ZEI and ZEII control methods is to obtain optimum spring constants, C_I and C_{II}, respectively. The optimum constants minimize the displacement and strain energy errors described in Eqs. (2.21) and (2.22). The 'num' denotes the numerical solutions and 'local' indicates the exact solutions in Eqs. (2.21) and (2.22). N is the total number of particles.

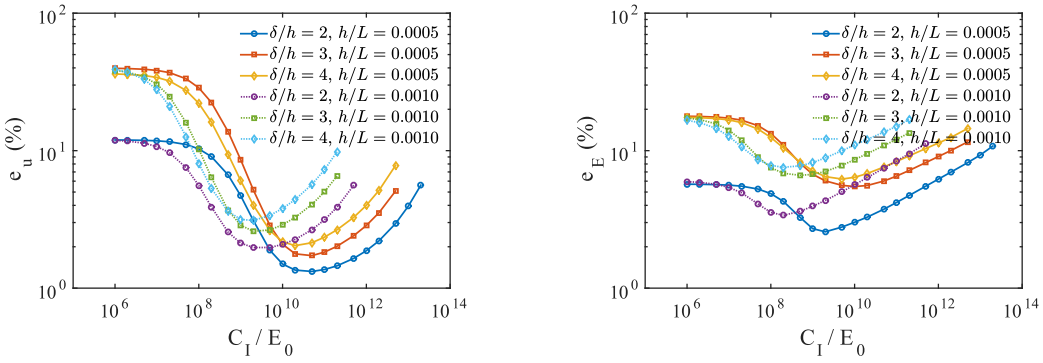
$$e_u = \sqrt{\frac{\sum_i^N \left(\mathbf{u}_i^{num} - \mathbf{u}_i^{local}\right)^T \left(\mathbf{u}_i^{num} - \mathbf{u}_i^{local}\right) V_i}{\sum_i^N \left(\mathbf{u}_i^{local}\right)^T \left(\mathbf{u}_i^{local}\right) V_i}} \tag{2.21}$$

$$e_E = \sqrt{\frac{\frac{1}{2}\sum_i^N \left(\boldsymbol{\epsilon}_i^{num} - \boldsymbol{\epsilon}_i^{local}\right)^T \left(\boldsymbol{\sigma}_i^{num} - \boldsymbol{\sigma}_i^{local}\right) V_i}{\frac{1}{2}\sum_i^N \left(\boldsymbol{\epsilon}_i^{local}\right)^T \left(\boldsymbol{\sigma}_i^{local}\right) V_i}} \tag{2.22}$$

Figs. 2.7 and 2.8 show the effect of C_I and C_{II} on the performance of ZEI and ZEII methods, respectively. The following conclusions can be drawn from the figures: (1) the displacement and strain energy errors are minimized for slightly different values of constants; (2) the optimum values depend on the particle spacing, h; (3) Finally, the horizon size does not affect the optimum constants. However, the obtained errors increase for larger horizon size, and thus the efficiency of these methods reduces by increased horizon size, δ/h. Since the PD formulations is nonlocal, it is expected the error approaches zero only for vanishing values of the horizon size. In comparison studies of the current and proposed treatments of the zero-energy mode, $C_I/E_0 = 5 \times 10^{10}$ and $C_{II}/E_0 = 1 \times 10^{20}$ are used for $h/L = 0.0005$, while $C_I/E_0 = 2 \times 10^9$ and $C_{II}/E_0 = 1 \times 10^{18}$ for $h/L = 0.0010$.

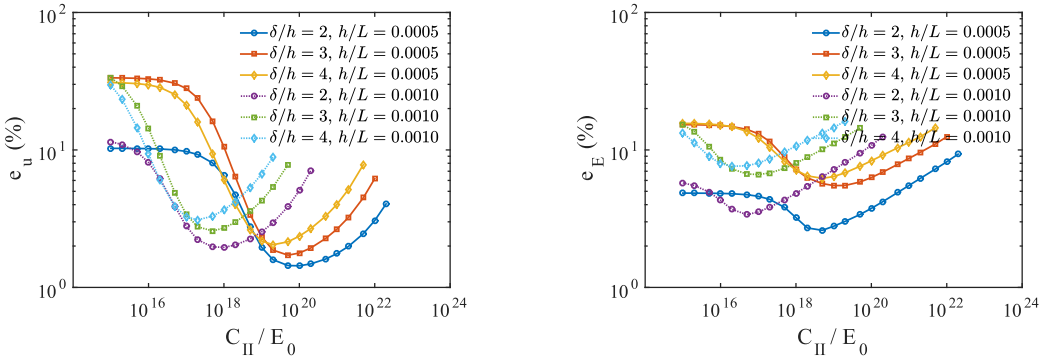
The relative errors obtained with the proposed higher-order approximate deformation gradient tensor are compared to the errors determined from using other available control methods described in Section 2.2. The results are also provided for the case with no zero-energy mode control. Fig. 2.9 presents the relative displacement errors for two various particle spacing, and Fig. 2.10 presents the relative strain energy errors. It is indicated from the figures that the proposed higher-order approximation method can effectively suppress the zero-energy mode and decrease the relative error in both axial displacements and strain energy solutions. For the two particle spacing sizes considered in this study, the proposed method generates the least errors relative to available methods.

In addition, the proposed method is not affected by increasing horizon size, as indicated by the reduced displacement errors as shown in Figs. 2.9(a) and 2.9(b). In contrast, with



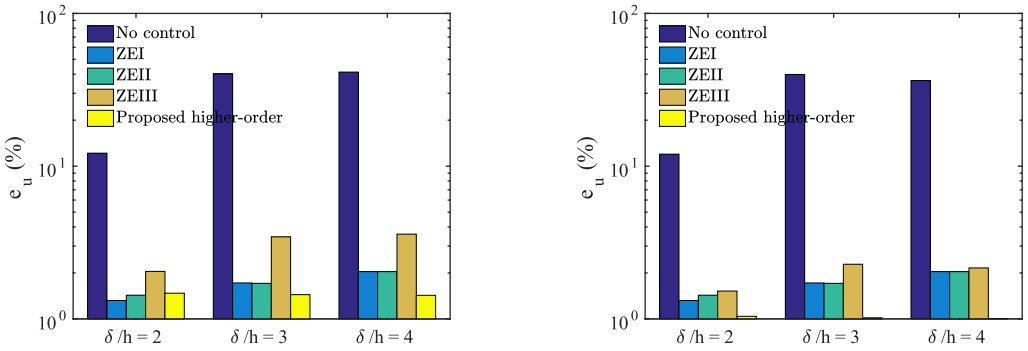
(**a**) e_u (**b**) e_E

Figure 2.7: The impact of constant C_I on the (a) relative displacement error and (b) relative strain energy error for various discretization patterns.



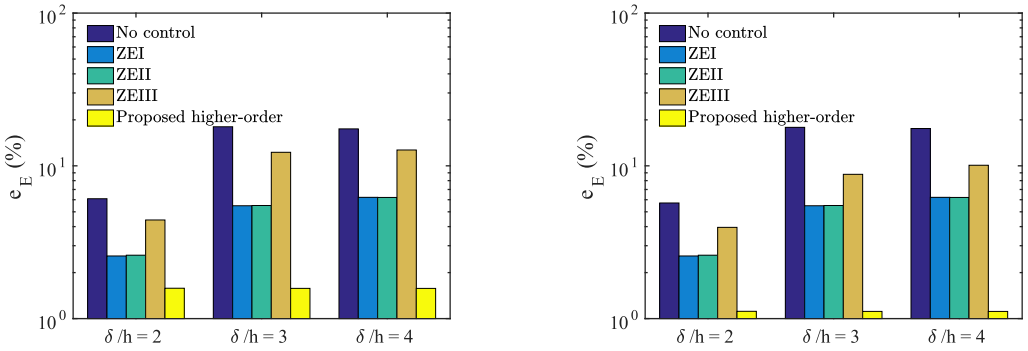
(**a**) e_u (**b**) e_E

Figure 2.8: The impact of constant C_{II} on the (a) relative displacement error and (b) relative strain energy error for various discretization patterns.



(**a**) $h/L = 0.001$ (**b**) $h/L = 0.0005$

Figure 2.9: The impact of zero-energy mode control methods on relative displacement error.



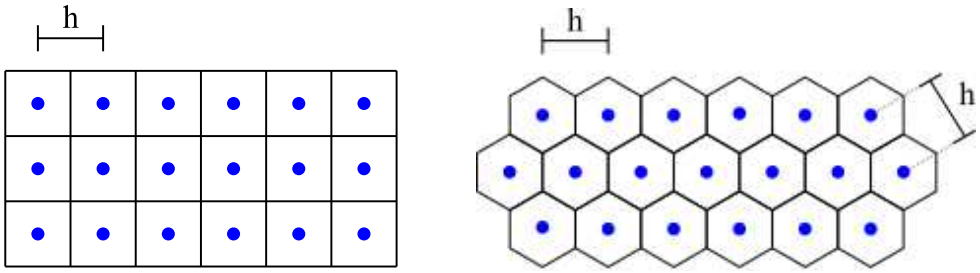
(**a**) $h/L = 0.001$ (**b**) $h/L = 0.0005$

Figure 2.10: The impact of zero-energy mode control methods on relative strain energy error.

other available methods, the relative error decreases as horizon size increases. However, the stabilized displacement treatment (ZEIII) fails to effectively decrease the strain energy error as shown in Figs. 2.10(a) and 2.10(b).

2.4.3 Formulation: 2D discretization

The higher-order approximation to the deformation gradient tensor is applied to a 2D problem in this section. Two different discretization patterns, quadrilateral and hexagonal,



(**a**) Quadrilateral pattern (**b**) Hexagonal pattern

Figure 2.11: Two discretization patterns used in 2D problems.

are considered as shown in Fig. 2.11. This study is limited to horizon-particle spacing $\delta/h < 4$ and provides an implementation method for all conceivable shapes of the horizon. This discretization scheme aims at identifying possible distribution of the neighboring particles based on the horizon size.

For the quadrilateral pattern, eight different horizon selections (Q1 to Q8 shown in Fig. 2.12) are made based on the horizon size. The circles, representing the horizon with the radius of δ, is used to obtain the neighboring particles which interact with each particle. The weight function is assumed radially symmetric, and therefore, the identical constants are assigned for particles within the same radius.

Similar to the 1D discretization, the key idea here is to allocate specific weight functions and obtain higher-order approximate deformation gradient tensor shown in Eq. (2.15). The constant, ω_1, defines the weight function of the nearest particles and is assumed the unity in all models. This assumption is necessary as weight functions are determined by dependent weight factors. The number of remaining weights generally determine the order of the approximation. 2D Taylor series expansions are used to obtain the higher-order approximation to the deformation gradient tensor. Table 2.3 provides the weight functions and the order of errors for eight models presented in Fig. 2.12.

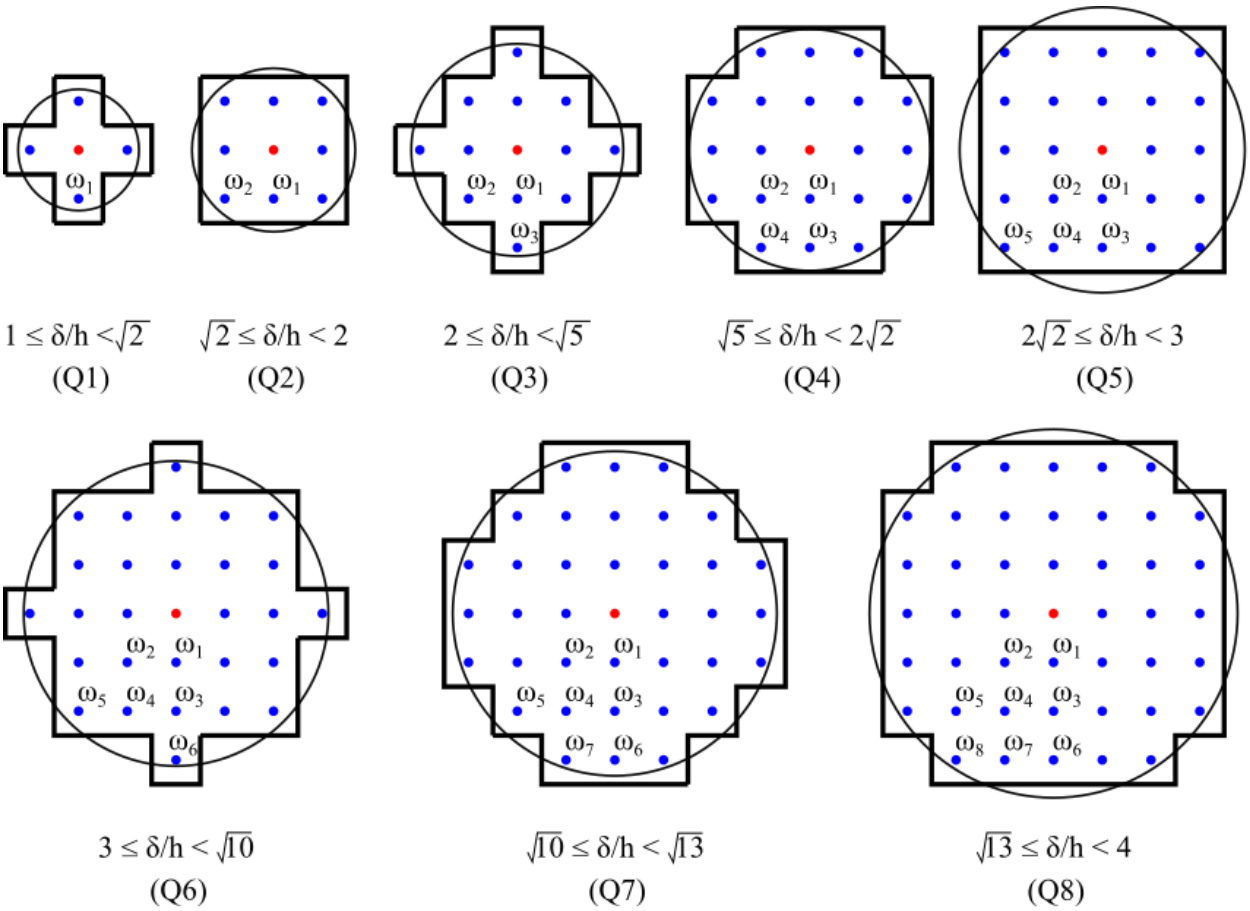


Figure 2.12: All possible horizon shapes with $\delta/h < 4$ for quadrilateral pattern.

For the hexagonal pattern, three different schemes are studied which correspond to the three horizon sizes illustrated in Fig. 2.13. Table 2.4 provides the weight functions and the order of errors.

Similar to the 1D case with $\delta/h = 1$, the particle arrangement in models with small horizon sizes (i.e., Q1, Q2 and H1) does not allow a deformation gradient tensor with an error term higher than $O(h^2)$ (refer to Table 2.3 and Table 2.4). The Q1 and H1 cases need a single weight function, ω_1, which is a numeral value (e.g., 1). Consequently, a higher-order approximation could not be achieved for the Q1 and H1 cases. Although the Q2 case includes

Table 2.3: Weight functions to obtain highest-order approximate deformation gradient tensor for quadrilateral pattern.

Model	Weight functions								Order of error
	ω_1	ω_2	ω_3	ω_4	ω_5	ω_6	ω_7	ω_8	
Q1	1								$O\left(h^2\right)$
Q2	1	1							$O\left(h^2\right)$
Q3	1	0	-1/16						$O\left(h^4\right)$
Q4	1	-8/46	-4/46	1/46					$O\left(h^4\right)$
Q5	1	8/14	-2/14	1/14	-1/14				$O\left(h^4\right)$
Q6	1	32/87	-15/87	-8/87	2/87	1/87			$O\left(h^6\right)$
Q7	1	-130/325	-61/325	34/325	-10/325	-1/325	1/325		$O\left(h^6\right)$
Q8	1	-68/148	-11/148	-5/148	-4/148	4/148	-2/148	1/148	$O\left(h^6\right)$

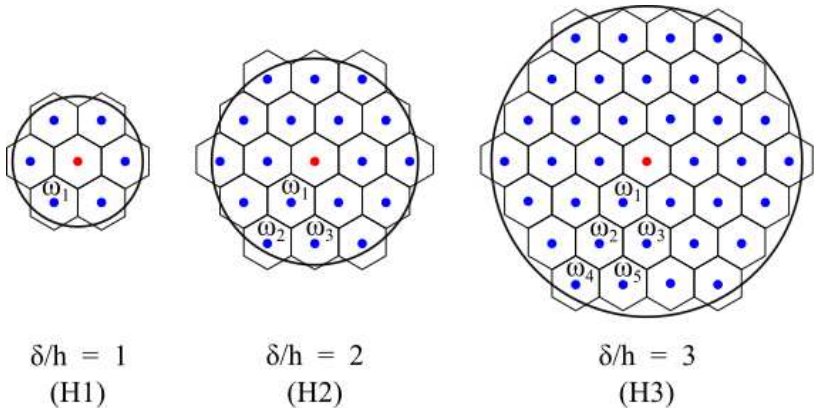


Figure 2.13: Particles in the hexagonal pattern ($\delta/h < 4$).

two weight functions, ω_1 and ω_2, the number of particles is insufficient to produce a higher order error term.

2.4.4 Example: A 2D plate with a rectangular hole subjected to tension

A 2D plate with a rectangular hole under tension loading is introduced in this section to study the effect of the proposed higher-order approximation scheme used to define the deformation gradient tensor on the suppression of the zero-energy mode. In the 2D analysis performed herein, a plane stress condition is assumed. The $100\,mm \times 40\,mm$ plate (Fig. 2.14) is fixed at

Table 2.4: Weight functions to obtain a higher-order approximate deformation gradient tensor using the hexagonal pattern.

Model	Weight functions					Order of error
	ω_1	ω_2	ω_3	ω_4	ω_5	
H1	1					$O\left(h^2\right)$
H2	1	-1/25	-1/25			$O\left(h^4\right)$
H3	1	-19/287	-18/287	1/287	1/287	$O\left(h^6\right)$

one end and is subjected to displacement loading of $0.4\,mm$ on the other side. The material model is assumed to be isotropic elastic with Young's modulus of $E = 210MPa$ and Poisson's ratio of $\nu = 0.3$. A $4\,mm \times 10\,mm$ rectangular hole is located in the center of the plate. The model is discretized using quadrilateral and hexagonal mesh patterns with two different particle spacing of $h = 1\,mm$ and $h = 2\,mm$, noting that the results presented in this sub-section are provided for $h = 1\,mm$, unless the spacing otherwise indicated.

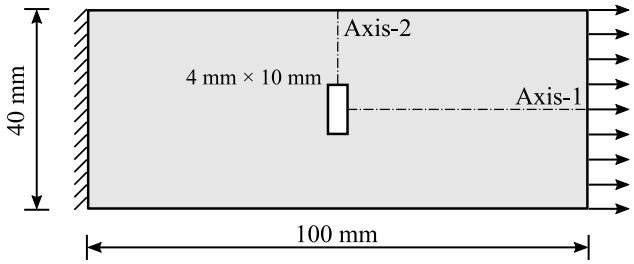


Figure 2.14: 2D plate with an opening subjected to tension.

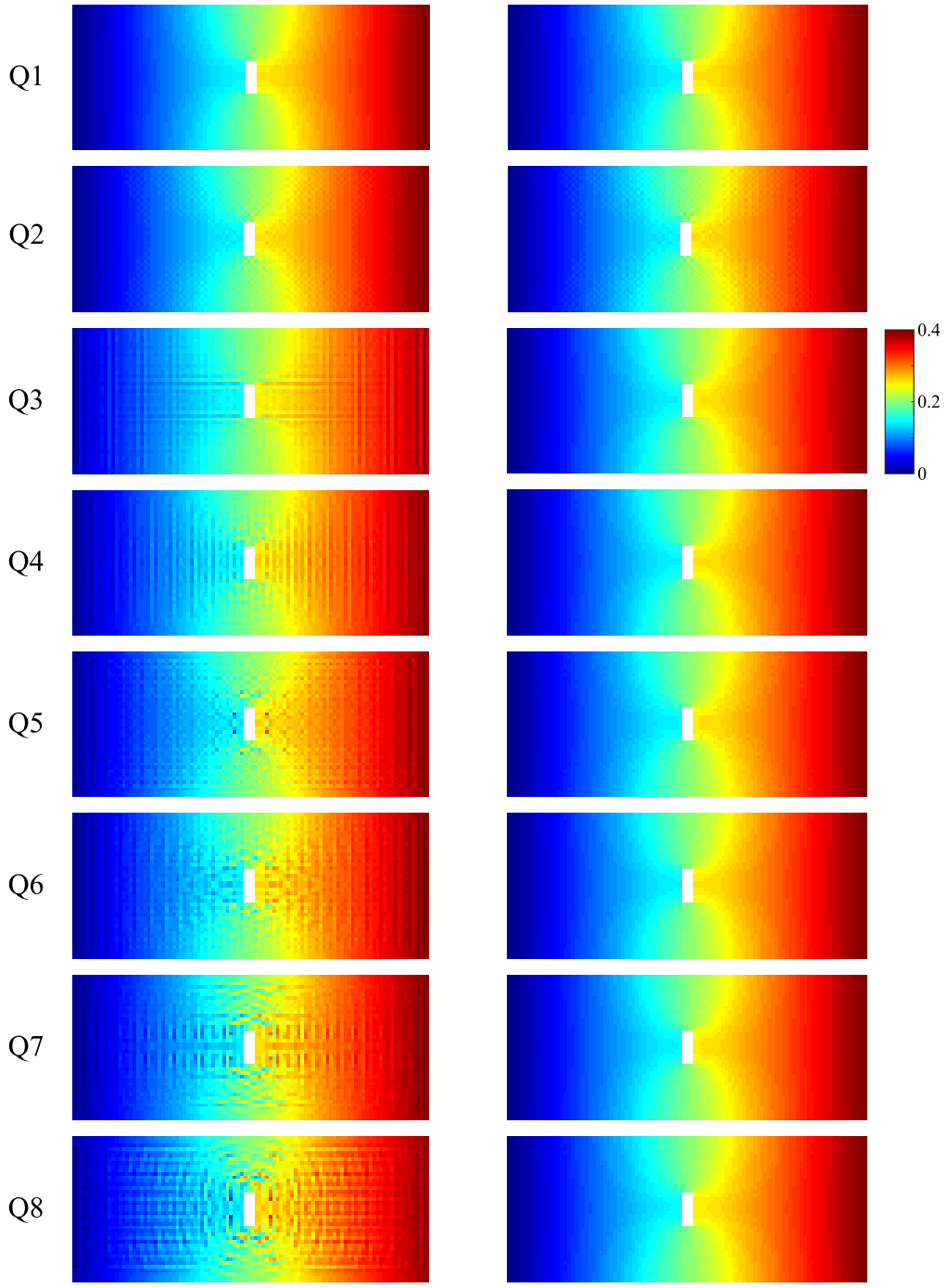
Fig. 2.15 provides a comparison of horizontal displacement, u_x, contours obtained for 'no zero-energy mode control' and proposed 'higher-order control' cases for quadrilateral models with $h = 1\,mm$. Fig. 2.15(a) presents the simulation results for the constant weight function, $\omega = 1$, while Fig. 2.15(b) shows the simulation results for the proposed higher-order approximation method with weight functions provided in Table 2.3. It is clear from the figure that a lack of control on zero-energy mode leads to oscillations. Furthermore, the results presented in Fig. 2.15(a) illustrate that the oscillations in the displacement field increases as the horizon size increases, whereas Fig. 2.15(b) shows negligible difference. The results

from using the higher-order approximate deformation gradient tensor (Fig. 2.15b) clearly illustrate that the proposed method effectively suppresses the zero-energy mode oscillations and provides smooth displacement fields regardless of the horizon size.

Fig. 2.16 provides a comparison for the results obtained from hexagonal mesh models and shows that the implementation of the proposed weight functions provided in Table 2.4 is also as effective for hexagonal mesh pattern in controlling zero-energy mode and thus producing the smooth displacement contours without oscillations as shown in Fig. 2.16(b).

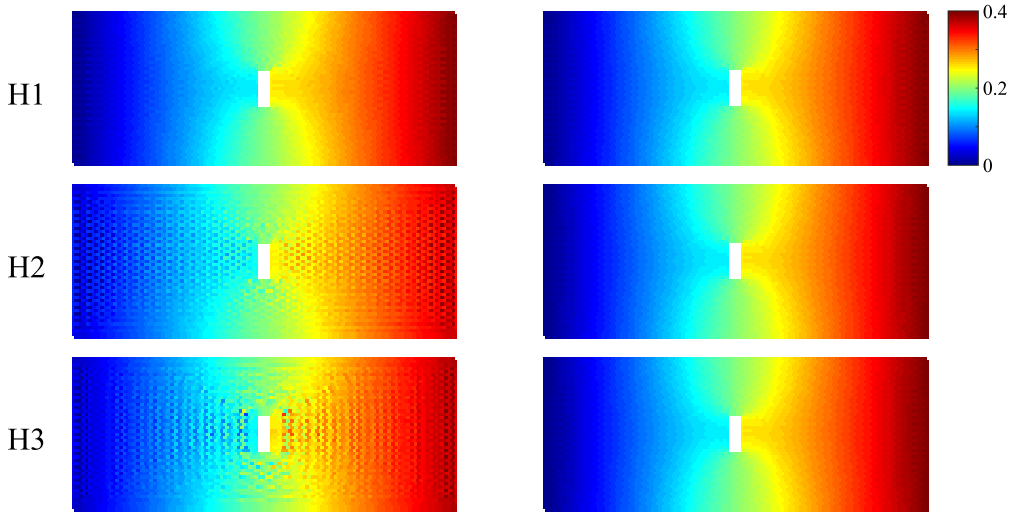
Studies were performed to quantify the effect of the proposed higher-order approximation. The results are presented with respect to the two symmetry axes of the plate, Axis-1 and Axis-2. The distributions of the horizontal displacement, u_x, and horizontal stress, σ_x, along Axis-1 direction obtained from the NOSBPD simulation with no zero-energy control are presented in Fig. 2.17 for quadrilateral models. The ZEI control method and the proposed higher-order control method are compared with the results from a FEA analysis including multiple mesh refinement. The results are provided only for selected quadrilateral mesh cases, Q4, Q6 and Q8. The weight function for simulations with no zero-energy control and ZEI is assumed to be unity, $\omega = 1$. In addition, the optimum value for constant C_I for the current example is obtained as $E \times 10^{-3}$ and $E \times 10^{-4}$ for $h = 1\,mm$ and $h = 2\,mm$, respectively, through a study similar to the 1D problem in Section 2.4.2.

For the case with no zero-energy control method, a larger horizon size results in more discrepancy than the FEA results obtained in both displacement and stress fields. Both control methods, ZEI and proposed higher-order approximation are able to suppress the spurious zero-energy mode oscillations in all three models. However, the effectiveness of ZEI is slightly decreased by increasing horizon size, whereas the proposed higher-order approximation is more effective for increased horizon sizes. As seen in both fields, the results with higher-order approximation best agree with the FEA results. For clarity of presentation, Fig. 2.17 only includes the results of ZEI because of ZEII and ZEIII are almost identical to the results of ZEI.



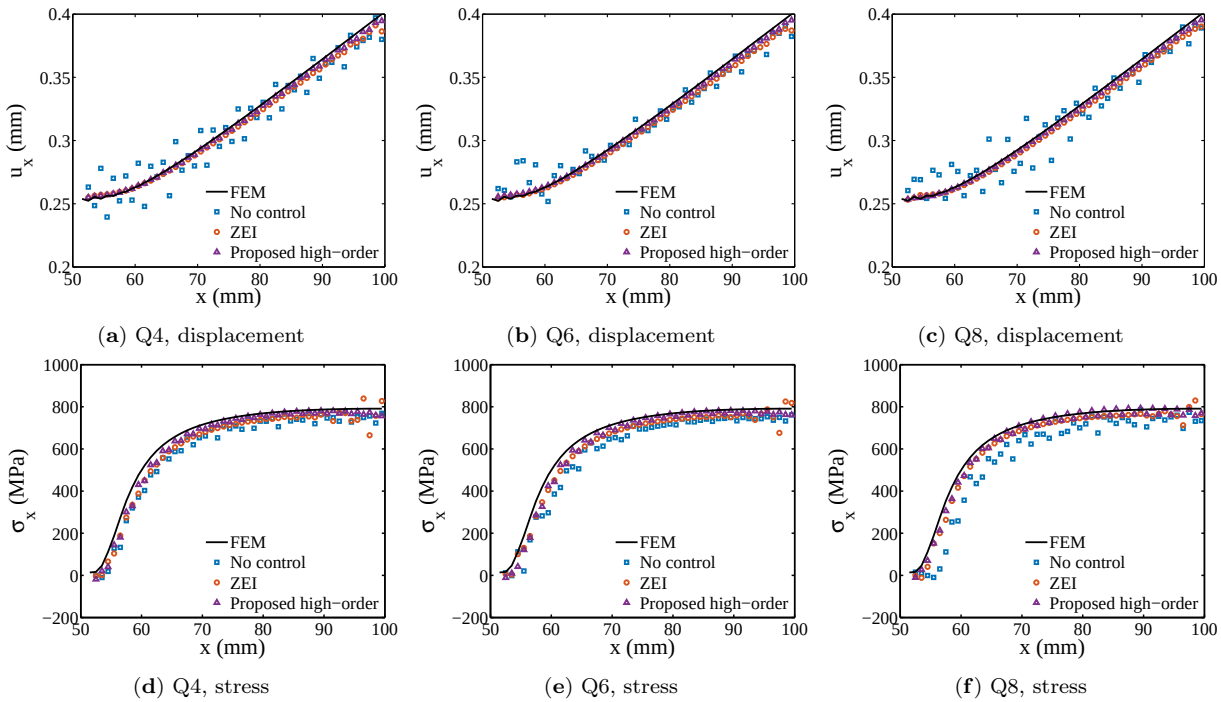
(**a**) No control, $\omega = 1$ (**b**) Proposed higher-order

Figure 2.15: Comparison of the horizontal displacement, u_x, distribution of quadrilateral models for no zero-energy mode control and for higher-order approximation method.



(**a**) No control, $\omega = 1$ (**b**) Proposed higher-order

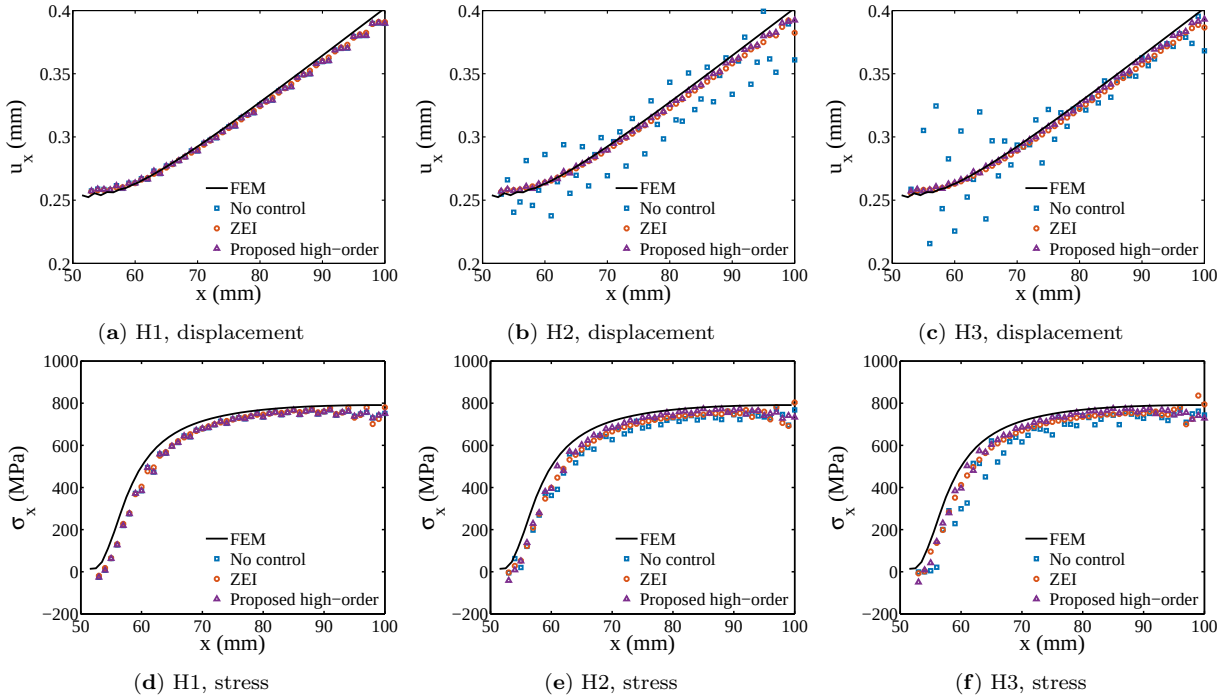
Figure 2.16: Comparison of the horizontal displacement, u_x, distribution of hexagonal models for no zero-energy mode control and for higher-order approximation method.



(**a**) Q4, displacement (**b**) Q6, displacement (**c**) Q8, displacement

(**d**) Q4, stress (**e**) Q6, stress (**f**) Q8, stress

Figure 2.17: Peridynamic prediction of horizontal displacements and stresses along Axis-1 for quadrilateral models comparing to FEA results.



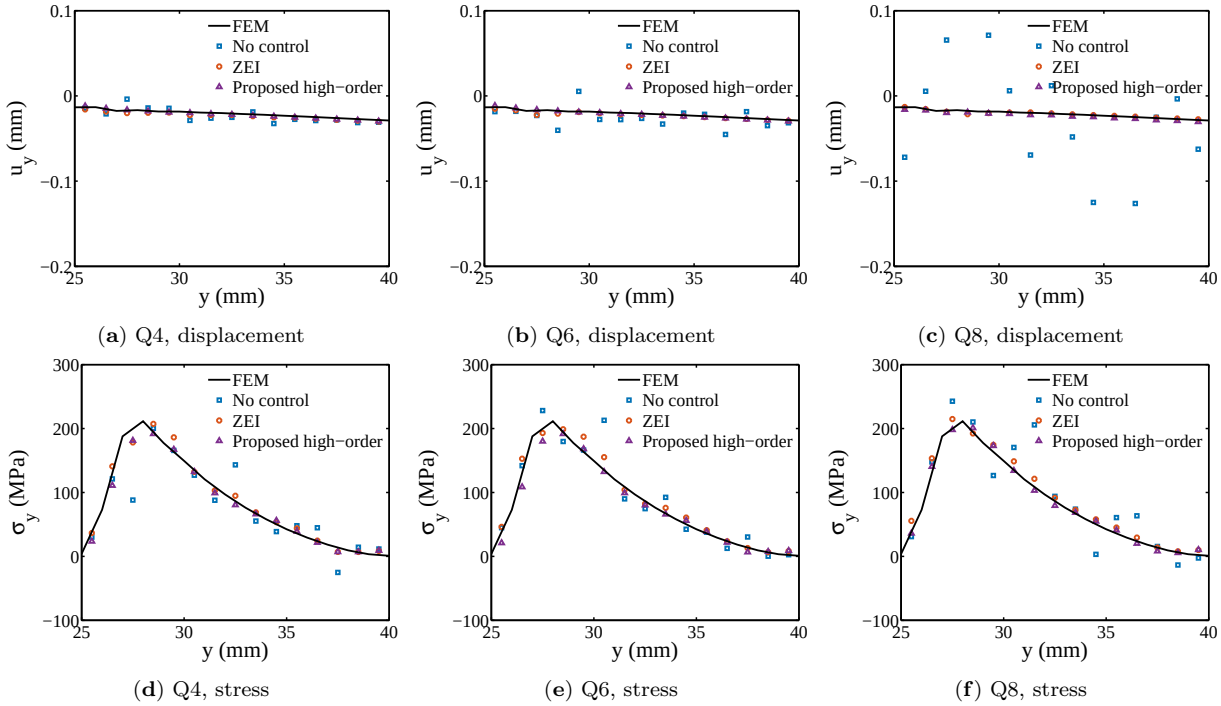
(**a**) H1, displacement (**b**) H2, displacement (**c**) H3, displacement

(**d**) H1, stress (**e**) H2, stress (**f**) H3, stress

Figure 2.18: Peridynamic prediction of horizontal displacements and stresses along Axis-1 for hexagonal models comparing to FEA results.

The horizontal displacement, u_x, and horizontal stress, σ_x, is also provided for hexagonal models in Fig. 2.18. For model H1, as expected, the proposed higher-order approximation method resembles the results from no zero-energy mode control. However, the results have good agreement with FEA results because the nonlocal peridynamic simulation converge to local (FEA) results for $\delta \to 0$. For H2 and H3 with larger horizon sizes, the absence of control on the zero-energy mode results is significant oscillations in the displacement fields. The stress is also much lower than predicted FEA results. Although, the ZEI control method is successful in smoothing displacement field and capturing the FEA results, the higher-order approximation provides the best predictions for the three studied hexagonal models.

The vertical displacement, u_y, and vertical stress, σ_y, are also provided along Axis-2 for quadrilateral models and for hexagonal models in Figs. 2.19 and 2.20, respectively. As seen in Fig. 2.19, the obtained vertical displacement appears disordered for no zero-energy



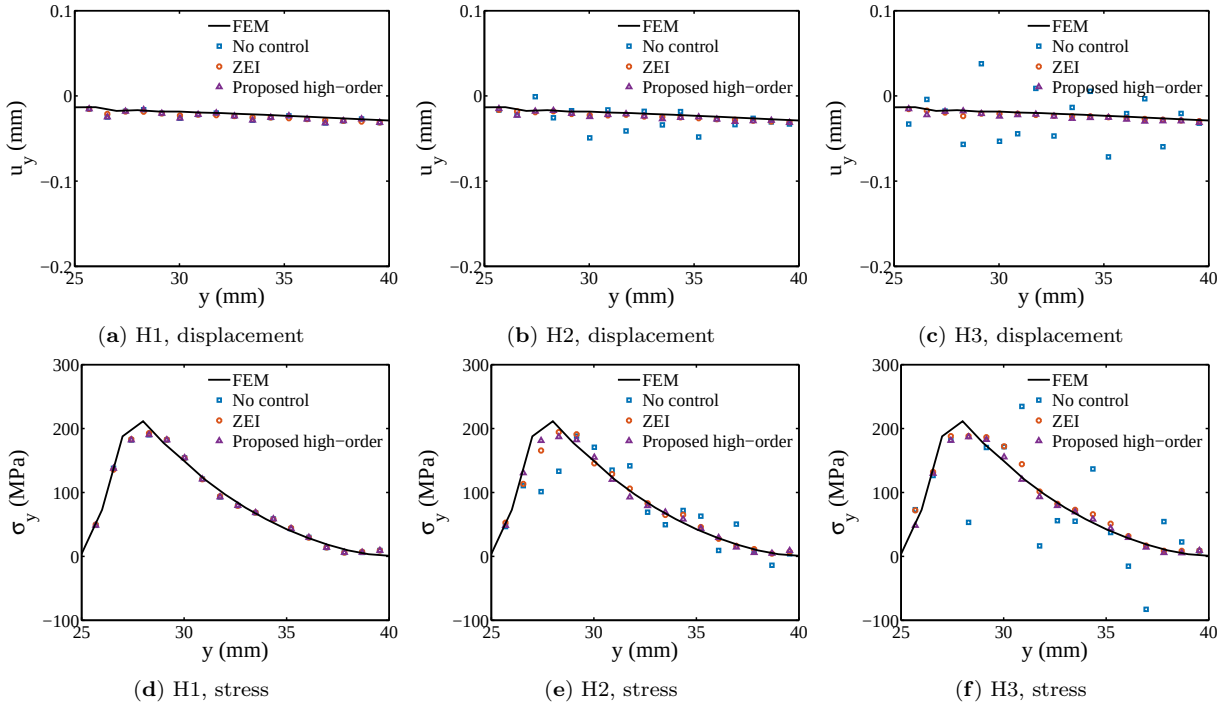
(**a**) Q4, displacement (**b**) Q6, displacement (**c**) Q8, displacement

(**d**) Q4, stress (**e**) Q6, stress (**f**) Q8, stress

Figure 2.19: Peridynamic prediction of horizontal displacements and stresses along Axis-2 for quadrilateral models comparing to FEA results.

mode control. However, both ZEI and proposed higher-order approximation methods are as effective as the results from the FEA in smoothing the displacement solutions. In the vertical stress fields, the proposed higher-order approximation agrees better with the FEA results. It is determined from this example that the proposed higher-order approach is more robust than other models, especially for varying horizon size. In other words, the advantage of the proposed method over other methods, in terms of suppressing oscillations, is extended to the stress solutions.

The displacement and strain energy errors (using Eqs. (2.21) and (2.22)) are provided along Axis-1 and Axis-2 for two different particle spacing size and are depicted in Figs. 2.21 and 2.22, respectively. It is obvious that the overall response follow the same concept and the following conclusions can be derived from the results. The errors of the results

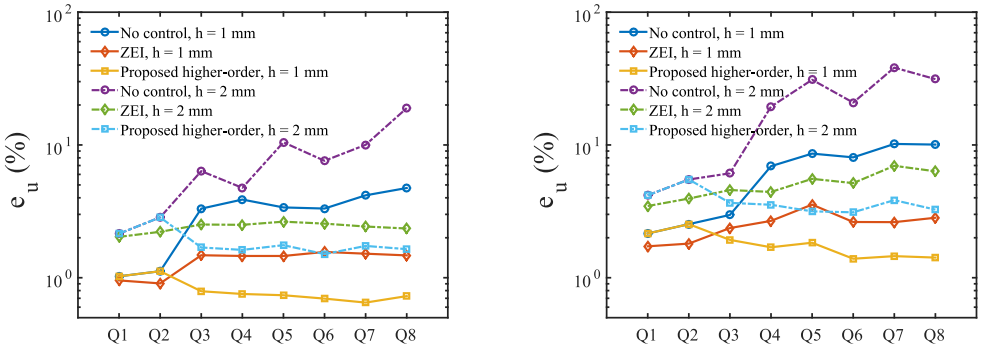


(**a**) H1, displacement (**b**) H2, displacement (**c**) H3, displacement

(**d**) H1, stress (**e**) H2, stress (**f**) H3, stress

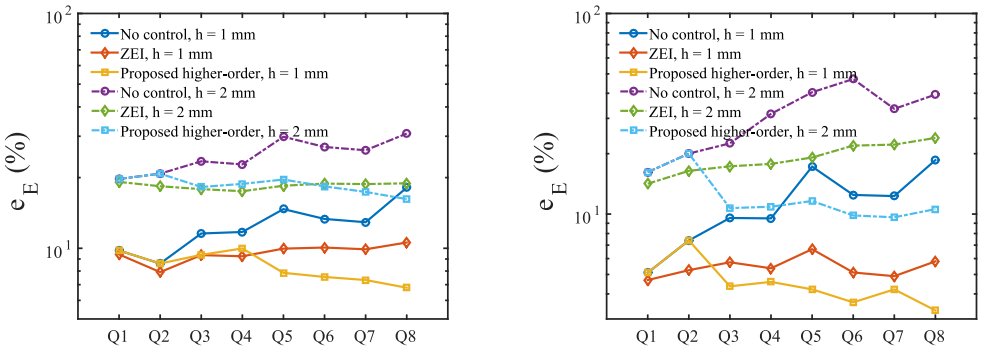
Figure 2.20: Peridynamic prediction of horizontal displacements and stresses along Axis-2 for hexagonal models comparing to FEA results.

with no control on the zero-energy mode increase for larger horizons. The ZEI controls the zero-energy mode and decreases the errors, however, its efficiency is reduced for larger horizon sizes. For instance, an increase in relative errors can be found for displacement and strain energy fields obtained using ZEI control method along Axis-2. On the other hand, the higher-order approximation method applicable for Q3-Q8, yields the lowest error among other simulations herein. Furthermore, the errors with higher-order simulations are gradually decreased with increasing the horizon size from Q3 to Q8. Finally, the simulation with smaller particle spacing (more particles) results in reduced displacement and strain energy errors; and therefore, small particle spacing is a feasible way to decrease the zero-energy mode oscillation although it significantly increases the computational expense.



(**a**) Axis-1 (**b**) Axis-2

Figure 2.21: Displacement errors along a) Axis-1 and b) Axis-2 for various quadrilateral models.



(**a**) Axis-1 (**b**) Axis-2

Figure 2.22: Strain energy errors along a) Axis-1 and b) Axis-2 for various quadrilateral models.

2.4.5 Example: Quasi-static crack growth in Compact Tension specimen

A 2D model with plane stress condition is developed to reproduce an experimental study in which Samal et al. [54] conducted a fracture test with a Compact Tension (CT) specimen, as illustrated in Fig. 2.23.

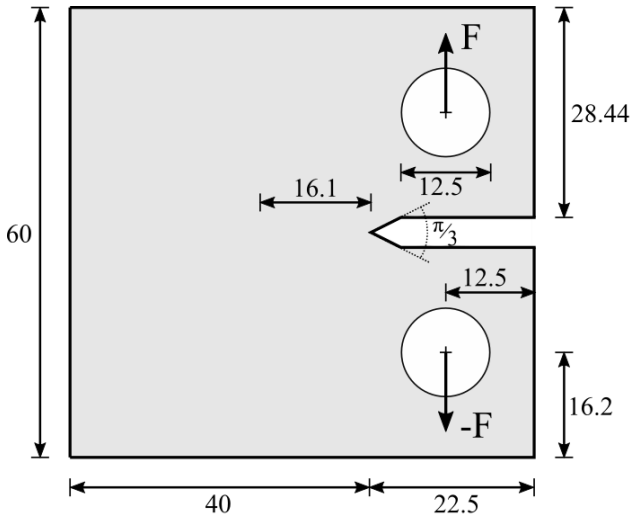


Figure 2.23: The compact tension specimen (Lengths given in millimeters, and the thickness of the specimen is 25 mm).

The material model is assumed to be nonlinear elastic-plastic, with $E = 210GPa$, $\nu = 0.3$ and the initial yield stress, $\sigma_0 = 405\,MPa$. An isotropic hardening law is employed as shown in Eq. (2.23), where ϵ_p is the equivalent plastic strain; B and n are the material constants. This study uses determined constants, $B = 513\,MPa$ and $n = 0.39$ from experimental stress-plastic strain curve of the material DIN22NiMoCr3-7 [54].

$$\sigma_y = \sigma_0 + B\left(\epsilon_p\right)^n \tag{2.23}$$

This paper adopts the procedure used by Tupec et al. [23] to implement the continuum damage model in the peridynamic framework. To do so, the weight function for the bond between particles $\mathbf{x}$ and $\mathbf{x}'$ must be modified by the following weight function:

$$\hat{\omega} = \omega\left(\xi\right)\omega_D\left(D, D'\right) \tag{2.24}$$

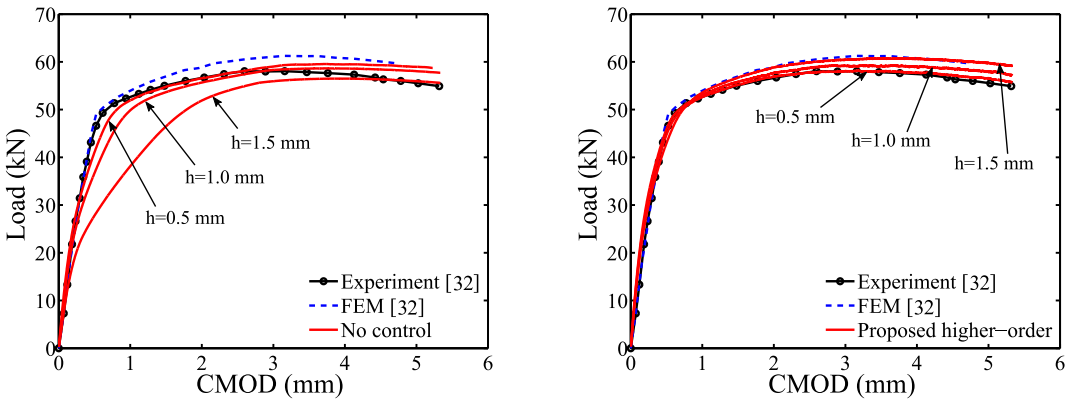
In Eq. (2.24), D and D' are the damage parameters corresponding to the particles $\mathbf{x}$ and $\mathbf{x}'$, respectively. ω_D is introduced to determine the bond breakage between the peridynamic particles and is assumed 1 as shown in Eq. (2.25), unless one of the particles is fully damaged as defined by Eq. (2.26). ϵ_f is the critical plastic strain. The general form of ϵ_p depends on the material parameters and stress triaxiality [55]; however in this study, a constant value of $\epsilon_p = 0.8$ is obtained from the 1D tension test results [54].

$$\omega_D\left(D, D'\right) = \begin{cases} 0 & : D = 1 \quad or \quad D' = 1 \\ 1 & : otherwise \end{cases} \tag{2.25}$$

$$D = \begin{cases} \int_0^{\epsilon_p} \frac{d\epsilon_p}{\epsilon_f} & : D < 1 \\ 1 & : D \geq 1 \end{cases} \tag{2.26}$$

The CT model in Fig. 2.23 is discretized using a quadrilateral mesh pattern with three different particle-spacing sizes: $h = 1.5\,mm$, $h = 1.0\,mm$ and $h = 0.5\,mm$. The horizon-to-particle spacing ratio, δ/h of 3.4 is used in the analysis of these models. It is determined from Fig. 2.12 and Table 2.3 that the weight function for model Q7 is used to apply the proposed higher-order approximation method in order to control the zero-energy mode. Fig. 2.24 provides a comparison of load-CMOD (crack mouth opening displacement) responses from the peridynamics analysis model as well as the experiment and numerical model presented by Samal et al. [54].

It is noted that the results generated without using the zero-energy control mode are provided in Fig. 2.24(a), whereas Fig. 2.24(b) provides the results produced by using the proposed higher-order control method. It is concluded from Fig. 2.24(a) that peridynamics analysis results are highly mesh-dependent without the zero-energy control method. Furthermore, there is a discrepancy between the analysis and experimental results when the largest particle-spacing size ($h = 1.5\,mm$) is used, whereas the prediction improves when the smallest particle spacing is used. However despite of the smallest particle spacing size



(**a**) No control, $\omega = 1$ (**b**) Proposed higher-order

Figure 2.24: Load-CMOD responses of the CT specimen.

($h = 0.5\,mm$), the discrepancy with the experimental results persists, particularly in the plateau region of the load-CMOD curves.

On the contrary, Fig. 2.24(a) shows that the results produced by using the proposed higher-order control method agrees well with the experimental results when studied with various particle-spacing sizes. The results obtained using the smallest particle spacing size results in an improved agreement with the experimental results, relative to previously produced finite element analysis results which include adaptive mesh refinements at localized crack locations.

2.5 Discussion

2.5.1 Random particle distribution in 1D model

Although the majority of studies using peridynamics utilize a uniform particle distribution, the proposed higher-order formulation may also be developed for a random particle distribution where the particle spacing among all of its particles and each particle's volume are not constant. For a realization of the proposed formulation using a random particle distribution,

a one-dimensional formulation is illustrated below for a possible implementation in a 1D problem.

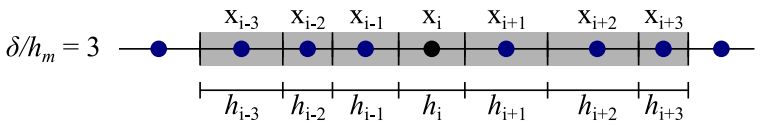


Figure 2.25: A schematic 1D irregular particle distribution.

In a 1D formulation, a non-uniform discretization scheme is used as shown in Fig. 2.25, where the length of particle $\mathbf{x}_i$ is randomly selected within the following range:

$$h_i = h_m[(1-a),(1+a)] \tag{2.27}$$

where h_m is the median particle spacing; a is a randomness parameter, which ranges between 0 and 1 and defines the variation from the median particle spacing, h_m. $a = 0$ yields a uniform discretization with a constant particle spacing, $h = h_m$, whereas for $a = 1$, the particle spacing is randomly chosen between 0 and $2h_m$. It is clear that for the studied irregular discretization, the weight function in Fig. 2.3 does not provide a higher-order approximation for the deformation gradient tensor. In order to obtain a higher-order approximation for such irregular discretization, an exponential weight function is introduced as follows:

$$\omega(\xi) = e^{(-c\xi/h_m)} cos(\pi\xi/h_m) \tag{2.28}$$

where c is a constant obtained to approximate the weight function with discrete values provided in Fig. 2.3 for each horizon size δ/h_m. For $\delta/h_m = 3$, Fig. 2.26 represents the proposed exponential weight function for $c = 2$ in Eq. 2.28 as well as discrete weight functions of ω_1, ω_2 and ω_3 for h_m, $2h_m$ and $3h_m$, respectively. ω_1 is obtained by assuming $\xi = h_m$ in Eq. 2.28, $\omega_2/\omega_1 = -1/10$, and $\omega_3/\omega_1 = 1/135$ (see Fig. 2.3 for $\delta/h = 3$).

For the example problem studied in Section 2.4.2, where $h_m/L = 0.001$ and $\delta/h_m = 3$, the displacement and energy errors (obtained by Eqs. 2.21 and 2.22) are presented in Fig. 2.27

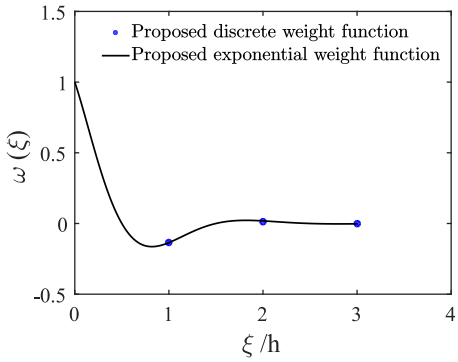
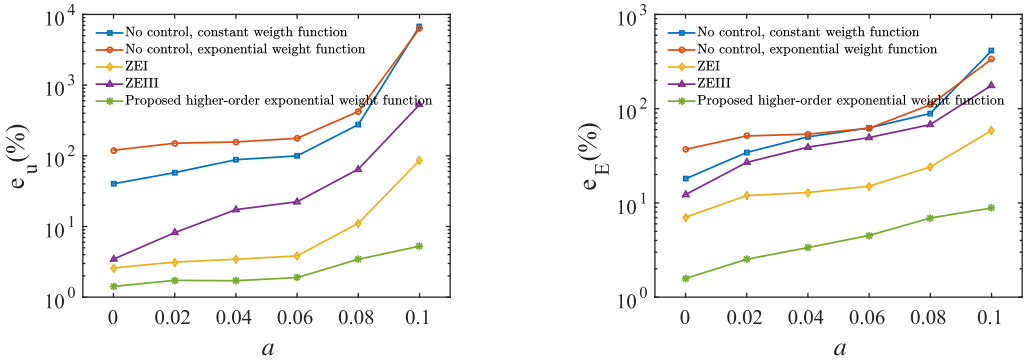


Figure 2.26: Proposed higher-order weight function vs. discrete higher-order weight function for $\delta/h_m = 3$.



(**a**) displacement error (**b**) Strain energy error

Figure 2.27: (a) Displacement error; (b) strain energy error for five zero-energy control cases with random particle distributions.

for varying the randomness parameter, a. The mean values are determined from multiple runs (~ 100) and presented in Fig. 2.27 for five zero-energy control methods.

The following conclusion can be obtained from Fig. 2.27:

- As $a \to 0$, the solutions are similar to those determined by the uniform discretization with a constant particle spacing of h_m. Furthermore as $a \to 0$, the weight function agrees with the discrete weight function provided in Fig. 2.3 for the higher-order

approximation. Similar to the results found in Section 2.4.2, the higher-order approach using a random particle discretization provides the least displacement and energy errors when compared to no-control and other available zero-energy control methods included in this study.

- As the randomness parameter, a, increases, the displacement and energy errors increases in all cases.

- However, the solution with proposed exponential higher-order weight function consistently yields the least errors. For $a = 0.1$, the higher-order method results in almost 10% displacement and energy errors, whereas the ZEI control method produces more than 100% displacement and energy errors. Based on the 1D problem studied herein, the proposed higher-order method appears promising for suppressing the zero-energy oscillation even when a random particle discretization is used.

- It is indicated that the original formulation with no zero-energy mode control results in instable solutions and significant error such as 10^4%, particularly for the irregular particle distribution. It is noted that the error was calculated using Eqs. (2.21) and (2.22) for completeness of Fig. 2.27, although it may be meaningless. Therefore, Fig. 2.27 illustrates that the instabilities in the solutions and errors have been significantly reduced by applying various control methods including the proposed one.

Although, the proposed higher-order approximation method is mainly applied to problems with constant horizon size in this study, some peridynamic applications such as adaptive mesh refinement and multiscale modeling require the use of non-uniform (or random) horizon sizes [25, 56].

The assumption of unequal horizon size for peridynamic particles results in unbalanced internal force in peridynamic governing equation (Eq. 2.1) known as "ghost forces". In addition to attempts to reduce the effect of ghost force problem [17, 19, 56, 57], the "dual horizon" concept is proposed [25]. It is worth mentioning that the dual-horizon method in non-ordinary

state-based peridynamic formulations uses the same approximation for the nonlocal deformation gradient tensor in Eq. 2.4. Therefore, the proposed higher-order exponential weight function can be effectively used in order to suppress zero-energy mode oscillation for problems with varying particle spacing size and/or varying horizon size. Nevertheless, it is important to further advance the proposed formulation to allow random particle distribution options for higher dimensions.

2.5.2 Development of a high-order approximation formulation for 3-dimensional problems

The higher-order approximation method has been successfully implemented for 1D and 2D problems in this study. Furthermore, the proposed method can be extended to solve 3D problems using a similar approach. For the proof of this concept, a reasonable horizon shape may be considered. The next step may conceivably involve the 3D Taylor series expansion to obtain a higher-order approximation to the deformation gradient tensor.

For example, a 3D formulation is provided for the horizon shape that may be obtained for $\delta/h = 2$. For clarity, one-eighth of a single horizon is illustrated in Fig. 2.28. For each particle in the horizon of the main particle, $\mathbf{x}$, a discrete weight function is assigned with respect to the distance from each particle to the particle, $\mathbf{x}$. For the particle discretization shown in Fig. 2.28, four weight functions may be selected: $\omega_1 = \omega(h)$, $\omega_2 = \omega(\sqrt{2}h)$, $\omega_3 = \omega(\sqrt{3}h)$ and $\omega_4 = \omega(2h)$. Assigning the unity for the weight function of nearest particles ($\omega_1 = 1$), the remaining weight functions may be determined by using the 3D Taylor series expansion in order to obtain a higher-order approximation for the deformation gradient tensor. For the horizon size ($\delta/h = 2$), using $\omega_2 = -1/3$, $\omega_3 = 1/6$ and $\omega_4 = -1/48$, the formulation results in the $O(h^2)$ order in the calculation of nonlocal deformation gradient tensor. For larger horizon sizes, more particles may be involved in a horizon of each particle; therefore, higher-order approximations can be obtained. In summary, a three-dimensional expansion of

the proposed formulation (or a generalization of the higher-order formulation) is achievable although additional work is necessary for careful formulations.

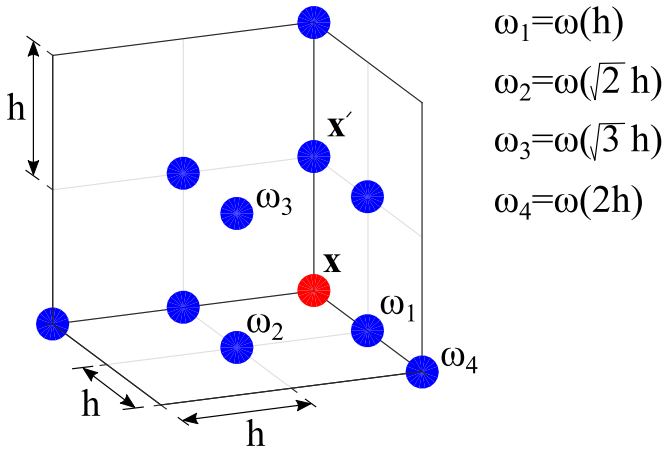


Figure 2.28: Illustration of horizon in a 3D discretization for $\delta/h_m = 2$.

2.6 Conclusion

The spurious zero-energy mode has known to be a problem for peridynamic solutions. The proposed higher-order approximation to the nonlocal deformation gradient tensor provides an effective solution for suppressing the spurious zero-energy mode reportedly found in the non-ordinary state-based peridynamics. Simulation results show that the proposed method outperforms other corresponding approaches in suppressing the zero-energy mode, and is more robust against the simulation model size, especially when the model is sensitive to horizon size. However, the computational complexity caused by the higher-order expansion does not appear to affect the computational efficiency. For the parameters studied herein, the proposed method is superior to other methods available in literature as it enhances the stress and displacement plots without increasing the computational expense. That is, the solutions are unaffected by horizon size and thus can be more effective for large models. Future work includes the extension of the proposed method to large-scale 3D models and evaluation of computational intricacy associated with the proposed higher-order expansion in such models.

Chapter 3

Meshless Modeling Framework for Fiber Reinforced Concrete Structures[1]

[1] A. Yaghoobi and M. G. Chorzepa. "Meshless modeling framework for fiber reinforced concrete structures." Computers & Structures 161 (2015): 43-54. Reprinted here with permission of publisher.

ABSTRACT

In this study, a meshless analysis framework based on the non-ordinary state-based peridynamic method is proposed to predict the response of fiber reinforced concrete (FRC) structures. The approach includes a semi-discrete method in modeling the fiber reinforcement. With this approach, additional degrees of freedom from fibers are not present, and thus the computational efficiency is enhanced. Furthermore, there is no need to monitor concrete crack paths as the crack initiation, growth, and coalescence are an inherent outcome of the proposed framework. This is demonstrated through several examples. The accuracy is maintained for a failure analysis of FRC beams under bending.

3.1 Introduction

Concrete is one of the most important structural materials but weak in tension, on account of its brittle, non-fibrous cementitious matrix. Steel reinforcement bars or fibers are added to compensate for the weakness in conventional civil structures. The tensile cracks begin with the onset of isolated nano-cracks and grow to form micro-cracks, which grow together to form macro-cracks and visible cracks [58]. The fibers arrest these cracks by forming bridges across them; however, a bond failure between fibers and concrete occurs and widens the crack width. Generally, macro-, micro-, and nano-fibers enhance tensile strength, ductility, and toughness (ability to deform without fracture or to absorb energy) and thus are important characteristics of engineered composite structures.

Numerical modeling of large structures has become a practical alternative to physical experiments which are often financially burdensome [59]. For this reason, effective numerical modeling techniques are vital to predict the response of concrete structures. Furthermore, engineers often resort to computer simulation models when it comes to evaluating composite structures (i.e. design by analysis). Increasing availability of experimental data has allowed for the development and validation of analytical methods.

Modeling of FRC composites, however, is often limited to the finite element analysis (FEA) framework. In a FEA model, it is particularly challenging to accurately represent the fiber distribution and orientations. Available modeling methods that integrate multi-scale fibers are as follows: (1) Steel or synthetic macro fibers are typically modeled with truss elements in solid concrete elements in an explicit finite element analysis program; and (2) Multi-scale modeling has been successfully incorporated for modeling small fibers such as collagen fibers ($\sim 300\,nm$ in length) found in biomechanics modeling (e.g., human tissue) [60].

Luccioni et al. [61] proposed a simple homogenization approach. In this approach, FRC members are considered as composites composed of a cementitious matrix and fibers. Concrete is modeled with an elasto-plastic model, and steel fibers are represented as orthotropic elasto-plastic material additions that can debond and slip in the cement matrix. In this approach, constitutive equations of fibers must include the debonding and slipping phenomena in order to include the inelastic material behavior without explicitly modeling the fibers.

The bond-slip behavior is determined from a fiber pull-out test or mechanical properties. By discretely modeling the fibers, the bond-slip behavior may be physically represented in an analysis model. Therefore, two discrete modeling methods have been primarily developed for cement-based composites. First, in fully-discrete models, fibers are discretized to possess independent degrees of freedom. Therefore, the reinforcing elements are able to freely position within the computational domain, irrespective of the cementitious element mesh.

One of the early implementation methods includes modeling of steel reinforcing bars [62] as two-node frame elements. While such approach may be successful in modeling steel reinforcing bars in structural concrete, its application in modeling fiber reinforcement is inefficient due to a large number of fibers and associated computational expense. In the semi-discrete model on the other hand, each fiber does not possess independent degrees of freedom although it is implicitly represented. In this approach, the fiber forces can be

represented within a computational domain, irrespective of the discretization of the matrix phase.

Radtke et al. [63] simulated the mechanical behavior and failure patterns of FRC composites by transferring the fiber forces to the background finite element mesh. The fiber end points are located at the finite element nodes. In another study, Radtke et al. [64] developed a novel partition of unity (PU) finite element approach to represent individual fibers in elastic and fracturing continua. The approach accounts for the constitutive behavior of the matrix, fiber, and fiber-matrix interface. The displacement discontinuities produced by fiber slippage, relative to the cementitious matrix, are represented by enrichment functions within the PU finite element framework.

Cunha et al. [65] studied a FRC fracture using linear two-node cable elements, connected in series, to represent individual fibers in concrete. Properties of the fiber-cement matrix interface are determined from empirical data. Fiber nodes are perfectly bonded to the background mesh, and the effects of bond-slip are indirectly characterized by transforming load-slip relations, for different fiber embedment angles, to tensile stress-strain behavior of the fiber elements. Kang et al. [66] developed a semi-discrete approach for FRC modeling in the FEA framework. This approach provides computational efficiency but distributes fiber pullout forces along the fiber embedment length, rather than lumping such forces at fiber end points.

The Finite Element method is a powerful numerical approach for solving partial differential equations of continua. It is widely used to solve nonlinear problems of solids and structures as well as problems of theory of elasticity [67–70]. However, it requires spatial derivatives and has had challenges in characterizing discrete cracks. Therefore, the proposed meshless method includes efforts to move away from and overcome the limitations associated with the finite element method. Furthermore, meshless methods contain great potential to model history dependent materials in problems with large distortions without highly distorted meshing or difficulties of material boundaries [71]. Many early meshless methods

required background cells [71]. Examples of these are particle-in-cell methods which combine Eulerian and Lagrangian methods [72]. The Smoothed Particle Hydrodynamics (SPH) method [73] is also based on a meshless approach; however, it requires spatial derivatives and has had challenges in characterizing discrete cracks.

Despite of a wide range of analysis methods developed over years, previous studies on concrete structures are mostly limited to the FE method [63–66]. However, there are challenges with existing finite element analysis (FEA) method in characterizing fiber reinforced concrete: (1) The FEA framework is not able to characterize the interactions between dissimilar materials [74], and thus fibers are assumed perfectly bonded to the cementitious matrix [63, 66]. The proposed meshless method, on the other hand, enables evaluation of fiber pull-out failure; (2) An external criterion or a pre-defined crack location is needed in the FEA framework in order to characterize crack initiation and crack propagation; (3) Furthermore, crack growth is represented by a local refinement of element size; (4) Finally, characterization of concrete damage such as spalling or fragmentations are often provided by removing elements.

The following sections present a novel, yet efficient, FRC modeling approach and its capabilities. The proposed fiber modeling scheme is created in a meshless analysis framework developed from the non-ordinary peridynamic formulation. The original form of the peridynamic theory, bond-based peridynamics (BBPD), includes a central pair-wise force function to describe the interactions between material particles [15, 16] . The bond-based peridynamics have been primarily used for a fracture analysis of plain and reinforced concrete under quasi-static loading [75, 76] as well as impact loading [16, 77, 78]. However, the simplification of central pair-wise force limits its application to isotropic, linear, and micro-elastic materials as the Poissons ratio must be 1/4 [28, 29, 36]. To address this deficiency, Gerstle et al. [27] introduced the micropolar peridynamics (MPPD) by adding pair-wise moments in additional to the pair-wise forces to simulate linear elastic materials with varying Poissons

ratios. The capability of MPPD in modeling concrete has been successfully demonstrated through several studies [27, 32, 79].

Additional analysis methods had been introduced to generalize the peridynamic formulation: (1) The ordinary state based peridynamics (OSBPD) generalizes the bond-based peridynamics to include any Poissons ratio by defining central force states of unequal magnitudes [28, 80]; and (2) In the non-ordinary state based peridynamic (NOSBPD) method, non-parallel and unequal force states are used to model interactions between material points [28, 29, 39]. Therefore, the NOSBPD method can be applied to material models with any Poissons ratio. Furthermore, the bond relationships between the material points are able to transfer loads in all directions. Therefore, it is possible to apply constitutive models conventionally used in the finite element analysis (FEA) framework. The proposed model herein presents an implementation of concrete constitutive models in the NOSBPD framework and includes the first attempt to represent fibers in such framework.

3.2 Formulation: Meshless Modeling Methodology for FRC Structures

3.2.1 Fiber Modeling

Previous studies [63,81–84] have focused on the formulation of fiber reinforcement in concrete based on the two numerical methods shown in Fig. 3.1. Fully-discrete models consider independent degrees of freedom for the fibers, while semi-discrete models calculate the traction force in the fibers and transfer it to the background matrix.

Traditionally in a fully-discrete finite element analysis model, fibers are populated as truss or beam elements and coupled to solid concrete elements by the Lagrange constraints. Therefore, the fully-discrete fiber model may appear more representative of FRC composites and thus appealing. In the presence of thousands and potentially millions of fibers, however, creating fiber elements and thus increasing degrees of freedom may not be the most efficient approach. The semi-discrete approach more effectively represents the fiber-concrete

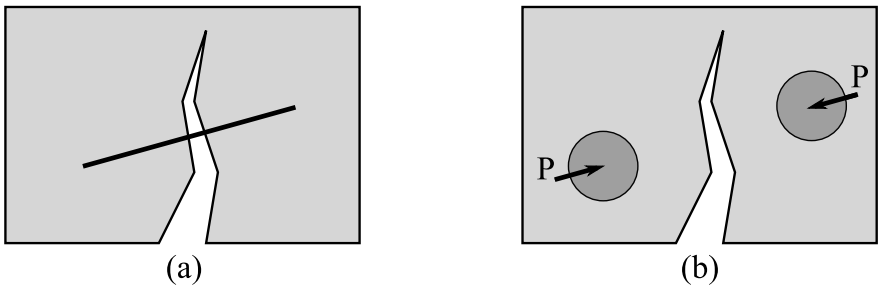


Figure 3.1: Modeling of fiber reinforcement. (a) Fully-discrete method: an explicitly modeled fiber as a truss or beam element; (b) Semi-discrete method: fiber force is distributed over selected elements around fiber end points.

composite action by distributing the fiber forces to the cementitious matrix without adding the degrees of freedom.

Regardless of the above two described fiber modeling methods, a reformulation of the background matrix (i.e. concrete) mesh is necessary when a crack develops in the cementitious matrix and crosses the fiber reinforcement. Therefore, a new meshless framework based on the peridynamics is proposed herein to enhance this computational inefficiency, as well as to overcome singularity problems found in the classical finite element models. The peridynamics is formulated in terms of integro-differential equations and is valid anywhere in the continuum, regardless of any fracture or discontinuities in the medium [16, 28]. The peridynamic method discretizes the background medium (i.e., cementitious matrix) into particles and represents the material model by defining a bond between particle points within a finite distance, δ, referred to as 'horizon' as shown in Fig. 3.2. Therefore, the fiber-concrete interaction can be simply represented by assigning a bond relationship between a fiber end point and concrete particles in a computational model.

The proposed fiber reinforced concrete (FRC) modeling framework adopts the peridynamic formulation for concrete modeling and the semi-discrete method for fiber modeling. Furthermore, the interaction between the cementitious and fiber particles is represented

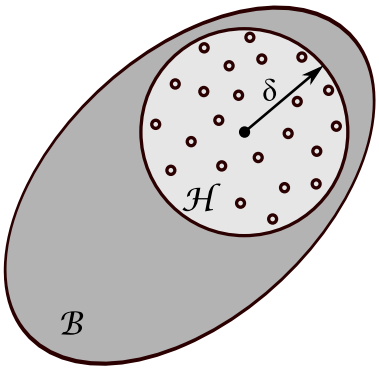


Figure 3.2: Horizon of a material point, H, within a peridynamic body B.

by particle bonds employed in the non-ordinary peridynamic formulation. When the fully-discrete method is used, fiber particles are generated in addition to the background cementitious particles. Each fiber particle has a bond relationship with its background particles as well as other fiber particles.

In the proposed semi-discrete fiber modeling approach, the resulting fiber forces are distributed to the background particles within a horizon of the fiber end points as shown in Fig. 3.1. To simulate the fiber action in the semi-discrete method, the fiber forces are applied to the background mesh. The matrix or cementitious material is treated as a system, and thus the virtual work done by the internal force should be equal to the work performed by external forces including fiber forces. As a result, an extra term, W_{fib}, represents the fiber-matrix interaction in the following virtual work equation:

$$\delta W_{int} = \delta W_{ext} + \delta W_{fib} \tag{3.1}$$

where the internal virtual work, W_{int}, describes the cementitious matrix material; W_{fib} and W_{ext} represent the virtual work produced by the fibers and applied external loads, respectively. W_{fib} is determined from fiber bonds in a fully-discrete fiber model and distributed forces in a semi-discrete fiber model. To enhance the computational efficiency, it is proposed

to distribute the fiber forces to the cementitious particles in a finite embedment distance or horizon by a weight function. The weight function may be linear to give the greatest influence to the points closest to the fiber end points as shown in Fig. 3.3(b), or constant as illustrated in Fig. 3.3(a).

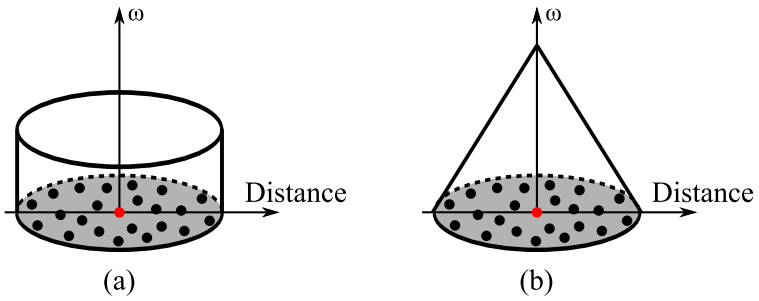


Figure 3.3: Distribution of fiber forces with respect to fiber end point (red point): (a) Constant Weight Function (CWF) and (b) Linear Weight Function (LWF).

Therefore, the fiber traction force, P, is distributed among the particles within the horizon of a fiber end point as shown in Fig. 3.3, and the force applied to a matrix particle, i, is defined as:

$$P_i = \omega_f \left(|\boldsymbol{\xi}_i| \right) P \tag{3.2}$$

$|\boldsymbol{\xi}_i|$ is the relative position of the fiber end particle; $\omega_f \left(|\boldsymbol{\xi}_i| \right)$ is the fiber weight function to distribute fiber traction force to nearby matrix material particles. Since the sum of the weighed measures from particles within a horizon (of a fiber end point) should be equal to the unity, the constants are determined as follows: $c_1 = 1/n$ and $c_2 = \delta/(n\delta - \sum_{i=1}^{n} |\boldsymbol{\xi}_i|)$ for constant and linear weight functions, respectively, where n is the number of particles within the horizon of the fiber end point.

3.2.2 Proposed non-ordinary state-based peridynamic formulation

Gerstle et al. used a modified bond-based peridynamics called micropolar peridynamics to model concrete structures and convectional reinforcements [27, 85]. The proposed analysis

framework aims to take an advantage of the peridynamic method in modeling of FRC composite materials and to represent the mechanical (or chemical) interactions between fibers and cementitious matrix. In this study, it is proposed that the bond between the composite materials (fibers and cementitious matrix) is represented by the NOSBPD method. In the state-based peridynamics, the relative position of two particle points is defined as the position state, $\underline{\mathbf{X}}\langle \mathbf{x}' - \mathbf{x} \rangle = \mathbf{x}' - \mathbf{x} = \boldsymbol{\xi}$. The deformation state, $\underline{\mathbf{Y}}$ is the position state in the deformed configuration and expressed as:

$$\underline{\mathbf{Y}}\langle \mathbf{x}' - \mathbf{x} \rangle = (\mathbf{x}' + \mathbf{u}') - (\mathbf{x} + \mathbf{u}) \tag{3.3}$$

where $\mathbf{u}'(\mathbf{x}', t)$ and $\mathbf{u}(\mathbf{x}, t)$ are the displacements at points $\mathbf{x}'$ and $\mathbf{x}$, respectively. The angle bracket, $\langle\rangle$ is used to indicate that the state operates on the vector in $\langle\rangle$. Fig. 3.4 illustrates the peridynamic states.

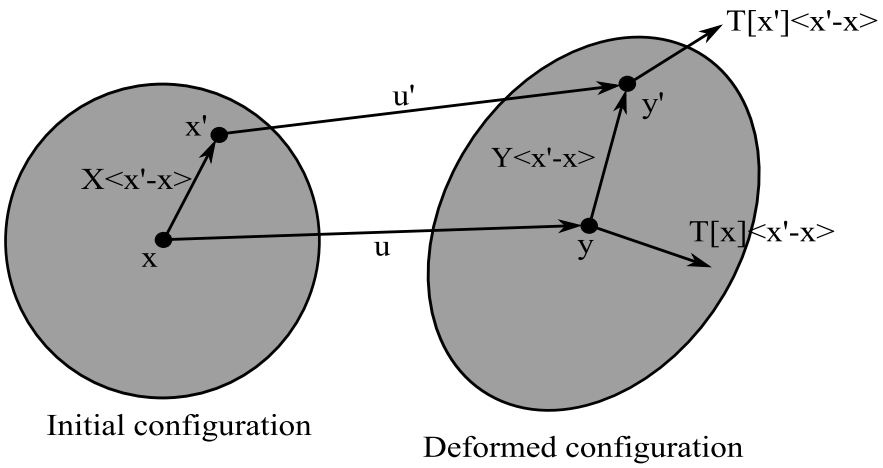


Figure 3.4: Peridynamic states: Position state X, deformation state Y, and force state T.

The deformation state, $\underline{\mathbf{Y}}$ represents the basic kinematic quantity used for a constitutive model in the state-based peridynamic method. Therefore, for an elastic material, the strain energy density, W, is given by a constant function of the deformation state, instead of deformation gradient tensor, $F = \partial y / \partial x$, used in the classical continuum mechanics. In order to employ a constitutive model from the classical solid mechanics in the non-ordinary state-based peridynamics (NOSBPD), a deformation gradient tensor must be described in

forms of peridynamic states. An approximation of the non-local deformation gradient tensor was proposed by Silling [28] as:

$$\mathbf{F}(\mathbf{x}) = [\int_{\mathcal{H}} \omega(|\boldsymbol{\xi}|)(\mathbf{Y}(\boldsymbol{\xi}) \otimes \boldsymbol{\xi})\, \mathrm{d}V_{\boldsymbol{\xi}}].\mathbf{B}(\mathbf{x}) \tag{3.4}$$

$$\mathbf{B}(\mathbf{x}) = [\int_{\mathcal{H}} \omega(|\boldsymbol{\xi}|)(\boldsymbol{\xi} \otimes \boldsymbol{\xi})\mathrm{d}V_{\boldsymbol{\xi}}]^{-1} \tag{3.5}$$

where H is the intersection of the body with a neighborhood of radius δ centered at the point $\mathbf{x}$. $\otimes$ denotes the tensor (dyadic) product of two vectors, and $\omega(|\boldsymbol{\xi}|)$ is a dimensionless scalar-valued weight function. The weight function is taken to be the unity indicating all points in the horizon of any selected point,$\mathbf{x}$, have equal influence. A zero-value weight function indicates the bond between $\mathbf{x}$ and $\mathbf{x}'$ is disengaged. $\mathbf{B}$ represents the shape tensor.

For an elastic peridynamic body subjected to an external body force, $\mathbf{b}$, the equilibrium equation is expressed in terms of peridynamic states:

$$\int_{\mathcal{H}_{\mathbf{x}}} \{\underline{\mathbf{T}}[\mathbf{x}]\langle\mathbf{x}' - \mathbf{x}\rangle - \underline{\mathbf{T}}[\mathbf{x}']\langle\mathbf{x} - \mathbf{x}'\rangle\}\mathrm{d}V_{\mathbf{x}'} + \mathbf{b}(\mathbf{x}, t) = 0 \tag{3.6}$$

where $\underline{\mathbf{T}}$ represents the force state. The force state is defined in terms of changes in strain energy density, $W(\underline{\mathbf{Y}})$, for any infinitesimal change in the deformation state, $d\underline{\mathbf{Y}}$, and formulated as follows [29]:

$$\underline{\mathbf{T}}\langle\mathbf{x} - \mathbf{x}'\rangle = \omega(|\boldsymbol{\xi}|)[\sigma]^T\mathbf{B}\boldsymbol{\xi} \tag{3.7}$$

where σ is the first Piola Kirchhoff stress tensor. For a linearly elastic material, Breitenfeld et al. [39] developed a numerical discretization scheme to solve the peridynamic equilibrium equations (Eq. 3.6). Appendix A gives a representation of their discretization for a 2D plane stress model.

3.2.3 Failure model

In the peridynamics theory, bond failure modes such as damage or crack nucleation, coalescence, and propagation are associated with bonds and bond fractures. A failure criterion for breaking the physical bonds between material particles in the NOSBPD formulation was proposed by Foster et al. [37]. This criterion gives the threshold (or critical) energy density, w_c, such that a bond breakage occurs when the amount of energy density stored in a bond, w_ξ, reaches the threshold. As a consequence, there is no physical interaction between two material particles. The energy density stored in a bond is defined as:

$$w_\xi = \int_0^\eta \{\underline{\mathbf{T}}[\mathbf{x}]\langle \mathbf{x}' - \mathbf{x}\rangle - \underline{\mathbf{T}}[\mathbf{x}']\langle \mathbf{x} - \mathbf{x}'\rangle\} \cdot \mathrm{d}\boldsymbol{\eta} \tag{3.8}$$

which resembles the well-known work or conservation of energy equation where the integration of forces acting on a body over the travel distance (or path length) gives the work done by the external force. Noting that $\boldsymbol{\eta}$ defines the relative displacement vector and is computed by $\mathbf{u}' - \mathbf{u}$. The critical energy density can be defined in terms of material properties and has been experimentally determined for a 2D body as follows [37]:

$$w_c = \frac{3G_f}{h\delta^3} \tag{3.9}$$

where the energy release rate, G_f, represents the energy required to open a new fracture surface of a unit area. In this study, the weight function is modified as follows to implement the failure criterion:

$$\omega\left(|\boldsymbol{\xi}|\right) = \begin{cases} 0 & : w_\xi > w_c \\ 1 & : otherwise \end{cases} \tag{3.10}$$

3.2.4 Constitutive model for the cementitious matrix

The proposed meshless framework can adopt constitutive relationships and material models conventionally used in the classical continuum mechanics formulation. The material behavior

of cementitious matrix is assumed to be linear elastic, and strain softening occurs once concrete is damaged. An exponential damage model is selected to represent the strain softening and thus is used in defining the constitutive equation:

$$\boldsymbol{\sigma} = (1 - \lambda)\, \mathbf{D} : \boldsymbol{\epsilon} \tag{3.11}$$

where λ is the damage variable ranging from zero to one. The damage variable, λ, is described as a function of equivalent strain, ϵ_{eq}, determined by Eq. (3.13) [86].

$$\lambda = \begin{cases} 0 & : \epsilon_{eq} < \epsilon_0 \\ 1 - \frac{\epsilon_0}{\epsilon_{eq}} e^{-\frac{\epsilon_{eq} - \epsilon_0}{\epsilon_f - \epsilon_0}} & : \epsilon_0 \leq \epsilon_{eq} < \epsilon_0 - (\epsilon_f - \epsilon_0)\, ln\left(\frac{\sigma_{res}}{\epsilon_0 E}\right) \\ 1 - \frac{\sigma_{res}}{E \epsilon_{eq}} & : \epsilon_{eq} > \epsilon_0 - (\epsilon_f - \epsilon_0)\, ln\left(\frac{\sigma_{res}}{\epsilon_0 E}\right) \end{cases} \tag{3.12}$$

where $\epsilon_0 = f_t/E$, f_t is the tensile strength; E is the Young's modulus; ϵ_f is the parameter affecting the slope of the softening branch; the last term in Eq. (3.12) maintains a reasonable residual stress level, σ_{res}, such that $(1 - \lambda)$ does not become zero.

A modified von Mises definition is used to calculate the equivalent strain, ϵ_{eq}, [87]:

$$\epsilon_{eq} = \frac{k - 1}{2k\,(1 - 2\nu)} I_1 + \frac{1}{2k} \sqrt{\frac{(k-1)^2}{(1-2\nu)^2} I_1^2 + \frac{6k}{(1+\nu)^2} J_2} \tag{3.13}$$

where k represents the ratio of the compressive strength, f_c, and the tensile strength, f_t; ν denotes the Poisson's ratio, and I_1 and J_2 are the first and second invariants of the strain tensor.

3.2.5 Constitutive model for fiber reinforcement

To ensure a uniform distribution of the fiber reinforcement in the cementitious matrix, seed points are distributed by using the *rand* function available in FORTRAN. The points represent the midpoints of the fiber reinforcement. It is proposed to grow fibers in two opposite directions at randomly selected angles. This growth is suspended when the fiber length reaches the selected fiber length or when two ends reach the model boundaries.

In the semi-discrete fiber model, it is reasonable to assume that the reaction forces from the fibers to the matrix can be represented by fiber pull-out loads. Experimental results are generally available to determine the fiber pull-out loads, P, and fiber pull-out distance, Δ. In the proposed FRC model, a micro-mechanical model developed by Lin et al. [88] is adopted to calculate the fiber pull-out force. It is proposed that the fiber failure response is represented in two phases: fiber debonding and pull-out.

During the debonding stage ($0 \leq \Delta \leq \Delta_0$), the fiber force is determined as:

$$P(\Delta) = \sqrt{\frac{\pi^2 \tau_0 E_f d_f^3 (1+\theta)}{2} \Delta + \frac{\pi^2 G_d E_f d_f^3}{2}} \tag{3.14}$$

where θ is determined by $E_f V_f / (E V_m)$, E is the matrix elastic modulus; V_m is the matrix volume fraction; V_f is the fibre volume fraction; E_f is the fibre elastic modulus; d_f is the fibre diameter; G_d is the fibre-matrix chemical bond strength (defined as energy per area), and τ_0 is the frictional stress on the debonded interface.

During the fiber-pull out stage ($\Delta_0 \leq \Delta \leq l_e$), the fiber force is described by:

$$P(\Delta) = \pi d_f \tau_0 [1 + \beta \frac{\Delta - \Delta_0}{d_f}] (l_e - \Delta + \Delta_0) \tag{3.15}$$

where β is the fiber-matrix interface slip-hardening parameter; l_e is the fiber embedment length, and Δ_0 is the fiber pull-out distance at the onset of the pull-out stage is determined by:

$$\Delta_0 = \frac{2\tau_0 l_e^2 (1+\theta)}{E_f d_f} + \sqrt{\frac{8 G_d l_e^2 (1+\theta)}{E_f d_f}} \tag{3.16}$$

In the proposed meshfree method, it is assumed that a fiber contributes to the cementitious matrix material model when it bridges a crack. In the proposed model, a crack is associated with damaged matrix particles. Therefore, it is necessary to introduce a fiber damage parameter, λ_f, to activate the fiber. Fiber damage parameter ranges between 0 and 1 and is equal to the largest damage parameter of the particles around the fiber as shown in Fig. 3.5. $\lambda_f = 0$ indicates no damage within a set of particles bridged by the fiber, and thus

the fiber force is not applied to the model. Whereas, $\lambda_f > 0$ represents that at minimum one particle around the fiber is damaged. In such case, the fiber is engaged in the model, and the scaled fiber force, P_f, is applied to the model.

$$P_f = \lambda_f P \tag{3.17}$$

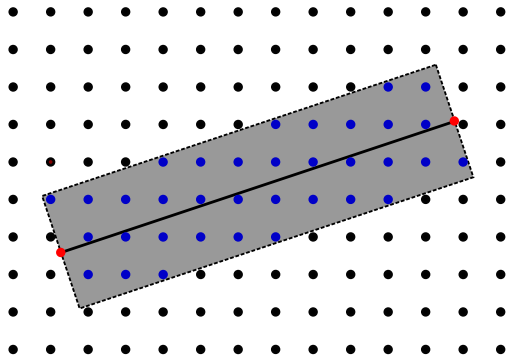


Figure 3.5: Schematic for interaction of fiber and matrix points.

3.2.6 Numerical solution

The peridynamic method is primarily developed to solve time-dependent problems. In this study, the dynamic relaxation method is used to obtain quasi-static solutions of the discretized NOSBPD equilibrium equation. The mass and damping coefficients are chosen to obtain the steady-state solutions in a manner that minimizes the time steps.

Appendix B shows how the dynamic relaxation method is implemented in the proposed meshless FRC modeling framework.

3.3 Verification of the proposed meshless method

To verify proposed features in the meshless FRC model, a 2D rectangular concrete member clamped at one side and subjected to tension at the other end as shown in Fig. 3.6 is studied to (1) determine an efficient particle discretization scheme; (2) verify fiber forces in a locally damaged area, and (3) study the effect of fiber volume fractions on the FRC member ductility

and strength. A 2D planar concrete model is created in the proposed meshless framework. The material model parameters are: $E = 20,000\ N/mm^2$, $\nu = 0.2$, $\epsilon_f = 0.05$, $k = 10$, and $f_t = 4.0\ N/mm^2$. The same model geometry and parameters are used for the following three subsections unless otherwise noted. A weak zone and a notch are introduced to the 2D concrete model in Sections 3.3.2 and 3.3.3, respectively.

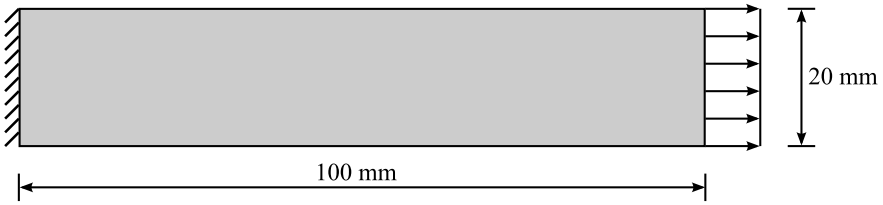


Figure 3.6: The rectangular plate used in convergence study

3.3.1 Particle discretization and convergence

A convergence study shown in Fig. 3.7 is carried out to obtain the most effective discretization scheme. The term, effectiveness in this study, refers to obtaining acceptable errors within a reasonable processing time. This convergence study is a necessary step to verify the proposed modeling framework for analysis of FRC structures. Two types of convergence tests are performed for the rectangular concrete model presented in Fig. 3.6:

(1)(δh)− convergence, where the horizon size, δ, decreases with decreasing particle spacing, h (Fig. 3.7b), and (2)δ−convergence, where δ increases while h remains unchanged (Fig. 3.7c).

The convergence criterion evaluates relative errors between the applied tensile force and computed internal force in the model. Fig. 3.8a shows that the smallest particle spacing, h, minimizes the errors for a constant ratio of δ/h. However, it is determined from Fig. 3.8b that the most accurate results are obtained with $\delta/h = 3.015$ for a constant value of h. This finding is consistent with the previous studies [16, 17, 20] performed in the peridynamics framework.

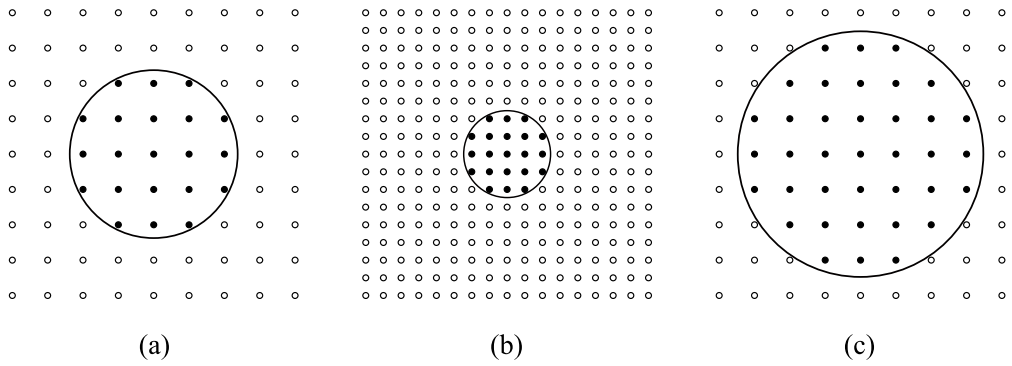


Figure 3.7: Graphical representation showing discretization of particles. (a) Reference state, (b) (δh)-convergence, and (c) δ-convergence.

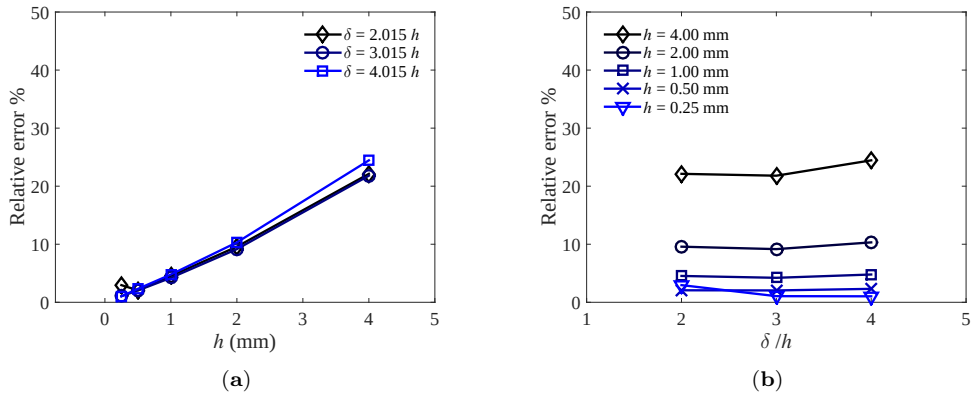


Figure 3.8: The relative error, (a) (δh)−convergence, and (b) δ−convergence

Fig. 3.9 depicts the computational time for each convergence study with respect to the fastest run-time. It is evident from the figure that decreasing h for fixed δ/h (Fig. 3.9a) and increasing δ for fixed h (Fig. 3.9b) logarithmically increase the processing time. Therefore, it is concluded from this convergence study that discretizing concrete members with $h = 1\,mm$ and $\delta/h = 3.015$ is the most efficient.

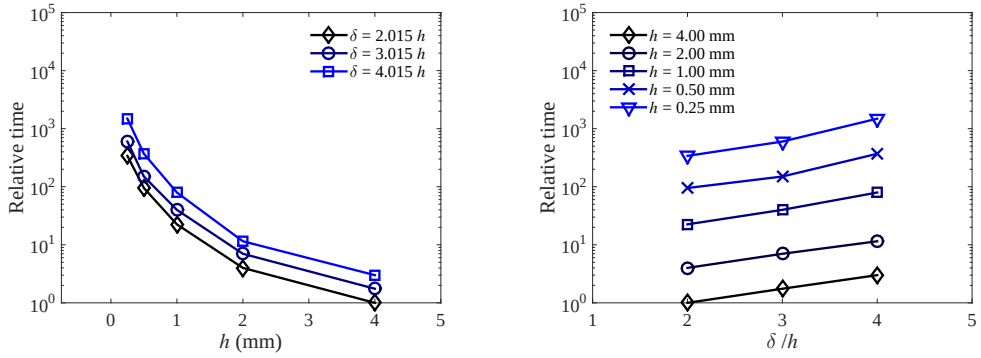


Figure 3.9: The relative processing time, (a) $(\delta h)-$convergence, and (b) $\delta-$convergence.

3.3.2 Verification of fiber modeling method

As shown in Fig. 3.10, a weak zone is introduced to represent a localized damage area in the 2D concrete model. The width of the weak zone is $10\,mm$. In addition, a thread of fiber with length of $60\,mm$ is embedded in the concrete matrix.

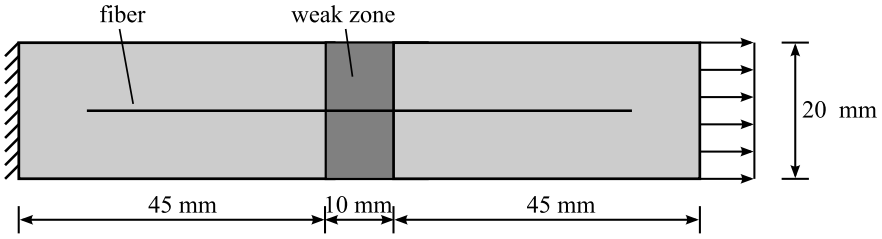


Figure 3.10: A plate with single fiber in tension.

This simple model can represent the behavior of fiber reinforcement bridging cracks in the proposed cementitious matrix model and verify the fiber forces determined in a localized area. The following fiber pull-out force parameters (see Eqs. 3.14-3.16) are used: $E_f = 22,000\,N/mm^2$, $G_d = 0.06\,J/mm^2$, $\tau_0 = 2.5\,N/mm^2$, $\beta = 1$, $d_f = 0.4\,mm$ and $l_f = 60\,mm$. For the other portion of the member, the tensile strength is chosen sufficiently large to avoid damage growth.

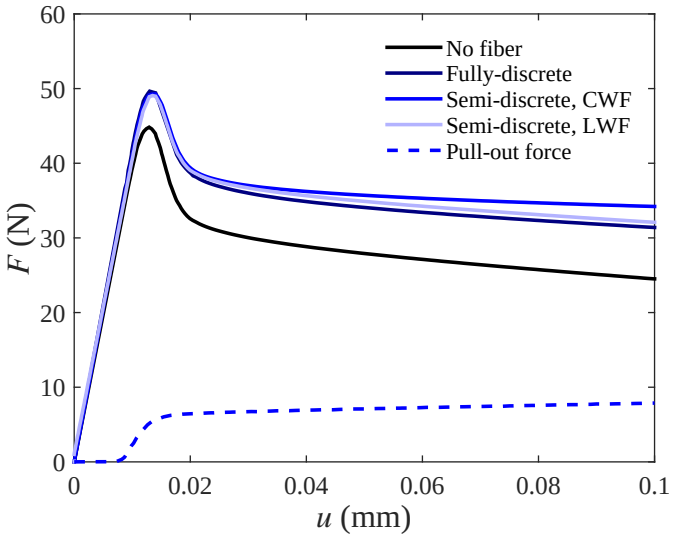


Figure 3.11: Force-displacement plot of the composite material.

In this subsection, the fully- and semi-discrete fiber models with constant and linear weight functions are compared as shown in Fig. 3.11. The force-displacement curves obtained from each model as well as the fiber pull-out force, are plotted. The fiber reinforcement is activated when damage initiates in the weak zone. The fiber pull-out force gradually increases as shown in Fig. 3.11. It is reasonable to assume that the cementitious matrix and fibers are two independent parallel systems sharing the total load by means of the bond relationships. Therefore, the total force applied on the composite system may be estimated by combining load developed in the cementitious matrix (blue line) and the fiber pull-out force (red dashed line). Given that the fully-discrete model were considered to yield the most accurate load prediction, the semi-discrete model with LWF gives better predictions, compared to the results from the CWF model. Therefore, the semi-discrete model with a LWF is proposed to be used in modeling of FRC composites.

3.3.3 Verification of fiber distribution method

A percentage of the total volume of fiber reinforcement is referred to as 'fiber volume fraction' and denoted as V_f. To illustrate the effect of fiber volume fractions on the tensile strength of concrete member and distribution of concrete damage, two opposing semi-circular notches are introduced to the same planar FRC member as shown in Fig. 3.12. As suggested in available literature [63], initial imperfections from pores and shrinkage are represented by reducing concrete strength of arbitrarily selected particles to 2.0 N/mm^2.

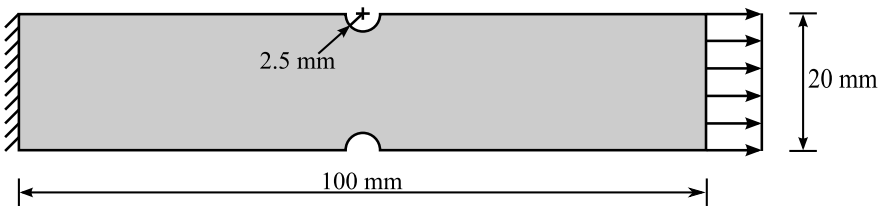


Figure 3.12: 2D FRC plate with two semi-circle symmetric notches.

The concrete matrix is reinforced with 20 mm straight steel fibers with three different fiber volume fractions of 0.6%, 1.2%, and 2.4%. The dispersion of fibers in a 2D concrete member is shown in Fig. 3.13. Fibers are dispersed randomly within the matrix material.

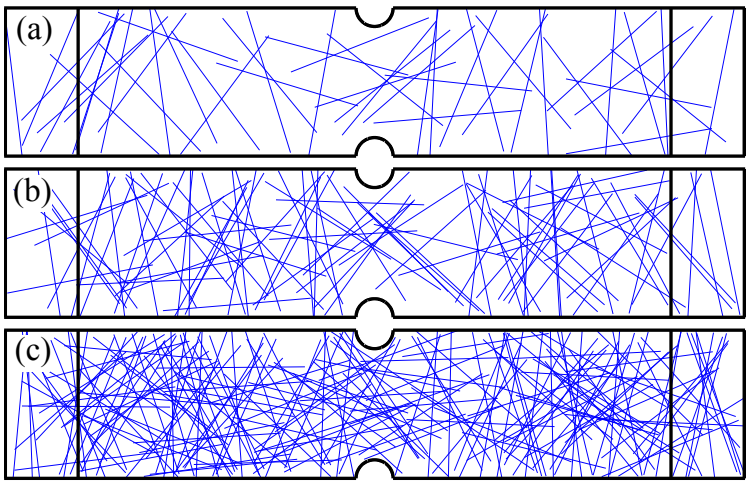


Figure 3.13: Randomly distributed fibers in the notched plate:(a) $V_f = 0.6\%$, (b) $V_f = 1.2\%$, and (c) $V_f = 2.4\%$.

The load-displacement curves obtained from the plain concrete and FRC models are depicted in the Fig. 3.14. As anticipated, FRC members with higher fiber volume fractions generally yield higher peak force and provide more ductility.

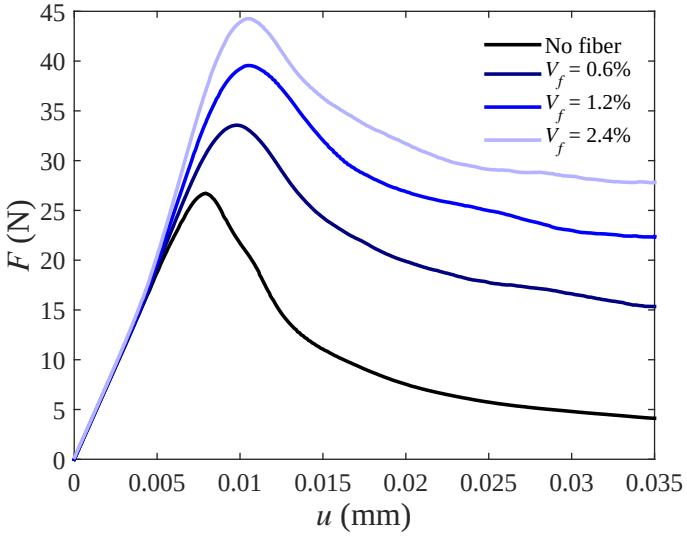


Figure 3.14: Force-displacement plot of the notched plate.

Fig. 3.15 provides damage contours for selected displacement values: (1) 0.001 mm which corresponds to the peak force and (2) 0.002 mm, which corresponds to the backbone of the softening portion in the load-deflection curve. In the contour, the blue color represents undamaged concrete ($\lambda = 0$ in Eq. 3.12) particles, whereas the red color indicates fully damaged particles ($\lambda = 1$). It is important to note that the FRC2.4 model appears most damaged, although not severely damaged in the weak zone, because it sustains the largest tension force for the predicted displacements (0.001 and 0.002 mm).

In the case of the plain concrete model, particles between the two notches are severely to completely damaged; however, particles in the other areas are hardly damaged. By increasing the fiber volume fraction, the damage is distributed to the other parts of the concrete model. For the FRC0.6 model, concrete damage is initiated in the notched area. However, some particles in the notched area are not fully damaged at the peak load but gradually develop the localized damage in the area.

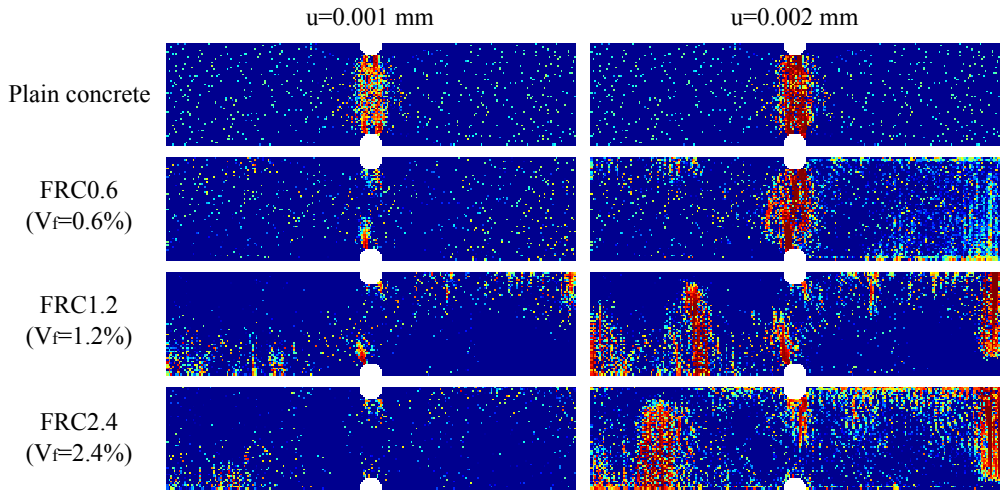


Figure 3.15: Damage patterns for varying fiber volume fractions at selected displacements.

The FRC2.4 model develops limited damage in the notched area at the peak load, while the damage pattern is distributed to the other parts of the concrete member. The proposed FRC model is capable of distributing the tension force by means of fiber links embedded in concrete such that the concrete member does not fail by localized damage or a stress concentration. The model finds the weakest locations in the FRC composite section and relieves the stress concentration from the notched area.

As the fiber volume fraction increases, the localized damage in the notched area is not observed. For the FRC2.4 model, the damage pattern is uniformly distributed in the concrete model. Similar uniform damage patterns are observed as the displacement increases (see Fig. 3.15). Although some particles in the notched area are completely damaged, the fiber addition distributes the particle damage from the notched area to the other part of the concrete model. As anticipated, the fibers distribute the applied load from the localized notched location to the other locations in the FRC model, and thus decrease the stress concentration at the notched location.

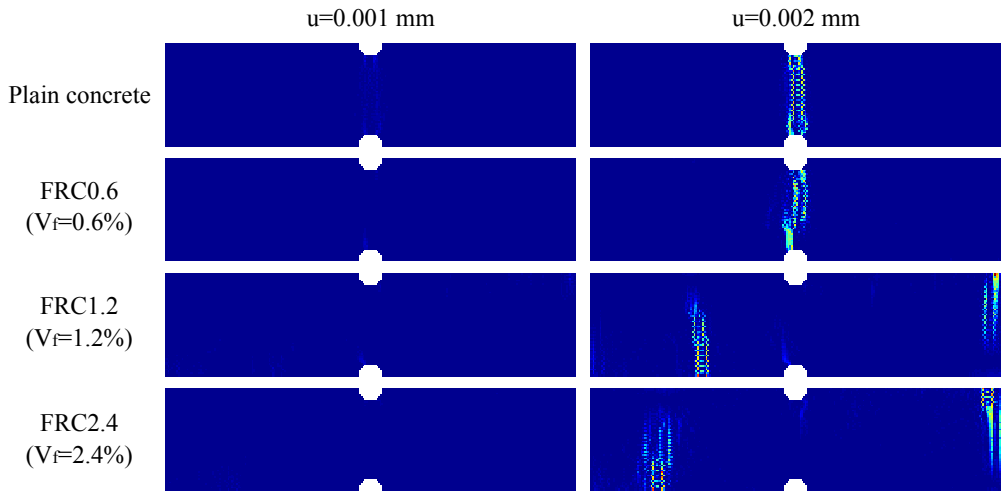


Figure 3.16: Strain energy contours for varying fiber volume fractions at selected displacements.

Fig. 3.16 includes the strain energy contours. Fibers distribute the strain energy in the concrete member such that the maximum strain energy in the beam models with higher fiber volume fractions ($V_f = 1.2\%$ and 2.4%) is identified in areas near the loading edge. On the other hand, in case of the plain concrete and FRC0.6 models with a low volume fraction, the localized notched area is identified to show the maximum strain energy. The results are consistent with the anticipated physical behavior of FRC members with a notch.

3.4 Comparison of Predictions and Experimental Results

3.4.1 Available four point bending test of FRC beams

The proposed meshless FRC model is validated by predicting the behavior of experimentally tested FRC beams [89] subjected to four-point bending as shown in Fig. 3.17. Two sets of published experimental results are compared against numerical results determined by the proposed meshless FRC model. The numerical method is validated by comparing the load-deflection plots obtained from the experiment conducted by Korming et al. [89].

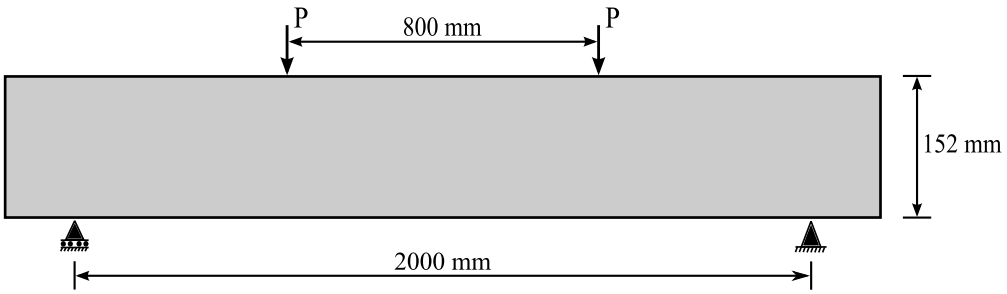


Figure 3.17: Beam geometry and four-point bending test setup.

The concrete beams have a cross section of 152 mm by 100 mm with a clear span of $2,000\ mm$. A 2D planar model is developed for a plain concrete beam and a FRC beam, respectively. The FRC beam contains straight steel fibers with the length of 24 mm and diameter of $0.4\,mm$. The fiber volume fraction is 1.27%. The material model parameters are: $E = 20,000\ N/mm^2$, $\nu = 0.2$, $\epsilon_f = 0.05$, $k = 10$ and $f_t = 4.0\ N/mm^2$. The strength of ten percent of the total particles are reduced to $2.0\ N/mm^2$ to represent initial imperfections. The model parameters used to calculate the fiber pull-out force are: $E_f = 200,000\ N/mm^2$, $G_d = 0.06\ J/mm^2$, $\tau_0 = 2.5\ N/mm^2$, $\beta = 1$, $d_f = 0.4\ mm$ and $l_f = 24\ mm$. The fiber embedment length is half of the fiber length.

Fig. 3.18 includes comparisons of the predicted results from the meshless FRC beam model and experimental results from the four point bending test. The predicted uncracked stiffness of the plain concrete beam shows a good agreement with experimental results. In the case of FRC beam, the proposed methodology is able to predict the failure response. The meshless FRC beam model is able to predict the flexural strength and displacement. Marginal differences are observed as the beam develops the nonlinear behavior and flexural cracks. The differences in the load-deflection curves are attributed to the fiber and cementitious material bond failure criteria, distribution of initial imperfections, and material constitutive models. It is concluded from this validation that the proposed meshless FRC model has the potential

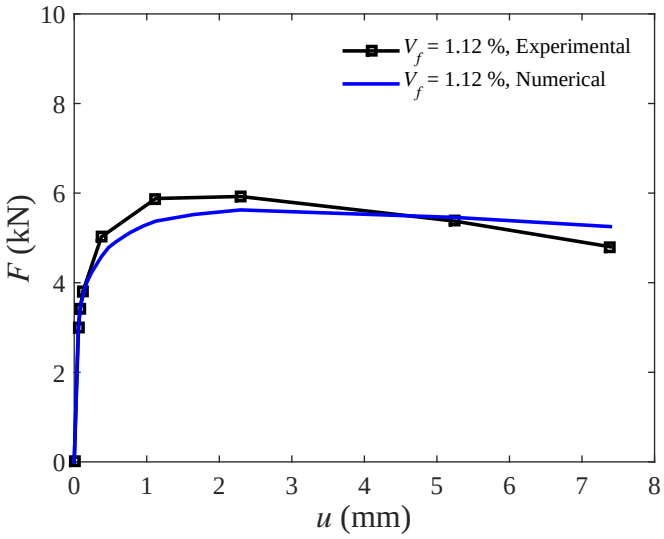


Figure 3.18: Comparison of numerically obtained force-deflection results and experimental results [89] for 4 point bending beam with $V_f = 1.12\%$.

for accurately representing the ductile failure behavior (i.e. sustain large deformation beyond the failure strength) of FRC beams.

3.4.2 Available three point bending test of a FRC beam

To further validate the proposed FRC modeling method, FRC beams subjected to three-point bending [90] are studied in the proposed meshless framework. The beams had a dimension of $210 * 50.6 * 25.4\,mm$ and a notch ($17\,mm$ deep and $1\,mm$ wide) at the mid-span location. The clear span of the tested beams was $203\,mm$. In this experiment [90], carbon microfibers with a length of $3\,mm$ and a diameter of $0.030\,mm$ were used. The fiber volume fraction of 4% was selected in the test.

A 2D planar meshless model shown in Fig. 3.19 is developed to predict the failure behavior of a carbon fiber reinforced concrete beam. The material property associated with the fiber pull-out force differed from the earlier presented beam model (see Fig. 3.17) is:

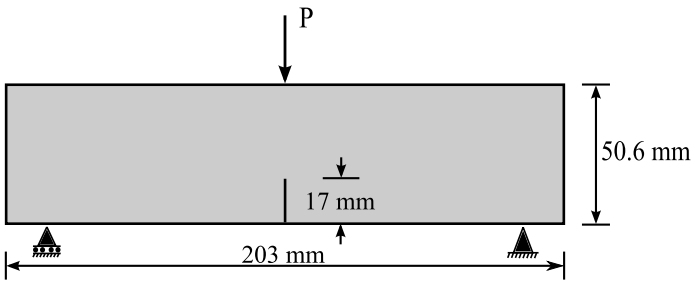


Figure 3.19: 2D three point bending beam model.

$E_f = 27,000\ N/mm^2$. In this study, crack mouth opening displacement (CMOD) was measured as deflection for force carried by the beam. The load-CMOD curves were provided for a plain concrete beams and FRC beams.

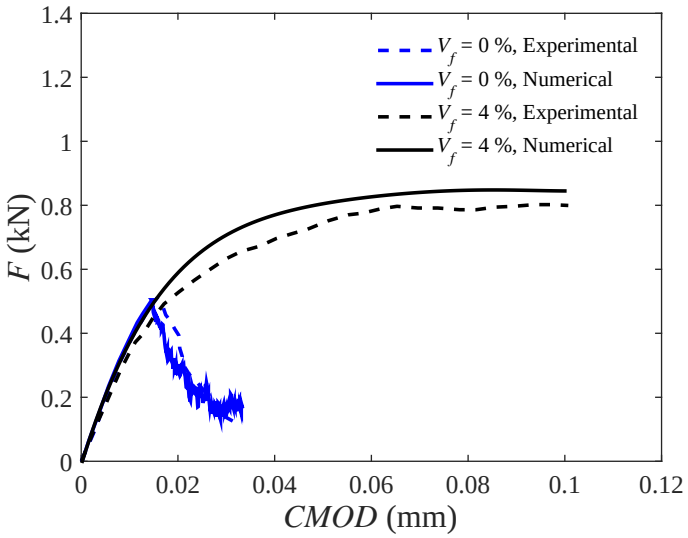


Figure 3.20: Comparison of analytical and experimental results [90] for 3 point bending beam.

The results from the notched FRC model are presented in the Fig. 3.20. It is noticeable that the proposed meshfree method is capable of predicting the beam failure behavior in the presence of a notch or localized crack. The damaged patterns illustrate the major advantages of peridynamics and the proposed FRC model. The governing equations are valid anywhere in the model, regardless of any discontinuities in the model. In the proposed analysis, any

failure mode can be predicted based on the definition of bond breakage criteria (Eq. 3.10) between particles.

It is evident that the proposed meshfree FRC modeling method can accurately represent the strength increase and ductility gained from the fiber additions.

3.5 Discussion and future work

It is worth discussing the applications and limitations of the proposed fiber modeling approach, validation of the analysis results, the rate of convergence, computation time, and future work.

3.5.1 Validity of proposed fiber modeling method

It is important to understand the validity of the proposed fiber modeling method (i.e., application of fiber forces at the end points). The modeling approach may not be effective for long fibers greater than $76.2\,mm$ in length or reinforcing steel bars as the member force is distributed nonlinearly along the bond development length. This study finds that applying lumped forces at fiber ends yields a good agreement with empirical results for selected macro fiber size.

3.5.2 Validation of analysis results

In the absence of material and bond properties, the analysis results may be validated in a component level. For instance, a FRC beam may represent a sub-assembly of a FRC structure. Therefore, the validation may be conducted for a small specimen and used to illustrate the structural performance of a structure. In this study, the linear force distribution (Fig. 3.3a) is found sufficient to predict the behavior of a FRC beam member. Once it is validated against a sub-assembly test, the analysis approach may be used to evaluate the structural performance of a large FRC structure. A sensitivity analysis may be performed to study the effect of various fiber-cement bond models and material properties which provide

the best agreement with the empirical results from a sub-assembly test (e.g., a beam test). A fully-discrete model may be included in the sensitivity study as it represents the simplest form of the fiber modeling approach.

3.5.3 Rate of convergence

The order of convergence is equal to one, which is sufficient for a fast convergence rate, and the error is estimated within 2% for the small particle spacing ($0.25 < h < 0.50\,mm$). For $h = 4\,mm$, the error ranges between 20 and 25%. The error is highly sensitive to material spacing, h, and therefore, large particle spacing may result in inaccurate results. The authors realize that many factors can affect the bending behavior of fiber reinforced concrete presented in Fig. 3.20; however, no fine-tuning of material properties is made although they improve the results. The analysis results are reproduced solely from the reported test and analysis parameters presented in this manuscript.

3.5.4 Computational time

It is noted that the total computational time is sensitive to the number of processors, parallel programming, programming language, and many other factors. In this study, the proposed model is implemented in Fortran 90 and use 8 computational nodes with 12-core Intel Xeon processors. Fig. 3.9 presents the processing time of each run, relative to the case with the greatest particle spacing ($h = 4\,mm$ and $h = 2.015$), in order to evaluate the effect of decreasing particle distance. The total computational time recorded for this study is 1.9 seconds for the case with $h = 4\,mm$ and $d/h = 2.015$.

3.5.5 Future work

The capability of peridynamics in 3D problems has been successfully illustrated in numerous studies [16, 39]. Therefore, it is possible to extend the proposed fiber modeling approach to 3D problems. The 3D fiber modeling may potentially improve the computational accuracy

by characterizing more realistic fiber orientations in 3D. The future research work includes the validation of the proposed fiber modeling approach for 3D problems. In addition, the proposed model will be used to characterize the performance of FRC members subjected to impact loading.

3.6 Conclusion

Modeling of fiber fracture and bond damage is important for assessment of FRC composite structures. In this study, a meshless FRC modeling framework is introduced. The proposed model is able to characterize the crack nucleation and crack growth observed from available FRC beam tests. In using the proposed semi-discrete fiber modeling method, the traction forces in the fiber reinforcement are distributed to the background concrete particles by a weight function. Discrete cracks were modeled by a set of bond relationships between cementitious particles such that no representation of the crack surface is necessary. This inherent feature makes the proposed meshless method ideally suited for FRC composites regardless of the fiber reinforcement size. Furthermore, it enhances the accuracy of discrete damage pattern predictions. Therefore, the proposed method may be extended to predict the response of fiber-reinforced polymer (FRP) concrete structures as well as nano- and micro-fiber reinforced concrete structures and other composites.

Chapter 4

Fracture analysis of fiber reinforced concrete structures in the micropolar peridynamic analysis framework[1]

[1]A. Yaghoobi and M. G. Chorzepa. "Fracture analysis of fiber reinforced concrete structures in the micropolar peridynamic analysis framework." Engineering Fracture Mechanics 169 (2017): 238-250. Reprinted here with permission of publisher.

ABSTRACT

In this study, an effective meshless model is proposed for fracture analysis of cracks in fiber reinforced concrete structures. The cementitious material is modeled using the micropolar peridynamic approach which is a generalized form of the bond-based peridynamics. A semi-discrete approach is incorporated in the micropolar peridynamic framework to study the effect of fiber reinforcement on the fracture analysis of cracks in cementitious materials. Therefore in the proposed fiber reinforced concrete modeling approach, the macro-scale fibers are randomly distributed in the cementitious material, and the forces developed in the fibers are indirectly applied to the cementitious material particles. This fracture analysis method used for fiber-cementitious material composites improves the computational efficiency. Furthermore in contrast to the finite element method, there is no need for mesh refinement and monitoring crack initiations/propagations in the proposed peridynamic framework. The crack development is an inherent feature of the proposed analysis framework. The accuracy of the proposed fracture analysis model is demonstrated through a comparison of available experimental results and simulation outcomes of fiber reinforced concrete beams with a notch at varying locations along the span.

4.1 Introduction

Fibers enhance the mechanical properties of the cementitious composite structures by providing bridges across cracks. Many experimental studies have been demonstrated that fibers significantly improve tensile strength, ductility, and load carrying capacity [91–93]; however, the performance of fiber reinforced cementitious composites is highly dependent on the fiber volume fraction, orientation, and spatial distribution [94, 95]. Therefore, it is important to develop a novel, yet practical, analytical method to investigate multiple parameters that affect the strength of fiber reinforced concrete (FRC) structures and provide an alternative to laboratory tests.

A comprehensive review of the literature illustrates that previous numerical studies on the behavior of the FRC structures can be classified in two main categories: homogenization and discrete methods. A homogenization method generally represents FRC composites as a homogenized isotropic material, and thus the effect of fibers is considered in the material properties and fracture models [61]. In this approach, experimental results or analytical approaches are used to determine the model parameters [61,96]. On the other hand, a discrete modeling method has gained popularity in the recent years [63, 66, 97], discretely modeling individual fibers in composites. For FRC composites, two forms of discrete models have been developed: (1) fully-discrete and (2) semi-discrete models.

In a fully-discrete model, fibers are populated as truss or beam elements and coupled to solid concrete elements [98]. Therefore, the fully-discrete method may appear to be a better representation of FRC composites as it perceptibly reflects the spatial distribution and orientation of fibers. However, in presence of thousands and potentially millions of fibers, increasing degrees of freedom (DoF) by explicitly modeling macro or micro-scale fibers is not the most efficient numerical method. In order to address this deficiency, a semi-discrete concept was developed in which fibers are not explicitly modeled. As an alternative, the reaction forces between the fibers and concrete are applied to the cementitious material matrix. As a result, the semi-discrete method provides the ability to study the effect of fiber distribution and orientation at an acceptable computational expense.

Two approaches are mainly used to distribute the fiber reaction forces to the cementitious matrix: (1) lumped-force and (2) distributed-force methods. In the lumped-force approach, the crack bridging force by fibers is lumped at the crack surface or at the corresponding matrix nodes. On the other hand, in the distributed-force approach, the reaction force is uniformly distributed along the embedment length of the fiber. Radtke et al. [63] simulated the mechanical behavior and failure patterns of FRC composites by transferring the fiber forces to the background finite element mesh. Fiber forces are assumed to be equal to the fiber pull-out force from the micro-mechanical model developed by Lin et al. [88]. Furthermore, the

fibers are relatively short, and thus they [63] assumed that the fiber forces can be transferred to the fiber end nodes. However to avoid the stress concentration and mesh sensitivity, the resulting fiber forces are distributed over a finite area around the fiber ends. Kang et al. [66] developed a semi-discrete approach for FRC modeling using the finite element analysis (FEA) method. This approach shares the same concept developed by Radtke et al. [63], yet it distributes the fiber pullout forces along the fiber embedment length, rather than lumping such forces at fiber ends.

Regardless of the above described fiber modeling methods, studies on FRC structures are mostly limited to the FEA framework [99–101]. However, the FEA has some deficiencies which play an important role in FRC simulations. Above all, FEA fails to model the interface or bond between dissimilar materials unless the bond surface is explicitly defined. Furthermore, an external failure criteria for crack initiation and propagation path is needed. Crack growth is generally predicted, and remeshing elements is necessary during the failure process. In recent years, nonlocal meshfree methods have been an alternative to the FEA method in various continuum mechanics applications, particularly in fracture mechanics.

The peridynamics, first introduced by Silling [15], is a reformulation of the classical continuum mechanics in terms of integro-differential equations, and thus is valid anywhere in a deformable body regardless of any discontinuity. The peridynamic method discretizes the background medium into particles and represents the material model by defining the bond between particle points selected within a finite distance, referred to as horizon. The original peridynamics, known as bond-based peridynamics (BBPD), is limited to modeling materials with a Poissons ratio of 1/4 [16, 28, 30, 102]. Gerstle et al. [27] enhanced BBPD by allowing the bond of two material points to develop not only pairwise forces, but also pairwise peridynamic moments. The resulting model, called micropolar peridynamics (MPPD), can simulate linear elastic materials with varying Poissons ratios.

This study provides an effective scheme to model fracture behavior of FRC structures based on the micropolar peridynamics. In the proposed approach, there are two important

components: (1) modeling the cementitious material and (2) modeling the fibers. The cementitious material (or concrete) is discretized into material particle points, and a set of nonlinear bond forces between concrete material particles are defined. A semi-discrete fiber modeling method is used to represent the fiber-concrete interaction. To do this, forces developed in the fibers are distributed to the background cementitious material points around fibers. It is noteworthy that the peridynamic material relationship (force and stretch) is modified to include tensile softening in the concrete material. The effectiveness and accuracy of the proposed approach is demonstrated through a comparison with available experimental results and simulation outcomes.

4.2 Background

4.2.1 Bond-based peridynamics

A nonlocal theory, known as Peridynamics (PD), was originally proposed by Silling [15] for modeling discontinuous cracks and material fracture to overcome fundamental mathematical difficulties in solving differential equations. This method uses integral equations in order to describe the material particle motions. Peridynamics assumes that any material particle, $\mathbf{x}$, which belongs to the spatial region, $\mathbf{R}$, interacts with any arbitrary material particle, $\mathbf{x}'$, within a finite distance of δ. The interaction between the material particles is defined by a "bond" relationship between material particles. In the bond-based peridynamics, the interaction between material particles is limited to a pairwise force function, $\mathbf{f}$, defined by Eq. (4.1), as shown in Fig. 4.1a, where $\mathbf{u}$ and $\mathbf{u}'$ denote the displacement of material particles, $\mathbf{x}$ and $\mathbf{x}'$:

$$\mathbf{f} = \mathbf{f}\left(\mathbf{x}, \mathbf{x}', \mathbf{u}, \mathbf{u}'\right) \qquad\qquad |\mathbf{x}' - \mathbf{x}| \leq \delta \tag{4.1}$$

Therefore, the quasi-static equilibrium equation of material particle, $\mathbf{x}$, is obtained from a summation of all bond forces as shown in Eq. (4.2), where $\mathbf{b}$ is the external body force density

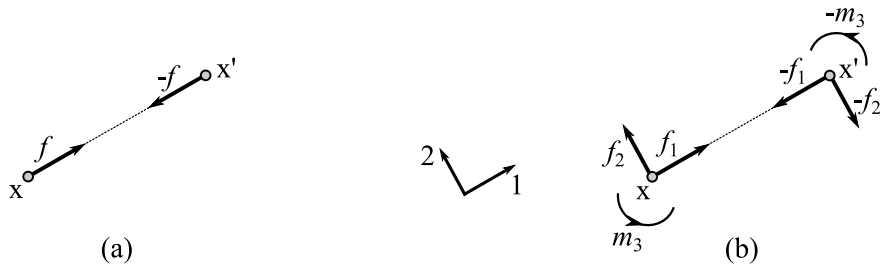


Figure 4.1: Schematics of force components between two material particles in the (a) bond-based and (b) micropolar peridynamics.

field, $\mathrm{d}V_{\mathbf{x}'}$ is the infinitesimal volume of particle $\mathbf{x}'$ and $\mathcal{H}_{\mathbf{x}}$ is the domain of neighboring material points and is referred to as a "horizon".

$$\int_{\mathcal{H}_{\mathbf{x}}} \mathbf{f}\left(\mathbf{x}, \mathbf{x}', \mathbf{u}, \mathbf{u}'\right) \mathrm{d}V_{\mathbf{x}'} + \mathbf{b}\left(\mathbf{x}\right) = \mathbf{0} \tag{4.2}$$

In a two-dimensional problem, the 'horizon' is usually taken as a circular domain centered at the point, $\mathbf{x}$, with a radius of δ. In a similar manner, the horizon becomes a sphere in 3-dimensional problems. For a homogeneous material which does not depend on time-dependent deformations, the magnitude of pairwise force, f, can be obtained as a function of stretch, s, in the form of $f = f\left(s\right)$, where the stretch, s, is defined by Eq. (4.3):

$$s = \frac{\left|\left(\mathbf{x}' + \mathbf{u}'\right) - \left(\mathbf{x} + \mathbf{u}\right)\right| - \left|\mathbf{x}' - \mathbf{x}\right|}{\left|\mathbf{x}' - \mathbf{x}\right|} \tag{4.3}$$

It is noteworthy that the pairwise force function, $\mathbf{f}$, contains the material constitutive information [103–105]. For example, for elastic materials, $\mathbf{f}$, is a linear function of s, whereas for materials with nonlinearity and damage parameters, it is defined by a nonlinear function of the stretch, s.

4.2.2 Micropolar peridynamics

The assumption of a central pairwise bond force described in Section 4.2.1, however, is limited to materials with the Poison's ratio of 1/3 in 2-dimensional plane stress and 1/4 for plane strain and 3-dimensional problems. Gerstle et al. [27] introduced the micropolar peridynamics model, a generalized bond-based peridynamics formulation, by allowing pairwise moments to act between the material points, as illustrated in Fig. 4.1b. Therefore in addition to Eq. (4.2), the quasi-static equilibrium is expressed in terms of moments as presented in Eq. (4.4), where $\boldsymbol{\theta}$ denotes the material particle rotation; $\mathbf{m}$ is the pairwise peridynamic moments; and $\mathbf{m}_b$ is the externally applied moment vector per unit volume.

$$\begin{aligned} \int_{\mathcal{H}_{\mathbf{x}}} \mathbf{f}\left(\mathbf{x}, \mathbf{x}', \mathbf{u}, \mathbf{u}', \boldsymbol{\theta}, \boldsymbol{\theta}'\right) \mathrm{d}V_{\mathbf{x}'} + \mathbf{b}\left(\mathbf{x}\right) = \mathbf{0} \\ \int_{\mathcal{H}_{\mathbf{x}}} \mathbf{m}\left(\mathbf{x}, \mathbf{x}', \mathbf{u}, \mathbf{u}', \boldsymbol{\theta}, \boldsymbol{\theta}'\right) \mathrm{d}V_{\mathbf{x}'} + \mathbf{m_b}\left(\mathbf{x}\right) = \mathbf{0} \end{aligned} \tag{4.4}$$

Generally, the micropolar peridynamics assumes that the bond relationship between two material points interact as a beam element, rather than a truss element used in the bond-based peridynamics. Consequently, Sau [106] formulated the 2-dimensional linearized pairwise micropolar peridynamic forces by $\mathbf{F} = \mathbf{KU}$, where the force vector, $\mathbf{F} = [f_1', f_2', m_3', f_1, f_2, m_3]$ includes force and moment components. The displacement vector is represented by $\mathbf{U} = [u_1', u_2', \theta_3', u_1, u_2, \theta_3]$ and $\mathbf{K}$ is the micro-beam stiffness matrix shown in Eq. (4.5):

$$\mathbf{K} = \begin{bmatrix} c/l & 0 & 0 & -c/l & 0 & 0 & 0 \\ 0 & 12d/l^3 & 6d/l^2 & 0 & 0 & -12d/l^3 & 6d/l^2 \\ 0 & 6d/l^2 & 4d/l & 0 & 0 & -6d/l^2 & 2d/l \\ -c/l & 0 & 0 & c/l & 0 & 0 & 0 \\ 0 & -12d/l^3 & -6d/l^2 & 0 & 0 & 12d/l^3 & -6d/l^2 \\ 0 & 6d/l^2 & 2d/l & 0 & 0 & -6d/l^2 & 4d/l \end{bmatrix} \tag{4.5}$$

In Eq. (4.5), the undeformed bond length, l, is defined by $|\mathbf{x}' - \mathbf{x}| \leq \delta$. The micro-elastic constants, c and d, are obtained by evaluating the internal energy of all associated peridynamic bonds of a given material particle, and comparing this elastic energy to the strain energy determined by classical mechanics method [85]. Gerstle et al. [32] proposed the material parameters, c and d, for a plane stress problem as follows:

$$c = \frac{6E}{\pi\delta^3\,(1-\nu)}, \qquad\qquad d = \frac{E}{6\pi\delta}\left(\frac{1-3\nu}{1-\nu}\right) \tag{4.6}$$

The two constants are defined as a function of varying Poisson's ratios (between -1 and 0.5) and allow the micropolar peridynamics formulation for modeling of structures made of linear elastic materials. Therefore, micropolar peridynamics have been extensively implemented for modeling plain and reinforced concrete with steel reinforcing bars [27, 32, 79, 85, 107].

4.3 Proposed analysis method

In this study, the micropolar peridynamic model is selected to enhance fracture modeling of cracks in concrete structures, particularly fiber reinforced concrete structures. In a previous study [40], it was demonstrated that a meshless analysis approach such as the peridynamics formulation provides inherent capability of modeling cracks and crack propagation paths and ultimately a structural failure. In this study, it is shown that the proposed micropolar peridynamics analysis framework is particularly efficient for modeling fiber reinforced cementitious composites.

4.3.1 Modeling cementitious matrix

The background cementitious material is analytically represented in a micropolar peridynamics analysis framework. To model the material behavior of the cementitious matrix, the micropolar force vector is modified through the introduction of the correction factor for damage in the bond as follows: $\mathbf{F} = (1-\lambda)\mathbf{KU}$, where λ is the damage coefficient between

0 and 1. $\lambda = 0$ indicates no damage in the bond, whereas $\lambda = 1$ represents a fully damaged (or broken) bond. The expression of damage coefficient in this work is given in Eq. (4.7) as a function of the bond stretch, s.

$$\lambda(s) = \begin{cases} 1 & s < s_{uc} \\ 0 & s_{uc} \leq s < s_{0t} \\ 1 - \frac{s_{0t}}{s} e^{-\frac{s - s_{0t}}{s_{ft} - s_{0t}}} & s_{0t} \leq s < s_{ut} \\ 1 & s_{ut} \leq s \end{cases} \tag{4.7}$$

The damage coefficient expression in Eq. (4.7) includes the condition where the bond is fully damaged and consequently is broken beyond the ultimate tensile and compressive stretch limits: s_{ut} and s_{uc}, respectively. For small bond stretches, $s_{uc} \leq s < s_{0t}$, no damage is introduced in the bond. In tension, an exponential part in the expression of damage is implemented for $s_{0t} \leq s < s_{ut}$ which resembles the softening models of concrete after yield point. s_{ft} controls the slope of the softening branch. The exponential softening function in this work is introduced in place of the linear softening function used in original micropolar peridynamic modeling of concrete by Grestle et al. [27]. Using the damage coefficient in Eq. (4.7), the micropolar force vector-bond stretch relationship is illustrated in Fig. 4.2.

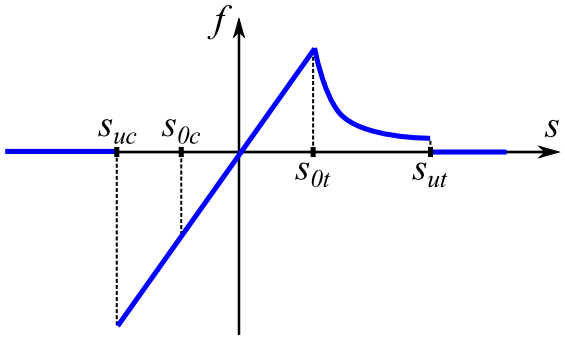


Figure 4.2: Proposed bond force-stretch relationship for modeling concrete material.

In addition to the parameters in Eq. (4.7), the tensile stretch limit, s_{0t}, and the compressive stretch limit, s_{0c}, correlate to the uniaxial tensile strength, f_t, and uniaxial compressive strength, f_c, respectively. The ultimate tensile stretch limit, s_{ut}, and the ultimate compressive

stretch limits, s_{uc}, are related to the fracture energy, G_f, and uniaxial compressive energy absorption capacity of the concrete, respectively. Reference [107] includes further discussion on evaluation of the stretch limits for concrete materials.

4.3.2 Modeling of fiber-concrete interaction

As discussed in the 'Introduction' section, it is computationally inefficient to explicitly model the fiber reinforcement due to a large number of fibers and associated computational expense from increased degrees of freedom. In order to avoid this problem in the proposed semi-discrete model, each fiber does not possess independent degrees of freedom. In this approach, fibers and fiber-background cement matrix interface can be represented by the interaction forces applied to the material particle points. Radtke et al. [63] assumed that the forces can be represented by experimentally determined fiber pull-out forces. It is possible to lump fiber forces at the fiber end points as shown Fig. 4.3a due to relatively short length of macro-scale fibers (typically ranges between $5\,mm$-$30\,mm$). However, Kang et al. [66] introduced a more realistic approach by distributing the fiber forces along the fiber length (see Fig. 4.3b). In this study, the resulting fiber forces are distributed uniformly among concrete material particles adjoining the fiber and treated as external body forces to the background concrete material points, as illustrated in Fig. 4.4.

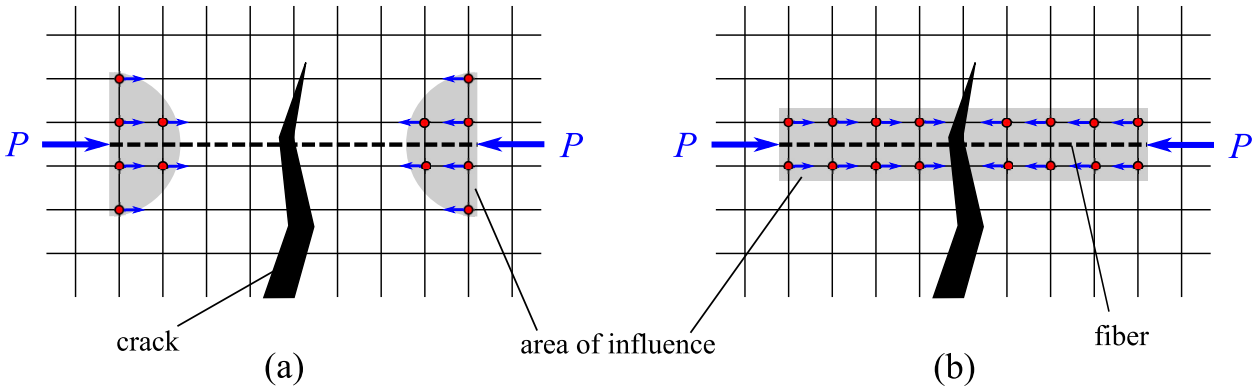


Figure 4.3: Semi-discrete fiber modeling in FEA showing the fiber force simply distributed to element nodes (a) around the fiber ends; and (b) along the fiber embedment length.

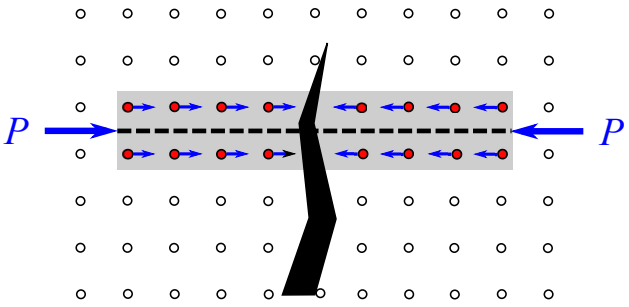


Figure 4.4: Semi-discrete fiber modeling approach employed in the proposed peridynamics framework in which the fiber force is distributed to cementitious material points over the fiber length.

The fiber pull-out behavior has been empirically determined and defined by a force versus pull-out displacement relationship [88]. Various micro-mechanical models derived from properties of the fiber-matrix interface have been proposed to represent the force-pullout displacement relation [88].

In this study, the fiber pull-out failure is represented in two phases including fiber debonding and fiber pull-out [88]. The relative displacement of the fiber end points is used to represent the fiber pull-out distance, Δ. During the debonding stage ($0 \leq \Delta < \Delta_0$), the fiber pull-out force is determined by Eq. (4.8), where Δ_0 denotes the fiber pull-out distance at the onset of the pullout failure:

$$P(\Delta) = \sqrt{0.5\pi^2 E_f d_f^3 \left(\tau_0 (1+\eta) + G_d\right)} \tag{4.8}$$

In Eq. (4.8), η is determined by $(E_f v_f) / (E v_m)$, where E, E_f, v_m and v_f are matrix elastic modulus, fiber elastic modulus, matrix volume fraction and fiber volume fraction, respectively. d_f is the fiber diameter; G_d is the fiber-matrix chemical bond strength (defined as energy per area), and τ_0 is the frictional stress on the debonded interface.

During the fiber pull-out stage ($\Delta_0 \leq \Delta < l_e$), the pull-out force is described by Eq. (4.9), where β is the fiber-matrix interface slip-hardening parameter; l_e is the fiber embed-

ment length, and Δ_0 is the fiber pull-out distance at the onset of the pull-out stage, and is determined by Eq. (4.10).

$$P(\Delta) = \pi d_f \tau_0 [1 + \beta \frac{\Delta - \Delta_0}{d_f}] (l_e - \Delta + \Delta_0) \tag{4.9}$$

$$\Delta_0 = \frac{2\tau_0 l_e^2 (1+\eta)}{E_f d_f} + \sqrt{\frac{8 G_d l_e^2 (1+\eta)}{E_f d_f}} \tag{4.10}$$

4.3.3 Activation of fiber pull-out forces

The fiber reinforcement becomes actively engaged with the cementitious particles when it bridges a crack. In peridynamics, cracks are associated with damaged bonds, therefore in the proposed peridynamic framework, the fiber is activated when it crosses a damaged bond [40]. To implement this on-and-off feature in the proposed model, a fiber activation parameter, λ_f is introduced. The fiber activation parameter represents the largest damage parameter (determined by Eq. 4.7) of the bonds along the fiber, and thus can take values in the range of 0 and 1. The pull-out distance is multiplied by λ_f and a scaled pull-out distance parameter, $\Delta_f = \lambda_f \Delta$, is introduced to obtain the fiber pull-out force. $\lambda_f = 0$ indicates no damage within a set of bonds bridged by the fiber, whereas $\lambda_f = 1$ represents that at least one bond is fully damaged engaging the fiber reinforcement associated with the particle.

The bond with the maximum damage also determines the fiber pull-out distribution scheme as seen in Fig. 4.5. The fiber pull-out force is distributed uniformly to both sides of the bond associated with maximum damage parameter, λ_f.

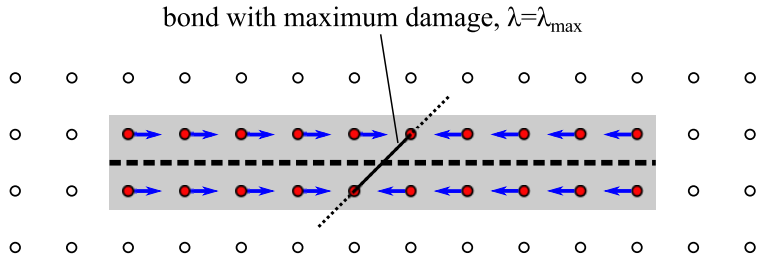


Figure 4.5: A schematic showing fiber activation and engagement, noting that the fiber force is uniformly distributed along the fiber length.

4.3.4 Numerical method used for failure analysis

The peridynamic method is primarily developed to solve time-dependent problems. However, most of the experimental predictions are under steady-state condition. Thus, there is a need to obtain steady-state solutions of the peridynamic equations. In this study, the dynamic relaxation method is adopted to obtain quasi-static solutions of the discretized peridynamic equilibrium equations. Further details on application of dynamic relaxation on peridynamic equations are included in [40,53]. Parallel FORTRAN computing on an UNIX cluster is used to generate the results presented in this study.

4.3.5 Random nature of concrete

Concrete is a heterogeneous composite that consists of cement paste and aggregates that have variable material properties. When comparing experimental and analytical results, it is helpful to consider a range of parameter values for the analytical results. An attempt was made to simulate the variability of the concrete particle strengths by assuming that 5% (by number) of the concrete particles' strength is reduced by 25%. Another 5% (by the particle number) had a percentage strength reduction of 50%. Particles are chosen by random selection. In a similar manner, fiber end locations are also randomly selected within the beam model.

4.4 Implementation of the proposed method in fracture analysis

4.4.1 FRC model in the proposed meshless framework

The proposed method is validated by modeling a FRC beam in the peridynamic analysis framework and comparing the analysis results with available experimental results of the fiber reinforced concrete beams tested by Carpinteri and Brighenti [95]. The experiment includes simply supported concrete beams subjected to three point bending. Each of the tested beams had a notch on the bottom face with a notch depth of $30\,mm$ and width of $2\,mm$. The two

test variables are the notch location ($a/l = 0$, $a/l = 1/6$, and $a/l = 1/4$) and fiber volume fraction ($v_f = 0\%$, $v_f = 2.5\%$, and $v_f = 5.0\%$).

Fig. 4.6 shows a 2-dimensional planner notched beam model developed in the proposed meshless FRC analysis framework. The cementitious material properties provided in [95] are used in the analysis: the water/cement ratio of 0.55, $E = 31.3\,GPa$, $\nu = 0.2$, $f_t = 4.63\,MPa$, and $f_c = 47.8\,MPa$. Based on [32], the parameters in expression of damage coefficient (Eq. 4.7) are obtained as: $s_{0t} = f_t/E$, $s_{ut} = 30s_{0t}$, $s_{0c} = f_c/E$ and $s_{uc} = 1000s_{0u}$. s_{ft} is taken 0.001. The mechanical properties of steel fibers are $l_f = 44\,mm$, $A_f = 0.754\,mm^2$, $E_f = 210\,GPa$, and $f_u = 800\,MPa$. The pull-out force parameters in Section 4.3.2 are taken from [63] as: $G_d = 0.06\,J/mm^2$, $\tau_0 = 2.5\,N/mm^2$, $\beta = 1$ and $l_e = 0.5l_f$. The beam model is discretized with a particle spacing, h, of $1\,mm$ and horizon size, δ, of $3\,mm$, yielding the horizon size-to-particle size ratio, δ/h, of 3. In the numerical analysis, initial imperfections from changes in the size of pores during shrinkage or expansion of cement paste are represented by applying a material strength reduction factor to arbitrarily selected material particles as described in Section 4.3.5. A total of five separate randomly selected distributions of particle strengths were analyzed for each experimental result.

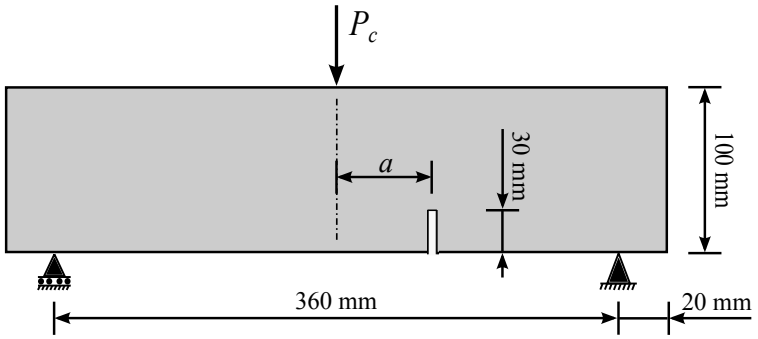


Figure 4.6: Test setup and configuration of a FRC beam with a notch under three point bending.

4.4.2 Results

Figs. 4.7 through 4.9 presents a comparison of numerical force-displacement results obtained from the proposed meshless analysis and the experimental results [95] for a FRC beam with

a notch at the mid-span ($a/l = 0$). Figs. 4.10 through 4.12 and Figs. 4.13 through 4.15 present the force-displacement results from the same FRC beam model; however, the notch is placed away from the midspan ($a/l = 1/6$ and $a/l = 1/4$, respectively). In each group of three figures ($a/l = 0$, $1/4$, $1/6$), the analysis results for varying fiber volume fractions of $v_f = 0\%$, $v_f = 0.25\%$, and $v_f = 0.50\%$ are presented. As discussed, the results are provided only for five randomly selected runs. The initial slope in the experimental load-displacement relationship is not linear, presumably due to initial loading or bearing plate setup; however, the stiffness of the tested beams had ultimately reached the anticipated initial stiffness. It is noteworthy that the load-displacement curves obtained from the analysis had to be shifted from their initial position to directly compare the initial stiffness from the experimental results.

For each fiber reinforced beam specimen tested by Carpinteri and Brighenti [95], it is important to note that two sets of experimental results are reported, whereas five sets of the numerical results are provided. The mean curve of five runs is also provided in the load-displacement plots in Figs. 4.7 through 4.15. The numerically obtained crack paths are also compared with experimental results in Figs. 4.7 through 4.15. It is also noted that the crack pattern shown in Fig. 4.12 is different from the analysis results as the vertical crack may be attributed to the 'Experiment II' results, although it is not clearly stated in the paper. The force-displacement relationship from 'Experiment I' agrees better with the numerical observations and is expected to yield similar crack pattern.

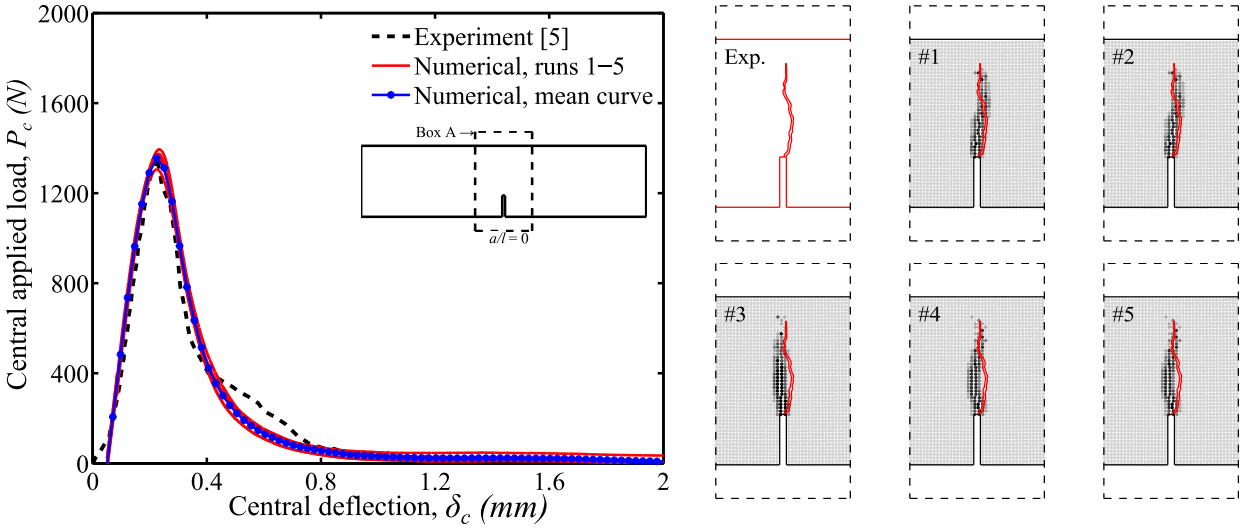


Figure 4.7: FRC beam with a notch located at $a/l = 0$ and a fiber volume fraction of 0%.

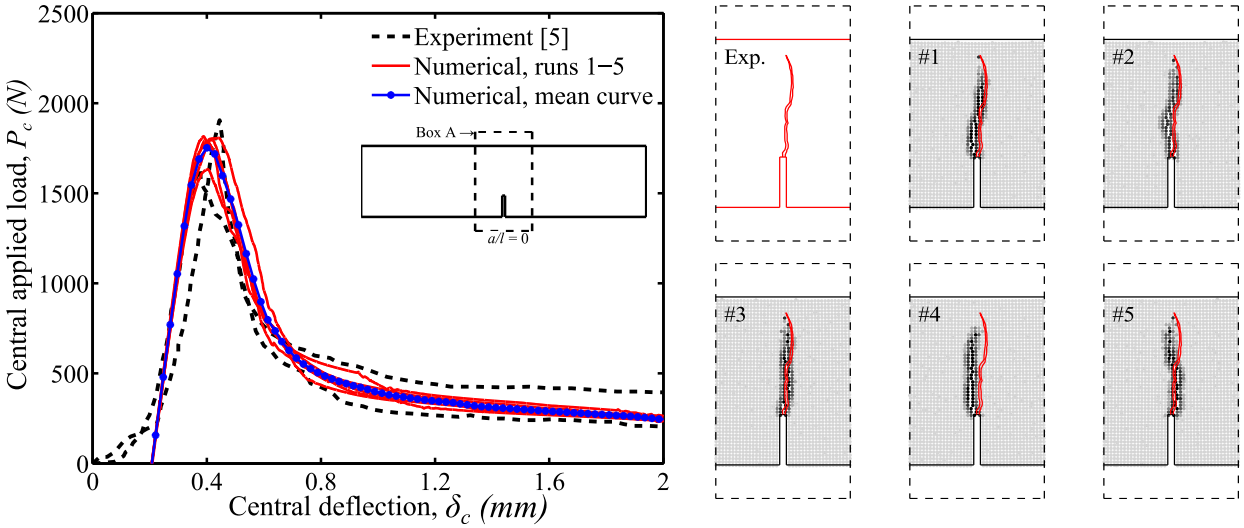


Figure 4.8: FRC beam with a notch located at $a/l = 0$ and a fiber volume fraction of 0.25%.

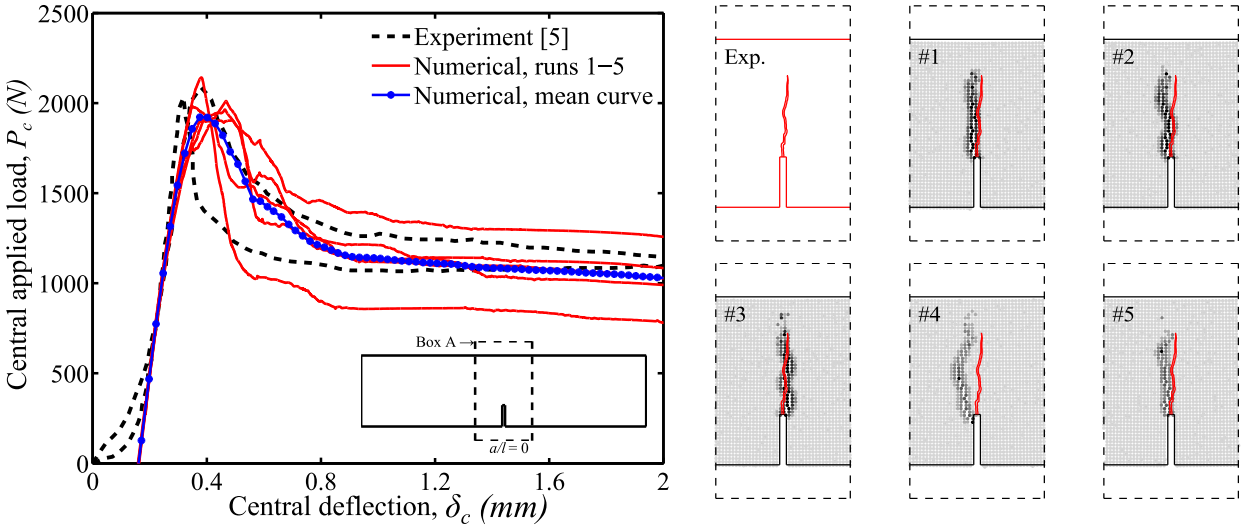


Figure 4.9: FRC beam with a notch located at $a/l = 0$ and a fiber volume fraction of 0.50%.

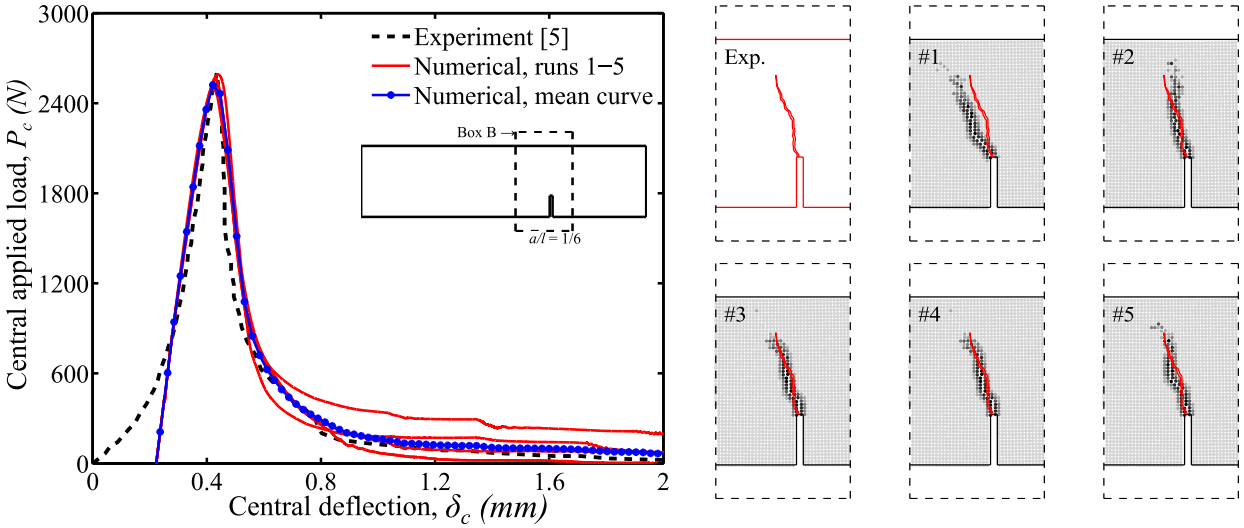


Figure 4.10: FRC beam with a notch located at $a/l = 1/6$ and a fiber volume fraction of 0%.

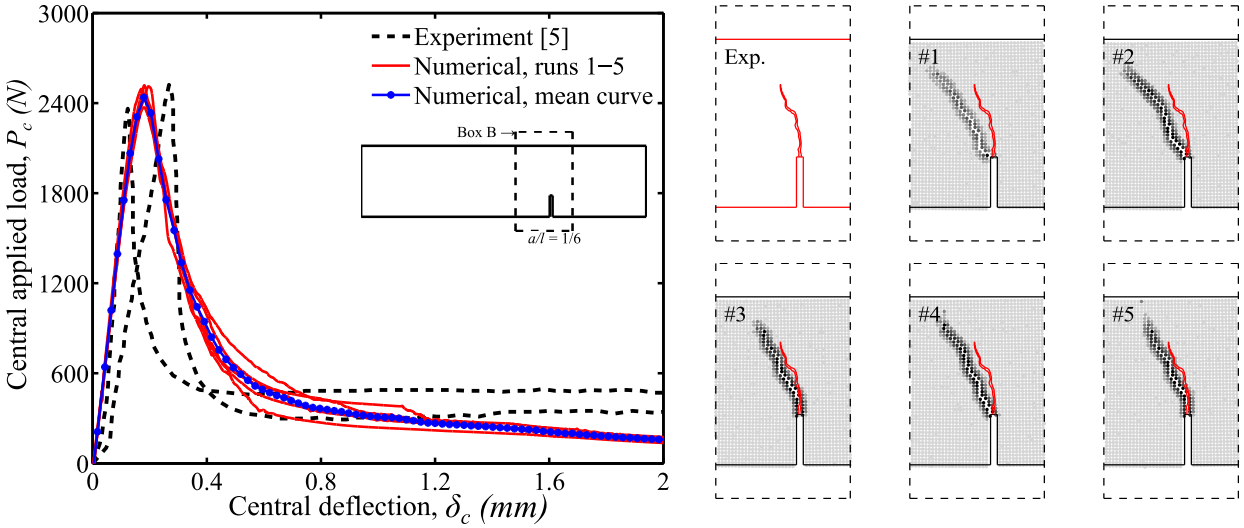


Figure 4.11: FRC beam with a notch located at $a/l = 1/6$ and a fiber volume fraction of 0.25%.

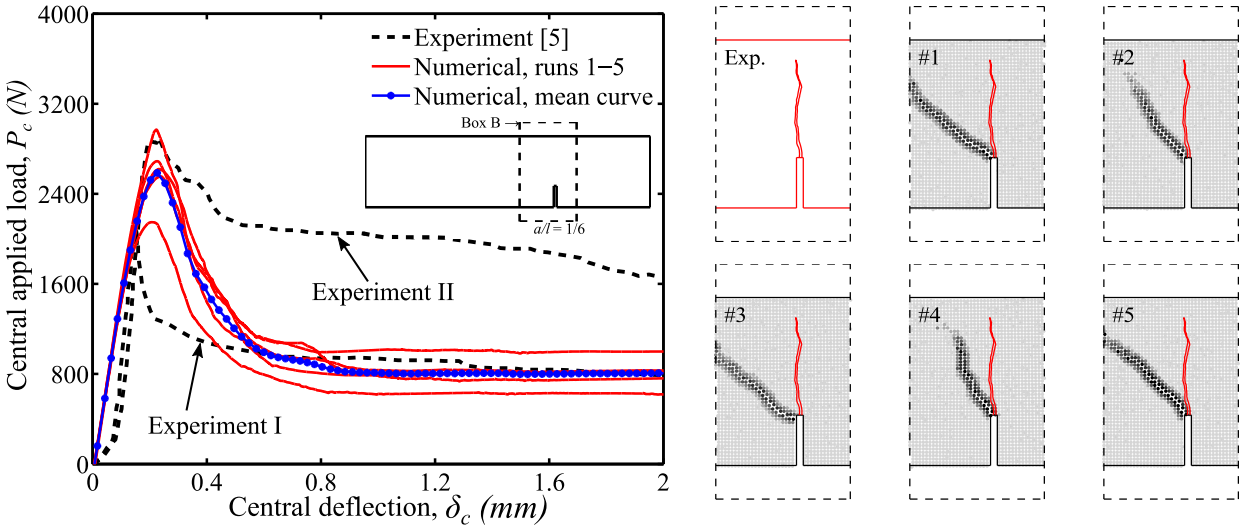


Figure 4.12: FRC beam with a notch located at $a/l = 1/6$ and a fiber volume fraction of 0.50%.

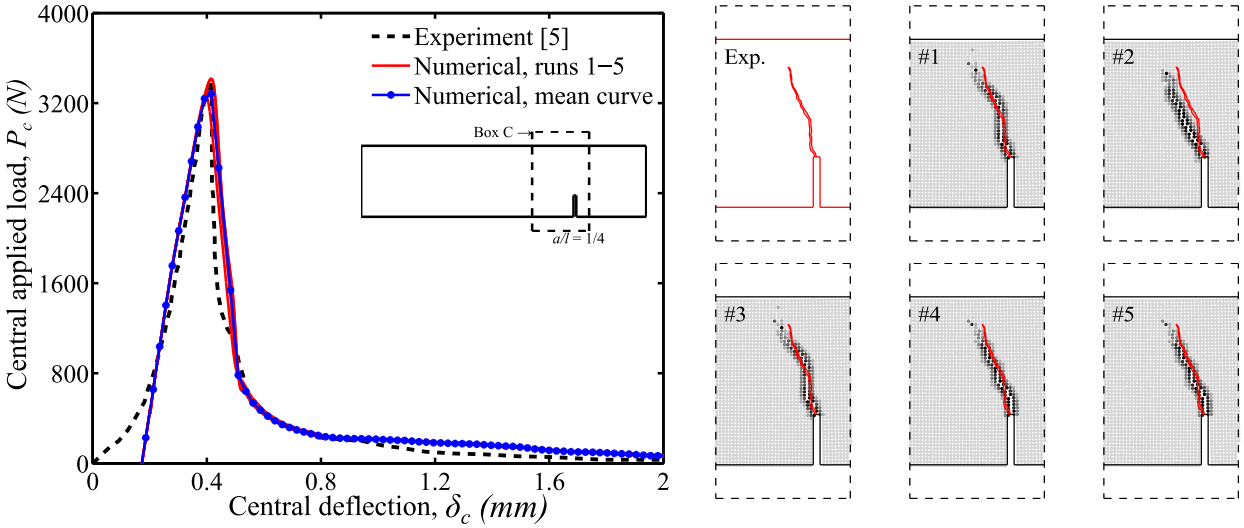


Figure 4.13: FRC beam with a notch located at $a/l = 1/4$ and a fiber volume fraction of 0%.

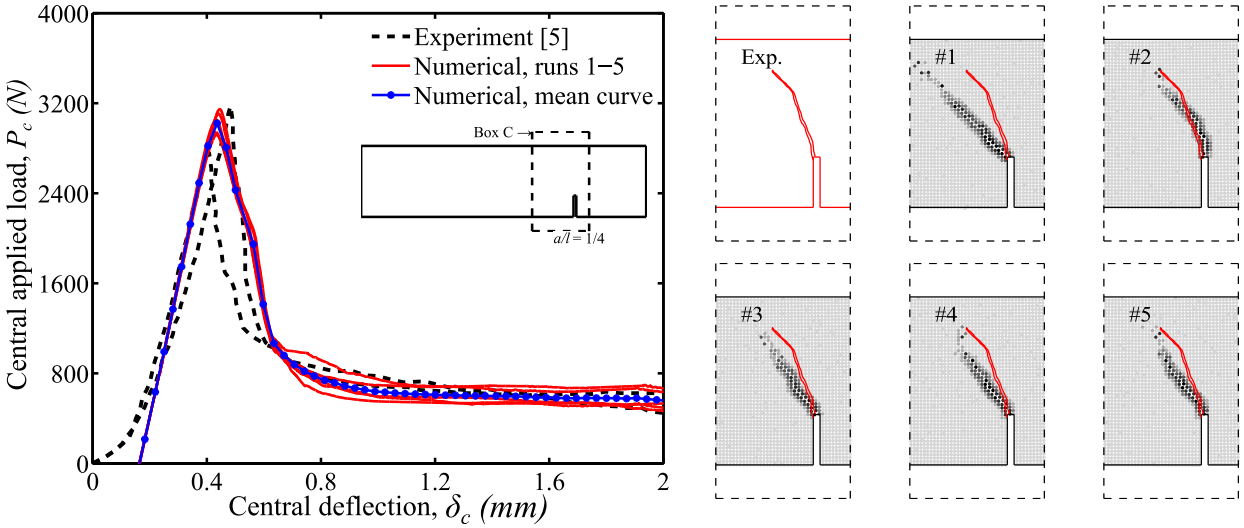


Figure 4.14: FRC beam with a notch located at $a/l = 1/4$ and a fiber volume fraction of 0.25%.

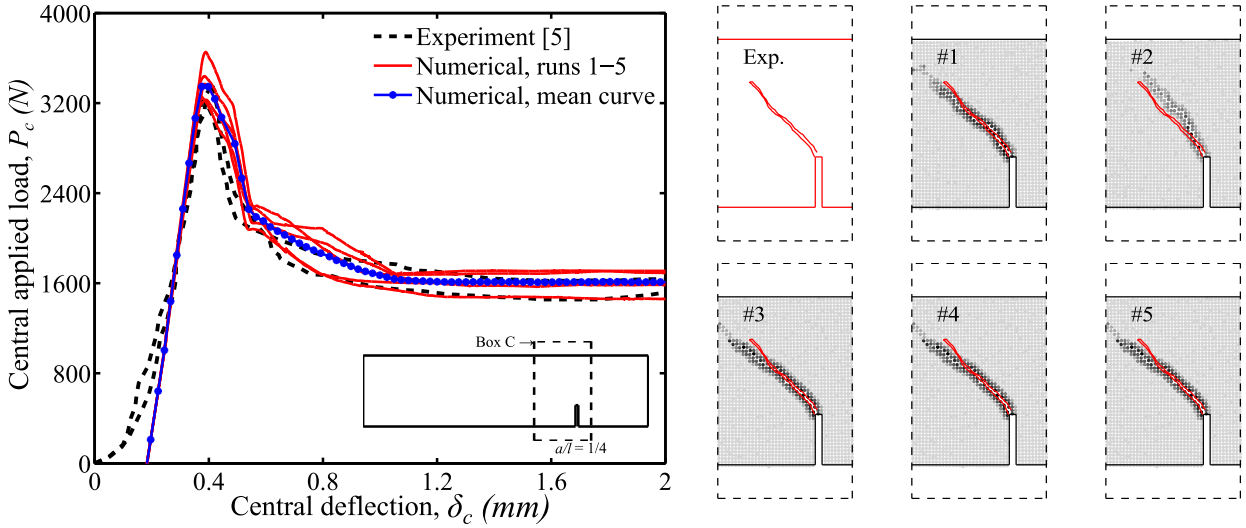


Figure 4.15: FRC beam with a notch located at $a/l = 1/4$ and a fiber volume fraction of 0.50%.

Fig. 4.16 shows both the experimental and numerical relationships between average ultimate load and fiber volume fraction for each notch location. Fig. 4.17 shows the same results for residual load (measured at deflection equals to $2\,mm$).

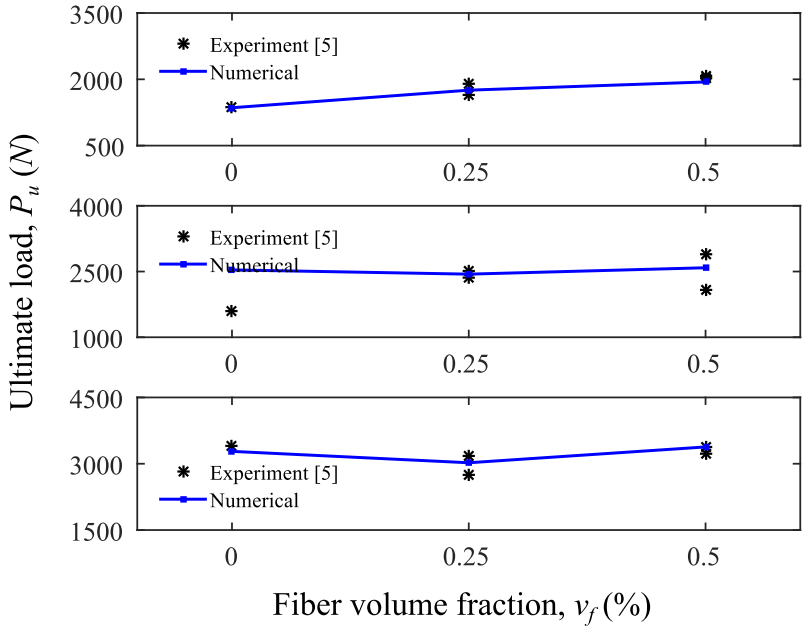


Figure 4.16: The ultimate force, P_u, for varying fiber volume fraction v_f.

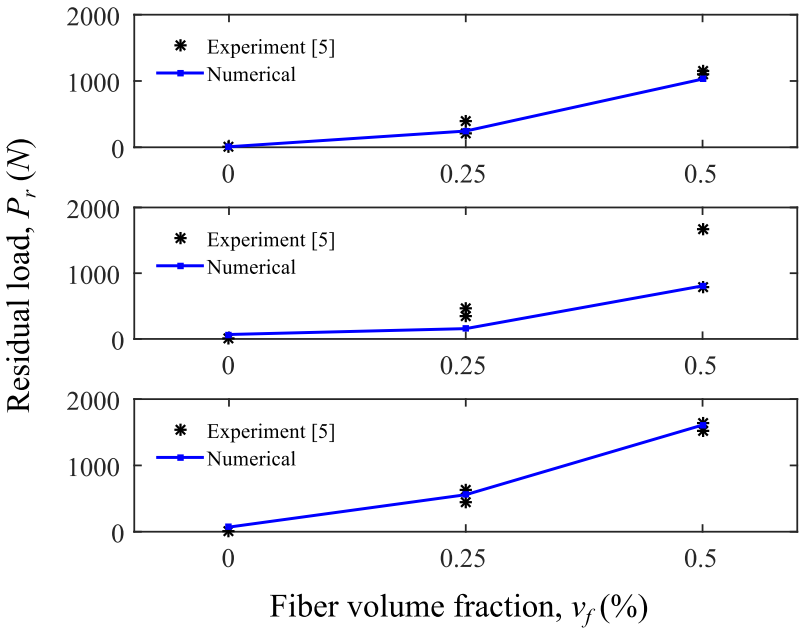


Figure 4.17: The residual force, P_r, where the deflection equals to $2\,mm$ for varying fiber volume fraction v_f.

Fig. 4.18 illustrates the progression of the crack growth for increasing fiber volume fraction for the beam notched at midspan ($a/l = 0$).

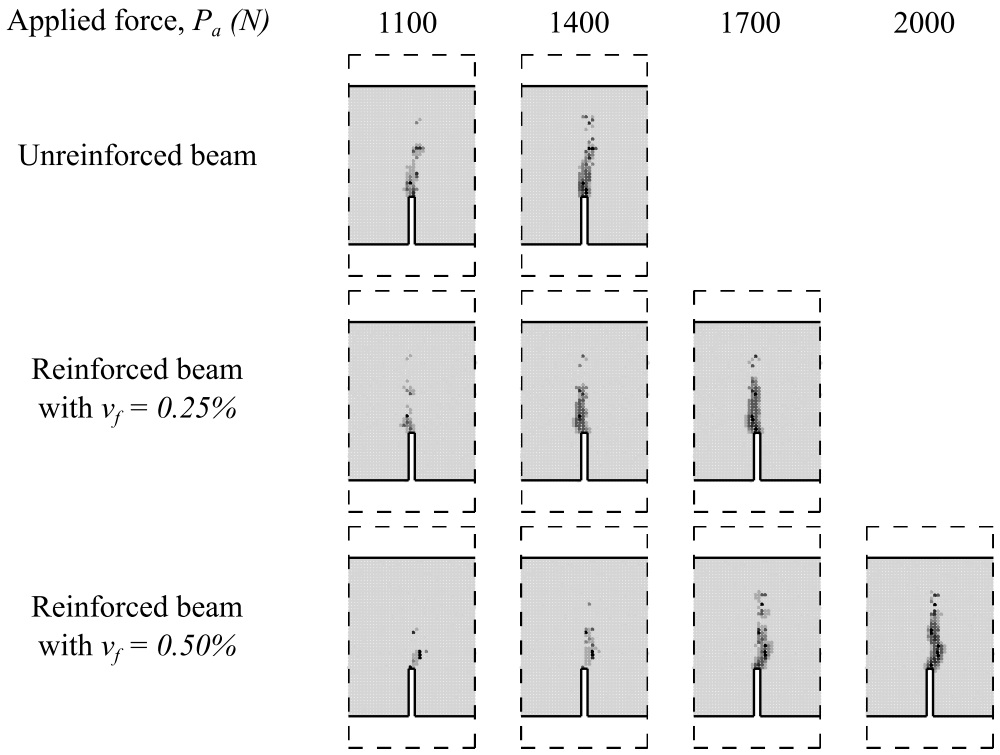


Figure 4.18: A progression of the crack growth for increasing fiber reinforcement fraction.

4.5 Discussion of results

The behavior of notched fiber reinforced concrete beams is complex as illustrated by Figs. 4.7 through 4.15. The proposed numerical approach is able to reproduce this complex behavior and predict the critical results needed for design.

1. Crack angle: The crack angle decreases as the notch location moves from center span toward the support and as the fiber volume fraction increases. The numerical model accurately predicts this result as shown in Figs. 4.7 through 4.15 (One exception is the experimental result for $a/l = l/6$ notch location and with 0.5% fiber volume fraction. In this case, the crack is vertical which is surprising.).

2. Load versus displacement curve: The numerical results accurately reproduce the force displacement curves including the general character of the curves and the displacement corresponding to maximum load as shown in Figs. 4.7 through 4.15.

3. Ultimate load: The experimental ultimate load depends on the notch location and the fiber volume fraction. Fig. 4.16 shows that the numerical results are able to accurately predict the effects of these two variables on the ultimate load.

4. Residual load: The experimental residual load also depends on the notch location and the fiber volume fraction. Fig. 4.17 shows that the numerical results are able to accurately predict the effects of these two variables on the residual load.

5. Random material properties: A simplistic approach was used to investigate the effect of random material properties on overall behavior. However, the results illustrate behavior that is reasonably consistent with the randomness of the experimental results in that the effect of random properties increases with fiber volume fraction. Furthermore, the random properties do not strongly affect ultimate load, but significantly affect crack angle and residual strength which appears to be consistent with the experimental results.

6. Crack control: Fig. 4.18 shows that increasing the fiber volume fraction significantly retards crack formation.

4.6 Conclusion

A micropolar peridynamics framework with a semi-discrete fiber modeling approach is proposed herein. The results of the analysis of fiber reinforced notched concrete beams was successfully implemented using the proposed modeling framework. The proposed method is shown to be highly effective in representing the complex response of notched fiber reinforced beams as demonstrated by comparison of experimental and analytical results.

Chapter 5

Mesoscale Fracture Analysis of Multiphase Cementitious Composites Using Peridynamics[1]

[1]A. Yaghoobi, M. G. Chorzepa, S.S. Kim and S.A. Durham. "Mesoscale Fracture Analysis of Multiphase Cementitious Composites Using Peridynamics." Materials 10.2 (2017): 162. Reprinted here with permission of publisher.

ABSTRACT

Concrete is a complex heterogeneous material, and thus, it is important to develop numerical modeling methods to enhance the prediction accuracy of the fracture mechanism. In this study, a two-dimensional mesoscale model is developed using a non-ordinary state-based peridynamic (NOSBPD) method. Fracture in a concrete cube specimen subjected to pure tension is studied. The presence of heterogeneous materials consisting of coarse aggregates, interfacial transition zones, air voids and cementitious matrix is characterized as particle points in a two-dimensional mesoscale model. Coarse aggregates and voids are generated using uniform probability distributions, while a statistical study is provided to comprise the effect of random distributions of constituent materials. In obtaining the steady-state response, an incremental and iterative solver is adopted for the dynamic relaxation method. Load-displacement curves and damage patterns are compared with available experimental and finite element analysis (FEA) results. Although the proposed model uses much simpler material damage models and discretization schemes, the load-displacement curves show no difference from the FEA results. Furthermore, no mesh refinement is necessary, as fracture is inherently characterized by bond breakages. Finally, a sensitivity study is conducted to understand the effect of aggregate volume fraction and porosity on the load capacity of the proposed mesoscale model.

5.1 Introduction

Concrete is the most widely-used construction material, and therefore, it is important to understand its fracture mechanism. Many studies consider concrete as a homogeneous material at the macroscopic scale. This assumption often results in inaccurate predictions of crack paths and load carrying capacity because concrete is a heterogeneous material. At the mesoscale, concrete is composed of four phases: coarse aggregate, air void, paste and the interfacial transition zone (ITZ), which exists between the coarse aggregate and paste. Mesoscale

modeling is inevitable because the heterogeneity of concrete material is reflected at this scale and enhances the prediction of the fracture mechanism and macroscale behavior. As such, there has been increasing interest in mesoscopic material modeling to better characterize the fracture behavior in concrete.

Numerical simulations are an effective and practical alternative to experimental studies for investigating fracture in heterogeneous materials, such as concrete. Furthermore, analytical methods provide a useful tool for optimizing concrete mixtures by studying the effect of constituent material properties and variables, such as aggregate size, shape, surface texture, grading and volume fraction at the mesoscale. The use of imaging technology enables the determination of mesoscale particle size and location. The most recent imaging techniques include X-ray computed tomography scanning [1,108,109] to provide two- and three-dimensional mesoscopic aggregate and air void distributions.

5.1.1 Mesoscale Modeling

Mesoscale modeling using such imaging technology significantly enhances the accuracy of damage predictions. However, the application is not always practical. Two numerical alternative approaches exist utilizing a parameterization, which involves analytically generating heterogeneity: (1) by explicitly modeling different phases [3,110,111]; and (2) implicitly creating random fields, satisfying certain correlation functions [112–114]. In the direct explicit modeling approach, aggregates and air voids are randomly positioned within a specimen based on their sizes and gradation until the volumetric fraction is met.

The "take-and-place" method [110, 111] has been widely used among several available techniques to numerically generate mesoscopic heterogeneous material phases. In this method, the coarse aggregate is randomly positioned within a domain. When an aggregate intersects with existing aggregates, the position is re-sampled. The maximum aggregate volume fraction that can be achieved by this method is approximately 60% [115]. Mier and

van Vliet [116] developed the "random particle drop" method in order to achieve a higher aggregate volume fraction.

5.1.2 Analysis Methods Available for Fracture Modeling

Several models are available in the literature for fracture analysis of concrete members. Most popular models are based on the finite element method (FEM) [1–6], the discrete element method (DEM) [7,8] and lattice modeling methods [9–14]. The majority of fracture analysis models utilize the FEM, where for instance, failure is represented by inserting a zero-thickness cohesive interface element between homogeneous concrete elements. In this cohesive zone method (CZM), cohesive elements are surface elements that are placed along the element boundaries. Therefore, crack growth is mesh dependent because it occurs only between finite elements where cohesive elements are present. Furthermore, crack paths are highly sensitive to mesh alignment and/or refinement, particularly when they are unknown or unspecified a priori [1,3,4].

When strong discontinuities exist, advanced finite element methods, such as the extended finite element method (XFEM) [2,5], are used. The concept of XFEM was introduced as a technique that models crack initiation and growth within the realm of the FEM without mesh refinement. Local enrichment functions, with additional degrees of freedom, are included in the standard finite element approximation. Typically, the discontinuous displacement enrichment method is used to capture the displacement discontinuity across a crack and around a crack tip. Although XFEM has been successfully used to predict fracture in heterogeneous materials, an external criterion is needed to predict crack growth [2]. Major disadvantages of this method include significantly increased computational expense and complex enrichment functions, which make implementation difficult. Wavelet spectral finite element (WSFE) analysis and its implementation in Abaqus (WSFE-based UEL), developed by Khalili et al. [117,118], are among the novel FE methods in order to reduce the computational expense of finite element analyses.

In the discrete method, discrete elements (or particles) interact by means of contact forces. In the lattice modeling approach, a continuum is represented by a network of discrete elements. Schlangen and Van Mier [10] proposed a mesoscale model for simulating fracture in heterogeneous brittle materials utilizing the discrete modeling approach. Schlangen and Garboczi [12] studied the effect of lattice element type, mesh orientation and fracture criteria on the accuracy of fracture prediction.

While discrete and lattice modeling methods provide promising tools for fracture analysis of concrete at the mesoscale, characterizing parameters that define interactions among various phases in a heterogeneous material demands extra effort. Peridynamics is a non-local method first introduced by Silling [15]. The peridynamic method is well suited for modeling solid bodies with discontinuities. The solution algorithm is more robust than that of the finite element method because partial differential equations used in the classical solid mechanics are replaced by spatial integral equations (a sum of bond forces), which are also defined at discontinuities, such as cracks. Crack initiation and propagation are inherently represented by defining a bond relationship between particles using a constitutive model. Furthermore, the bond relationship between dissimilar material phases is inherently integrated in the peridynamic method.

Two methods are primarily used: bond-based peridynamics (BBPD) [15, 16] and micropolar peridynamics (MPPD) [27, 34]. BBPD and MPPD assume that the bond force developed between material particle points is similar to those in a truss and a beam element, respectively. Therefore, these two methods resemble a lattice modeling approach. In addition to the similarity in defining the bond forces, peridynamics distinctly provide a set of material particles, whereas a continuum is discretized using a network of discrete elements in the lattice modeling method. Each material particle in peridynamics represents an infinitesimal volume and has its mass lumped at the center. The material continuity is provided by a "force-field" generated between particles.

In the bond-based peridynamics, independent interactions of a pair of material points were represented by a central-pairwise force. This assumption restricted BBPD to a Poisson's ratio of 1/4 in three-dimensional models [16, 30]. Although, MPPD addressed this issue by introducing rotational degrees of freedom into the bond-based peridynamic model [27], it was difficult to represent all aspects of material response, particularly when a collective response among material particle bonds was involved (e.g., a volume change). To avoid this type of restriction, a generalized peridynamic formulation, so-called non-ordinary state-based peridynamics (NOSBPD), was introduced. The main goal of NOSBPD was to allow interactions among the bonds [29]. Therefore, the collective deformation of the bonds around a material point defines the response of the point [28]. In NOSBPD, each bond between two material points is capable of carrying loads in all directions, which allows characterizing materials with any thermodynamically-admissible Poisson's ratio [28, 39, 41]. Furthermore, the NOSBPD is capable of representing genuine material behaviors, such as a volume or shear angle change. Furthermore, the force state is represented by the classical stress and strain tensors, which enable the use of constitutive and damage models from the classical mechanics theory.

5.1.3 Summary of Work Presented in the Remaining Sections

This study includes a proposed mesoscale modeling approach in which heterogeneous concrete material is represented by four phases in the NOSBPD framework. A statistical approach is used to generate more realistic coarse aggregate size and distribution and to provide statistically-significant analysis results with a reasonable computational cost. Furthermore, crack or damage patterns are studied for varying particle spacing, aggregate volume fraction and air void content. Finally, the accuracy of the proposed model is compared with available experimental and analytical (or FEM) results.

5.1.4 Novel Aspects of the Research

The novel aspects of this study include, but are not limited to: (a) damage (e.g., crack initiation and propagation) inherently characterized by the peridynamic analysis framework; (b) promising potential for developing into a multiscale coupling approach with the FEM and, thus, for practical modeling applications; (c) a practical parametric design, including varying aggregate/air void distributions and material dense packing, available for material engineers; (d) enhancement in predicting the mesoscopic fracture mechanism in cementitious composites.

5.2 Proposed Mesoscale Concrete Model

In the majority of available studies, concrete is considered as a homogeneous material for simplicity. However, this assumption yields results that are inaccurate in predicting crack paths and load carrying capacity because concrete is a complex heterogeneous material. Its heterogeneity plays an important role in fracture analysis. Therefore, it is proposed that a two-dimensional mesoscopic model be used herein to account for the heterogeneity, whereas a microscopic model is feasible at the expense of additional computational resources in order to represent micro-structural inhomogeneity.

5.2.1 Mesoscopic Constituent Materials

Concrete is mainly composed of two phases at the mesoscale: coarse aggregate and paste. In addition, a third phase exists in the interface between the coarse aggregate and paste. Each of these three phases is heterogeneous in its composition. Proportions and characteristics of each phase vary with mixture composition. In the proposed mesoscale model, concrete is considered a heterogeneous material consisting of four phases to account for porosity: the coarse aggregate, air void, cementitious paste and the interfacial transition zone (ITZ), which exists between the coarse aggregates and cementitious matrix. In

mesoscale modeling, the paste represents a mixture of microscale fine aggregates, cementitious hydration products, such as calcium-silicate-hydrate and calcium hydroxide, and water. Each phase is described below.

Cementitious matrix: A cementitious matrix itself at the microscale is a heterogeneous material that consists of fine aggregates, hardened cement paste with embedded pores. In the numerical mesoscale studies, cementitious matrix is assumed to be homogenous. The homogenized properties of the matrix are dependent on various factors, including cementitious type and content, water-cement ratio, compaction, which controls the amount of pores, and environmental conditions during the hardening process [119].

Coarse aggregate: Mechanical properties of concrete mixtures are highly affected by coarse aggregate material (limestone or granite), source, size, gradation, shape (river gravel or crushed gravel), texture and distribution. Most normal strength concrete mixtures are composed of 40%–50% coarse aggregates by volume and 60%–80% when combined with fine aggregates [120].

Interfacial transition zone (ITZ): The interfacial region is formed between the coarse aggregates and hydrated cement paste and yields the weakest link in cementitious composites due to higher concentrations of soluble calcium hydroxide in the region [119]. The properties of composites are often governed by the nature of this interface layer. This highly heterogeneous region with a thickness between 20 and 100 μm plays an essential role in the macroscopic behavior of concrete structures. Many experimental studies are devoted to characterizing the homogeneous mechanical properties of this ITZ. The results indicate that micro-cracks are mostly initiated from this region and that increased aggregate volume/size is associated with reduced tensile strength due to increased ITZ area [121, 122].

Air void: Mesoscopic air voids are distributed throughout the cement paste and could lower the compressive strength of the concrete.

Figure 5.1 shows a schematic of four phases in a two-dimensional mesoscale concrete model. Figure 5.2 shows the position and distribution of the coarse aggregates and air voids

in selected numerical specimens. In this figure, P_{agg} and P_{pore} represent the aggregate volume fraction and porosity, respectively. Figure 5.3 shows the gradation of the coarse aggregate for varying aggregate volume fractions described in the following section.

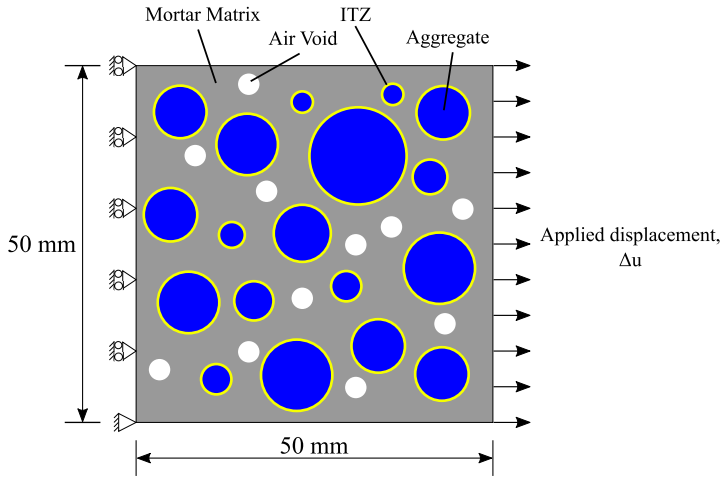


Figure 5.1: Schematic of mesoscale multiphase model subjected to tension.

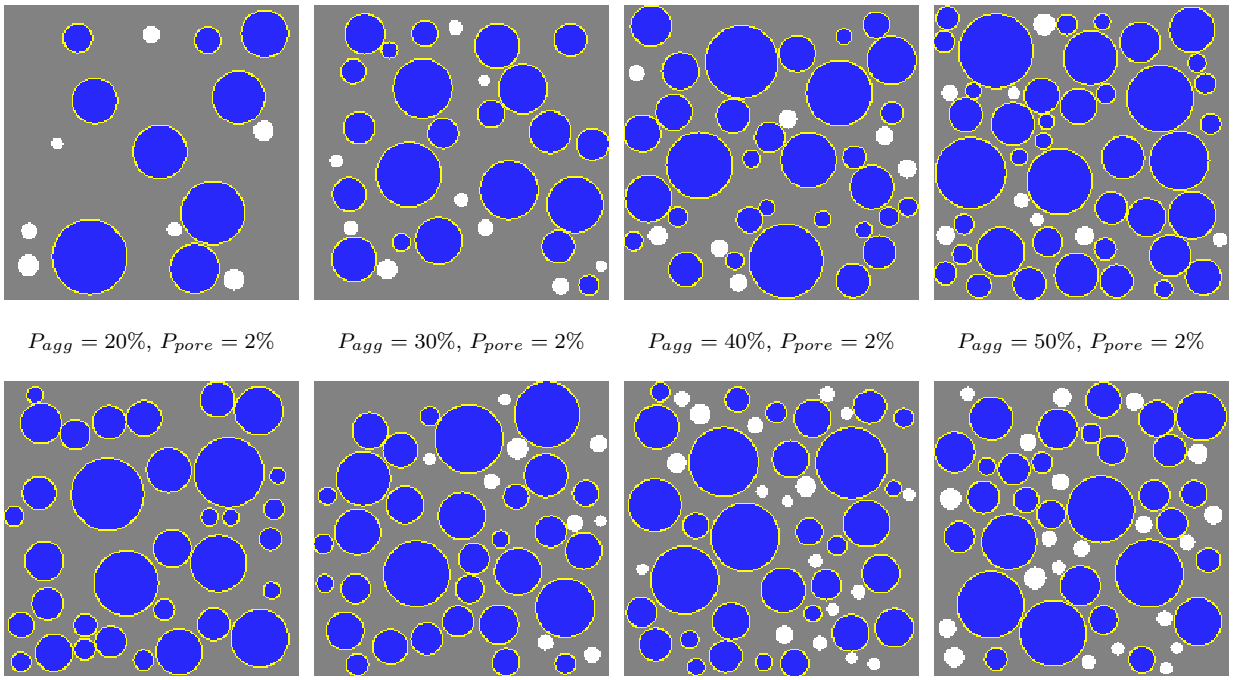


Figure 5.2: Numerical specimens with varying aggregate volume fraction and porosity.

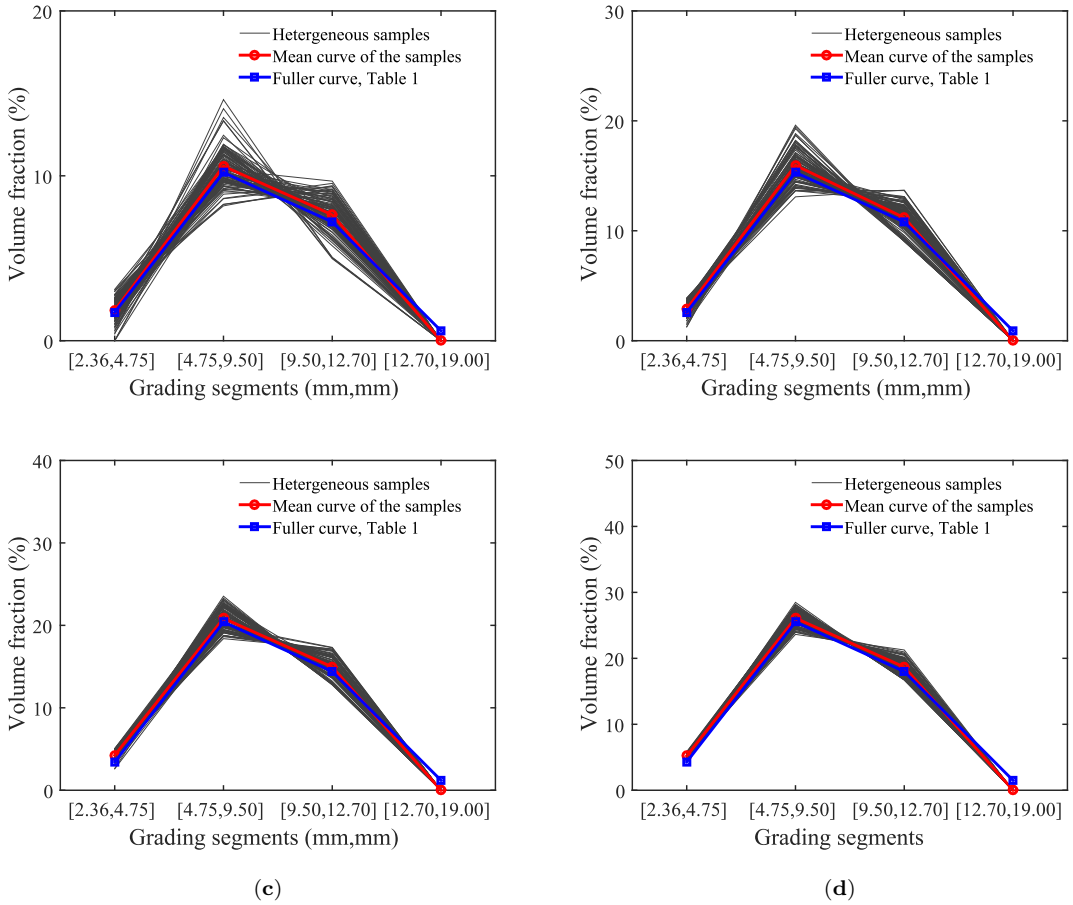


Figure 5.3: Aggregate gradations achieved by simulation versus the Fuller curve. (**a**) $P_{agg} = 20\%$; (**b**) $P_{agg} = 30\%$; (**c**) $P_{agg} = 40\%$; (**d**) $P_{agg} = 50\%$.

5.2.2 Distribution of Constituent Materials into Multi-Phases

Coarse aggregate: A random particle selection procedure is used in creating a mesoscale model. This particle placement approach, the so-called "take-and-place method" [110], is adopted in the proposed model to locate aggregates within an element domain. The aggregate shape is assumed circular, although other shapes such as angular are feasible and have been used in other mesoscale analyses [110, 123]. Regardless, a grading curve must be provided to determine the volumetric ratio of the coarse aggregate and gradation. The Fuller curve is used in this study as it is widely employed to generate the optimum density and strength of concrete mixtures [10, 120].

Equation (5.1) determines the cumulative percentage of aggregate passing a sieve with an aperture size of d, where d_{max} is the maximum size of aggregate to be used, and the constant $m = 0.45 - 0.7$ determines the shape of the grading curve. Equation (5.2) gives the total area of aggregates, A_{agg}, within the grading segment of $[d_i, d_{i+1}]$, where A_{model} is the total area of a numerical model and d_{min} is the minimum aggregate size:

$$P(d) = 100(\frac{d}{d_{max}})^m \tag{5.1}$$

$$A_{agg}[d_i, d_{i+1}] = \frac{P(d_{i+1}) - P(d_i)}{P(d_{max}) - P(d_{min})} P_{agg} A_{model} \tag{5.2}$$

Beginning with the largest segment, the following procedure is used to determine the aggregate size and location in a given domain for each grading segment:

1. Determine the total area of the coarse aggregate, A_{agg}, with the aggregate size between d_i and d_{i+1}, using Equation (5.1).

2. Generate a random number, which defines the aggregate diameter, d, within the segment $[d_i, d_{i+1}]$. The aggregate diameter, d, is obtained by $d = d_i + \eta(d_{i+1} - d_i)$, where η is a variable selected from a uniform distribution of numbers between zero and one by using the "$RANDOM_NUMBER$"command in FORTRAN.

3. Generate two sets of random numbers to define the location of current aggregate. Two numbers are selected from a uniform distribution, with equal probability for all values, of the random variables between zero and one.

4. Check the placement of aggregate: Two conditions must be met to position the aggregate. First, the aggregate must be located within the analytical specimen boundary with a minimum clearance distance from the specimen boundary, γ_1. There must be no overlapping area between current aggregate and previously-placed aggregate, if any. A minimum distance of γ_2 between the two aggregates must be considered. These two

conditions assure that the current aggregate is reasonably surrounded by the cementitious matrix. For the coarse aggregate distribution, $0.1d$ and $0.1(d+d)/2$ are used for γ_1 and γ_2, respectively. d is the diameter of the current aggregate being positioned, and d is the diameter of previously-positioned aggregate.

5. Repeat the random placement in Steps 2–3 until the conditions in Step 4 are satisfied.

6. Determine the total area of generated aggregates, A_{agg}, in this segment, and find the remaining aggregate area by subtracting A_{agg} from the total aggregate area, A_{agg}, determined in Step 1.

7. Repeat Steps 2–6 until the remaining area is no longer available to generate additional aggregate in the grading segment.

Air voids: Once the generation and placement of the coarse aggregates is complete, the same procedure is used to create air voids ranging between 2 and 4 mm in diameter.

ITZ: A thin layer ranging between 20 and 100 μm must be selected to represent the interface of coarse aggregate and paste. In this study, it is reasonable to select a single layer of particles surrounding coarse aggregates because the particle spacing studied herein is greater than 100 μm. With this simple assumption, ITZ and its associated damage is dependent on the particle spacing, although it is possible to use a smaller particle spacing in the ITZ. Therefore, it is essential to complete a convergence study to determine the particle size appropriate for characterizing the fracture mechanism in ITZ.

Cementitious matrix: The remaining particle points are used to form the cementitious matrix.

5.2.3 Formulation of the Proposed Analysis Framework

The kinematics of the peridynamics for a two-dimensional body is illustrated in Figure 5.4. A particle located at position $\mathbf{x}$ interacts with its surrounding particles within an area of influence, the so-called "horizon", where δ is the horizon size. It is important to recognize the

position vector-state, $\mathbf{X}\langle \mathbf{x}' - \mathbf{x} \rangle = \boldsymbol{\xi} = \mathbf{x}' - \mathbf{x}$. It is also referred to as the "bond" between two particles, $\mathbf{x}$ and $\mathbf{x}'$, and represents the relative position in the undeformed body, $\mathbf{B}_0$. The deformation vector-state, $\mathbf{Y}\langle \mathbf{x}' - \mathbf{x} \rangle = \boldsymbol{\xi} + \boldsymbol{\eta} = \mathbf{y}' - \mathbf{y}$, maps the bond, $\mathbf{X}\langle \mathbf{x}' - \mathbf{x} \rangle$, in the deformed body, $\mathbf{B}$, where $\boldsymbol{\eta} = \mathbf{u}' - \mathbf{u}$ is the relative displacement of particles, $\mathbf{x}$ and $\mathbf{x}'$.

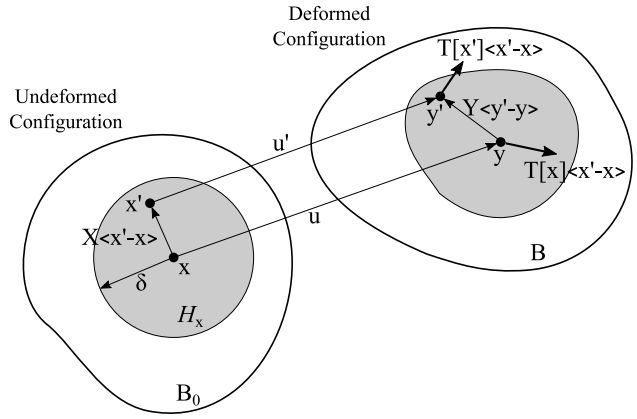


Figure 5.4: Kinematics of state-based peridynamics.

In the NOSBPD [28], the steady-state equilibrium equations for the particle, $\mathbf{x}$, are given in Equation (6.5), where $\mathbf{b}$ is the body force applied on the particles, $\mathbf{x}$, and $dV_{\mathbf{x}'}$ is the volume of the particle $\mathbf{x}'$. The force vector-state, $\mathbf{T}$, is obtained by Equation (6.6), where $\boldsymbol{\omega}(\xi)$ denotes a constant weight function and $\xi = |\boldsymbol{\xi}| = |\mathbf{x}' - \mathbf{x}|$. The stress tensor, $\boldsymbol{\sigma}$, is the first Piola–Kirchhoff stress, and the shape factor, $\mathbf{K}$, at particle $\mathbf{x}$ is defined by Equation (6.4). The symbol $\otimes$ denotes the tensor product.

$$\int_{\mathcal{H}_{\mathbf{x}}} \left(\mathbf{T}[\mathbf{x}]\langle \mathbf{x}' - \mathbf{x} \rangle - \mathbf{T}[\mathbf{x}']\langle \mathbf{x} - \mathbf{x}' \rangle \right) \mathrm{d}V_{\mathbf{x}'} + \mathbf{b}(\mathbf{x}) = \mathbf{0} \tag{5.3}$$

$$\mathbf{T}[\mathbf{x}]\langle \mathbf{x}' - \mathbf{x} \rangle = \boldsymbol{\omega}(\xi)\, \boldsymbol{\sigma} \cdot \mathbf{K}^{-1} \cdot (\mathbf{x}' - \mathbf{x}) \tag{5.4}$$

$$\mathbf{K}(\mathbf{x}) = \int_{\mathcal{H}_{\mathbf{x}}} \boldsymbol{\omega}(\xi) \left[(\mathbf{x}' - \mathbf{x}) \otimes (\mathbf{x}' - \mathbf{x}) \right] \mathrm{d}V_{\mathbf{x}'} \tag{5.5}$$

A nonlocal approximation of the deformation gradient tensor, $\mathbf{F}$, is defined by Silling et al. [28] to formulate the classical continuum mechanics' constitutive equations in peridynamics:

$$\mathbf{F}(\mathbf{x}) = [\int_{\mathcal{H}_\mathbf{x}} \omega(\xi)[(\mathbf{y}' - \mathbf{y}) \otimes (\mathbf{x}' - \mathbf{x})]\mathrm{d}V_{\mathbf{x}'}] \cdot \mathbf{K}^{-1} \tag{5.6}$$

The small strain tensor for isotropic elastic materials is determined by $\boldsymbol{\epsilon} = 1/2(\mathbf{F} + \mathbf{F}^T) - \mathbf{I}$, where the stress is obtained by $\boldsymbol{\sigma} = \mathbf{C}\boldsymbol{\epsilon}$; $\mathbf{C}$ is the isotropic elastic moduli matrix; and $\mathbf{I}$ is the identity matrix.

In the proposed approach, a higher-order polynomial approximation is used for the deformation gradient tensor in order to successfully suppress an instability problem found in NOSBPD [39, 124]. Furthermore, an incremental and iterative solver is used to obtain the steady-state solutions. That is, the dynamic relaxation (DR) method is adopted to iteratively obtain solutions for a displacement increment, $\Delta\mathbf{u}$. This iteration is necessary because the model oscillates about the equilibrium position until the size of the displacement vector for all particles becomes smaller than the dynamic relaxation threshold, ε [40, 125]. This type of dynamic relaxation method determines steady-state solutions for a dynamic system by introducing fictitious mass and damping matrices and is particularly effective for solving highly nonlinear problems, including geometric and material nonlinearities.

There are several studies [20, 39] that correlate the particle spacing, h, and horizon size, δ, to the rate of convergence in solutions. The vast majority of findings suggests that it is most effective when the horizon size is about three-times the particle spacing (i.e., $\delta \approx 3h$) [23, 126]. In this study, $\delta = 3.1h$ is selected. Therefore, the particle spacing size, h, is the only variable that can affect the discretization size of a mesoscale model in this study.

5.2.4 Determination of Statistically-Significant Sample Size

One hundred samples are generated using the procedure described in Section 5.2.2 in order to study a statistically-significant numerical sample size. Two criteria are mainly used to determine the sample size: (1) average stress convergence and (2) average peak stress convergence.

5.3 Analysis of a Concrete Specimen in Tension

5.3.1 Description of a Numerical Model

A two-dimensional mesoscale representative model is studied to demonstrate the capabilities of the proposed method. Figure 5.1 shows a schematic of the numerical specimen and its loading condition. The specimen geometry and loading condition are selected because both experimental and analytical results are presented by Wang et al. [111], and thus, the analysis results can be verified by the cohesive FEM results and validated against experimental results. A quadrilateral discretization scheme is used to distribute material points needed for peridynamics analysis. The particle points generated within the air voids are removed from the analysis model as described in Section 5.2.2. Table 5.1 provides the gradation of the coarse aggregate obtained from Wang et al. [111].

Table 5.1: Gradation of the coarse aggregate [111].

Sieve size (mm)	19.00	12.70	9.50	4.75	2.36
Total percentage passing (%)	100	97	61	10	1.4

5.3.2 Material Models

An isotropic damage model is used to describe the stress-strain relationships of constituent materials. Table 5.2 provides the material properties used for the analysis. The material softening due to micro-cracking is introduced in the material constitutive model using a damage variable, D, as shown in Equation (5.7):

$$\boldsymbol{\sigma} = (1 - D)\mathbf{C}\boldsymbol{\epsilon} \tag{5.7}$$

Table 5.2: Material properties [111].

Constituent	**Young's Modulus, E (MPa)**	**Poisson's Ratio, ν**	**Fracture Energy, G_f (N/mm)**
Aggregate	70,000	0.2	-
Mortar	25,000	0.2	0.06
ITZ	25,000	0.2	0.03

The damage variable, D, ranges from 0–1 for undamaged and fully-damaged materials, respectively, and is determined by Equation (5.8), where ϵ_{eq} is the equivalent strain determined by Equation (5.9), on the basis of the modified von Mises equivalent strain; $\epsilon_0 = f_t/E$; f_t is the tensile strength; f_c is the compressive strength; $k = f_c/f_t$ and is assumed as 10. E is Young's modulus; ϵ_f is the parameter affecting the slope of the softening branch; and $\epsilon_f = 0.02$ is used in this study. This value is selected by comparing the analysis results obtained by the proposed peridynamic and finite element methods. That is, for each mesh size studied herein, a range of ϵ_f is considered for defining the softening curve. It is concluded that the mesh size has an insignificant effect on the parameter, ϵ_f, when generating the PD analysis results that agree with the finite element analysis results. It is also concluded that the PD analysis results are insensitive for ϵ_f ranging between 0.019 and 0.021 and best agree with the FEA results when ϵ_f of 0.02 is used.

$$D = \begin{cases} 0 & : \epsilon_{eq} < \epsilon_0 \\ 1 - \frac{\epsilon_0}{\epsilon_{eq}} e^{-\frac{\epsilon_{eq} - \epsilon_0}{\epsilon_f - \epsilon_0}} & : \epsilon_0 \leq \epsilon_{eq} \end{cases} \tag{5.8}$$

$$\epsilon_{eq} = \frac{k-1}{2k(1-2\nu)} I_1 + \frac{1}{2k} \sqrt{\frac{(k-1)^2}{(1-2\nu)^2} I_1^2 + \frac{6k}{(1+\nu)^2} J_2} \tag{5.9}$$

In determining the equivalent strain in Equation (5.9), $I_1 = tr(\boldsymbol{\epsilon})$ and $J_2 = tr(\boldsymbol{\epsilon}.\boldsymbol{\epsilon}) - \frac{1}{3} tr^2(\boldsymbol{\epsilon})$ are the invariants of the strain tensor. The bond breakage procedure proposed by Tupec et al. [23] is used in this study. In their approach, a bond breakage criterion is applied to a pair of the particles, $\mathbf{x}$ and $\mathbf{x}'$. The weight function, used to define the bond between two points, $\mathbf{x}$ and $\mathbf{x}'$, is replaced with the following weight function:

$$\hat{\omega} = \omega(\xi)\,\omega_D(D, D') \tag{5.10}$$

In Equation (5.10), $\omega(\xi)$ is the radially-symmetric weight function, which quantifies the reduced degree of interaction as a function of the distance away from the material points. $\omega_D(D, D')$ is zero if one of the particles is fully damaged; otherwise, it is one. D and D is the damage parameter for $\mathbf{x}$ and $\mathbf{x}'$, respectively. Since Equation (5.8) does not yield one, the damage variable, D, is assumed as one ($D = 1$) if D calculated by Equation (5.8) is greater than 0.99. This value is the critical damage threshold, D_{cr}, selected for this study.

In the peridynamic theory, the damage is associated with the bond breakage. In this study, the state of material damage is described by a single parameter, D, at each material point (see Equation (5.8)). Therefore, it is required to define a bond breakage criterion between a pair of particles, $\mathbf{x}$ and $\mathbf{x}'$, based on their damage parameters, D and D', respectively. Therefore, the damage parameters, D and D', are applied to compute the bond breakage threshold at two separate particle points, which belong to two material components, respectively. For example, the parameters are used to define the threshold force at the two particle points, which belong to a coarse aggregate and a cementations concrete matrix, respectively. It is important to note that the two damage parameters are also used to represent the damage between two particles from the same material (e.g., a coarse aggregate).

5.4 Analysis Results and Discussion of the Results

The analysis results indicate that the proposed mesoscale mesh-free approach combined with a simple material damage model is capable of characterizing the fracture behavior of the concrete specimen subjected to pure tension.

5.4.1 Effect of Particle Spacing and Convergence

In peridynamics, particle spacing and the horizon size are studied to determine the extent of discretization and convergence, whereas the mesh size is varied in the FEM. The specimen

subjected to pure tension is discretized with three particle spacings, h: 1/2, 1/3 and 1/4 mm, as illustrated in Figure 5.5. For each discretization size, 100 heterogeneous models are sampled and analyzed, and the results are presented in Figure 5.6. The following solver parameters remain unchanged for this discretization study: $\Delta u = 5 \times 10^{-4}$ mm and $\varepsilon = 10^{-7}$.

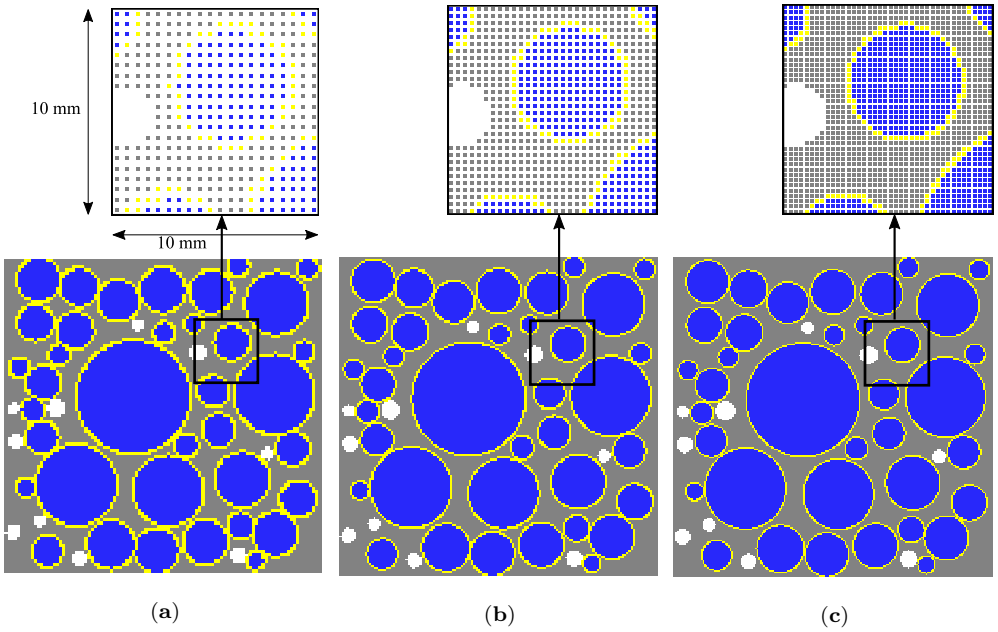


Figure 5.5: Numerical specimens with varying particle spacing, h. (**a**) $h = 1/2$ mm; (**b**) $h = 1/3$ mm; (**c**) $h = 1/4$ mm.

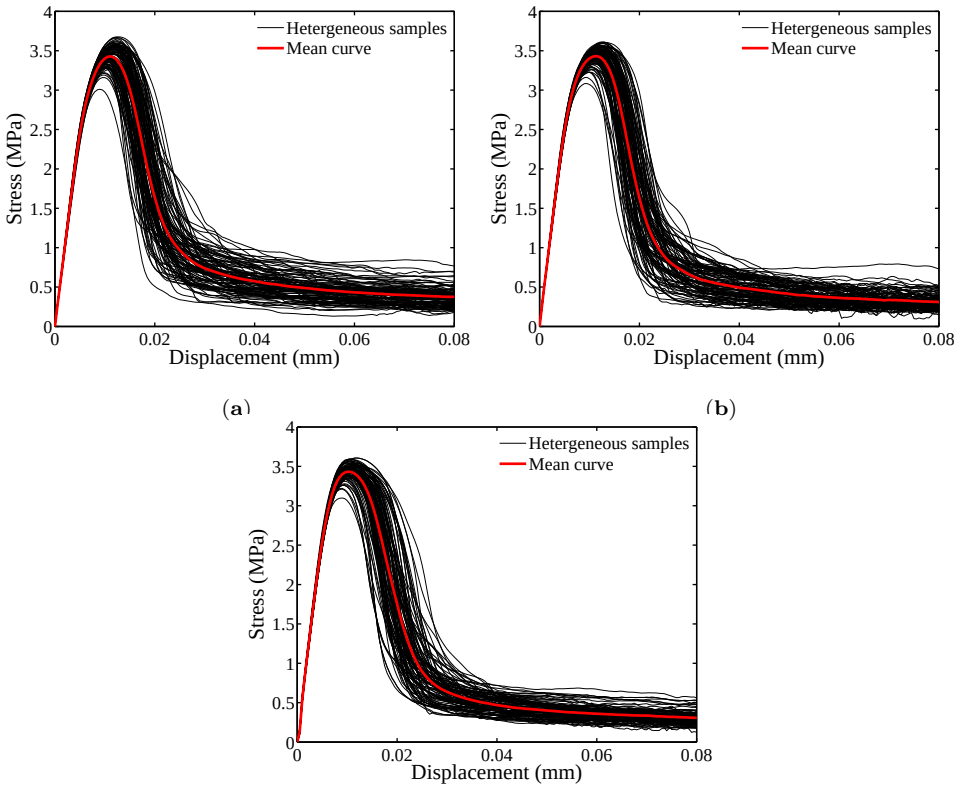
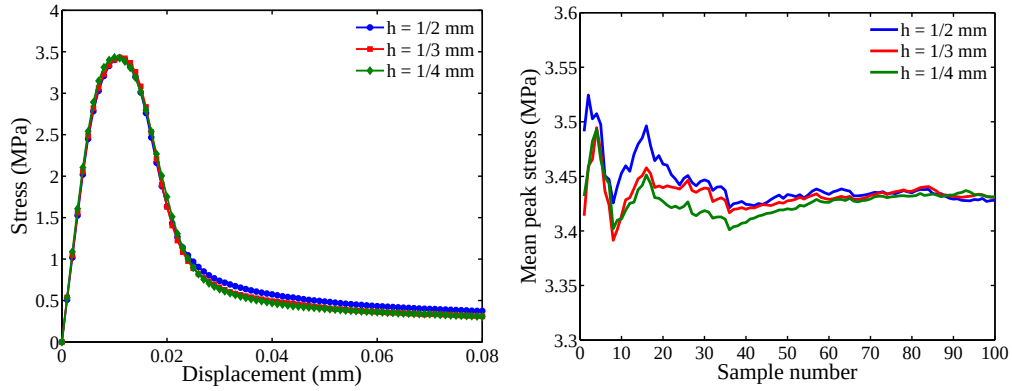


Figure 5.6: Tensile stress versus applied displacement for varying particle spacing. (**a**) $h = 1/2$ mm; (**b**) $h = 1/3$ mm; (**c**) $h = 1/4$ mm.

Figure 5.6 presents the applied displacement versus corresponding tensile stress computed from the mesoscale models for varying particle spacing, h. In the 100 heterogeneous samples, the stress-displacement relationship is highly nonlinear and always includes the linear-elastic and softening parts, regardless of the particle spacing size. However, the residual stresses deviate more from the mean curve for $h = 1/2$ mm (see Figure 5.6a) than those determined when $h = 1/3$ and $1/4$ mm are used (see Figure 5.6b,c). Furthermore, it is clear from Figure 5.7a that the stress converges when the particle spacing of $1/3$ mm or smaller is used. Figure 5.7b indicates that the mean peak stress converges when 70 or more samples are generated for the studied particle spacing. Figure 5.8 illustrates the crack pattern developed for each discretization scheme while aggregate location and position in the specimen remains unchanged. For $h = 1/2$ mm, the damaged area in Figure 5.8a is more extensive than those

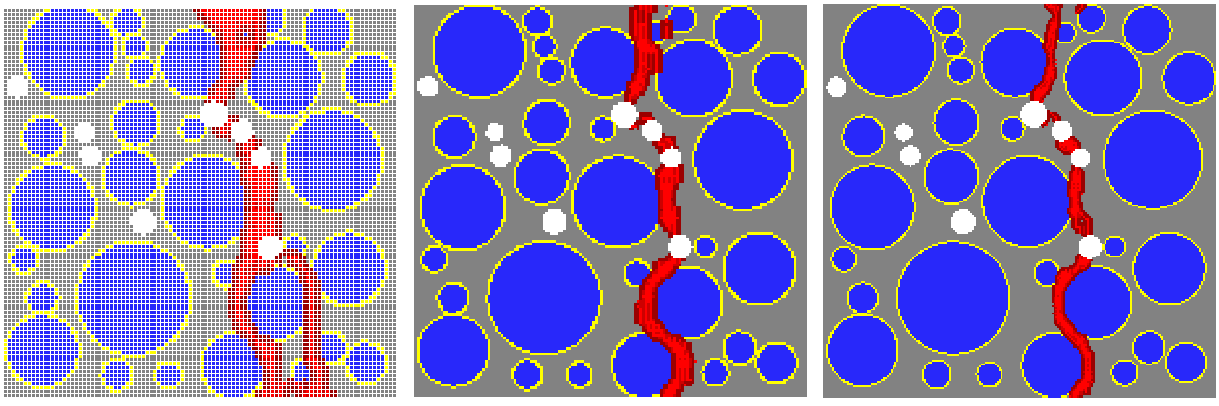
observed in Figure 5.8b,c, which is anticipated because the horizon size increases as the particle spacing increases ($\delta = 3h$) in the proposed model. The damage patterns for $h = 1/3$ and $1/4$ mm are comparable.

In the aggregate placement procedure, a clearance distance from the specimen boundary is given to prevent cracks from initiating at the interface exposed to the surface. Therefore, in the results presented in Figure 5.8, the interface transition zone is not intended to be exposed to the bounding surface.



(**a**) (**b**)

Figure 5.7: Effect of discretization on: (**a**) mean stress-displacement curves; and (**b**) sample number with reference to mean peak stress.



(**a**) (**b**) (**c**)

Figure 5.8: Effect of particle spacing size on crack pattern. (**a**) $h = 1/2$ mm; (**b**) $h = 1/3$ mm; (**c**) $h = 1/4$ mm.

While the stress and damage pattern are effective indicators for convergence, the computational cost is another important factor in determining the particle spacing (or discretization size). Figure 5.9 shows the effect of particle size on the relative simulation time. It is scaled with respect to the simulation time needed for the specimen with $h = 1/3$ mm. The analyses are completed using parallel computing and four processors on a UNIX cluster. The model with the particle size of $1/2$ mm is four-times faster than that with $h = 1/3$ mm, while the computational time decreases by a factor of 2.3 when the mesoscale model is discretized with $h = 1/3$ mm, when compared to the model with $h = 1/4$ mm. Therefore, based on stress convergence, damage patterns and the relative computational cost for the remaining study, mesoscale models are generated with the particle spacing of $1/3$ mm and sample size of 100.

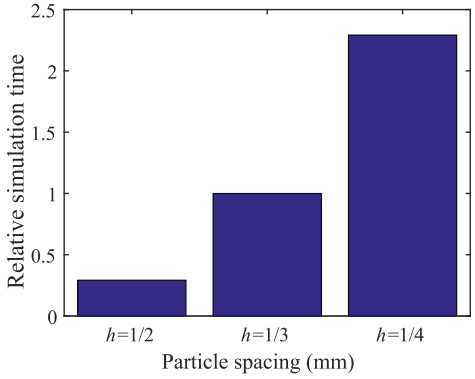
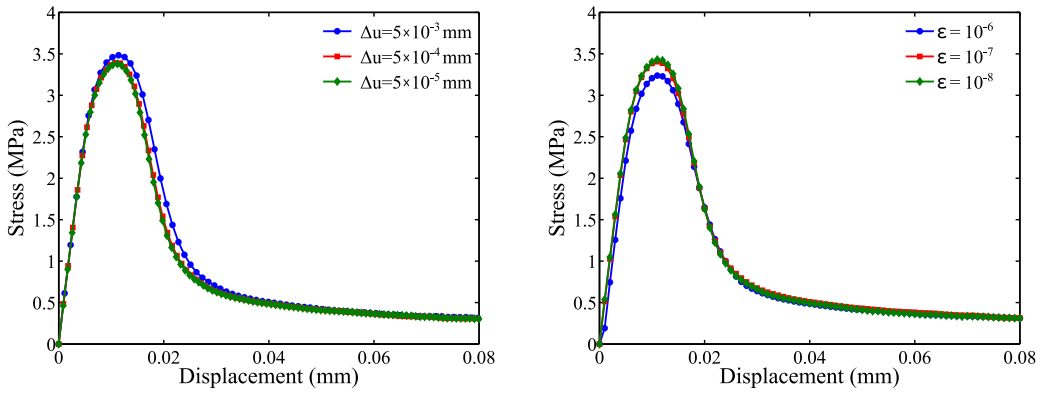


Figure 5.9: Effect of discretization on simulation time.

5.4.2 Effect of Loading Increment and Dynamic Relaxation Threshold

To obtain the implicit solutions for a quasi-static peridynamic equilibrium equation (Equation (6.5)), an incremental and iterative method is developed. For a displacement state of δu, the dynamic relaxation method is adopted to iteratively update the displacement field, u, until $||\delta u|| < \varepsilon$, where ε is a small numerical cut-off. Therefore, the steady-state solver parameters include the displacement loading increment, Δu, and dynamic relaxation threshold, ε. The effect of these two parameters on the accuracy and convergence of the analysis results is studied. Three displacement loading increments, Δu, of 5×10^{-3} mm, 5×10^{-4} mm, and

5×10^{-5} mm, are considered with a fixed value of $\varepsilon = 10^{-7}$. As shown in Figure 5.10a, the stress results converge when Δu of 5×10^{-4} mm or smaller is used.



(**a**) (**b**)

Figure 5.10: Effect of (**a**) the displacement loading increment and (**b**) the dynamic relaxation threshold on the mean stress curve.

The effect of the dynamic relaxation (DR) threshold, ε, on the analysis results is investigated. Three values of 10^{-6}, 10^{-7} and 10^{-8} are considered for ε with a fixed $\Delta u = 5 \times 10^{-4}$ mm. The stress appears to converge when ε becomes 10^{-7} or smaller. Furthermore, the effect of these two variables on the relative simulation time is shown in Figure 5.11a,b, respectively. It is observed that the simulation time is highly (by a factor of six) affected by the change in the displacement loading increment, whereas the simulation time increases by 40%–50% when the dynamic relaxation threshold increases by a factor of ten.

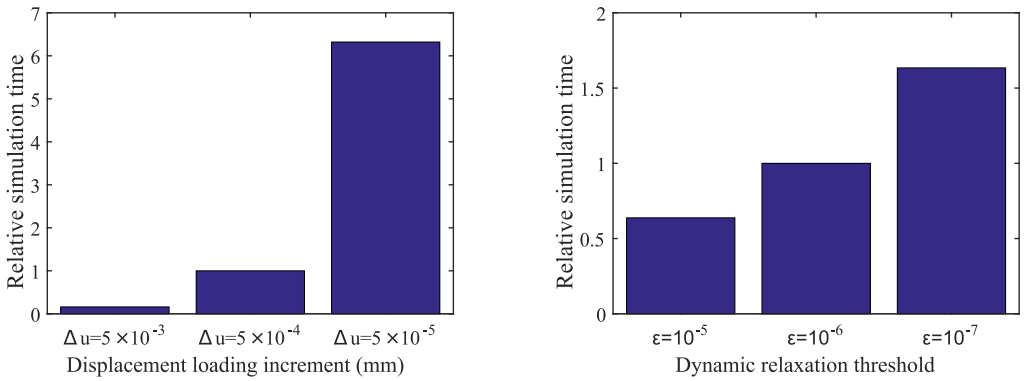


Figure 5.11: The effect of (**a**) the displacement loading increment and (**b**) the dynamic relaxation threshold on the simulation time.

5.4.3 Comparison with Available Finite Element Analysis Results

Based on the convergence study presented in Sections 5.4.1 and 5.4.2, the mesoscale model is analyzed with the following two parameters: Δu of 5×10^{-4} mm and ε of 10^{-7}, in conjunction with the particle spacing of 1/3 mm and sample size of 100. The analysis results are compared with the cohesive FEM results produced by Wang et al. [111] as shown in Figure 5.12.

Figure 5.12 indicates that the mesoscale model analyzed in the proposed peridynamics analysis framework yields similar results to the two-dimensional FEA results. This result is remarkable because Wang et al. [111] used multiple levels of mesh refinement and complex damage models to obtain the FEM results, whereas the proposed mesoscale model including four phases is relatively simple to generate, and the bonds between material particles are defined by simple damage models (see Section 5.3.2). The experimental results [127] are provided in Figure 5.12 as a point of reference and are discussed in Section 5.6.

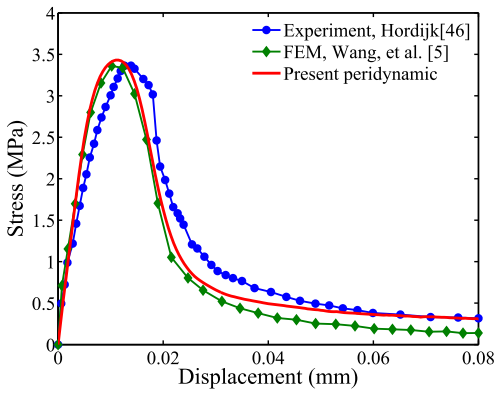


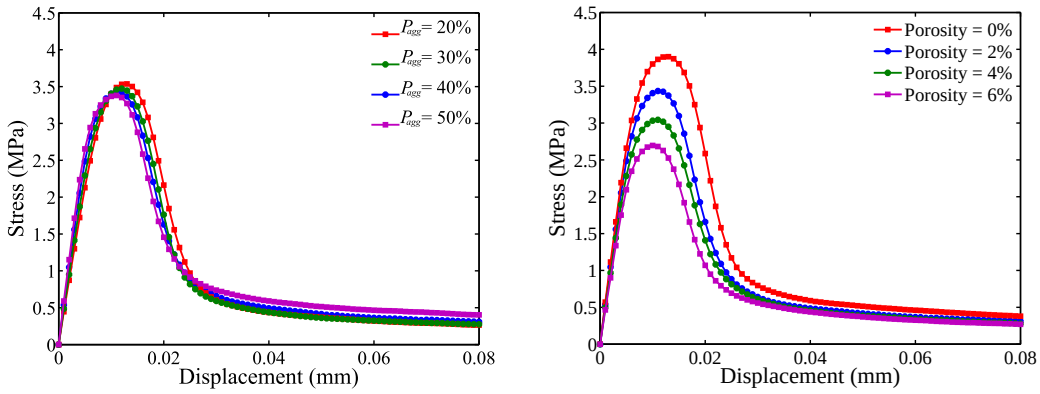
Figure 5.12: Comparison with experimental and available FEM results.

5.5 Sensitivity Study

This section includes the sensitivity analysis capability of the proposed mesoscale model. Two variables, aggregate volume and porosity, are considered to study the effect of the variables on the stress results, although no experimental results are available to validate such analysis.

5.5.1 Effect of Aggregate Volume Fraction

Four coarse aggregate volume fractions, P_{agg}, of 20%, 30%, 40% and 50% are studied with a constant porosity, $P_{pore} = 2\%$. For each of the four cases, 100 samples are studied to best represent the heterogeneous material phases. Figure 5.13a provides the stress-displacement relationship. The initial slope increases in the linear elastic region as the aggregate volume increases; however, the peak stress decreases due to increased ITZ resulting from increased aggregate volume, where the tensile strength is significantly lower than other materials. For the parameters studied herein, it is concluded that the peak load carrying capacity is reduced by increased aggregate volume. In general, the load carrying capacity may or may not increase [128–130], depending on the mix-design of cement paste and aggregate type selected.



(**a**) (**b**)

Figure 5.13: Effect of (**a**) aggregate volume fraction, P_{agg}, and (**b**) porosity, P_{pore}, on the mean stress curve.

5.5.2 Effect of Porosity

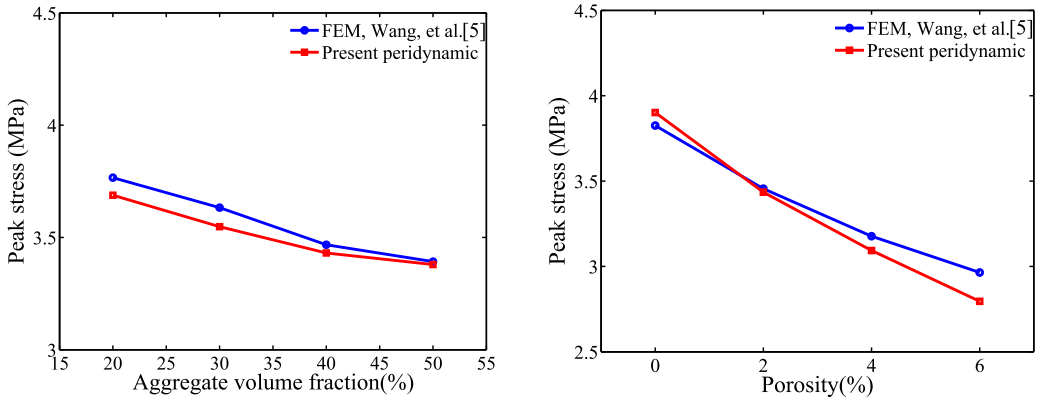
Porosity, P_{pore}, of 2%, 4% and 6% is considered to study the effect of air void content on the stress-displacement relationship. For each of the contents studied, 100 samples are analyzed with a constant coarse aggregate volume fraction, $P_{agg} = 40\%$. Both the linear elastic modulus and peak load decrease as the porosity increases as shown in Figure 5.13b.

5.5.3 Comparison with the FEM Results and Damage Patterns

Figure 5.14 shows a comparison of the sensitivity study results from the proposed mesoscale approach and FEM. The results are in good agreement despite the fact that considerably different analysis methods and material models are used in the mesoscale model. Figures 5.15–5.21 present selected samples showing the crack patterns from the 100 samples used in the sensitive study. Seven selected cases corresponding to the four coarse aggregate volume fractions and four air contents are presented in the figures. It is concluded from this sensitivity study that the damage pattern is highly dependent on the distribution of the coarse aggregate and air voids and that one or two discrete cracks develop in the tensile specimen. It is also concluded from the proposed mesoscale model that the air voids and ITZs play an essential

role in defining a crack path, which is not surprising, because they are the two weakest elements in the multiphase materials.

In Figures 5.15–5.21, microscopic cracks, represented by damaged points in this model and thus invisible in these figures, originate from the interface zone. The weakest area involves increased numbers of air voids and interface zones. These micro-scale cracks coalesce, and the resulting mesoscale crack, which is visible in these figures, grows into the boundaries. As observed in the crack patterns, positioning an air void close to the surface does not always warrant a crack initiation.



(**a**) (**b**)

Figure 5.14: Mean peak stress for varying (**a**) aggregate volume fraction, P_{agg}, and (**b**) porosity, P_{pore}.

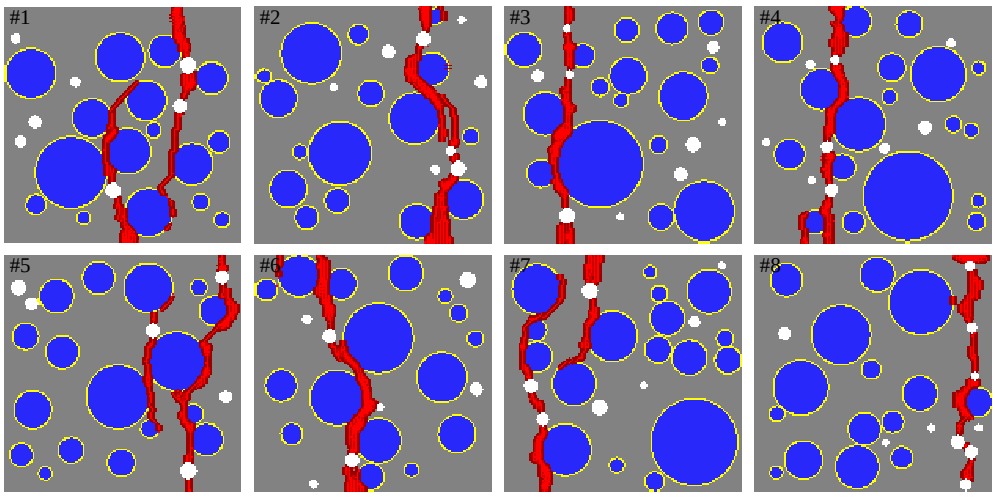


Figure 5.15: Crack pattern for selected specimens with $P_{pore} = 2\%$ and $P_{agg} = 20\%$.

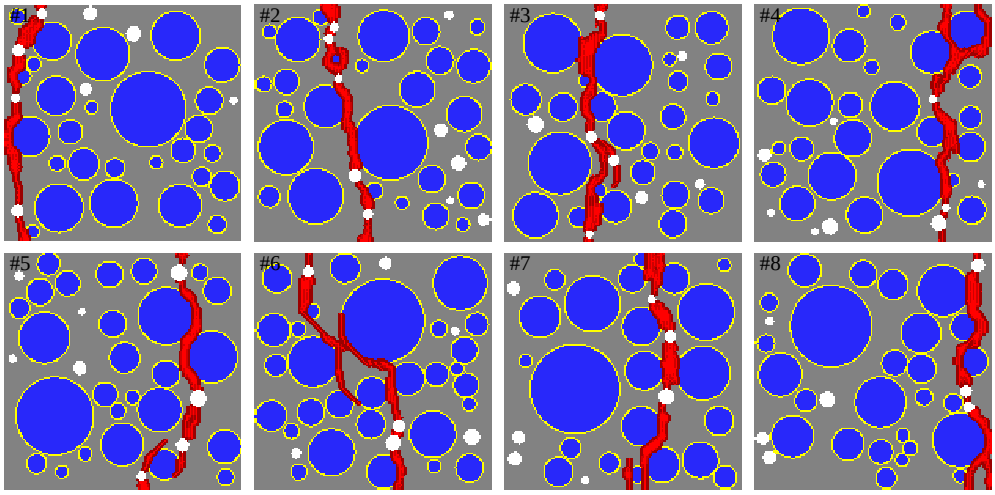


Figure 5.16: Crack pattern for selected specimens with $P_{pore} = 2\%$ and $P_{agg} = 30\%$.

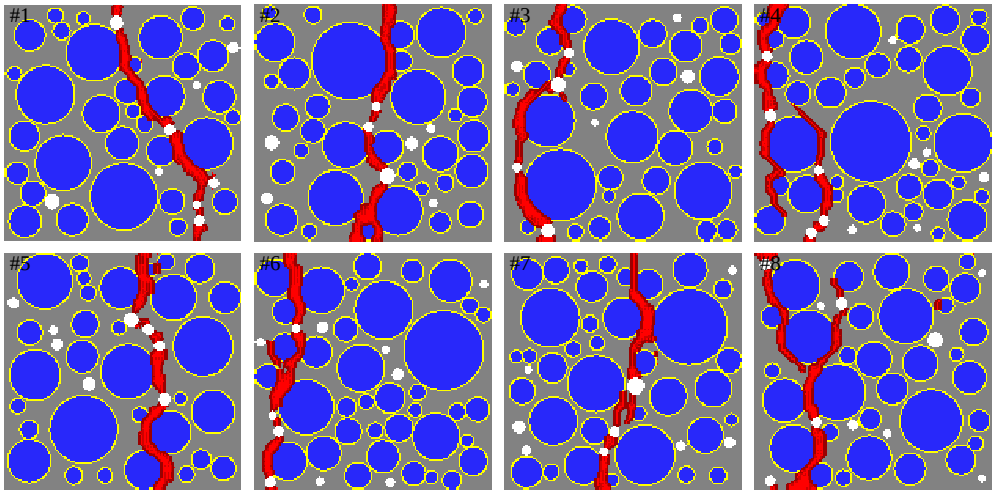


Figure 5.17: Crack pattern for selected specimens with $P_{pore} = 2\%$ and $P_{agg} = 40\%$.

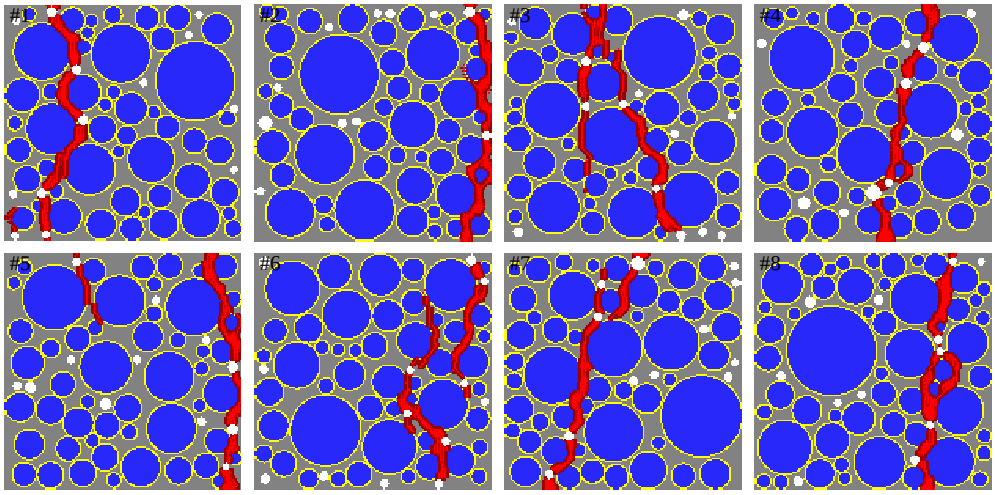


Figure 5.18: Crack pattern for selected specimens with $P_{pore} = 2\%$ and $P_{agg} = 50\%$.

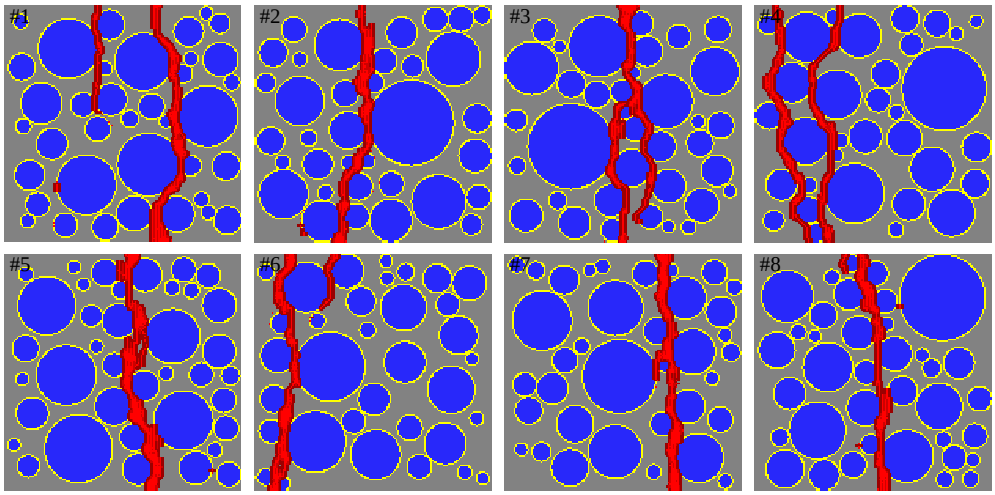


Figure 5.19: Crack pattern for selected specimens with $P_{pore} = 0\%$ and $P_{agg} = 40\%$.

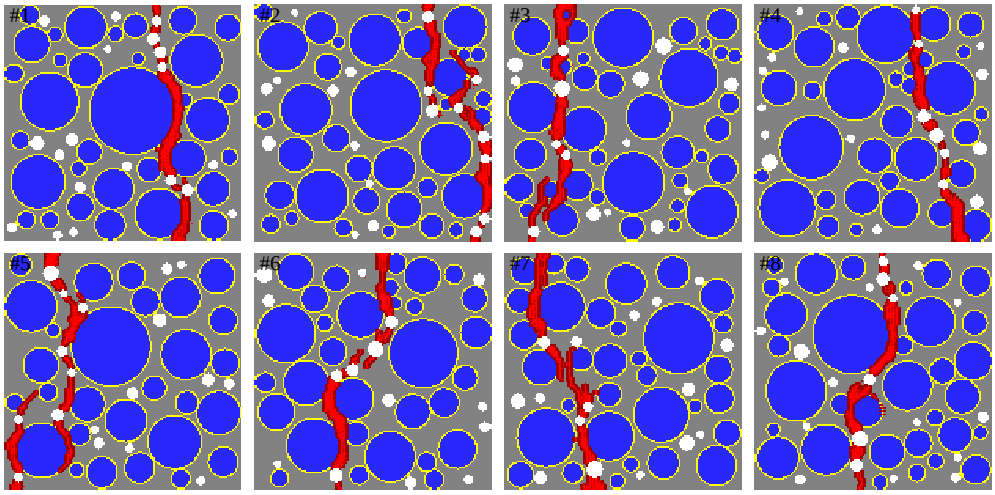


Figure 5.20: Crack pattern for selected specimens with $P_{pore} = 4\%$ and $P_{agg} = 40\%$.

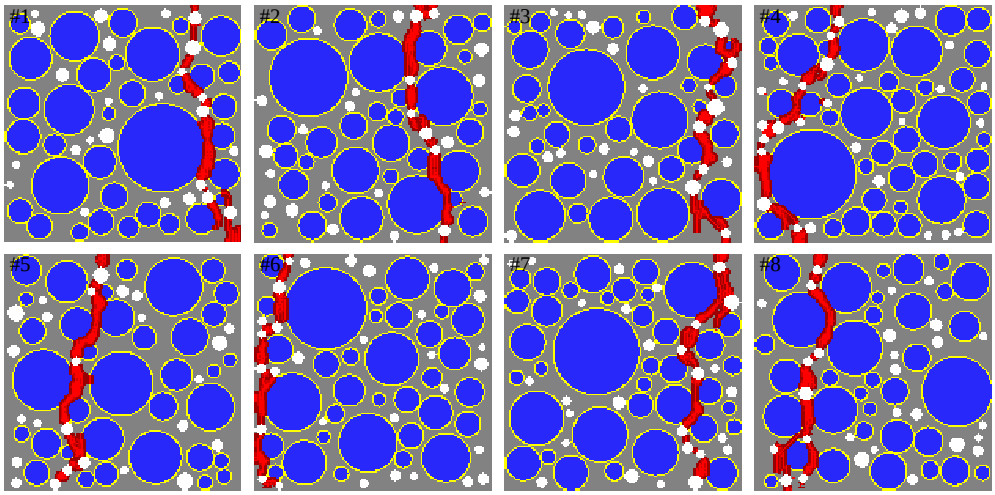


Figure 5.21: Crack pattern for selected specimens with $P_{pore} = 6\%$ and $P_{agg} = 40\%$.

5.6 Discussion

The stress-displacement curves agree well with available two-dimensional FEM results with the following limitations: (1) the numerical model includes the two-dimensional planar fracture assumption; (2) statistically-determined aggregate/air void distributions, which are physically different from the experimental specimen. Therefore, the experimental comparison only has qualitative meaning. The accuracy of the analysis is quantified by a comparison with

the two-dimensional FEM results of Wang et al. [111]. It is also important to note that no damage is assumed to occur between the material points in an aggregate. This is attributed to a simple elastic material model used to represent the aggregate material. Therefore, in this model, cracks are not able to go through the aggregates because the elastic strength of aggregate is higher than that of the cement paste.

Mesoscale modeling of cementitious composites is challenging due to heterogeneous material constituents and the highly complex cracking mechanism. While the proposed approach builds a distinct framework for fracture analysis of concrete specimens, future work includes the implementation of the following features and tools for:

1. Studying the influence of particle shape and surface texture of the coarse aggregate.

2. Refinement in particle spacing and/or horizon size in ITZs to reduce the computational time while providing accuracy.

3. Enhancing material models and damaged parameters for complex loading conditions, such as shear.

4. Extending the proposed analysis approach to three-dimensional (3D) models in which, for instance, non-planar (or 3D) fracture surfaces are characterized.

5. Advanced computational techniques to optimize computational expense.

While the proposed mesoscale model is well suited to predict the fracture mechanism, comprising bond failure and crack initiation/propagation at the mesoscale, practical applications of this model may involve developing a successful coupling approach using both mesoscale and finite element modeling methods, in which concrete structures are practically characterized by finite elements. For the proposed approach to be pragmatic, the finite element model will need to be selectively refined using the multiscale coupling approach discussed in Section 5.1.4, which characterizes the mesoscale damage in a selected region.

5.7 Conclusions

The macroscale description of fracture behavior in cementitious composites is highly dependent on the heterogeneous constituent materials at a mesoscopic level. Therefore, it is important to characterize such a fracture mechanism in mesoscopic materials by using effective numerical techniques. In this study, it is found that mesoscale modeling of concrete members in a non-ordinary peridynamics analysis framework is highly effective for fracture analysis. The stress-displacement curves agree well with available experimental results and FEM results. The simple two-dimensional mesoscale model generated in peridynamics is well suited to understand the effect of gradation, aggregate distribution and proportions of constituent materials, as well as to predict the fracture mechanism, comprising bond failure and crack initiation/propagation at the mesoscale. The following conclusions are made by examining the results of this analytical study:

1. The results indicate that particle spacing affects the stress convergence, as well as crack patterns. For the tensile loading condition considered herein, the particle spacing of 1/3 mm provides the most effective discretization with a reasonable computational effort.

2. The results of the mesoscale analysis show that the simulation time is sensitive to the displacement loading increment used for dynamic relaxation. Based on the analysis results reported in this paper, the optimal displacement increment and DR threshold is 5×10^{-4} mm and 10^{-7}, respectively, for tensile loading.

3. By means of interfacial transition zones (ITZs) characterized in the proposed mesoscale model, it is capable of reflecting the effect of varying coarse aggregate volume fractions on the load carrying capacity.

4. It is concluded that the strength reduction due to increased air content is reflected in the proposed model, by removing particle points from the areas of voids.

5. Finally, in the proposed mesoscale peridynamics analysis, it is possible to identify a statistically-significant sample size for reasonably representing coarse aggregate gradation and distribution and to predict the fracture mechanism in concrete specimens.

Chapter 6

Formulation of symmetry boundary modeling in non-ordinary state-based peridynamics and coupling with FEA[1]

[1]A. Yaghoobi and M. G. Chorzepa. "Formulation of symmetry boundary modeling in non-ordinary state-based peridynamics and coupling with FEA." Accepted by Mathematics and Mechanics of Solids. Reprinted here with permission of publisher, 2017

ABSTRACT

Peridynamics is an effective method in computational solid mechanics for dealing with discontinuities. However, its computational cost limits its applications, especially when used in the most general form, non-ordinary state-based peridynamics. This paper considers two approaches which decrease the computational cost. The first approach accounts for symmetry boundary conditions in a peridynamic body. In nonlocal peridynamics, boundary conditions are applied to an area. Therefore, to model symmetry boundary condition, assuming fixed particles around the symmetry axis yields to incorrect results. The present formulation introduces constraints which allow modeling local symmetry conditions. Second, the finite element-peridynamic coupling method is adopted to non-ordinary state-based peridynamics. The coupling method enables using peridynamics around discontinuities like cracks, and the faster finite element for the surrounding body. These two methods effectively reduce the solution time with an acceptable accuracy. The validity of these approaches is studied through various examples. Also, ductile crack growth in a compact tension specimen is studied applying the presented methods. Good agreement is found when comparing experimental results with corresponding numerical results obtained using either fully peridynamic or coupled models.

6.1 Introduction

Local models in continuum mechanics assume that the stress at a local (or selected) point depends on the deformation of the point, whereas non-local models account for the state of the entire body to determine the stress [131]. The development of nonlocal models was motivated by the need to: 1) Capture small deviations from local continuum models resulting from material heterogeneity 2) Achieve convergence 3) Establish the boundary value problem on a correct basis; and 4) Capture size-effects observed in experiments and discrete simu-

lations [131]. A great variety of nonlocal models have emerged during the last two decades and have enabled modeling of damage and plastic flow in materials.

Peridynamics introduced by Silling [15] is one of the nonlocal mesh-free methods which reformulate the classical continuum mechanics by substituting the governing partial differential equations with integral equations. Therefore, the peridynamics equation of motion is valid everywhere despite the presence of cracks and other discontinuities. Peridynamics has undergone significant changes since first proposed. When first introduced, so called bond-based peridynamics (BBPD) was proposed. It considered independent central interaction forces between any pair of material particles. As a consequence of this assumption, the bond-based method was restricted to a fixed value of Poisson's ratio (ν=1/4) [16, 30]. Due to this limitation, BBPD had lost its credence for modeling material response such as plasticity. Subsequently, non-ordinary state-based peridynamics (NOSBPD) has gained popularity and become the most general form of peridynamics which allows material particle bonds to transfer loads in all directions [28, 36]. Therefore, the NOSBPD can represent material behavior with any Poissons ratio. Furthermore, the bond forces in the NOSBPD are defined by stress tensors. For this reason, the classical constitutive equations and failure criteria can be implemented in the NOSBPD analysis framework [29, 40–42].

The methodology by which boundary conditions are applied in the peridynamics is somewhat different from the classical continuum mechanics' approach. In the classical mechanics, the boundary condition, called "natural or traction boundary conditions", is applied on the surface of the body. For example in the finite-element method, they are applied only on the nodes at the boundary[16, 132]. The equation of motion for a peridynamic particle is described as a volume integral over all particles within a finite distance from the particle, rather than determining the local value resulting from spatial derivatives of a stress field. Therefore, the application of boundary condition, either forces or displacement conditions, simply on the boundary similar to the classical mechanics approach is not sufficient since their volume integrations result in a zero value [133]. Consequently, in peridynamics, a boundary

condition must be applied on a volume, [134]. When symmetric boundary modeling is used in peridynamics, the application of forces or displacements over a fixed volume of material, rather than on a fixed surface, interferes modeling symmetry boundary conditions. Therefore, a special treatment is required to model symmetry in nonlocal peridynamics.

The peridynamics theory is valid at discontinuities and it is able to predict and model damage initiation and growth without additional failure criteria. However, it is computationally more demanding compared to the finite element method [102]. Therefore, several approaches are introduced to couple the peridynamic theory and the finite element method in order to take the advantages of the generality of the peridynamic and effectiveness of the finite element method (FEM). They all share the main idea that the region with a discontinuity is analyzed using peridynamic particles while the finite element method is utilized for the remaining region. The sub-region modeling approach utilized by Oterkus et al. [135] and Agwai et al. [136]. In their approach, the global system is first analyzed using the FEM. Subsequently, the PD is employed to perform a failure analysis in a sub-domain where the failure was anticipated. Macek and Silling [132] implemented a PD model in a conventional finite element analysis (FEA) code using truss elements and thus suggested a FEM-BBPD coupling approach. This approach utilizes traditional truss elements to couple peridynamic particles and FEM nodes. A morphing technique was proposed by Lubineau et al. [137] to couple local and nonlocal theories. A transition (morphing) zone is introduced in which the constitutive parameters are affected. Then, an unified model is introduced to represent both local and nonlocal continuum models. Depending on the constitutive parameters, the model can cover completely non-local, local, or the transition (hybrid) region. The morphing approach was utilized for anisotropic continua [138] and in coupling state-based peridynamics with the classical continuum mechanics method by Han et al. [139].

Seleson et al. [140] proposed a force-based model that coupled the PD theory and classical elasticity. They used nonlocal weights composed of integrals of coupling functions. A generalized form of this method was also provided for coupling peridynamics and higher-

order gradient models. The coupling approach proposed by Kilic and Madenci [133] solved the equation of the motion for FEM and the PD systems simultaneously. To do so, an overlap region must be introduced where both peridynamic and the finite element equations of motion are satisfied in this region. The displacement and the velocity fields of the overlap region is obtained from the FEM system of equation, while the body force obtained from the PD system in the overlap region is applied to the FEM system as the external forces. Another coupling approach is proposed by Liu and Hong [76]. In their approach, bond-based peridynamics and the finite element are coupled by introducing interface elements which surrounds the PC sub-region. To provide the coupling, additional peridynamic particles are embedded in the interface elements. The interface elements and embedded peridynamic particles share the same kinematics, and therefore, the deformation of the embedded particles are determined by an interpolation of the nodal deformation of the interface elements, not through the peridynamic equation of motion. The force exerted in the embedded particles are distributed to the nodes of the interface elements to determine the interpolated deformation. In other words, coupling was completed the PD subregion by applying the displacement boundary condition to the embedded particles, and also performed on the FEM region by applying coupling forces on nodes of the interface element. In this approach, the equation of motion of two regions are solved independently in each time step. Furthermore, two approaches are investigated in distributing the embedded forces to the nodes. In the first approach, the force are distributed to all nodes of the interface element, while in the second method, the force is distributed to nodes located on the interface plane between FEM and PD regions.

This paper presents two approaches in order to decrease the computational expense of the non-ordinary state-based peridynamic analysis. The first method is the symmetry boundary modeling approach which halves the solution time of a symmetric body. The method introduces symmetry particles where their kinetics are obtained through symmetry rules. The accuracy of the approach is studied through 1D and 2D symmetric models in Sections 6.5.1 and 6.5.2, respectively. The results show good agreement with both exact solutions and fully

peridynamic solutions, whereas 'fixed' boundary models fail to secure the accuracy near the symmetry axis. In the other approach, the interface element coupling method is adopted to couple the non-ordinary state-based peridynamics and the finite element methods. The proposed coupling model enhances the accuracy by using peridynamics around discontinuities, while the faster FE method is utilized to model the remaining body for efficiency. The calibration of the coupling model is performed using a 2D plate under tension in Section 6.5.3, and the method is tested through a 2D notched plate in Section 6.5.4. A Compact Tension (CT) specimen model is used in Section 6.5.5 to study the performance of the presented symmetry boundary and coupling models together in a brittle crack growth study. The combination of these two approaches significantly reduces the execution time, while the accuracy is assured.

6.2 Formulation

6.2.1 Non-ordinary state-based peridynamics

This section provides the background knowledge on the non-ordinary state-based peridynamics theory. Refer to Silling's work [28] for further details on formulations and their derivatives. Peridynamics is a reformulation of the classical continuum mechanics substituting integral equations for spatial differential equations. The integral equations used in peridynamics are valid in presence of discontinuities such as cracks. In the peridynamics framework, the material particle located at $\mathbf{x}$, interacts with other particles, around the particle $\mathbf{x}$, within a finite distance, δ. The interaction between particles is referred to as a "bond", and the area of influence is represented by the "horizon", $\mathcal{H}$. Its radius is defined by the "horizon size", δ. The rigid body in reference is defined by '$\mathbf{B}_0$' and the deformed body, '$\mathbf{B}$' is illustrated in Fig. 6.1.

In the undeformed body $\mathbf{B}_0$, the relative position of two particles $\mathbf{x}$ and $\mathbf{x}'$, is represented by a position vector-state and defined as:

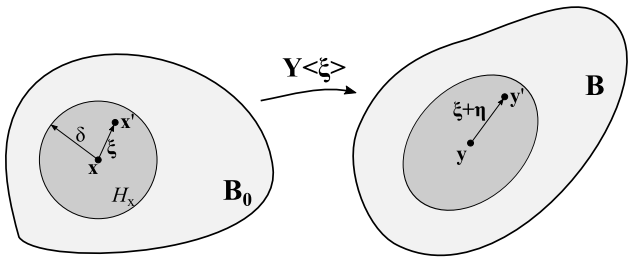


Figure 6.1: Configuration of a continuum body in the Peridynamics framework.

$$\mathbf{X}\langle \mathbf{x}' - \mathbf{x} \rangle = \boldsymbol{\xi} = \mathbf{x}' - \mathbf{x} \tag{6.1}$$

The deformed configuration of the position vector-state in the deformed body $\mathbf{B}$, is defined by the deformation vector-state, $\mathbf{Y}$:

$$\mathbf{Y}\langle \mathbf{x}' - \mathbf{x} \rangle = \boldsymbol{\xi} + \boldsymbol{\eta} = \mathbf{y}' - \mathbf{y} \tag{6.2}$$

where $\boldsymbol{\eta} = \mathbf{u}' - \mathbf{u}$ is the relative displacement of particles $\mathbf{x}$ and $\mathbf{x}'$; $\mathbf{u}$ and $\mathbf{u}'$ are the displacements of the particles $\mathbf{x}$ and $\mathbf{x}'$, respectively. The deformation vector-state, $\mathbf{Y}$, in the non-ordinary state-based peridynamics, plays the same role as the deformation gradient tensor, $\mathbf{F}$, used in the classical continuum mechanics and thus defines the material constitutive relationship. However, to incorporate classical continuum mechanics constitutive equation in terms of $W(\mathbf{F})$, where W is the strain energy, Silling [28] defined the nonlocal approximation for the deformation gradient tensor as follows:

$$\mathbf{F}(\mathbf{x}) = [\int_{\mathcal{H}_{\mathbf{x}}} \omega(\xi)\,[(\mathbf{y}' - \mathbf{y}) \otimes (\mathbf{x}' - \mathbf{x})]\mathrm{d}V_{\mathbf{x}'}] \cdot \mathbf{K}^{-1} \tag{6.3}$$

where ω is the weight function which depends only on the distance between two particles or bond size, $\xi = |\boldsymbol{\xi}|$. $\otimes$ denotes the dyadic product, and $\mathrm{d}V_{\mathbf{x}'}$ represent a finite volume of the particle $\mathbf{x}'$. $\mathbf{K}$ is a shape tensor, determined by Eq. (6.4), at particle $\mathbf{x}$:

$$\mathbf{K}(\mathbf{x}) = \int_{\mathcal{H}_\mathbf{x}} \omega(\xi)\left[(\mathbf{x}' - \mathbf{x}) \otimes (\mathbf{x}' - \mathbf{x})\right] \mathrm{d}V_{\mathbf{x}'} \tag{6.4}$$

In the quasi-static loading condition, the conservation of the linear momentum for the peridynamic body, $\mathbf{B}$, under the body forces of $\mathbf{b}$ is expressed as follows:

$$\int_{\mathcal{H}_\mathbf{x}} \left(\mathbf{T}[\mathbf{x}]\langle \mathbf{x}' - \mathbf{x}\rangle - \mathbf{T}[\mathbf{x}']\langle \mathbf{x} - \mathbf{x}'\rangle\right) \mathrm{d}V_{\mathbf{x}'} + \mathbf{b}(\mathbf{x}) = \mathbf{0} \tag{6.5}$$

The force vector-state, $\mathbf{T}$, can be obtained from:

$$\mathbf{T}[\mathbf{x}]\langle \mathbf{x}' - \mathbf{x}\rangle = \omega(\xi)\, \boldsymbol{\sigma} \cdot \mathbf{K}^{-1} \cdot (\mathbf{x}' - \mathbf{x}) \tag{6.6}$$

$\boldsymbol{\sigma} = \partial W / \partial \mathbf{F}$ is the first Piola-Kirchhoff stress. For an isotropic elastic material with small strain tensor of $\boldsymbol{\epsilon} = 1/2(\mathbf{F} + \mathbf{F}^T) - \mathbf{I}$, the stress is obtained by $\boldsymbol{\sigma} = \mathbf{C} : \boldsymbol{\epsilon}$, where $\mathbf{C}$ is the isotropic elastic moduli matrix, and $\mathbf{I}$ is the identity matrix.

In the discretized form of the equilibrium equation, the integral of the body force is replaced with a summation of forces from finite volumes:

$$\sum_{j=1}^{n_i} \{\mathbf{T}[\mathbf{x}_i]\langle \mathbf{x}_j - \mathbf{x}_i\rangle - \mathbf{T}[\mathbf{x}_j]\langle \mathbf{x}_i - \mathbf{x}_j\rangle\} \Delta V_j + \mathbf{b}(\mathbf{x}_i) = 0 \tag{6.7}$$

where $\mathbf{x}_j$ denotes a particle within the horizon of the particle $\mathbf{x}_i$, and n_i is the number of particles within the horizon of the particle $\mathbf{x}_i$. The deformation gradient tensor and shape tensor are rewritten as:

$$\mathbf{F}(\mathbf{x}_i) = \left[\sum_{j=1}^{n_i} \omega(|\mathbf{x}_j - \mathbf{x}_i|)\left(\mathbf{Y}\langle \mathbf{x}_j - \mathbf{x}_i\rangle \otimes (\mathbf{x}_j - \mathbf{x}_i)\right) \Delta V_j\right] . \mathbf{K}(\mathbf{x}_i) \tag{6.8}$$

$$\mathbf{K}(\mathbf{x}_i) = \left[\sum_{j=1}^{n_i} \omega(|\mathbf{x}_j - \mathbf{x}_i|)\left((\mathbf{x}_j - \mathbf{x}_i) \otimes (\mathbf{x}_j - \mathbf{x}_i)\right) \Delta V_j\right]^{-1} \tag{6.9}$$

The non-ordinary state-based peridynamics is faced with an instability problem called the zero-energy mode, particularly in regions with high strain gradients. The zero-energy mode is associated with a weak coupling between a material particle and its surrounding particles,

which results in erroneous oscillations in deformation and stress fields [39]. Introducing a viscose term in the peridynamic equation of motion reduces the zero-energy mode oscillation; however, an extra effort is required to control the unwanted oscillations in the solutions. Several methods have been developed by Littlewood [46], Breitenfeld et al. [39] and Wu and Ren [47] to suppress the zero-energy mode. A higher-order approximation can be applied by assigning specific weight functions. Similar approaches are provided in [124] for 1D and 2D discretization. This study uses a higher-order peridynamic approximation for the deformation gradient tensor in order to successfully suppress the zero-energy mode.

6.2.2 Finite element method

The general knowledge on finite element method is provided in this section, insofar as needed in description of the coupling methodology. The steady-state equilibrium satisfying the conservation of linear momentum in the classical continuum mechanics is obtained by eliminating the time dependent acceleration term as shown below:

$$\nabla \cdot \boldsymbol{\sigma} - \mathbf{b} = \mathbf{0} \tag{6.10}$$

where the stress tensor is determined by $\boldsymbol{\sigma} = \mathbf{C} : \boldsymbol{\epsilon}$, and the small strain tensor is $\boldsymbol{\epsilon} = 1/2(\mathbf{F} + \mathbf{F}^T) - \mathbf{I}$, where the deformation tensor is determined by $\mathbf{F} = \nabla \mathbf{u}$. In the finite element analysis method, the domain is discretized into elements, and the displacement field, $\mathbf{u}$, within an element with n nodes is obtained by interpolating the nodal displacements (of elements) by means of shape functions as shown below:

$$\mathbf{u}^e = \mathbf{N}^e \mathbf{U}^e \tag{6.11}$$

where $\mathbf{N}^e$ is the displacement interpolation matrix which includes shape functions of nodes, N_i, and $\mathbf{U}^e$ is the nodal displacement vector:

$$\mathbf{N}^e = \begin{bmatrix} N_1 & 0 & 0 & & N_n & 0 & 0 \\ 0 & N_1 & 0 & ... & 0 & N_n & 0 \\ 0 & 0 & N_1 & & 0 & 0 & N_n \end{bmatrix} \tag{6.12}$$

$$\mathbf{U}^e = \begin{bmatrix} u_1 & v_1 & w_1 & ... & u_n & v_n & w_n \end{bmatrix} \tag{6.13}$$

The shape function is mostly expressed using the coordinates of elements as $N_i = N_i(\hat{\xi}, \hat{\eta}, \hat{\psi})$. The sign $\hat{()}$ distinguishes FEM symbols from similar symbols used in peridynamics. The strain vector is evaluated by Eq. (6.14), where $\mathbf{B}^e = \mathbf{D}^e\mathbf{N}^e$ and $\mathbf{D}^e$ is the matrix consisting of the derivative operations.

$$\boldsymbol{\epsilon}^e = \mathbf{B}^e\mathbf{U}^e \tag{6.14}$$

$$\mathbf{D}^e = \begin{bmatrix} \frac{\partial}{\partial x} & & \\ & \frac{\partial}{\partial y} & \\ & & \frac{\partial}{\partial z} \\ \frac{\partial}{\partial y} & \frac{\partial}{\partial x} & \\ & \frac{\partial}{\partial z} & \frac{\partial}{\partial y} \\ \frac{\partial}{\partial z} & & \frac{\partial}{\partial x} \end{bmatrix} \tag{6.15}$$

In the finite element analysis method, the element stiffness matrix is obtained by Eq. (6.16), and in a discretized body, the weak form formulation for the conservation of linear momentum (Eq. 6.10) takes the form of Eq. (6.17), where $\mathbf{K}^g = \Sigma_e \mathbf{K}^e$ is the general stiffness matrix assembled from the element stiffness matrices; $\mathbf{U}^g$ and $\mathbf{F}^g_{ex}$ are the nodal displacement vector and external force vector (including body and surface forces), respectively.

$$\mathbf{K}^e = \int_{V^e} \mathbf{B}^e\mathbf{C}^e\mathbf{B}^e \mathrm{d}V^e \tag{6.16}$$

$$\mathbf{K}^g\mathbf{U}^g = \mathbf{F}^g_{ex} \tag{6.17}$$

6.2.3 Dynamic relaxation method

Dynamic relaxation is an explicit iterative method to obtain the steady-state solution of continuum mechanics problems. Consider a deformed body in its equilibrium state, $\mathbf{F}_{in}(\mathbf{U}) = \mathbf{F}_{ex}$, where $\mathbf{U}$ is the displacement vector. Dynamic relaxation introduces artificial mass and damping terms to the equilibrium equation as: $\mathbf{M}^{DR}\ddot{\mathbf{U}} + \mathbf{C}^{DR}\dot{\mathbf{U}} + \mathbf{F}_{in}(\mathbf{U}) = \mathbf{F}_{ex}$. Thus, the steady-state solution of the resulting dynamic equations is the same as the solution of the original quasi-static system. $\mathbf{M}^{DR}$ is the artificial mass matrix and its diagonal elements, m_{ii}, are determined by Eq. (6.18) [125]:

$$m_{ii} \geq \frac{1}{4}(\tau^n)^2 \sum_j |k_{ij}| \tag{6.18}$$

where τ^n is the pseudo time increment of the nth iteration. k_{ij} is the element of system stiffness matrix $\mathbf{K}^{DR} = \partial \mathbf{F}_{in}(\mathbf{U}) / \partial \mathbf{U}$.

The NOSBPD expression for the system stiffness matrix is given by Yaghoobi and Chorzepa [40]. For the FE system, the global matrix $\mathbf{K}^g$ in Eq. (6.17) represents the system stiffness matrix $\mathbf{K}^{DR}$. The artificial damping matrix is assumed to be proportional to the mass matrix at each pseudo time increment as $\mathbf{C}^{DR} = c^n \mathbf{M}^{DR}$, where c^n is given by Underwood [125]:

$$c^n = 2\{\frac{(\mathbf{U}^n)^T \mathbf{F}_{in}(\mathbf{U}^n)}{(\mathbf{U}^n)^T \mathbf{M}^{DR}\mathbf{U}^n}\}^{1/2} \tag{6.19}$$

Therefore, with residual of $\mathbf{R}^n = \mathbf{F}_{in}(\mathbf{U}^n) - \mathbf{F}_{ex}$, the central difference scheme with respect to pseudo time is employed to determine the displacement vector for each time interval:

$$\dot{\mathbf{U}}^{n+(1/2)} = \frac{2 - \tau^n c^n}{2 + \tau^n c^n}\dot{\mathbf{U}}^{n-(1/2)} + \frac{2\tau^n}{2 + \tau^n c^n}\left(\mathbf{M}^{DR}\right)^{-1}\mathbf{R}^n \tag{6.20}$$

$$\mathbf{U}^{n+1} = \mathbf{U}^n + \tau^{n+1}\dot{\mathbf{U}}^{n+(1/2)} \tag{6.21}$$

The iteration will performed until the error reach an acceptable value, $||\mathbf{U}^{n+1} - \mathbf{U}^n|| < \gamma$, where γ is a maximum allowable error, called "dynamic relaxation cut-off".

6.3 Symmetry boundary modelling

In the finite element analysis method, the boundary conditions including either constraints or loads are applied on the boundary surface (a node in 1D, a line in 2D and an area in 3D) [68]. However, in a nonlocal peridynamic analysis framework, the boundary conditions are applied to particles within a specified distance from the boundary. The distance usually is taken to be equal to or bigger than the horizon size used for the model developed in peridynamics. It is reasonable to apply constraints or loading conditions on the area of the boundary. However, this makes it difficult to model symmetry boundary conditions. The work dealing with symmetry boundary conditions in a peridynamic framework has not appeared to be investigated. The present work considers the symmetry boundary condition using a consistent quadrilateral discretization pattern. Consider a peridynamic body with a symmetry. Due to the symmetry, only half the body is depicted in Fig. 6.2. The symmetric plane, $Plane-23$ is shown in Fig. 6.2. In the figure, the axis of symmetry is defined in the direction normal to the plane of symmetry. Therefore, for the body presented in Fig. 6.2, the positive direction of symmetry is represented by $Axis-1$. To model the symmetry boundary, it is proposed to include a set of particles, refer to as 'symmetry particles' in this study, as shown in Fig. 6.2. For the particle $\mathbf{x}$ within a finite distance (e.g., horizon size, δ) from the plane of symmetry, a corresponding symmetry particle, $\mathbf{x}^s$, is located where $(x_1^s, x_2^s, x_3^s) = (-x_1, x_2, x_3)$ with the symmetry direction of $Axis-1$.

The required components for computation, including deformation state, shape tensor, and deformation gradient tensor, are determined for symmetry particles from their corresponding body particles using symmetry rules. In a similar manner, the strain and stress tensors are obtained using symmetry rules. This way, the symmetry particles are not included in the global equilibrium equation. However, they are considered to evaluate the shape tensor (Eq. 6.4), and the deformation gradient tensor (Eq. 6.3), and also are considered in the equilibrium equation (Eq. 6.5) of the body particles.

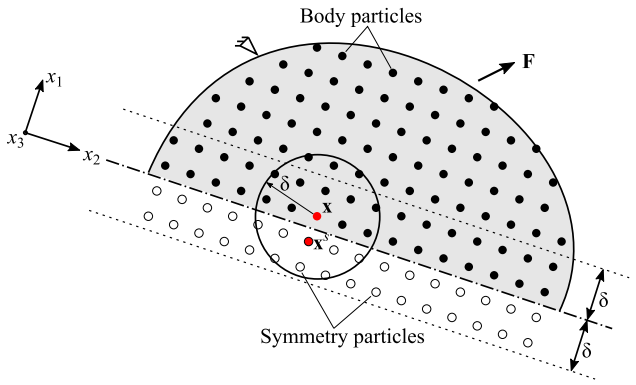


Figure 6.2: A schematic for introducing symmetry particles.

Due to the symmetry, the shape tensor of a symmetry particle is equal to its corresponding body particle, $\mathbf{K}(\mathbf{x}^s) = \mathbf{K}(\mathbf{x})$. To obtain the other mathematical components of the symmetry particle, a symmetry matrix must be defined to impose the symmetry condition on the three axes as follows:

$$\mathbf{I}^s = \begin{cases} I^s_{ii} = -1 & : Axis - i \text{ is the symmetry direction} \\ I^s_{ii} = 1 & : \text{otherwise} \\ I^s_{ij} = 0 & : i \neq j \end{cases} \tag{6.22}$$

For example, the symmetry matrix for the body in Fig. 6.2, with symmetry direction of $Axis - 1$, is defined by:

$$\mathbf{I}^s = \begin{bmatrix} -1 & 0 & 0 \\ 0 & 1 & 0 \\ 0 & 0 & 1 \end{bmatrix} \tag{6.23}$$

The displacement vector of the symmetry particle $\mathbf{x}^s$, is simply obtained with respect to its corresponding body particle $\mathbf{x}$, as:

$$\mathbf{u}(\mathbf{x}^s) = \mathbf{I}^s \mathbf{u}(\mathbf{x}) \tag{6.24}$$

Substituting Eq. (6.24) in Eq. (6.3), the deformation gradient tensor of the symmetry particle is obtained as:

$$\mathbf{F}\left(\mathbf{x}^s\right) = \mathbf{I}^s \mathbf{F}\left(\mathbf{x}\right) \mathbf{I}^s \tag{6.25}$$

Therefore, the strain and stress tensors are obtained by the following operations: $\boldsymbol{\epsilon}\left(\mathbf{x}^s\right) = \mathbf{I}^s \boldsymbol{\epsilon}\left(\mathbf{x}\right) \mathbf{I}^s$ and $\boldsymbol{\sigma}\left(\mathbf{x}^s\right) = \mathbf{I}^s \boldsymbol{\sigma}\left(\mathbf{x}\right) \mathbf{I}^s$. The implementation of the proposed approach in 1D and 2D problems are presented in this study. For the 1D symmetry problem shown in Fig. 6.3, the 1×1 symmetry tensor is $\mathbf{I}^s = -1$. Therefore, the components of the symmetry particle are obtained by: $u_1\left(\mathbf{x}^s\right) = -u_1\left(\mathbf{x}\right)$, $\epsilon_1\left(\mathbf{x}^s\right) = \epsilon_1\left(\mathbf{x}\right)$ and $\sigma_1\left(\mathbf{x}^s\right) = \sigma_1\left(\mathbf{x}\right)$.

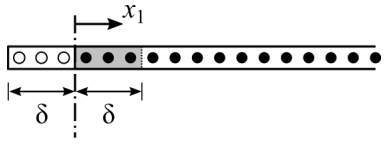


Figure 6.3: Symmetry modeling in 1D.

For the 2D problem, three types of symmetry are accounted for in the Cartesian coordinates, namely x_1-symmetry, x_2-symmetry and x_1x_2-symmetry as seen in Fig. 6.4. The symmetry matrix for each type is presented below:

$$\mathbf{I}^s = \begin{bmatrix} -1 & 0 \\ 0 & 1 \end{bmatrix} \text{ for } x_1\text{-symmetry}$$

$$\mathbf{I}^s = \begin{bmatrix} 1 & 0 \\ 0 & -1 \end{bmatrix} \text{ for } x_2\text{-symmetry}$$

$$\mathbf{I}^s = \begin{bmatrix} -1 & 0 \\ 0 & -1 \end{bmatrix} \text{ for } x_1x_2\text{-symmetry}$$

Table 6.1 presents the displacement, strain, and strain fields (in Voigt or vector notation) for symmetry particles in a 2D problem, with respect to the three symmetry types defined in Fig. 6.4.

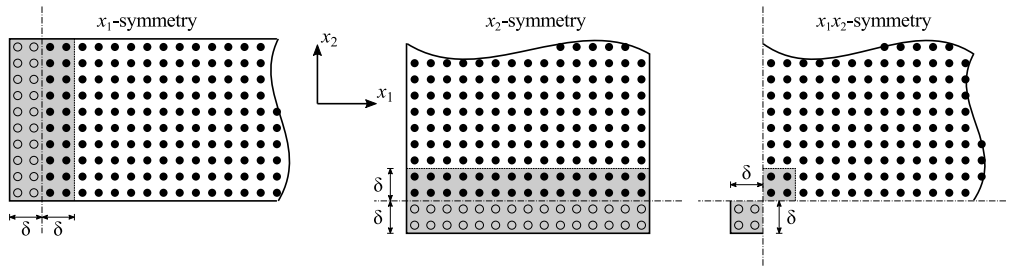


Figure 6.4: Three types of symmetry alongside Cartesian coordinates.

Table 6.1: Deformation, strain and stress fields of symmetry particles in 2D.

Symmetry Type	Deformation	Strain	Stress
x_1-symmetry	$\left\{ \begin{array}{c} u_1(\mathbf{x}^s) \\ u_2(\mathbf{x}^s) \end{array} \right\} = \left\{ \begin{array}{c} -u_1(\mathbf{x}) \\ u_2(\mathbf{x}) \end{array} \right\}$	$\left\{ \begin{array}{c} \epsilon_1(\mathbf{x}^s) \\ \epsilon_2(\mathbf{x}^s) \\ \epsilon_{12}(\mathbf{x}^s) \end{array} \right\} = \left\{ \begin{array}{c} \epsilon_1(\mathbf{x}) \\ \epsilon_2(\mathbf{x}) \\ -\epsilon_{12}(\mathbf{x}) \end{array} \right\}$	$\left\{ \begin{array}{c} \sigma_1(\mathbf{x}^s) \\ \sigma_2(\mathbf{x}^s) \\ \sigma_{12}(\mathbf{x}^s) \end{array} \right\} = \left\{ \begin{array}{c} \sigma_1(\mathbf{x}) \\ \sigma_2(\mathbf{x}) \\ -\sigma_{12}(\mathbf{x}) \end{array} \right\}$
x_2-symmetry	$\left\{ \begin{array}{c} u_1(\mathbf{x}^s) \\ u_2(\mathbf{x}^s) \end{array} \right\} = \left\{ \begin{array}{c} u_1(\mathbf{x}) \\ -u_2(\mathbf{x}) \end{array} \right\}$	$\left\{ \begin{array}{c} \epsilon_1(\mathbf{x}^s) \\ \epsilon_2(\mathbf{x}^s) \\ \epsilon_{12}(\mathbf{x}^s) \end{array} \right\} = \left\{ \begin{array}{c} \epsilon_1(\mathbf{x}) \\ \epsilon_2(\mathbf{x}) \\ -\epsilon_{12}(\mathbf{x}) \end{array} \right\}$	$\left\{ \begin{array}{c} \sigma_1(\mathbf{x}^s) \\ \sigma_2(\mathbf{x}^s) \\ \sigma_{12}(\mathbf{x}^s) \end{array} \right\} = \left\{ \begin{array}{c} \sigma_1(\mathbf{x}) \\ \sigma_2(\mathbf{x}) \\ -\sigma_{12}(\mathbf{x}) \end{array} \right\}$
x_1x_2-symmetry	$\left\{ \begin{array}{c} u_1(\mathbf{x}^s) \\ u_2(\mathbf{x}^s) \end{array} \right\} = \left\{ \begin{array}{c} -u_1(\mathbf{x}) \\ -u_2(\mathbf{x}) \end{array} \right\}$	$\left\{ \begin{array}{c} \epsilon_1(\mathbf{x}^s) \\ \epsilon_2(\mathbf{x}^s) \\ \epsilon_{12}(\mathbf{x}^s) \end{array} \right\} = \left\{ \begin{array}{c} \epsilon_1(\mathbf{x}) \\ \epsilon_2(\mathbf{x}) \\ \epsilon_{12}(\mathbf{x}) \end{array} \right\}$	$\left\{ \begin{array}{c} \sigma_1(\mathbf{x}^s) \\ \sigma_2(\mathbf{x}^s) \\ \sigma_{12}(\mathbf{x}^s) \end{array} \right\} = \left\{ \begin{array}{c} \sigma_1(\mathbf{x}) \\ \sigma_2(\mathbf{x}) \\ \sigma_{12}(\mathbf{x}) \end{array} \right\}$

6.4 Coupling of FE and NOSBPD methods

The nonlocal peridynamics method is effective when analyzing discontinuities such as cracks. However, the associated computational expense, especially in the non-ordinary state-based peridynamics, limits the practical application in large-scale simulation models. Coupling of nonlocal peridynamics and classical continuum mechanics may become a more viable option. The peridynamics used in a small region, where failure is expected, may provide an advantage when conducting a finite element analysis. The efficiency in the other region, where failure is not expected to occur, remains unchanged. An interface method was proposed by Liu and Hong [76] to couple the finite element method with bond-based peridynamics. The proposed study extends the interface method to the non-ordinary state-based peridynamics (NOSBPD) and thus couples the FE and NOSBPD methods. Furthermore, a numerical

algorithm is proposed to solve the coupled NOSBPD-FE equilibrium equations for a steady-state system using the dynamic relaxation method described in Section 6.2.3.

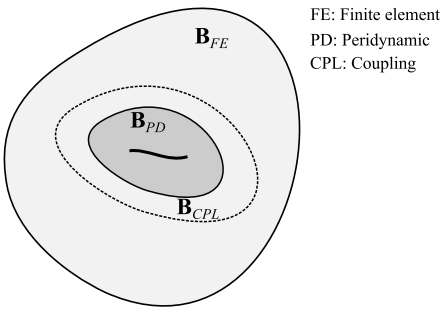


Figure 6.5: Schematic of the body, $\mathbf{B}$, showing sub-regions with the proposed NOSBPD-FE coupling method.

Consider a deformable body $\mathbf{B}$ with a discontinuity, such as a crack shown in Fig. 6.5. The interface method partitions the domain into the FE sub-region, $\mathbf{B}_{FE}$, and the PD sub-region, $\mathbf{B}_{PD}$. The FE and PD represents finite element and peridynamics, respectively. The PD sub-region surrounds the discontinuity (or a crack), and the FE sub-region includes the remaining areas, where $\mathbf{B}_{FE} \cup \mathbf{B}_{PD} = \mathbf{B}$. A coupling region, $\mathbf{B}_{CPL} \in \mathbf{B}_{FE}$, is defined as a part of FE sub-region. $\mathbf{B}_{CPL}$ surrounds the PD sub-region and bridges the finite element and the peridynamic systems as illustrated in Fig. 6.5. The schematic discretization of the coupling region is shown in Fig. 6.6a. Although the CPL region is discretized into finite elements, coupling peridynamic particles (CPL particles) are embedded in this sub-region. Since both CPL elements and CPL particles represent the same area, they must share the same kinematics.

The system of equilibrium equations for the FE sub-region and PD sub-region is solved independently for each region, and the coupling is ensured in the whole system by the following two main steps. In the first step, the deformations of the embedded CPL particles are obtained by interpolating the deformation of the CPL elements. The coupling is applied on the PD sub-region as a displacement boundary condition on CPL particles, which is consistent with the deformations of the CPL elements. Fig. 6.6b represents a schematic of a

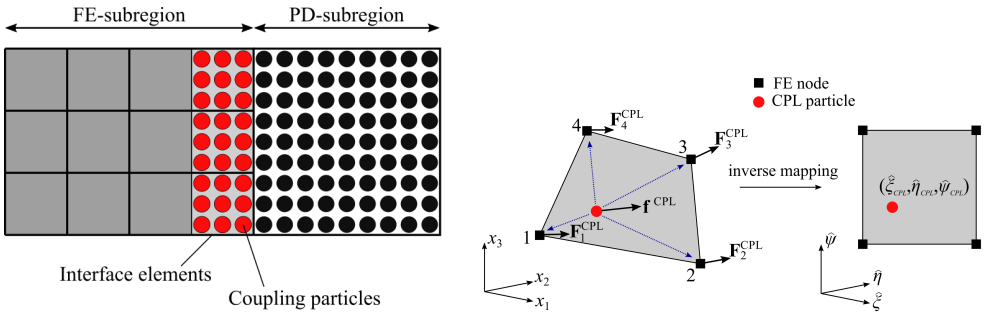


Figure 6.6: (a) Schematic provided to describe NOSBPD-FE coupling concept using interface elements, and (b) an interface element and distribution of coupling force to FE nodes.

coupled element with an embedded CPL particle. After evaluating the displacement of FE nodes, the element shape functions are used to determine the CPL particle displacement by:

$$\mathbf{U}_{CPL}^{PD} = \sum_{I}^{n_e} N_I(\hat{\xi}_{CPL}, \hat{\eta}_{CPL}, \hat{\psi}_{CPL})\mathbf{U}_I \tag{6.26}$$

where n_e is the number of nodes in the coupled element; $(\hat{\xi}_{CPL}, \hat{\eta}_{CPL}, \hat{\psi}_{CPL})$ are the natural coordinates of the CPL particle. The natural coordinates $(\hat{\xi}, \hat{\eta}, \hat{\psi})$ are obtained from the Cartesian coordinates (x_1, x_2, x_3) using an inverse isoparametric mapping technique [76].

In the second step, the boundary forces in the CPL particle are computed and then transferred to the CPL elements as coupling forces. The coupling force in a CPL particle is obtained from Eq. (6.27) by a summation of the interactions of the CPL particle with peridynamic particles in the PD sub-region. The interaction of the particles in the coupling region, $\mathbf{B}_{CPL}$, are not involved in calculation of coupling forces.

$$\mathbf{f}_i^{CPL} = \sum_{j=1}^{n_i^*} \{\mathbf{T}[\mathbf{x}_i^{CPL}]\langle \mathbf{x}_j - \mathbf{x}_i^{CPL}\rangle - \mathbf{T}[\mathbf{x}_j]\langle \mathbf{x}_i^{CPL} - \mathbf{x}_j\rangle\}\Delta V_j \tag{6.27}$$

where n_i^* is the number of PD sub-region particles in the horizon of the embedded CPL particle, $\mathbf{x}_i^{CPL}$. The coupling force of a CPL particle within an interface element e is transferred to nodes of the element.

The coupling force transferred to any selected node, I, in the interface element, e, is obtained by Eq. (6.28), where n_e is the number of CPL particles embedded in the element. In this study, node I indicates any selected node on the interface element. N_I is the shape function of the node I in element, e.

$$\mathbf{F}_I^{CPL} = \sum_{i=1}^{n_e} N_I(\hat{\xi}_{CPL}, \hat{\eta}_{CPL}, \hat{\psi}_{CPL}) \mathbf{f}_i^{CPL} \Delta V_i \tag{6.28}$$

Therefore, the equilibrium equation of the FE sub-region is determined by:

$$\mathbf{K}^g \mathbf{U}^g + \mathbf{F}^{CPL} = \mathbf{F}_{ex}^g \tag{6.29}$$

In NOSBPD-FE coupling, obtaining the coupling force in the interface element is different from BBPD-FE coupling. In the BBPD interaction of two particles $\mathbf{x}_i$ and $\mathbf{x}_j$ depends only on their relative displacement, that is $\mathbf{f}_{ij} \propto \mathbf{x}_j - \mathbf{x}_i$. It means that in coupling BBPD and FE, the displacements of embedded CPL particles interpolated from element nodal displacements are sufficient to calculate the coupling force. However, in NOSBPD formulation, the stress state, σ_i^{CPL} at the CPL particle is also required to obtain $\mathbf{T}[\mathbf{x}_i^{CPL}]$ (from Eq. 6.6) and then to calculate the coupling force, $\mathbf{f}_i^{CPL}$ (from Eq. 6.27).

Three approaches can be used to obtain the stress state of the CPL particles. The first approach is to calculate the stress at the CPL particles by interpolating the stress field of the corresponding interface element as:

$$\boldsymbol{\sigma}_{local}^{CPL} = \sum_{i}^{n_e} N_i(\hat{\xi}_{CPL}, \hat{\eta}_{CPL}, \hat{\psi}_{CPL}) \boldsymbol{\sigma}_i \tag{6.30}$$

The second approach is to interpolate the displacement field of the corresponding interface element and then follow the nonlocal approach to obtain the stress at CPL particles as follows in Section 6.2.1. In both approaches, the force corresponding to the CPL particles may not satisfy the equilibrium at either the PD sub-region or the FE sub-region. Therefore, it is proposed in this study that the stress at embedded particles can be evaluated by using a combination of two expressed approaches as shown in Eq. (6.31).

$$\boldsymbol{\sigma}^{CPL} = \alpha \boldsymbol{\sigma}^{CPL}_{nonlocal} + (1-\alpha)\boldsymbol{\sigma}^{CPL}_{local} \tag{6.31}$$

$\boldsymbol{\sigma}^{local}_{CPL}$ is obtained from Eq. (6.30), and $\boldsymbol{\sigma}^{nonlocal}_{CPL}$ is obtained through the peridynamic approach described in Section 6.2.1. The coefficient α is a weight factor where $0 \leq \alpha \leq 1$, and determines the contribution from each expression. As discussed, the dynamic relaxation method is applied to solve system of equations for the FE sub-region and PD sub-region, independently. The formation and solution of the equilibrium equations of the coupled system is described in Algorithm 1.

6.5 Results

6.5.1 Symmetry modeling: 1D bar with varying stiffness

A 1D bar model with a length of $2L$ is developed to study the accuracy of the proposed method and model the symmetry boundary condition as shown in Fig. 6.7a. The stiffness, E, of the bar varies along the length of bar as follows:

$$\frac{E(x)}{E_0} = \begin{cases} \sqrt{\frac{-x}{L}} & : x < 0 \\ \sqrt{\frac{x}{L}} & : x > 0 \end{cases} \tag{6.32}$$

The stiffness is close to zero in the middle of the bar to represent a crack or singularity. The exact analytical solution for the longitudinal displacement and strain fields of the bar under constant tension loading of σ_0, are presented in Eq. (6.33) and Eq. (6.34), respectively, where $\epsilon_0 = \sigma_0/E_0$.

$$\frac{u(x)}{L\epsilon_0} = \begin{cases} -2\sqrt{\frac{-x}{L}} & : x < 0 \\ 2\sqrt{\frac{x}{L}} & : x > 0 \end{cases} \tag{6.33}$$

$$\frac{\epsilon(x)}{\epsilon_0} = \begin{cases} 1/\sqrt{\frac{-x}{L}} & : x < 0 \\ 1/\sqrt{\frac{x}{L}} & : x > 0 \end{cases} \tag{6.34}$$

In the numerical study, a total of three peridynamic models were analyzed, a complete model and two symmetry models. In the complete model, the complete bar is discretized in peridynamic particles as seen in Fig 6.7b. Two rigid regions, with a length of b, are supplemented at each end of the 1D bar to uniformly apply tension loading. To ensure an uniform tension stress, σ_0, a body force of $f_b = \sigma_0/b$ is applied to the loading particles. In the symmetry models, to account for symmetry, only half of the bar is discretized into peridynamic particles as seen in Fig. 6.7c and d. Also, a rigid region is provided to the right side of the bar to apply tension loading, while a symmetry boundary area, with a length of δ, is added to the left side as proposed in Section 6.3. In the first symmetry boundary model, henceforward called "Fixed boundary model", the displacement of symmetry particles are restrained along the symmetry axis (x-direction) as shown in Fig. 6.7c. Due to the nonlocal nature of peridynamics, this assumption as the simplest way to apply symmetry, may not represent the local symmetry boundary modeling very well. In the second symmetry model, henceforward called "Symmetry boundary model", the particles in the symmetry area are given displacement and stress values as proposed in Section 6.3. The latter symmetry model ensures the zero displacement at the symmetry axis, and therefore best represents the the symmetry condition.

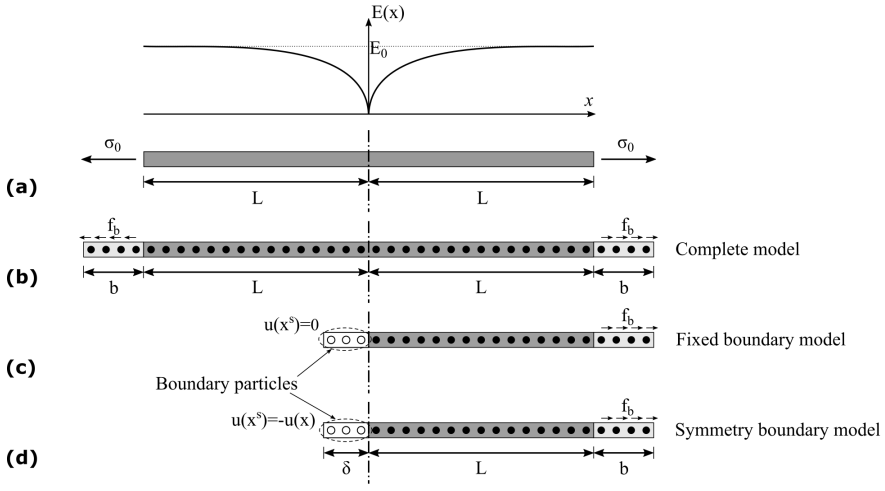
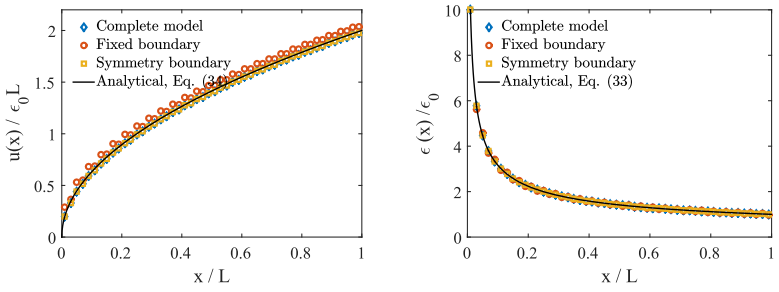


Figure 6.7: 1D bar under tension with varying stiffness, and peridynamic models to study symmetry modeling.



(**a**) $h/L = 0.001$, $\delta/h = 2$ (**b**) $h/L = 0.0005$, $\delta/h = 2$

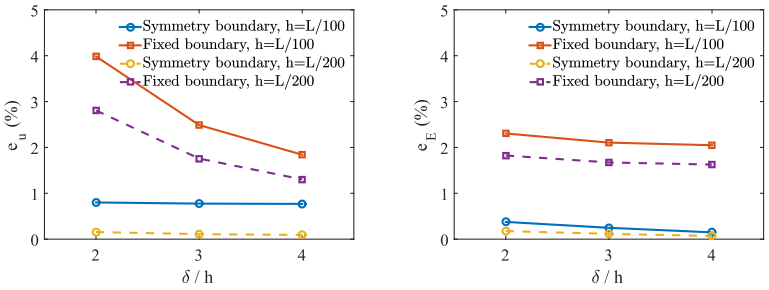
Figure 6.8: Comparison of numerical results with analytical results (a) displacement field, (b) strain field.

The longitudinal displacement and strain for the bar model are depicted in Fig. 6.8. The results are obtained for $h = L/100$, $\delta = 3h$ and $b = 12h$. As expected, the model imposing a symmetry boundary condition retrieves the same results as the complete model, and both have good agreement with analytical results. However, the model with fixed boundary particles exhibits more longitudinal displacement (see Fig. 6.8a). The strain obtained from the fixed boundary model is slightly different from the other models and analytical results (see Fig. 6.8b).

To further evaluate the performance of the proposed symmetry model, the results were obtained for varying discretization parameters, including particle spacing and horizon size. Fig. 6.9 shows relative displacement and relative strain energy errors computed by Eq. (6.35) and Eq. (6.36), respectively.

$$e_u = \sqrt{\frac{\sum_i^N \left(\mathbf{u}_i^{num} - \mathbf{u}_i^{local}\right)^T \left(\mathbf{u}_i^{num} - \mathbf{u}_i^{local}\right) V_i}{\sum_i^N \left(\mathbf{u}_i^{local}\right)^T \left(\mathbf{u}_i^{local}\right) V_i}} \tag{6.35}$$

$$e_E = \sqrt{\frac{\frac{1}{2}\sum_i^N \left(\boldsymbol{\epsilon}_i^{num} - \boldsymbol{\epsilon}_i^{local}\right)^T \left(\boldsymbol{\sigma}_i^{num} - \boldsymbol{\sigma}_i^{local}\right) V_i}{\frac{1}{2}\sum_i^N \left(\boldsymbol{\epsilon}_i^{local}\right)^T \left(\boldsymbol{\sigma}_i^{local}\right) V_i}} \tag{6.36}$$



(**a**) $h/L = 0.001$, $\delta/h = 2$ (**b**) $h/L = 0.0005$, $\delta/h = 2$

Figure 6.9: The effect of particle spacing, h, and horizon size, δ, on (a) relative displacement error, and (b) relative strain energy error, for the 1D problem.

The *num* denotes the numerical and *local* indicates exact solutions shown in Eq. (6.33) and Eq. (6.34). N is the total number of particles.

Fig. 6.9 shows that the proposed symmetry model produces much smaller errors in both displacement and strain energy fields. Furthermore, smaller particle spacing h (i.e., equivalent to a larger number of particles N) decreases the errors. It is finally worth noting that a larger horizon size slightly decreases the errors.

6.5.2 Symmetry modeling: 2D plate with hole under tension

A rectangular plate with a circular hole is analyzed to study the performance of the proposed symmetry model in plane stress 2D problems, as shown in Fig. 6.10a. The $100\ mm \times 40\ mm$ model with a circular hole with radius of $R = 5\ mm$, is subjected to a static tensile displacement of $0.2\ mm$. The material model is assumed to be linear elastic with $E = 210\ GPa$ and $\nu = 0.3$. Due to symmetry along the horizontal and vertical axes, the symmetry model is reduced to 1/4 of the complete model, as shown in Fig. 6.10b. The additional boundary areas are also shown in the figure. Three peridynamic models are studied in this section: i) a complete model, ii) a quarter model with fixed boundaries (the displacement of symmetry particles are restricted along symmetry axes), and ii) a quarter model with proposed

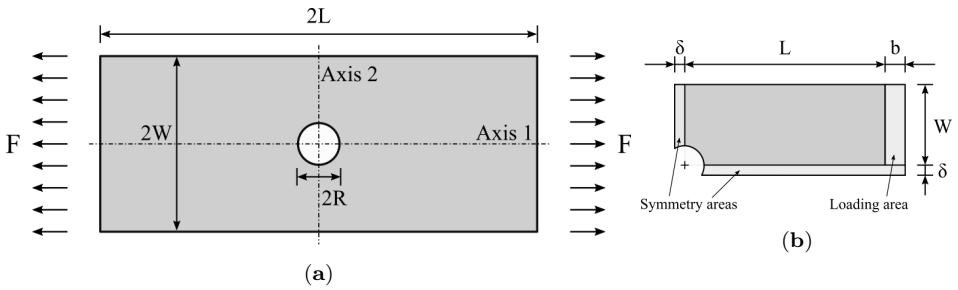
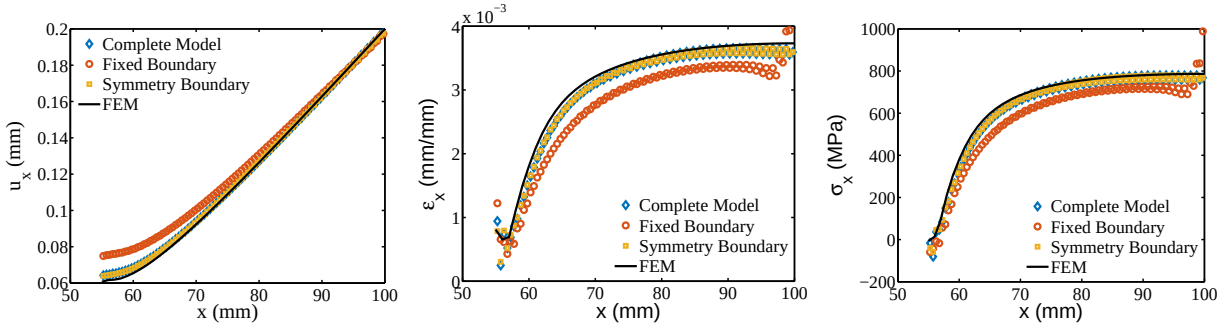


Figure 6.10: a) 2D model with circular opening, b) quarter model.

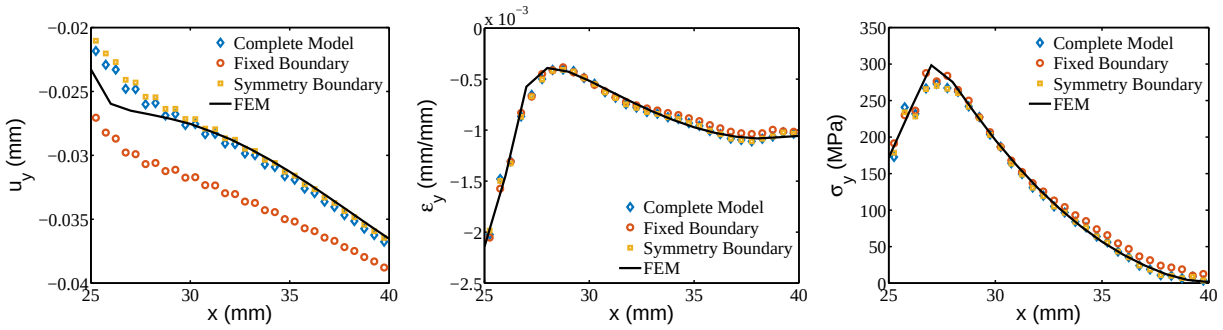


(**a**) horizontal displacement, u_x (**b**) horizontal strain, ϵ_x (**c**) horizontal stress, σ_x

Figure 6.11: Comparison of a) horizontal displacement, u_x, b) horizontal strain, ϵ_x, and c) horizontal stress, σ_x, along Axis 1 obtained from a complete model, 1/4 model with fixed and with symmetry boundary condition

symmetry modeling method (the displacement of symmetry particles are obtained through symmetry rules in Section 6.3). The analysis is conducted for $h = 1\ mm$ and $\delta = 3h$. The peridynamic results are provided in two symmetry axes and compared with the FEM results.

Fig. 6.11 represents the horizontal displacements and strain/stress results along the horizontal axis of symmetry. Fig. 6.12 shows the results along the vertical axis of symmetry. Both figures indicate that the results for the symmetry model agree well with those obtained from the complete 2D model, and with FEM results. However, the results obtained with the fixed boundary model do not agree well with complete model and FEM results.



(**a**) vertical displacement, u_y (**b**) vertical strain, ϵ_y (**c**) vertical stress, σ_y

Figure 6.12: Comparison of a) vertical displacement, u_y, b) vertical strain, ϵ_y, and c) vertical stress, σ_y, along Axis 2 obtained from a complete model, 1/4 model with fixed and with symmetry boundary condition

To show how discretization can affect the results, further studies are conducted by analyzing three different particle spacings, $h = 1\ mm$, $h = 1/2\ mm$ and $h = 1/3\ mm$, with $\delta = 3h$. The relative displacement and strain energy errors (obtained by Eqs. 6.35 and 6.36, respectively) along horizontal and vertical axes are provided in Fig. 6.13. The results for the complete model are not provided as they are very similar to the results from the symmetry boundary model. Regarding that smaller particle spacing size results in more accurate results in both fixed and symmetry boundary models, the symmetry boundary model are still more accurate than the fixed boundary model.

6.5.3 Coupling modeling: 2D plate under tension

In this sub-section, a 2D plate is analyzed to evaluate the performance of the proposed coupling approach. In the subsequent section, the 2D plate model with a circular opening (studied in the previous section) is evaluated using the proposed coupling approach. The $30\ mm \times 10\ mm$ elastic plane model is fixed on one edge, and a displacement of $0.2\ mm$ is applied at the opposite edge, as illustrated in Fig. 6.14. The material properties are: $E = 210\ GPa$ and $\nu = 0.3$. One-third of the plate model is discretized using peridynamic

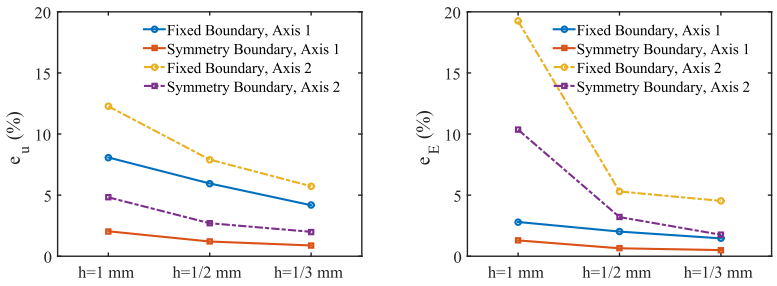


Figure 6.13: The effect of particle spacing, h, on (a) relative displacement error, and (b) relative strain energy error, along Axis 1 and Axis 2 for 2D specimen.

particles, and the 4-node rectangular elements are used for the rest. The effect of discretization scheme (including the peridynamic particle spacing, h_{PD}, and the element size, h_{FE}) and coupling factor, α, are studied through this example. To do so, the displacement field along the middle of the plate is provided and the relative displacement errors (see Eq. 6.35) are obtained for different discretization schemes and varying coupling factor, α. It is noted that the displacement error is calculated relative to the results obtained from a FE analysis of the full model.

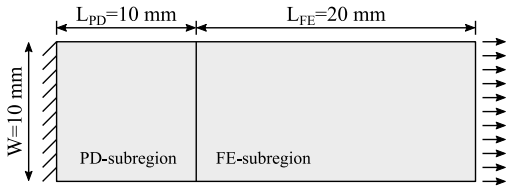


Figure 6.14: Schematics of 2D plane stress model under tension showing the PD and FE sub-regions.

The relative displacement error, e_u, are provided in Fig. 6.15 for two different discretization schemes: (i) $h_{PD} = 0.50\ mm$, $h_{FE} = 5.0\ mm$ and (ii) $h_{PD} = 0.25\ mm$, $h_{FE} = 2.5\ mm$ for varying coupling factor, α. As expected due to linearity of the problem, the relative displacement error is small. Also, the error in the FE part is much smaller than the error in the PD sub-region. Furthermore, a finer mesh (smaller h_{PD} and h_{FE}) results in smaller errors.

With $\alpha = 0$, where the stresses in embedded particles are obtained from interpolating the results from the coupling elements, the relative displacement error is higher. For $0 < \alpha \leq 1$, the error is significantly reduced. However, for this problem and described discretization schemes, the minimum error occurs for $\alpha = 0.5$.

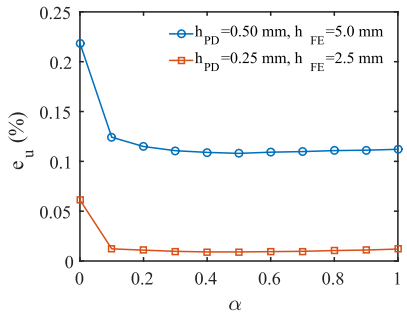
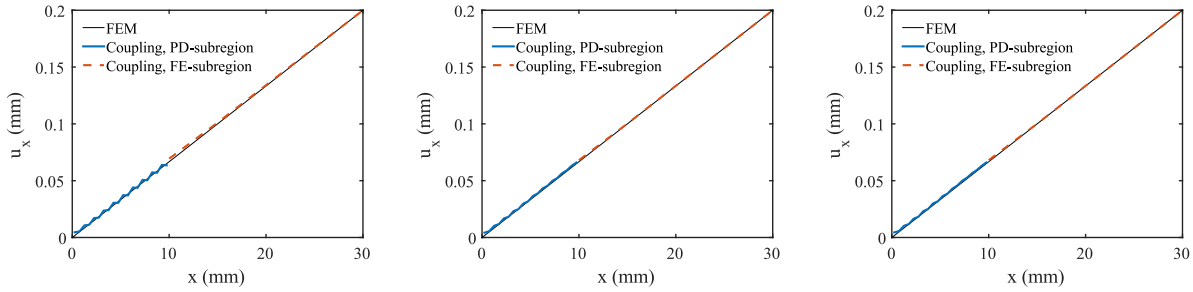


Figure 6.15: The effect of coupling factor α, on displacement error in PD-subregion.

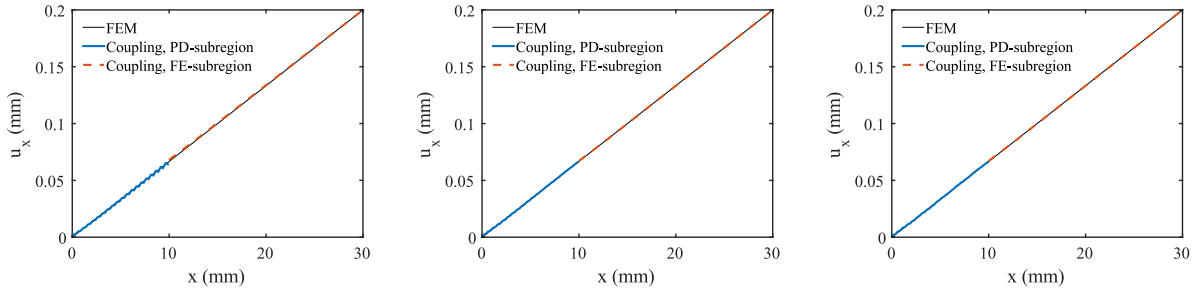
The longitudinal displacement in the middle, u_x, is also provided in Figs. 6.16 and 6.17 for the two discretization schemes, (i) and (ii), respectively. The results of coupling models with three different values of coupling factor, $\alpha = 0$, $\alpha = 0.5$, and $\alpha = 1$, are compared with the results from the full FE model. An excellent agreement between FE model and coupling models is achieved, which illustrates the capability of the proposed NOSBPD-FE coupling method. However, as shown in Fig. 6.16a and Fig. 6.16b, an oscillatory displacement field is obtained in the PD subregion for $\alpha = 0$, whereas $\alpha = 0.5$ and $\alpha = 1$ result in smooth displacement fields as shown in Fig. 6.16b,c and Fig. 6.17b,c. In the subsequently section and example, the coupling factor is selected as $\alpha = 0.5$, regardless of discretization scheme.

The effect of discretization scheme on the performance of the presented coupling method, was investigated through three different cases: 1) varying h_{PD} with a fixed h_{PD}/h_{FE} ratio, 2) varying h_{PD} with h_{FE} fixed, and 3) varying h_{FE} with h_{PD} fixed. The displacement error (Eq. 6.35) results are provided in Fig. 6.18. It is clear from the figure that for fixed h_{PD}/h_{FE} and fixed h_{FE}, the displacement error decreases for smaller h_{PD}. It is also determined that changing h_{FE} with fixed h_{PD} has no significant effect on the displacement error.



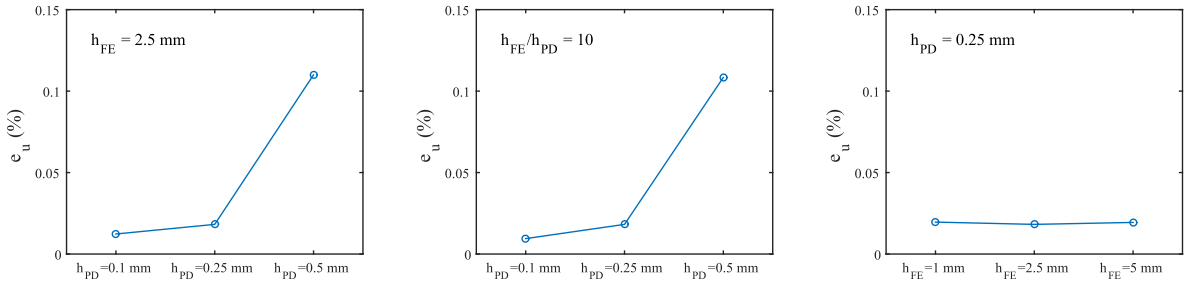
(**a**) $\alpha = 0$ (**b**) $\alpha = 0.5$ (**c**) $\alpha = 1$

Figure 6.16: The longitudinal displacement u_x, for various coupling factor α, with $h_{PD} = 0.50\ mm$ and $h_{FE} = 5.0\ mm$.



(**a**) $\alpha = 0$ (**b**) $\alpha = 0.5$ (**c**) $\alpha = 1$

Figure 6.17: The longitudinal displacement u_x, for various coupling factor α, with $h_{PD} = 0.25\ mm$ and $h_{FE} = 2.5\ mm$.



(**a**) varying h_{PD}, fixed h_{PD}/h_{FE} (**b**) varying , fixed h_{FE} (**c**) varying h_{FE} fixed h_{PD}

Figure 6.18: Displacement error for different discretization schemes.

6.5.4 Coupling modeling: 2D rectangular plate with a circular hole

The previous example is provided to test the capability (accuracy and discretization) of the NOSBPD-FE coupling approach. The rectangular plate specimen with circular notch presented in Section 6.5.2 is used in this section. As presented in Fig. 6.19, the model is divided into a FE/PD sub-regions, where a 20 $mm \times 20$ mm PD sub-region surrounds the circular opening. The FE sub-region surrounds the PD sub-region. Thus, neither boundary conditions nor loads are applied on the PD sub-region. The kinetics of PD particles are controlled through coupling elements. The FE sub-region is discretized into 5 $mm \times 5$ mm 4-node linear elements, while a relatively small particle spacing, $h_{PD} = 0.5$ mm, is selected to discretize the PD-subregion. It is anticipated that the proposed coupling approach reduces computational cost while conventional loading and local boundary conditions are applied to the FE sub-region.

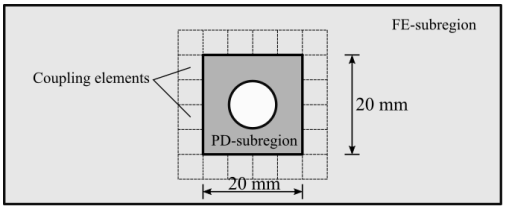
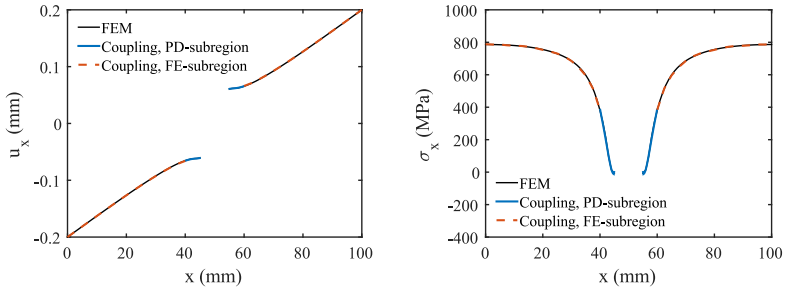


Figure 6.19: The FE-subregion and PD-subregion in the notched 2D model (see Fig. 6.10a).

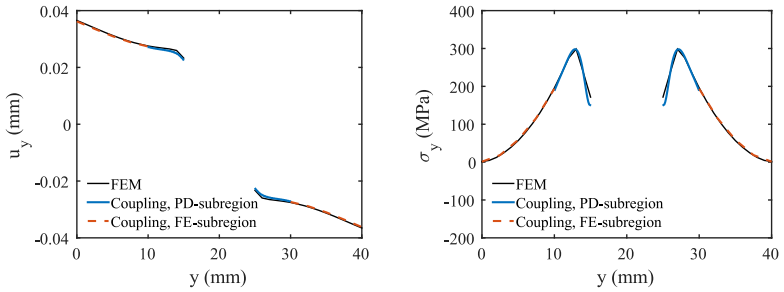
The longitudinal displacements and stresses along the axis of symmetry (Axis 1), obtained from the NOSBPD-FE coupling model, are compared with the results from a full FE analysis model in Fig. 6.20. Fig. 6.21 also provides a comparison of the vertical displacements and stresses along Axis 2. A good agreement in results between the coupling and the FE models is obtained. This indicates that NOSBPD-FE coupling method is effective in modeling a structure with a high deformation gradient.

Fig. 6.22 presents the longitudinal displacement and stress contours. The contours indicate that the coupled model is superior to the FEA results in predicting the displacement and stress fields around the opening. Therefore, the presented coupling model provides an



(**a**) displacement (**b**) stress

Figure 6.20: The longitudinal displacement and stress along Axis 1.



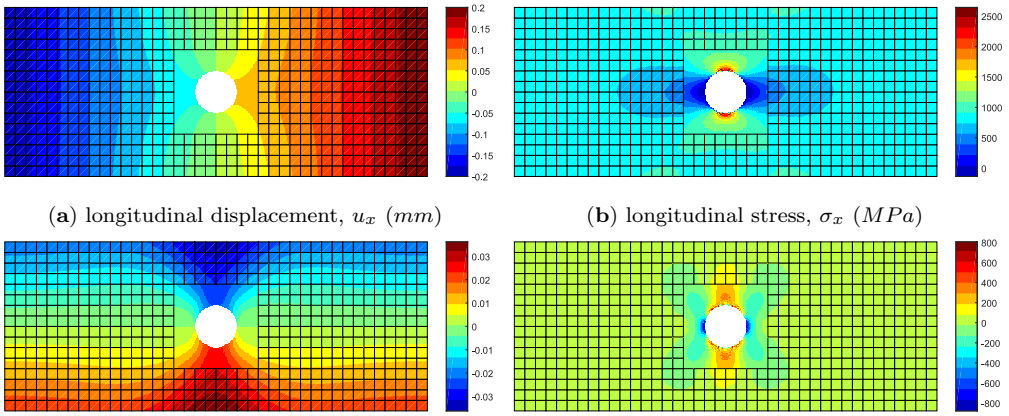
(**a**) displacement (**b**) stress

Figure 6.21: The vertical displacement and stress along Axis 2.

effective approach for modeling structures with local damage or singularities. While the peridynamics is more effective for modeling areas with singularities, the FE can be used to areas away from singularities.

6.5.5 Crack propagation in Compact Tension specimen

In addition to the 2D plate problem with a circular opening, a Compact Tension (CT) specimen was modelled to demonstrate the effectiveness of the proposed symmetry and coupling methods. This example problem is selected to show a propagation of damage (or a crack). A 2D model was developed to reproduce an experimental study conducted by Samal



(**a**) longitudinal displacement, u_x (mm) (**b**) longitudinal stress, σ_x (MPa)

(**c**) vertical displacement, $u_x(\ mm)$ (**d**) vertical stress, σ_y (MPa)

Figure 6.22: The longitudinal displacement and stress contour results for NOSBPD-FE coupling model.

et al. [54]. In their study, a fracture test conducted on a CT specimen, as illustrated in Fig. 6.23a. In the numerical analysis, four different models were analyzed to predict a crack propagation path in the CT specimen. Model I: a full peridynamics model discretized in peridynamic particles (Fig. 6.23a); Model II: a half model using the proposed symmetry boundary modeling approach discretized in peridynamic particles (Fig. 6.23b), Model III and IV: half models using symmetry boundary modeling approach discretized using the proposed coupling approach, including both peridynamic particles and conventional quadrilateral elements (Fig. 6.23c). The FE sub-region in coupled models, Model III and Model IV, was discretized in 4-node elements with an element size of $h_{FE} = 2\ mm$ and $h_{FE} = 5\ mm$, respectively. The particle spacing in peridynamic regions is $h_{PD} = 0.5\ mm$ in all four models. The horizon size was $\delta = 3h_{PD}$. The analysis of the compact tension sample is completed using a force-controlled analysis process. The applied force, F, is equally distributed among the particle positioned at the circumference of each circular opening.

The material model is assumed to be nonlinear elastic-plastic, with $E = 210\ GPa$, $\nu = 0.3$ and the initial yield stress, $\sigma_0 = 405\ MPa$. An isotropic hardening law is employed as

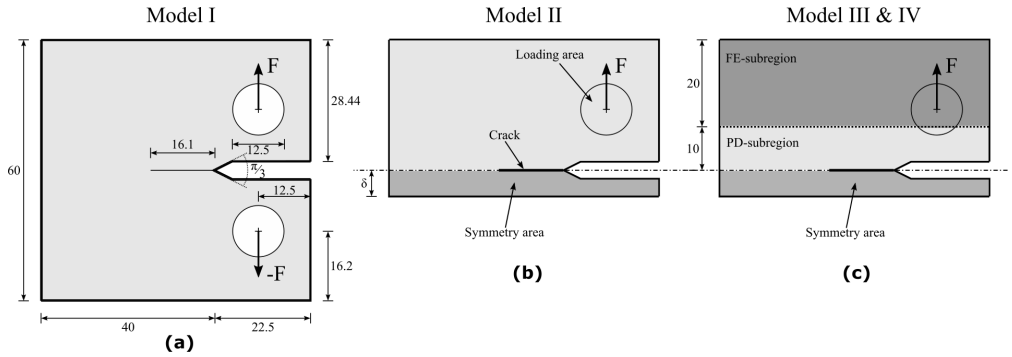


Figure 6.23: The compact tension specimen models (Lengths given in millimeters, and the thickness of the specimen is 25 mm).

$$\sigma_y = \sigma_0 + B(\epsilon_p)^n \tag{6.37}$$

where ϵ_p is the equivalent plastic strain; B and n are the material constants. This study uses the constants, $B = 513\ MPa$ and $n = 0.39$ determined from the experimental stress-plastic strain curve of the material DIN22NiMoCr3-7 [54]. As discussed in Section 6.2.1, the classical constitutive equation remains valid in the non-ordinary state peridynamics method. The strain determined in the peridynamic analysis is used to determine the plastic strain using the von-Mises yield surface and associate flow rule [141]. This paper adopts the procedure used by Tupek et al. [23], and implements the continuum damage model in the peridynamic framework. To do so, the weighting function for the bond between particles $\mathbf{x}$ and $\mathbf{x}'$ must be modified as follows:

$$\hat{\omega} = \omega(\xi)\omega_D(D, D') \tag{6.38}$$

In Eq. (6.38), D and D' are the damage parameters corresponding to the particles $\mathbf{x}$ and $\mathbf{x}'$, respectively. The damage parameter, D, represents the state of yielding at the particle $\mathbf{x}$ and is determined as a function of equivalent plastic strain and are obtained by

$$D = \begin{cases} \int_0^{\epsilon_p} \frac{d\epsilon_p}{\epsilon_f} & : D < 1 \\ 1 & : \text{otherwise} \end{cases} \tag{6.39}$$

where ϵ_f is the equivalent plastic strain to fracture. When the equivalent plastic strain reaches to its threshold value, ϵ_f, the damage parameter, D, equals to 1, and consequently all bonds connected to the particle are considered broken. Therefore, yielding of the material occurs before any bond breaks. As a result, the material yields before it breaks. This approach is similar to the method used by Tupek et al. [23] and reasonably represents the behavior of ductile materials. The general form of ϵ_f depends on the material parameters and stress state [55]; however in this study, a constant value of $\epsilon_f = 0.8$ is used based on 1D tension test results [54].

ω_D is introduced to determine the bond breakage between the peridynamic particles and was assumed to be 1, as shown in Eq. (6.40), unless one of the particles is fully damaged $D = 1$ or $D' = 1$. $\omega_D = 0$ means the bond between $\mathbf{x}$ and $\mathbf{x}'$ cannot carry load longer.

$$\omega_D = \begin{cases} 0 & : D = 1 \text{ or } D' = 1 \\ 1 & : \text{otherwise} \end{cases} \tag{6.40}$$

Fig. 6.24 provides a comparison of load-CMOD (crack mouth opening displacement) responses from the peridynamics analysis model as well as the experiment and numerical model presented by Samal et al. [54]. Good agreement is observed between the experimental results and full PD model (Model I) results. The experiment results also agree well with the results from the symmetry PD model (Model II). However, applying NOSBPD-FE coupling (Models III and IV) introduces a small discrepancy although the discrepancy decreases as the finite element mesh size reduces. Overall, the results from the two models reasonably agree with the experimental results.

Contours of the vertical displacement, u_y, for the four presented models are also provided in Fig. 6.25 for an applied displacement of 1.2 mm. It is evident from the figure that the

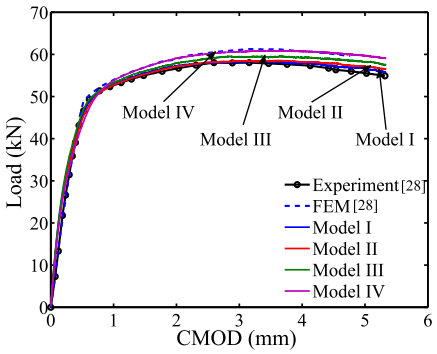
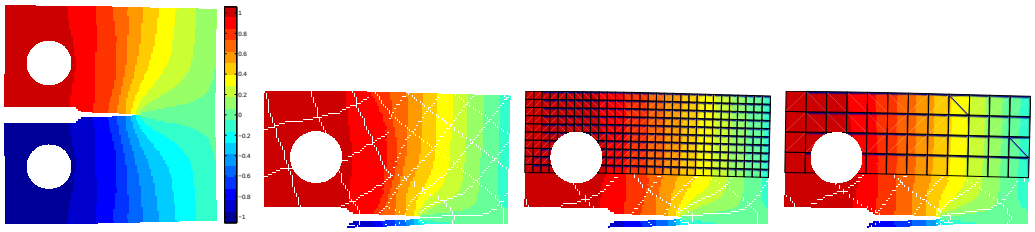


Figure 6.24: Comparison of the load-CMOD response for 4 CT models.



(**a**) Model I (**b**) Model II (**c**) Model III (**d**) Model IV

Figure 6.25: The vertical displacement, u_y, contours for presented CT specimen models subjected to displacement loading ($1.2\ mm$) at the center of hole(s).

proposed symmetry and coupling methods can be applied concurrently to achieve computationally effective solutions of more complicated problems.

The purpose of introducing a symmetry model for the NOSBPD as well as the NOSBPD-FE coupling method is to decrease the computational expenses of the NOSBPD analysis. Therefore, a comparison of time required for analysis must be discussed. Fig. 6.26 provides the simulation duration. The parallel-computing simulations are conducted using four ($3\ GHz$) processors on a UNIX cluster. The pseudo-algorithm provided in Section 6.4 (Algorithm 1) is parallelized using an Open Multi-Processing application programming interface (OpenMP). The program starts with a master thread, and additional threads are used where

parallel computing is desired. In this work, the parallel region includes loops, where the loop elements are independent of each other and are computed concurrently on multiple CPUs. The directive pair of "!$$OMP\ PARALLEL$" and "!$$OMP\ END\ PARALLEL$" is used in order to execute a block of code by multiple threads (e.g., an independent loop) in the current Fortran code. Refer to Lee et al. [142] for the details on parallelizing peridynamics code using OpenMP directives. The simulations are conducted using four threads on the UNIX cluster node. The processor model is $Intel(R)\ Xeon(R)\ CPU\ E5410$ @ 2.33 GHz; the cache size is 6144 KB. The bus speed is 1333 $MHz\ FSB$, and RAM is 16 GB in size.

The simulation time is provided for 1000 displacement loading steps, while the dynamic relaxation cut-off is assumed to be $\gamma = 10e - 3$. As expected, the half peridynamic model (Model II) halves the simulation time of the full peridynamic model (Model I). Coupling peridynamics with the finite element method also reduces the computation time by up to 72%.

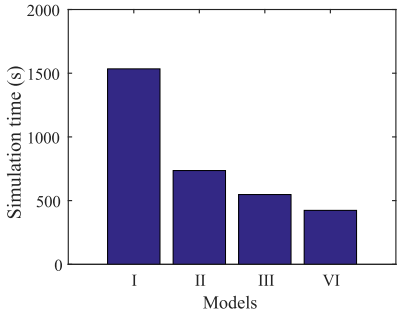


Figure 6.26: Comparison of simulation time for four models.

6.6 Conclusion

There is an increasing interest in non-ordinary state-based peridynamics because it allows the use of classical constitutive equations and thus failure criteria in a nonlocal modeling framework. The nonlocal peridynamics method is promising for modeling discontinuities and thus is highly regarded in fracture mechanics modeling. However, the non-ordinary state-based peridynamic method remains computationally more demanding than the finite

element method. This paper addresses two critical issues in an attempt to reduce the computational cost of peridynamic analysis: (1) The proposed nonlocal symmetry boundary method enhances both accuracy and efficiency by providing means to take advantage of symmetry boundary conditions. (2) Furthermore, the proposed NOSBPD-FE coupling scheme takes advantage of both peridynamics and finite element methods in a fracture analysis. The coupling scheme achieves the benefits of enhanced accuracy in areas with local damage (a crack or opening) by using a peridynamics analysis framework, while providing improved computational efficiency for areas without damage by means of the finite element method. The proposed nonlocal symmetry and NOSBPD-PD coupling approaches were applied to structures of increasing complexity, and were found to provide accurate results and reduce computation time.

Algorithm 1 Computational procedure used for the coupled NOSBPD-FE system

while $\gamma^{PD} > \gamma$ and $\gamma^{FE} > \gamma$ **do**

Peridynamic system

  for all PD particles and CPL particles **do**
    Calculate shape tensor, $\mathbf{K}$ (Eq. 6.4)
    Calculate deformation gradient tensor, $\mathbf{F}$ (Eq. 6.3)
    Calculate nonlocal strain, $\boldsymbol{\epsilon}_{nonlocal}$, and nonlocal stress, $\boldsymbol{\sigma}_{nonlocal}$
  end for
  for all PD particles **do**
    Calculate internal force, $\mathbf{F}_{in}^{PD}$ (Eq. 6.5)
  end for
  PD equilibrium equation, $\mathbf{F}_{in}^{PD} = \mathbf{F}_{ex}^{PD}$
  Apply Dynamic Relaxation for the PD system
  Update Displacement field, $\mathbf{U}_{n+1}^{PD} = \mathbf{U}_{n}^{PD} + \Delta\mathbf{U}_{n+1}^{PD}$
  Apply displacement boundary condition
  $\gamma^{PD} = \left|\left|\mathbf{U}_{n+1}^{PD} - \mathbf{U}_{n}^{PD}\right|\right|$

Coupling

  for all CPL particles **do**
    Calculate coupling displacement, $\mathbf{U}_{n+1}^{CPL}$ (Eq. 6.26)
    Calculate local stress, $\boldsymbol{\sigma}_{local}^{CPL}$ (Eq. 6.30)
    $\boldsymbol{\sigma}^{CPL} = \alpha\boldsymbol{\sigma}_{nonlocal}^{CPL} + (1-\alpha)\boldsymbol{\sigma}_{local}^{CPL}$
    Calculate coupling force, $\mathbf{f}^{CPL}$ (Eq. 6.27)
  end for
  for all interface elements **do**
    Calculate nodal coupling force, $\mathbf{F}^{CPL}$ (Eq. 6.28)
  end for

Finite element system

  for all elements (including interface elements) **do**
    Calculate element stiffness matrix, $\mathbf{K}^{e}$ (Eq. 6.16)
  end for
  Assemble global stiffness matrix, $\mathbf{K}^{g}$
  FE equilibrium equation, $\mathbf{K}^{g}\mathbf{U}^{g} + \mathbf{F}^{CPL} = \mathbf{F}_{ex}^{FE}$
  Apply dynamic relaxation to the FE system
  Update Displacement field, $\mathbf{U}_{n+1}^{FE} = \mathbf{U}_{n}^{FE} + \Delta\mathbf{U}_{n+1}^{FE}$
  Apply displacement boundary condition
  $\gamma^{FE} = \left|\left|\mathbf{U}_{n+1}^{FE} - \mathbf{U}_{n}^{FE}\right|\right|$
end while

Chapter 7

Conclusion

Concrete is a complex heterogeneous material, and thus, it is important to develop computational modeling methods to enhance the prediction accuracy of the fracture mechanism. In the present dissertation, it is aimed to create a multiscale modeling framework based on the peridynamic theory and to study the fracture behavior of cementitious composites. Peridynamics is a nonlocal method which effectively reformulates the classical continuum mechanics by substituting the governing partial differential equations with integral equations. It is concluded that the most general form of peridynamics, i.e., non-ordinary state-based peridynamics (NOSBPD), is well suited to investigate the complex fracture behavior observed in brittle cementitious composite materials. Although the implementation of the NOSBPD is in its infancy, it is concluded that a two-dimensional implementation of the peridynamic theory is successfully achieved. It is also concluded that the small strain assumption and derivation, including an incremental small strain material model, from the Continuum Mechanics theory is successfully utilized to implement and formulize the NOSBPD for mesoscale cementitious composite modeling. The dynamic relaxation method is also effectively adopted to obtain quasi-static solutions for the peridynamic system of equations of motion.

The NOSBPD method is known to suffer from the spurious zero-energy mode instability. In Chapter 2, it is concluded that this instability problem is efficiently controlled by a higher-order approximation to the nonlocal deformation gradient tensor. The proposed higher-order method provides an effective solution for suppressing the spurious zero-energy mode commonly found in the non-ordinary state-based peridynamics. The simulation results indicate that the proposed method outperforms the other available methods in suppressing

the zero-energy mode, and is more robust against changes in simulation model size, particularly when the model is sensitive to the horizon size. Therefore, it is concluded that the proposed method is superior to other methods available in literature as it enhances the accuracy of stress and displacement plots without increasing computational expense. That is, for the parameters studied herein, the solutions are unaffected by horizon size and thus is more effective for large models.

In Chapter 3, the fracture behavior of fiber reinforced concrete structures is studied using the peridynamic formulations, including the enhanced stability presented in Chapter 2. It is concluded that the proposed meshless framework is able to characterize the observed crack nucleation and crack growth of available FRC beam tests. In using the proposed semi-discrete fiber modeling method, the traction forces in the fiber reinforcement are distributed to the background concrete points by a weight function. Discrete cracks were modeled by a set of bond relationships between cementitious points such that no representation of the crack surface is necessary. This inherent feature makes the proposed meshless method ideally suited for FRC composites regardless of the fiber reinforcement size. Furthermore, it enhances the accuracy of discrete damage pattern predictions. Therefore, the proposed method may be extended to predict the response of fiber-reinforced polymer (FRP) concrete structures as well as micro-fiber reinforced concrete structures and other composites.

In Chapter 4, a micropolar peridynamic framework with a semi-discrete fiber modeling approach is shown to be highly effective in representing the complex response of notched fiber reinforced beams. The efficiency is demonstrated by a comparison of experimental and analytical results. The results of the analysis of fiber reinforced notched concrete beams indicate that the proposed micropolar peridynamic modeling framework provides the accuracy comparable to the NOSBPD method while enhancing the computational efficiency.

In Chapter5, the effect of concrete heterogeneity on its fracture behavior is studied at the mesoscopic scale. It is concluded that the macroscale description and modeling of fracture behavior in cementitious composites is highly dependent on the heterogeneous constituent

materials at a mesoscopic level, and that it is essential to characterize such fracture mechanism of mesoscopic materials by using effective numerical techniques. It is also concluded that mesoscale modeling of concrete members in the proposed non-ordinary peridynamic analysis framework is highly effective for fracture analysis. The stress-displacement curves agree well with available experimental results and FEM results. The simple two-dimensional mesoscale model generated in peridynamics is well suited to understand the effect of gradation, aggregate distribution and proportions of constituent materials, as well as to predict the fracture mechanism, comprising bond failure and crack initiation/propagation at the mesoscale. Furthermore, with the proposed mesoscale peridynamics analysis method, it is possible to identify a statistically-significant sample size for reasonably representing coarse aggregate gradation and distribution and to predict the fracture mechanism in concrete specimens.

The non-ordinary state-based peridynamic method is a promising computational tool for fracture analysis of brittle cementitious composites; however, it remains computationally more demanding than the finite element method in large-scale analysis problems. Therefore, in the last chapter of this dissertation, two critical issues are addressed, in an attempt to reduce the computational cost of the peridynamic analysis approach. The first approach successfully accounts for symmetry boundary conditions in a peridynamic body by introducing constraints which allow modeling local symmetry conditions. The second approach effectively couples the non-ordinary state-based peridynamics and the finite element methods. It is concluded that the proposed NOSBPD-FE coupling scheme achieves enhanced accuracy in areas with local damage (a crack or opening) by using a peridynamic analysis framework, while providing improved computational efficiency for areas without damage by means of the finite element method. Furthermore, these two methods effectively reduce the solution time with an acceptable accuracy.

Chapter 8

Future Work

The capabilities of peridynamics have been successfully validated in numerous studies and this dissertation. Based on considerable improvements made so far, it is recommended that the proposed fracture modeling approach and its two-dimensional (2D) implementation be extended to three-dimensional (3D) problems. The first and foremost important step towards the 3D implementation will involve an extension of the proposed higher-order method in controlling the zero-energy mode. Furthermore, it is also recommended that the computational intricacy associated with the proposed higher-order expansion is evaluated in large-scale computational models.

In the proposed 3D fiber modeling approach, it is necessary to improve the computational accuracy and characterize more realistic fiber orientations in 3D fiber reinforced concrete (FRC) structures. Future research work includes the implementation and validation of the proposed fiber modeling approach in 3D problems. For instance, such FRC modeling method will be capable of characterizing the state-of-art ultra-high performance concrete (UHPC) structures which include micro-scale steel fibers. In addition, the proposed FRC model will enable a reliable performance prediction of FRC members subjected to various loading conditions such as impact loading.

Mesoscale modeling of cementitious composites is a demanding task requiring a consideration of heterogeneous material constituents and highly complex cracking mechanism. While the proposed approach builds a distinct framework for fracture analysis of concrete specimens, future research includes an implementation of the following features and tools for:

1. Studying the influence of shape and surface texture of the coarse aggregate.

2. Reducing the computational time by refining particle spacing and/or horizon size in the interfacial transition zone (ITZs), while providing accuracy.

3. Enhancing material models and damaged parameters for complex loading conditions, such as shear.

4. Extending the proposed analysis approach to 3D models in which, for instance, non-planar (or 3D) fracture surfaces are characterized.

The proposed NOSBPD-FE coupling is an effective method to reduce the computation cost of peridynamic simulations; however, a pre-defined crack path is necessary in order to generate peridynamic points. The crack path is a prior unknown in complex engineering structures and components. Therefore, an implementation of the adaptive NOSBPD-PD coupling method is recommended to address this deficiency. In such model, a solid body is initially discretized by commonly used finite elements. Under incremental loading, the finite elements are substituted by peridynamic points when they reaches a critical state, which will be defined by a material model.

Finally, it is recommended that advanced computational methods such as parallel computing techniques be studied in order to optimize computational expense of peridynamic simulations without sacrificing accuracy in predicting fracture behavior of composite structures.

Bibliography

[1] Y. Huang, Z. Yang, W. Ren, G. Liu, C. Zhang, 3d meso-scale fracture modelling and validation of concrete based on in-situ x-ray computed tomography images using damage plasticity model, International Journal of Solids and Structures 67 (2015) 340–352.

[2] J. F. Unger, S. Eckardt, C. Könke, Modelling of cohesive crack growth in concrete structures with the extended finite element method, Computer Methods in Applied Mechanics and Engineering 196 (41) (2007) 4087–4100.

[3] X. Wang, M. Zhang, A. P. Jivkov, Computational technology for analysis of 3d meso-structure effects on damage and failure of concrete, International Journal of Solids and Structures 80 (2016) 310–333.

[4] M. Vořechovskỳ, V. Sadílek, Computational modeling of size effects in concrete specimens under uniaxial tension, International Journal of Fracture 154 (1-2) (2008) 27–49.

[5] B. Patzák, M. Jirásek, Process zone resolution by extended finite elements, Engineering Fracture Mechanics 70 (7) (2003) 957–977.

[6] E. Roubin, A. Vallade, N. Benkemoun, J.-B. Colliat, Multi-scale failure of heterogeneous materials: A double kinematics enhancement for embedded finite element method, International Journal of Solids and Structures 52 (2015) 180–196.

[7] Z. P. Bazant, M. R. Tabbara, M. T. Kazemi, G. Pijaudier-Cabot, Random particle model for fracture of aggregate or fiber composites, Journal of engineering mechanics 116 (8) (1990) 1686–1705.

[8] G. Cusatis, D. Pelessone, A. Mencarelli, Lattice discrete particle model (ldpm) for failure behavior of concrete. i: Theory, Cement and Concrete Composites 33 (9) (2011) 881–890.

[9] E. Schlangen, J. Van Mier, Experimental and numerical analysis of micromechanisms of fracture of cement-based composites, Cement and concrete composites 14 (2) (1992) 105–118.

[10] E. Schlangen, J. Van Mier, Simple lattice model for numerical simulation of fracture of concrete materials and structures, Materials and Structures 25 (9) (1992) 534–542.

[11] E. Schlangen, J. Van Mier, Micromechanical analysis of fracture of concrete, International Journal of damage mechanics 1 (4) (1992) 435–454.

[12] E. Schlangen, E. Garboczi, Fracture simulations of concrete using lattice models: computational aspects, Engineering fracture mechanics 57 (2) (1997) 319–332.

[13] G. Lilliu, J. G. van Mier, 3d lattice type fracture model for concrete, Engineering Fracture Mechanics 70 (7) (2003) 927–941.

[14] P. Grassl, M. Jirásek, Damage-plastic model for concrete failure, International journal of solids and structures 43 (22) (2006) 7166–7196.

[15] S. A. Silling, Reformulation of elasticity theory for discontinuities and long-range forces, Journal of the Mechanics and Physics of Solids 48 (1) (2000) 175–209.

[16] S. A. Silling, E. Askari, A meshfree method based on the peridynamic model of solid mechanics, Computers & Structures 83 (17) (2005) 1526–1535.

[17] F. Bobaru, M. Yang, L. F. Alves, S. A. Silling, E. Askari, J. Xu, Convergence, adaptive refinement, and scaling in 1d peridynamics, International Journal for Numerical Methods in Engineering 77 (6) (2009) 852–877.

[18] Y. D. Ha, F. Bobaru, Studies of dynamic crack propagation and crack branching with peridynamics, International Journal of Fracture 162 (1-2) (2010) 229–244.

[19] F. Bobaru, Y. D. Ha, Adaptive refinement and multiscale modeling in 2d peridynamics.

[20] W. Hu, Y. D. Ha, F. Bobaru, S. A. Silling, The formulation and computation of the nonlocal j-integral in bond-based peridynamics, International journal of fracture 176 (2) (2012) 195–206.

[21] W. Liu, J.-W. Hong, Discretized peridynamics for brittle and ductile solids, International Journal for Numerical Methods in Engineering 89 (8) (2012) 1028–1046.

[22] F. Bobaru, W. Hu, The meaning, selection, and use of the peridynamic horizon and its relation to crack branching in brittle materials, International Journal of Fracture (2012) 1–8.

[23] M. Tupek, J. Rimoli, R. Radovitzky, An approach for incorporating classical continuum damage models in state-based peridynamics, Computer Methods in Applied Mechanics and Engineering 263 (2013) 20–26.

[24] E. Askari, F. Bobaru, R. Lehoucq, M. Parks, S. Silling, O. Weckner, Peridynamics for multiscale materials modeling, in: Journal of Physics: Conference Series, Vol. 125, IOP Publishing, 2008, p. 012078.

[25] H. Ren, X. Zhuang, Y. Cai, T. Rabczuk, Dual-horizon peridynamics, International Journal for Numerical Methods in Engineering.

[26] K. Yu, Enhanced integration methods for the peridynamic theory, Ph.D. thesis, Citeseer (2011).

[27] W. Gerstle, N. Sau, S. Silling, Peridynamic modeling of concrete structures, Nuclear engineering and design 237 (12) (2007) 1250–1258.

[28] S. A. Silling, M. Epton, O. Weckner, J. Xu, E. Askari, Peridynamic states and constitutive modeling, Journal of Elasticity 88 (2) (2007) 151–184.

[29] T. L. Warren, S. A. Silling, A. Askari, O. Weckner, M. A. Epton, J. Xu, A non-ordinary state-based peridynamic method to model solid material deformation and fracture, International Journal of Solids and Structures 46 (5) (2009) 1186–1195.

[30] S. Silling, R. Lehoucq, Peridynamic theory of solid mechanics, Advances in Applied Mechanics 44 (2010) 73–168.

[31] S. A. Silling, F. Bobaru, Peridynamic modeling of membranes and fibers, International Journal of Non-Linear Mechanics 40 (2) (2005) 395–409.

[32] W. Gerstle, N. Sau, E. Aguilera, Micropolar peridynamic modeling of concrete structures, in: Proceedings of the 6th international conference on fracture mechanics of concrete structures, 2007.

[33] S. Silling, O. Weckner, E. Askari, F. Bobaru, Crack nucleation in a peridynamic solid, International Journal of Fracture 162 (1-2) (2010) 219–227.

[34] A. Yaghoobi, M. G. Chorzepa, Fracture analysis of fiber reinforced concrete structures in the micropolar peridynamic analysis framework, Engineering Fracture Mechanics 169 (2017) 238–250.

[35] J. T. Foster, Dynamic crack initiation toughness: Experiments and peridynamic modeling, DOI 10 (2009) 1001000.

[36] S. A. Silling, Linearized theory of peridynamic states, Journal of Elasticity 99 (1) (2010) 85–111.

[37] J. Foster, S. A. Silling, W. Chen, An energy based failure criterion for use with peridynamic states, International Journal for Multiscale Computational Engineering 9 (6) (2011) 675–688.

[38] J. T. Foster, S. A. Silling, W. W. Chen, Viscoplasticity using peridynamics, International journal for numerical methods in engineering 81 (10) (2010) 1242–1258.

[39] M. Breitenfeld, P. Geubelle, O. Weckner, S. Silling, Non-ordinary state-based peridynamic analysis of stationary crack problems, Computer Methods in Applied Mechanics and Engineering 272 (2014) 233–250.

[40] A. Yaghoobi, M. G. Chorzepa, Meshless modeling framework for fiber reinforced concrete structures, Computers & Structures 161 (2015) 43–54.

[41] M. G. Chorzepa, A. Yaghoobi, Innovative meshless computational method for the analysis of fiber-reinforced concrete (frc) structures, in: Geotechnical and Structural Engineering Congress 2016, 2016, pp. 1209–1221.

[42] M. Tupek, R. Radovitzky, An extended constitutive correspondence formulation of peridynamics based on nonlinear bond-strain measures, Journal of the Mechanics and Physics of Solids 65 (2014) 82–92.

[43] T. J. Hughes, The finite element method: linear static and dynamic finite element analysis, Courier Corporation, 2012.

[44] T. Belytschko, W. K. Liu, B. Moran, K. Elkhodary, Nonlinear finite elements for continua and structures, John Wiley & Sons, 2013.

[45] R. Becker, R. J. Lucas, An assessment of peridynamics for pre and post failure deformation, Tech. rep., DTIC Document (2011).

[46] D. J. Littlewood, A nonlocal approach to modeling crack nucleation in aa 7075-t651, in: ASME 2011 International Mechanical Engineering Congress and Exposition, American Society of Mechanical Engineers, 2011, pp. 567–576.

[47] C. Wu, B. Ren, A stabilized non-ordinary state-based peridynamics for the nonlocal ductile material failure analysis in metal machining process, Computer Methods in Applied Mechanics and Engineering 291 (2015) 197–215.

[48] C. Dyka, R. Ingel, An approach for tension instability in smoothed particle hydrodynamics (sph), Computers & structures 57 (4) (1995) 573–580.

[49] P. Randles, L. Libersky, Normalized sph with stress points, International Journal for Numerical Methods in Engineering 48 (10) (2000) 1445–1462.

[50] T. Belytschko, Y. Guo, W. K. Liu, S. P. Xiao, A unified stability analysis of meshless particle methods, International Journal for Numerical Methods in Engineering 48 (9) (2000) 1359–1400.

[51] T. Rabczuk, T. Belytschko, S. Xiao, Stable particle methods based on lagrangian kernels, Computer methods in applied mechanics and engineering 193 (12) (2004) 1035–1063.

[52] Q. Shizhong, An adaptive dynamic relaxation method for nonlinear problems, Computers & Structures 30 (4) (1988) 855–859.

[53] B. Kilic, E. Madenci, An adaptive dynamic relaxation method for quasi-static simulations using the peridynamic theory, Theoretical and Applied Fracture Mechanics 53 (3) (2010) 194–204.

[54] M. Samal, M. Seidenfuss, E. Roos, A new mesh-independent rousselier's damage model: Finite element implementation and experimental verification, International Journal of Mechanical Sciences 51 (8) (2009) 619–630.

[55] G. R. Johnson, W. H. Cook, Fracture characteristics of three metals subjected to various strains, strain rates, temperatures and pressures, Engineering fracture mechanics 21 (1) (1985) 31–48.

[56] S. Silling, D. Littlewood, P. Seleson, Variable horizon in a peridynamic medium, Journal of Mechanics of Materials and Structures 10 (5) (2015) 591–612.

[57] D. Dipasquale, M. Zaccariotto, U. Galvanetto, Crack propagation with adaptive grid refinement in 2d peridynamics, International Journal of Fracture 190 (1-2) (2014) 1–22.

[58] F. Sanchez, K. Sobolev, Nanotechnology in concrete–a review, Construction and Building Materials 24 (11) (2010) 2060–2071.

[59] S. Ma, X. Zhang, Material point method for impact and explosion problems, in: Computational Mechanics, Springer, 2009, pp. 156–166.

[60] S. P. Lake, M. F. Hadi, V. K. Lai, V. H. Barocas, Mechanics of a fiber network within a non-fibrillar matrix: model and comparison with collagen-agarose co-gels, Annals of biomedical engineering 40 (10) (2012) 2111–2121.

[61] B. Luccioni, G. Ruano, F. Isla, R. Zerbino, G. Giaccio, A simple approach to model sfrc, Construction and Building Materials 37 (2012) 111–124.

[62] D. Ngo, A. C. Scordelis, Finite element analysis of reinforced concrete beams, Journal Proceedings 64 (3) (1967) 152–163.

[63] F. Radtke, A. Simone, L. Sluys, A computational model for failure analysis of fibre reinforced concrete with discrete treatment of fibres, Engineering Fracture Mechanics 77 (4) (2010) 597–620.

[64] F. Radtke, A. Simone, L. Sluys, A partition of unity finite element method for obtaining elastic properties of continua with embedded thin fibres, International Journal for Numerical Methods in Engineering 84 (6) (2010) 708–732.

[65] V. M. Cunha, J. A. Barros, J. M. Sena-Cruz, A finite element model with discrete embedded elements for fibre reinforced composites, Computers & structures 94 (2012) 22–33.

[66] J. Kang, K. Kim, Y. M. Lim, J. E. Bolander, Modeling of fiber-reinforced cement composites: Discrete representation of fiber pullout, International Journal of Solids and Structures 51 (10) (2014) 1970–1979.

[67] M. Forrestal, D. Frew, J. Hickerson, T. Rohwer, Penetration of concrete targets with deceleration-time measurements, International Journal of Impact Engineering 28 (5) (2003) 479–497.

[68] T. Chakherlou, A. Yaghoobi, Numerical simulation of residual stress relaxation around a cold-expanded fastener hole under longitudinal cyclic loading using different kinematic hardening models, Fatigue & Fracture of Engineering Materials & Structures 33 (11) (2010) 740–751.

[69] A. Yaghoobi, Finite element analysis of pressure vessels and fastener holes in elastic-plastic region using radial return algorithm, Master's thesis, University of Tabriz, Tabriz, Iran (2009).

[70] A. Saeidpour, Analysis of shear buckling behavior of hydrostatic pressured curved panels, Master's thesis, Amirkabir University of Technology, Tehran, Iran (2011).

[71] B. Bush, Analytical evaluation of concrete penetration modeling techniques, Master's thesis, North Carolina State University, Raleigh, NC (2010).

[72] T. Belytschko, Y. Krongauz, D. Organ, M. Fleming, P. Krysl, Meshless methods: an overview and recent developments, Computer methods in applied mechanics and engineering 139 (1) (1996) 3–47.

[73] T. Rabczuk, J. Eibl, Simulation of high velocity concrete fragmentation using sph/mlsph, International Journal for Numerical Methods in Engineering 56 (10) (2003) 1421–1444.

[74] W. Hu, Y. D. Ha, F. Bobaru, Peridynamic model for dynamic fracture in unidirectional fiber-reinforced composites, Computer Methods in Applied Mechanics and Engineering 217 (2012) 247–261.

[75] D. Huang, Q. Zhang, P. Qiao, Damage and progressive failure of concrete structures using non-local peridynamic modeling, Science China Technological Sciences 54 (3) (2011) 591–596.

[76] W. Liu, J.-W. Hong, A coupling approach of discretized peridynamics with finite element method, Computer Methods in Applied Mechanics and Engineering 245 (2012) 163–175.

[77] S. A. Silling, E. Askari, Peridynamic modeling of impact damage, in: ASME/JSME 2004 Pressure Vessels and Piping Conference, American Society of Mechanical Engineers, 2004, pp. 197–205.

[78] P. Demmie, S. Silling, An approach to modeling extreme loading of structures using peridynamics, Journal of Mechanics of Materials and Structures 2 (10) (2007) 1921–1945.

[79] W. Gerstle, N. Sau, N. Sakhavand, On peridynamic computational simulation of concrete structures, ACI Special Publication 265.

[80] J. A. Mitchell, A nonlocal, ordinary, state-based plasticity model for peridynamics, Sandia Report SAND2011-3166, Sandia National Laboratories, Albuquerque, NM.

[81] G. Hofstetter, H. A. Mang, Computational mechanics of reinforced concrete structures, Informatica International, Incorporated, 1995.

[82] L. Sluys, R. De Borst, Failure in plain and reinforced concretean analysis of crack width and crack spacing, International journal of solids and structures 33 (20) (1996) 3257–3276.

[83] G. Ruiz, J. R. Carmona, D. A. Cendón, Propagation of a cohesive crack through adherent reinforcement layers, Computer methods in applied mechanics and engineering 195 (52) (2006) 7237–7248.

[84] T. Rabczuk, G. Zi, S. Bordas, H. Nguyen-Xuan, A geometrically non-linear three-dimensional cohesive crack method for reinforced concrete structures, Engineering Fracture Mechanics 75 (16) (2008) 4740–4758.

[85] W. Gerstle, N. Sau, S. Silling, Peridynamic modeling of plain and reinforced concrete structures, in: SMiRT18, Int. Conf. Structural Mech. Reactor Technol, 2005.

[86] M. Jirásek, B. Patzák, Consistent tangent stiffness for nonlocal damage models, Computers & structures 80 (14) (2002) 1279–1293.

[87] J. De Vree, W. Brekelmans, M. Van Gils, Comparison of nonlocal approaches in continuum damage mechanics, Computers & Structures 55 (4) (1995) 581–588.

[88] Z. Lin, T. Kanda, V. C. Li, On interface property characterization and performance of fiber reinforced cementitious composites, Concrete Science and Engineering 1 (3) (1999) 173–184.

[89] H. A. Kormeling, H. W. Reinhardt, S. P. Shah, Static and fatigue properties of concrete beams reinforced with continuous bars and with fibers, ACI Journal Proceedings 77 (1) (1980) 36–43.

[90] D. Lange, C. Ouyang, S. Shah, Behavior of cement based matrices reinforced by randomly dispersed microfibers, Advanced Cement Based Materials 3 (1) (1996) 20–30.

[91] P. Soroushian, Z. Bayasi, Fiber type effects on the performance of steel fiber reinforced concrete, Materials Journal 88 (2) (1991) 129–134.

[92] R. F. Zollo, Fiber-reinforced concrete: an overview after 30 years of development, Cement and Concrete Composites 19 (2) (1997) 107–122.

[93] J. Thomas, A. Ramaswamy, Mechanical properties of steel fiber-reinforced concrete, Journal of materials in civil engineering 19 (5) (2007) 385–392.

[94] P. Soroushian, C.-D. Lee, Distribution and orientation of fibers in steel fiber reinforced concrete, Materials Journal 87 (5) (1990) 433–439.

[95] A. Carpinteri, R. Brighenti, Fracture behaviour of plain and fiber-reinforced concrete with different water content under mixed mode loading, Materials & Design 31 (4) (2010) 2032–2042.

[96] V. P. Dutra, S. Maghous, A. Campos Filho, A homogenization approach to macroscopic strength criterion of steel fiber reinforced concrete, Cement and Concrete Research 44 (2013) 34–45.

[97] J. Bolander, S. Saito, Discrete modeling of short-fiber reinforcement in cementitious composites, Advanced Cement Based Materials 6 (3) (1997) 76–86.

[98] A. Abrishambaf, V. M. Cunha, J. A. Barros, A two-phase material approach to model steel fibre reinforced self-compacting concrete in panels, Engineering Fracture Mechanics 162 (2016) 1–20.

[99] R. Brighenti, A. Carpinteri, A. Spagnoli, D. Scorza, Cracking behaviour of fibre-reinforced cementitious composites: A comparison between a continuous and a discrete computational approach, Engineering Fracture Mechanics 103 (2013) 103–114.

[100] C. Octávio, D. Dias-da Costa, J. Alfaiate, E. Júlio, Modelling the behaviour of steel fibre reinforced concrete using a discrete strong discontinuity approach, Engineering Fracture Mechanics 154 (2016) 12–23.

[101] I. C. Mihai, A. D. Jefferson, P. Lyons, A plastic-damage constitutive model for the finite element analysis of fibre reinforced concrete, Engineering Fracture Mechanics 159 (2016) 35–62.

[102] E. Madenci, E. Oterkus, Peridynamic theory and its applications, Vol. 17, Springer, 2014.

[103] E. Oterkus, Peridynamic theory for modeling three-dimensional damage growth in metallic and composite structures.

[104] E. Oterkus, E. Madenci, Peridynamic analysis of fiber-reinforced composite materials, Journal of Mechanics of Materials and Structures 7 (1) (2012) 45–84.

[105] E. Oterkus, E. Madenci, Peridynamic theory for damage initiation and growth in composite laminate, in: Key Engineering Materials, Vol. 488, Trans Tech Publ, 2012, pp. 355–358.

[106] N. Sau, Peridynamic modeling of quasibrittle structures, THE UNIVERSITY OF NEW MEXICO, 2008.

[107] B. K. Tuniki, Peridynamic constitutive model for concrete, Ph.D. thesis (2012).

[108] P. Young, T. Beresford-West, S. Coward, B. Notarberardino, B. Walker, A. Abdul-Aziz, An efficient approach to converting three-dimensional image data into highly accurate computational models, Philosophical Transactions of the Royal Society of London A: Mathematical, Physical and Engineering Sciences 366 (1878) (2008) 3155–3173.

[109] W. Ren, Z. Yang, R. Sharma, C. Zhang, P. J. Withers, Two-dimensional x-ray ct image based meso-scale fracture modelling of concrete, Engineering Fracture Mechanics 133 (2015) 24–39.

[110] Z. Wang, A. Kwan, H. Chan, Mesoscopic study of concrete i: generation of random aggregate structure and finite element mesh, Computers & Structures 70 (5) (1999) 533–544.

[111] X. Wang, Z. Yang, J. Yates, A. Jivkov, C. Zhang, Monte carlo simulations of mesoscale fracture modelling of concrete with random aggregates and pores, Construction and Building Materials 75 (2015) 35–45.

[112] J. Leite, V. Slowik, H. Mihashi, Computer simulation of fracture processes of concrete using mesolevel models of lattice structures, Cement and concrete research 34 (6) (2004) 1025–1033.

[113] A. P. Jivkov, Q. Xiong, A network model for diffusion in media with partially resolvable pore space characteristics, Transport in Porous Media 105 (1) (2014) 83–104.

[114] Q. Xiong, A. P. Jivkov, J. R. Yates, Discrete modelling of contaminant diffusion in porous media with sorption, Microporous and Mesoporous Materials 185 (2014) 51–60.

[115] S. Shahbeyk, M. Hosseini, M. Yaghoobi, Mesoscale finite element prediction of concrete failure, Computational Materials Science 50 (7) (2011) 1973–1990.

[116] J. Van Mier, M. Van Vliet, Influence of microstructure of concrete on size/scale effects in tensile fracture, Engineering fracture mechanics 70 (16) (2003) 2281–2306.

[117] A. Khalili, D. Samaratunga, R. Jha, T. E. Lacy, S. Gopalakrishnanrth, Wavelet spectral finite element based user-defined element in abaqus for modeling delamination in composite beams, in: 23nd AIAA/ASME/AHS Adaptive Structures Conference, 2015.

[118] A. Khalili, R. Jha, D. Samaratunga, Spectrally formulated user-defined element in conventional finite element environment for wave motion analysis in 2-d composite structures, European Journal of Computational Mechanics (2016) 1–29.

[119] J. F. Unger, S. Eckardt, Multiscale modeling of concrete, Archives of Computational Methods in Engineering 18 (3) (2011) 341–393.

[120] P. Wriggers, S. Moftah, Mesoscale models for concrete: Homogenisation and damage behaviour, Finite elements in analysis and design 42 (7) (2006) 623–636.

[121] G. A. Rao, B. R. Prasad, Influence of the roughness of aggregate surface on the interface bond strength, Cement and Concrete Research 32 (2) (2002) 253–257.

[122] G. Guinea, K. El-Sayed, C. Rocco, M. Elices, J. Planas, The effect of the bond between the matrix and the aggregates on the cracking mechanism and fracture parameters of concrete, Cement and concrete research 32 (12) (2002) 1961–1970.

[123] S. Häfner, S. Eckardt, T. Luther, C. Könke, Mesoscale modeling of concrete: Geometry and numerics, Computers & structures 84 (7) (2006) 450–461.

[124] A. Yaghoobi, M. G. Chorzepa, Higher-order approximation to suppress the zero-energy mode in non-ordinary state-based peridynamics, Computers & Structures.

[125] P. Underwood, Dynamic relaxation(in structural transient analysis), Computational methods for transient analysis(A 84-29160 12-64). Amsterdam, North-Holland, 1983, (1983) 245–265.

[126] J. OGrady, J. Foster, Peridynamic plates and flat shells: a non-ordinary, state-based model, International Journal of Solids and Structures 51 (25) (2014) 4572–4579.

[127] D. A. Hordijk, Tensile and tensile fatigue behaviour of concrete; experiments, modelling and analyses, Heron 37 (1).

[128] M. Tasdemir, B. Karihaloo, Effect of type and volume fraction of aggregate on the fracture properties of concrete, Fracture Mechanics of Concrete Structures, de Borst et al (eds) Swets & Zeitlinger, Lisse, ISBN 90 (2651) (2001) 825.

[129] B. Akcay, A. S. Agar-Ozbek, F. Bayramov, H. N. Atahan, C. Sengul, M. A. Tasdemir, Interpretation of aggregate volume fraction effects on fracture behavior of concrete, Construction and Building Materials 28 (1) (2012) 437–443.

[130] O. Sengul, C. Tasdemir, M. A. Tasdemir, Influence of aggregate type on mechanical behavior of normal-and high-strength concretes, Materials Journal 99 (6) (2002) 528–533.

[131] Z. P. Bazant, M. Jirásek, Nonlocal integral formulations of plasticity and damage: survey of progress, Journal of Engineering Mechanics 128 (11) (2002) 1119–1149.

[132] R. W. Macek, S. A. Silling, Peridynamics via finite element analysis, Finite Elements in Analysis and Design 43 (15) (2007) 1169–1178.

[133] B. Kilic, E. Madenci, Coupling of peridynamic theory and the finite element method, Journal of Mechanics of Materials and Structures 5 (5) (2010) 707–733.

[134] A. T. Glaws, Finite element simulations of two dimensional peridynamic models, Ph.D. thesis, Virginia Tech (2014).

[135] E. Oterkus, E. Madenci, O. Weckner, S. Silling, P. Bogert, A. Tessler, Combined finite element and peridynamic analyses for predicting failure in a stiffened composite curved panel with a central slot, Composite Structures 94 (3) (2012) 839–850.

[136] A. Agwai, I. Guven, E. Madenci, Drop-shock failure prediction in electronic packages by using peridynamic theory, IEEE Transactions on Components, Packaging and Manufacturing Technology 2 (3) (2012) 439–447.

[137] G. Lubineau, Y. Azdoud, F. Han, C. Rey, A. Askari, A morphing strategy to couple non-local to local continuum mechanics, Journal of the Mechanics and Physics of Solids 60 (6) (2012) 1088–1102.

[138] Y. Azdoud, F. Han, G. Lubineau, A morphing framework to couple non-local and local anisotropic continua, International Journal of Solids and Structures 50 (9) (2013) 1332–1341.

[139] F. Han, G. Lubineau, Y. Azdoud, Adaptive coupling between damage mechanics and peridynamics: a route for objective simulation of material degradation up to complete failure, Journal of the Mechanics and Physics of Solids.

[140] P. Seleson, S. Beneddine, S. Prudhomme, A force-based coupling scheme for peridynamics and classical elasticity, Computational Materials Science 66 (2013) 34–49.

[141] R. De Borst, M. A. Crisfield, J. J. Remmers, C. V. Verhoosel, Nonlinear finite element analysis of solids and structures, John Wiley & Sons, 2012.

[142] J. Lee, S. E. Oh, J.-W. Hong, Parallel programming of a peridynamics code coupled with finite element method, International Journal of Fracture (2016) 1–16.

[143] L. Zhang, T. Yu, Modified adaptive dynamic relaxation method and its application to elastic-plastic bending and wrinkling of circular plates, Computers & structures 33 (2) (1989) 609–614.

Appendix A

Discretization of the force state

In this study, a numerical discretization scheme is used to solve the equilibrium equation given in Eq. 3.6. In a discrete system, the equilibrium equation for the selected particle i can be expressed by:

$$\sum_{j=1}^{n}\{\underline{\mathbf{T}}[\mathbf{x}_i]\langle\mathbf{x}_j-\mathbf{x}_i\rangle-\underline{\mathbf{T}}[\mathbf{x}_j]\langle\mathbf{x}_i-\mathbf{x}_j\rangle\}\mathrm{d}V_j+\mathbf{b}\left(\mathbf{x}_i\right)=0 \tag{A.1}$$

Also, the nonlocal deformation gradient and shape tensor at a the same node can be expressed as:

$$\mathbf{F}\left(\mathbf{x}_i\right)=[\sum_{j=1}^{n}\omega\left(|\mathbf{x}_j-\mathbf{x}_i|\right)\left(\mathbf{Y}\langle\mathbf{x}_i-\mathbf{x}_j\rangle\otimes\left(\mathbf{x}_j-\mathbf{x}_i\right)\right)\mathrm{d}V_j].\mathbf{B}\left(\mathbf{x}_i\right) \tag{A.2}$$

$$\mathbf{B}\left(\mathbf{x}_i\right)=[\sum_{j=1}^{n}\omega\left(|\mathbf{x}_j-\mathbf{x}_i|\right)\left(\left(\mathbf{x}_j-\mathbf{x}_i\right)\otimes\left(\mathbf{x}_j-\mathbf{x}_i\right)\right)\mathrm{d}V_j]^{-1} \tag{A.3}$$

Substituting of $\underline{\mathbf{Y}}\langle\mathbf{x}_j-\mathbf{x}_i\rangle=\left(\mathbf{u}_j-\mathbf{u}_i\right)+\left(\mathbf{x}_j-\mathbf{x}_i\right)$ and definition of the shape matrix tensor $\mathbf{B}$ (Eq. A.3), the deformation gradient can be rewritten as:

$$\mathbf{F}\left(\mathbf{x}_i\right)=[\sum_{j=1}^{n}\omega\left(|\mathbf{x}_j-\mathbf{x}_i|\right)\left(\mathbf{u}_j-\mathbf{u}_i\right)\otimes\left(\mathbf{x}_j-\mathbf{x}_i\right)\mathrm{d}V_j].\mathbf{B}\left(\mathbf{x}_i\right)+\mathbf{I} \tag{A.4}$$

For a linearly elastic material, the small strain tensor is $\boldsymbol{\epsilon}=1/2\left(\mathbf{F}+\mathbf{F}^T\right)-\mathbf{I}$. Thus, the discretized form of small strain matrix takes the form of:

$$\boldsymbol{\epsilon}\left(\mathbf{x}_i\right)=\frac{1}{2}[\sum_{j=1}^{n}\omega\left(|\mathbf{x}_j-\mathbf{x}_i|\right)\left[\left(\mathbf{u}_j-\mathbf{u}_i\right)\otimes\left(\mathbf{x}_j-\mathbf{x}_i\right)+\left(\mathbf{x}_j-\mathbf{x}_i\right)\otimes\left(\mathbf{u}_j-\mathbf{u}_i\right)\right]\mathrm{d}V_j].\mathbf{B}\left(\mathbf{x}_i\right) \tag{A.5}$$

For a 2D plane stress problem, the small strain tensor can be rewritten as:

$$\boldsymbol{\epsilon} = \begin{bmatrix} \epsilon_{11} & \epsilon_{22} & \epsilon_{12} \end{bmatrix} = \mathbf{KNU} \tag{A.6}$$

where $\mathbf{K}$ is a $3 * 4$ matrix and represent the shape matrix, $\mathbf{B}$, in Eq. A.5:

$$\mathbf{K} = \begin{bmatrix} B_{11} & 0 & B_{12} & 0 \\ 0 & B_{12} & 0 & B_{22} \\ B_{12} & B_{11} & B_{22} & B_{12} \end{bmatrix} \tag{A.7}$$

$\mathbf{N}$ is a $4 * 2(n+1)$ matrix,

$$\mathbf{N} = \begin{bmatrix} N^{(1)} & 0 & ... & \omega\xi_{ij}^{x} V_j & 0 & ... \\ 0 & N^{(1)} & ... & 0 & \omega\xi_{ij}^{x} V_j & ... \\ N^{(2)} & 0 & ... & \omega\xi_{ij}^{y} V_j & 0 & ... \\ 0 & N^{(2)} & ... & 0 & \omega\xi_{ij}^{y} V_j & ... \end{bmatrix} \tag{A.8}$$

where $N^{(1)} = -\sum_{j=1}^{n} \omega\left(|\xi_{ij}|\right) \xi_{ij}^{x} V_j$ and $N^{(2)} = -\sum_{j=1}^{n} \omega\left(|\xi_{ij}|\right) \xi_{ij}^{y} V_j$. Also, ξ_{ij}^{x} and ξ_{ij}^{y} denote the components of bond, ξ_{ij}, in x and y directions, respectively. $\mathbf{U}$ is nodal displacement vector at particle i, and defined as:

$$\mathbf{U} = \begin{bmatrix} u_i & v_i & u_1 & v_1 & ... & u_n & v_n \end{bmatrix} \tag{A.9}$$

Noting that product of $\mathbf{N}$ and $\mathbf{U}$ represents the terms containing u and x in Eq. A.5. The stress at location x_i is:

$$\boldsymbol{\sigma} = \begin{bmatrix} \sigma_{11} & \sigma_{22} & \sigma_{12} \end{bmatrix} = \mathbf{DKNU} \tag{A.10}$$

where $\mathbf{D}$ is the plane stress isotropic elastic material stiffness,

$$\mathbf{D} = \frac{E}{1-\nu^2} \begin{bmatrix} 1 & \nu & 0 \\ \nu & 1 & 0 \\ 0 & 0 & (1-\nu)/2 \end{bmatrix} \tag{A.11}$$

where E and ν are the Young's modulus and Poisson's ratio, respectively.

The following matrix $\mathbf{Q}$ is introduced to capture the term $\mathbf{B}\xi$ in Eq. 3.7, where $\mathbf{Q}^* = \mathbf{B}\xi$ as:

$$\mathbf{Q} = \begin{bmatrix} \mathbf{Q}_1^* & 0 & \mathbf{Q}_2^* \\ 0 & \mathbf{Q}_2^* & \mathbf{Q}_1^* \end{bmatrix} \tag{A.12}$$

Finally, the discretized form of the force state $\mathbf{T}$ applied on $\mathbf{x}_i$ from $\mathbf{x}_j$ takes the form of:

$$\underline{\mathbf{T}}[\mathbf{x_i}]\langle \mathbf{x}_j - \mathbf{x}_i \rangle = \omega \left(|\mathbf{x}_j - \mathbf{x}_i| \right) \mathbf{QDKNU} \tag{A.13}$$

Appendix B

Dynamic relaxation

Kilic and Madenci [53] effectively used the adaptive dynamic relaxation method [125] for obtaining steady-state solutions of bond based peridynamic equations. In this study, the dynamic relaxation (DR) method is adopted to obtain quasi-static solutions of the NOSBPD equilibrium equation, (Eq. A.1). The peridynamic quasi static equilibrium equations can be expressed in the general form as:

$$\mathbf{P}\left(\mathbf{U}^{*}\right)+\mathbf{b}\left(\mathbf{X}\right)=0 \tag{B.1}$$

where $\mathbf{X}=\{\mathbf{x}_1,\mathbf{x}_2,...,\mathbf{x}_M\}$ and $\mathbf{U}^{*}=\{\mathbf{u}^{*}\left(\mathbf{x}_1\right),\mathbf{u}^{*}\left(\mathbf{x}_2\right),...,\mathbf{u}^{*}\left(\mathbf{x}_M\right)\}$ are vectors of position and actual displacements of the whole system points under body force loading, $\mathbf{b}$, respectively. If instead of $\mathbf{U}^{*}$, an approximate solution, $\mathbf{U}$, is substituted into Eq. B.1, a residual due to imbalance, $\mathbf{R}=\mathbf{P}\left(\mathbf{U}\right)+\mathbf{b}$, appears. It is considered that the residual force vector leads to the movement of the system so that the corresponding dynamic equations become:

$$\mathbf{M}\ddot{\mathbf{U}}+\mathbf{C}\dot{\mathbf{U}}+\mathbf{P}\left(\mathbf{U}\right)+\mathbf{b}\left(\mathbf{X}\right)=0 \tag{B.2}$$

where $\mathbf{M}$ and $\mathbf{C}$ are fictitious mass and damping matrices. The word 'fictitious' indicates that the dynamic process described in Eq. B.2 is fictitious as the DR method is used so that $\mathbf{M}$ and $\mathbf{C}$ can be artificially chosen to obtain the steady state solution in a minimum number of pseudo time increment steps. Therefore, assuming the damping has the form of $\mathbf{C}=c\mathbf{M}$, the explicit iteration formulas for solving the approximate displacement vector, $\mathbf{U}$ is obtained by using the central difference scheme with respect to pseudo-time.

$$\dot{\mathbf{U}}^{n+(1/2)}=\frac{2-\tau^{n}c^{n}}{2+\tau^{n}c^{n}}\dot{\mathbf{U}}^{n-(1/2)}+\frac{2\tau^{n}}{2+\tau^{n}c^{n}}\mathbf{M}^{-1}\mathbf{R}^{n} \tag{B.3}$$

$$\mathbf{U}^{n+1} = \mathbf{U}^n + \tau^{n+1}\dot{\mathbf{U}}^{n+(1/2)} \tag{B.4}$$

where τ^n is the pseudo time increment of the nth iteration. c^n is calculated by [143]:

$$c^n = 2\{\frac{(\mathbf{U}^n)^T \mathbf{P}(\mathbf{U}^n)}{(\mathbf{U}^n)^T \mathbf{M}\mathbf{U}^n}\}^{1/2} \tag{B.5}$$

Furthermore to guarantee the numerical stability, the elements of $\mathbf{M}$, m_{ii}, are determined by the Gerschgorin theorem as [143]:

$$m_{ii} \geq \frac{1}{4}(\tau^n)^2 \sum_j |k_{ij}| \tag{B.6}$$

where k_{ij} is the element of $\mathbf{K}$ which is calculated by:

$$\mathbf{K} = \frac{\partial \mathbf{P}(\mathbf{U})}{\partial \mathbf{U}} \tag{B.7}$$

Considering definition of the $\mathbf{P}$, stiffness matrix is equal to:

$$\mathbf{K} = \sum_{j=1}^{m} \left(\frac{\partial \mathbf{T}[\mathbf{x}_i]}{\partial \mathbf{U}_i} - \frac{\partial \mathbf{T}[\mathbf{x}_j]}{\partial \mathbf{U}_j} \right) V_j \tag{B.8}$$

where $\mathbf{U}_i$ is the displacement vector of all points within the horizon of point $\mathbf{x}_i$. Note that, $\mathbf{T}[\mathbf{x}_i]$ is only function of displacement of points inside the horizon, then its derivative regard the displacement of exterior points is equal to zero. Considering the value of force vector in Eq. A.13, we have:

$$\frac{\partial \mathbf{T}[\mathbf{x}_i]}{\partial \mathbf{U}_i} = w(|\boldsymbol{\xi}|)\,\mathbf{QDKNI},\ \mathbf{I} = \frac{\partial \mathbf{U}_i}{\partial \mathbf{U}_i} \tag{B.9}$$

Finally an absolute row sum of the stiffness matrix can be written as:

$$\sum_j |k_{ij}| = \sum_{j=1}^{m} \left(abs\left(\sum_{k=1}^{m_i} w(|\boldsymbol{\xi}|)\,\mathbf{QDKNI} \right) + abs\left(\sum_{k=1}^{m_j} w(|\boldsymbol{\xi}|)\,\mathbf{QDKNI} \right) \right) V_j \tag{B.10}$$

where m_i and m_j are number of points inside the horizon of the points $\mathbf{x}_i$ and $\mathbf{x}_j$, respectively.